UNIVERSITÀ
DEGLI STUDI
DI PADOVA

Università degli Studi di Padova

Department of Management and engineering

Ph.D. COURSE: Product innovations engineering and mechatronics

CURRICULUM: Mechanics of materials

Development and characterization of a new generation of transition elements based secondary Al-Si-Cu-Mg foundry alloys

Thesis was written with the financial contribution of Erasmus Mundus Silkroute project

Coordinator: Prof. Roberto Caracciolo

Supervisor: Prof. Franco Bonollo

Co-Supervisor: Prof. Giulio Timelli

Ph.D. student: Jovid Rakhmonov

2017

I would like to dedicate this thesis to my family, my children Bunyod and Diyora.

ABSTRACT

Secondary Al-Si-Cu-Mg based foundry alloys are widely used in automotive industry to particularly produce powertrain cast components mainly due to their good ratio between weight and mechanical properties, and excellent casting characteristics.

Presence of impurity elements, such as Fe, Mn, Cr, Ti, V and Zr, in secondary Al-Si alloys is one of the critical issues since these elements tend to reduce alloy mechanical properties. There is an ongoing effort to control the formation of intermetallic phases containing transition metals, during alloy solidification. Although phases formation involving these transition metal impurities in non-grain-refined Al-Si alloys is well documented in the literature, the role of grain refinement in microstructural evolution of secondary Al-Si-Cu-Mg alloys needs further experimental investigations since chemical grain refinement is one of the critical melt treatment operations in foundries. The primary aim of this PhD work is thus defined to characterize the formation of intermetallic phases containing transition metals in secondary Al-7Si-3Cu-0.3Mg alloy before and after grain refinement by different master alloys and contribute to the understanding of the mechanisms underlying the microstructural changes occurring with the addition of grain refiner.

Another critical issue related to Al-Si-Cu-Mg alloys is their limited thermal stability at temperatures above 200 ^{o}C. The operating temperature in engine combustion chamber is reported to often exceed 200 ^{o}C during service. Moreover, a further increase of operating temperature is anticipated due to the expected engine power enhancement in near future, which indicates the necessity for the development of a new creep-resistant Al alloys. Deliberate addition of transition metals is believed to yield a new heat-resistant alloy by promoting the formation of thermally stable dispersoids inside α-Al grains. This study thus also attempted to investigate the effect of adding transition metals Zr, V and Ni on the solidification processing, microstructural evolution and room/high-temperature tensile properties of secondary Al-7Si-3Cu-0.3Mg alloy, one of the most used alloys in automotive engine manufacturing.

The influence of transition metal impurities on microstructural evolution of secondary Al-7Si-3Cu-0.3Mg alloy was investigated before and after chemical treatment with different master alloys: Al-10Sr, Al-5Ti-1B, Al-10Ti and Al-5B. The Al-10Zr, Al-10V and Al-25Ni master alloys were used for the experimental investigations of the effects of deliberate additions of transition metals on the solidification path, microstructure and mechanical properties of secondary Al-7Si-3Cu-0.3Mg alloy. Solidification path of the alloys was characterized by the traditional thermal analysis technique and differential scanning calorimetry (DSC). Optical microscope (OM), scanning electron microscope (SEM) equipped with energy-dispersive (EDS), wavelength-dispersive spectrometers (WDS) and electron backscattered diffraction (EBSD) and transmission electron microscopy (TEM) equipped with EDS were used to characterize the type, morphology and distribution of the phases precipitated during solidification and heat treatment of the studied alloys. The static tensile properties of the alloys were characterized at room (20 ^{o}C) and high temperatures (200 and 300 ^{o}C).

Experimental findings indicate that the Sr-modification and grain refinement of secondary Al-7Si-3Cu-0.3Mg alloy with Al-Ti-B can be enough effective despite the presence of transition metal impurities in the material and the variation of pouring temperature. However, the V and Zr (~100 ppm each) available in secondary Al-7Si-3Cu-0.3Mg alloy tended to promote the precipitation of harmful, primary AlSiTi intermetallics during solidification of grain-refined alloy. This implies that more effective optimization of grain refiner addition level in secondary Al foundry alloys can be achieved by considering the role of transition metal impurities, Ti, V and Zr, since the formation of primary AlSiTi particles causes (1) the depletion of Ti needed for effective α-Al grains growth restriction and (2) the formation of casting defects, such as shrinkage, due to their flaky morphology.

Iron available in secondary Al-7Si-3Cu-0.3Mg alloy as impurity only formed more desirable α-$Al_{15}(FeMn)_3Si_2$ phase in non-grain refined state. After grain refinement by Al-5Ti-1B, Fe was also involved in the formation of more deleterious β-Al_5FeSi phase. The TiB_2 particles acted as nucleation site for β-Al_5FeSi phase. Both higher cooling rate and higher Al-5Ti-1B addition levels tended to promote the formation of deleterious β-Al_5FeSi at the expense of α-$Al_{15}(FeMn)_3Si_2$ in the alloy refined by Al-5Ti-1B. This implies that rather than the ratio between Mn and Fe, the nucleation kinetics of Fe-rich intermetallics play a decisive role in the selection of competing α-$Al_{15}(FeMn)_3Si_2$ and β-Al_5FeSi intermetallic phases for the precipitation during alloy solidification. Moreover, grain refinement of secondary Al-7Si-3Cu-0.3Mg alloy by Al-5B showed comparable performance to that of Al-5Ti-1B master alloy, however, without any deleterious influence on the precipitation sequence of Fe-rich phases, i.e. deleterious β-Al_5FeSi reaction remained unfavourable during alloy solidification.

Experimental findings from the investigations of the effect of deliberate Zr and V addition revealed that Zr and V addition can induce the grain refinement of secondary Al-7Si-3Cu-0.3Mg alloy. While Zr addition yielded the formation of pro-peritectic Zr-rich particles, which are found to nucleate primary α-Al at low undercooling, the effect of adding V can be characterized by the enhancement of the degree of constitutional undercooling. Combined Zr and V addition showed more effective grain refinement level than their individual additions.

Majority of both Zr and V added to the alloy were retained inside α-Al matrix during solidification. As a result, limited amounts of Zr and V were rejected to the interdendritic liquid by the growing α-Al dendrites, then forming small-sized and rarely distributed intermetallics. Owing to its low solid solubility in α-Al, nickel available as impurity (~ 200 ppm) or after deliberate addition (0.25 wt.%) in secondary Al-7Si-3Cu-0.3Mg alloy was mainly bound to interdendritic, insoluble intermetallics, such as Al_6Cu_3Ni and $Al_9(FeCu)Ni$ phases. The presence of ~ 200 ppm Ni was sufficient to diminish to a certain extent the precipitation hardening effect of Cu. Interdendritic Zr/V/Ni-rich phases remained undissolved into the α-Al matrix during solution heat treatment. Therefore, the supersaturated transition metals in α-Al solid solution obtained during solidification was only involved in the solid-state precipitation occurring during heat treatment. Unlike Cu/Mg-rich strengthening precipitates that commonly form during aging, the Zr/V-rich precipitates tended to form during solution heat treatment. Other transition metals, such as Mn, Fe, Cr and Ti, which were present as impurities in secondary Al-7Si-3Cu-0.3Mg alloy significantly promoted the formation of

nano-sized Zr/V-rich precipitates inside α-Al grains. These thermally more stable precipitates, including novel α-Al(MnVFe)Si, were credited for the enhanced high-temperature strength properties of Al-7Si-3Cu-0.3Mg alloy by ~ 20 %.

Keywords: secondary Al-Si alloys, transition metals, solidification path, microstructure, intermetallics, heterogeneous nucleation, high-temperature strength.

ACKNOWLEDGEMENTS

I would like to express my sincere gratitude to:

- Prof. Franco Bonollo and Prof. Giulio Timelli for their excellent supervision, continuous encouragement and support.
- Erasmus Mundus Silkroute project for financial support.
- Dr. L. Capra (Raffineria Metalli Capra Spa, Italy), Mr. R. Zambelli (Raffmetal Spa, Italy) and Mr. G. Muneratti (Foseco) for the experimental support to the research.
- Mr. L. Mariani (Media System Lab Srl) and Dr. F. Reinauer (AMETEK EDAX BU) for the support with WDS analysis.
- Dr. Alberto Fabrizi for his assistance with SEM and TEM analyses.
- Mr. G. Mazzacavallo and Mr. D. Soliman, Dr. D. Calliari, Dr. E. Battaglia and Dr. S. Capuzzi for help with casting trials.
- My family and friends.

SUPPLEMENTS

The following supplements constitute the basis of this thesis.

Supplement I

J. Rakhmonov, G. Timelli and F. Bonollo, Influence of melt superheat and Sr modifier and Al-5Ti-1B grain refiner on microstructural evolution of secondary Al-Si-Cu alloys, Metallurgical and Materials Transactions A, 2016 (47A), 5511-5521

Supplement II

J. Rakhmonov, G. Timelli, F. Bonollo and L. Arnberg, Influence of grain refiner addition on the precipitation of Fe-rich phases in secondary AlSi7Cu3Mg alloy, International journal of metal-casting, 2017 (11), 294-304

Supplement III

J. Rakhmonov, G. Corradin, G. Timelli and H. Liu, Comparison of the effects of Al-5B and Al-5Ti-1B grain refiners on the formation of Fe-rich phases in secondary Al-7Si-3Cu-0.3Mg alloys, Proceedings of the 6th Decennial International Conference on Solidification Processing, Old Windsor, 2017, 162-165

Supplement IV

J. Rakhmonov, G. Timelli and F. Bonollo, Characterization of the effects of Zr, V and Ni on solidification path and microstructural evolution of secondary AlSi7Cu3Mg alloy, Material characterization, 2017 (128), 100-108

Supplement V

J. Rakhmonov, G. Timelli, A. Fabrizi and F. Bonollo, Effect of V and Zr Microalloying and Heat Treatment on Microstructure and Mechanical Properties of Secondary Al-7Si-3Cu-0.3Mg Alloy, submitted for publication in Metallurgical and materials transaction A, 2017

Other scientific contributions:

1. J. Rakhmonov, G. Timelli and F. Bonollo, The influence of AlTi5B1 grain refinement and cooling rate on the formation behaviour of Fe-rich compounds in secondary AlSi8Cu3 alloys, La metallurgia italiana, 2016 (6), 109-112
2. J. Rakhmonov, G. Basso and G. Timelli, Interaction of Ca, P trace elements and Sr modification in AlSi5Cu1Mg alloys, submitted for publication in Internation journal of Thermal analysis and calorimetry
3. J. Rakhmonov, G. Timelli and F. Bonollo, The effect of transition elements on high-temperature mechanical properties of Al-Si foundry alloys - a review, Advanced engineering materials, 2016 (18), 1096-1105

Co-supervision of BSc and MSc theses:

- Alberto Guarda: Thermal analysis of ZE41A magnesium foundry alloys for aeronautic applications, A. A. 2014-15
- Alessandro Bianco: Mechanical properties of AlSi7Mg foundry alloys produced with different casting parameters, A. A. 2014-15
- Nicola Magoga: Development of innovative AlMg5Si2Mn (EN AC-51500) aluminium foundry alloys, A. A. 2015-16
- Giulia Basso: Effect of Ca and Sr interaction on the eutectic modification of AlSi5Cu1Mg foundry alloys, A. A. 2015-16
- Davide Soliman: Development and characterization of innovative AlSi5Cu1Mg aluminium foundry alloys, A. A. 2016-17
- Alessandro de Morri: High-temperature fatigue behaviour of innovative aluminium foundry alloys, A. A. 2016-17
- Giovanni Corradin: Comparison of the effects of Al-B and Al-Ti-B grain refiners on solidification path and microstructural evolution of AlSi7Cu3Mg alloys, A. A. 2016-17

TABLE OF CONTENTS

1. INTRODUCTION

CHAPTER INTRODUCTION

This chapter summarizes the literature most pertinent to the subject of this thesis. It has been composed of four main sections: the first section describes background of Al-Si-Cu-Mg alloys, while the second section is about the solidification processing and microstructural evolution of Al-Si-Cu-Mg alloys; the third section outlines the role of heat treatment in Al-Si-Cu-Mg alloys and the fourth section discusses the high-temperature strengthening in Al-Si-Cu-Mg alloys via transition metals addition. Some materials presented in the fourth section has been published in the form of a review paper [1].

1.1. Al-Si BASED FOUNDRY ALLOYS: BACKGROUND

Al-Si based alloys are highly preferred in automotive industry due to their high strength to weight ratio as well as excellent castability, recyclability and thermal conductivity. Improved castability e.g. better fluidity, is critical for obtaining complex and sound castings having intricate shapes and thin walls. The secondary Al production process is highly attractive as it requires significantly less energy and emits less CO_2 to the atmosphere compared to the primary production route of Al alloys [2]. Over 90% of the Al alloys used in transportation industry comes from secondary sources, i.e. recycled material [3].

The Al-Si based alloys can be considered as the most important foundry alloys to produce automotive engine components, such as cylinder head and -block. In hypoeutectic Al-Si alloys, the Si content normally ranges between 5 and 12 wt. % (see Figure 1). Silicon significantly improves castability [4] and wear resistance [5], and also contributes to reducing the density and the coefficient of thermal expansion of aluminium alloys [4]. Moreover, Si contributes to the precipitation hardening of Al-Si-Cu-Mg alloys by interacting with Mg. Cu and Mg are commonly added to improve alloy strength properties mainly by precipitation hardening mechanism [3].

Several types of trace (impurity) elements in small amounts are normally present in secondary Al alloys; these elements can exert negative effects on mechanical properties and final quality of cast components [2]. Iron is considered as the most harmful and common trace element and causes the formation of interdendritic, needle-like compounds, which degrade alloy mechanical properties, particularly ductility.

Alloy composition and processing conditions can control the evolution of microstructure, which, in turn, defines alloy (mechanical) properties. The typical microstructural constituents of hypoeutectic Al-Si based foundry alloys are α-Al dendrites, eutectic Si particles and intermetallic phases, such as Al_2Cu, Mg_2Si and Fe-rich compounds. The refinement of microstructural constituents is beneficial; this is normally achieved through the application of high cooling rate

and/or chemical modification. The Al-Si-Cu-Mg alloys can be significantly strengthened via post-solidification heat treatment.

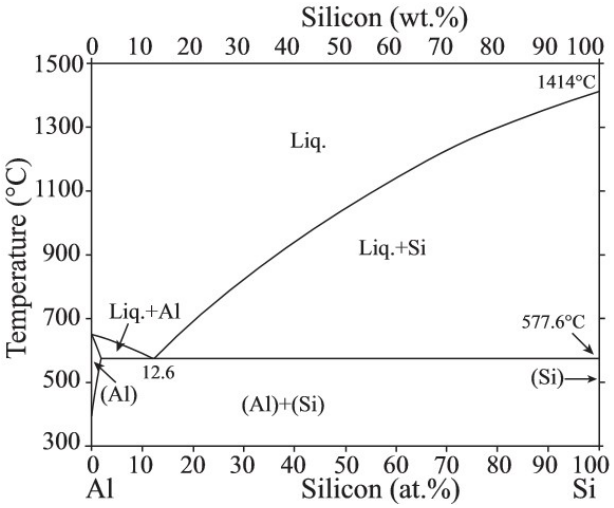

Figure 1. The equilibrium phases diagram of the Al–Si alloy system [6].

Although commercially available and currently used Al-Si-Cu-Mg alloys exhibit excellent strength properties, their mechanical performance at temperatures above 200 ^{o}C is poor because solute diffusion of Cu and Mg becomes faster at these temperatures, thus enabling the coarsening and/or dissolution of strengthening precipitates. However, a further expected enhancement of engine power in near future is thought to increase the operation temperature beyond 200 ^{o}C [7], which indicates the necessity for the development of a new creep-resistant Al-Si based foundry alloys.

1.2. SOLIDIFICATION OF Al-Si-Cu-Mg ALLOYS

Casting is an important and integral part of the manufacturing process of any metals and alloys. In addition, alloying of two or more elements is normally conducted in the liquid state as achieving uniform composition needs rapid diffusion. This means that gaining an understanding of the solidification behaviour of metals and alloys is essential to be able to control material properties.
Two subjects that underlie the solidification of metals and alloys are chemical thermodynamics and chemical kinetics. Chemical thermodynamics predicts the most stable phases at given temperature, pressure, compositions relating to only the initial and final states of a system. Chemical equilibrium is controlled by the Gibbs free energy (G) of the system which is minimized for equilibrium conditions. In contrast, chemical kinetics controls the dynamic system transformation between initial and final states and indicates the path and phase changes of a chemical reaction in a system when the limited atomic movement becomes dominant in a short process time. Hence, the solidification rate under a real time condition will be greatly influenced by the nucleation efficiency and the atom diffusion between phases [8, 9].
Solidification of hypoeutectic Al-Si based foundry alloys begins with the nucleation and growth of the primary α-Al, followed by subsequent precipitation of various phases containing alloying and trace elements. The typical cooling curve and summary of the reactions during solidification of A319 (Al-Si-Cu-Mg based) alloy are shown in Figure 2 and Table 1, respectively [10].

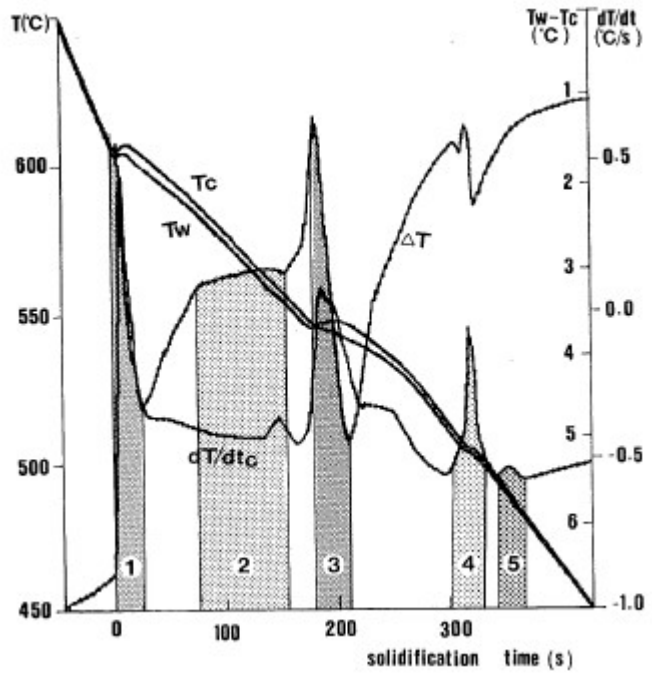

Figure 2. Thermal analysis data collected from center and wall regions during solidification of A319 (Al-Si-Cu-Mg based) alloy [10].

Table 1. Summary of reactions occurring during solidification of A319 alloys [10].

Reaction No.	Reaction type	Temp. °C
1	Formation of α-Al dendrite network	609
2	a) L → (Al) + $Al_{15}Mn_3Si_2$	590
	b) L → (Al) + $Al_{15}Mn_3Si_2$ + (Al_5FeSi)	
3	L → (Al) + Si + Al_5FeSi	575
4	L → (Al) + Al_2Cu +Si + Al_5FeSi	525
5	L → (Al) + Al_2Cu + Si + $Al_5Cu_2Mg_8Si_6$	507

The solidification rate defines the scale (coarseness) of the microstructure including the fraction, size and distribution of primary α-Al, eutectic Si and intermetallic phases, and the segregation profiles of solute elements inside α-Al grains. Increasing the solidification rate refines all microstructural features including grain size, secondary dendrite arm spacing (SDAS), eutectic Si particles and intermetallic phases [8, 11-17]. Large and brittle intermetallic phases form during slow solidification, which may initiate or link fracture, thus decreasing elongation to failure. Moreover, the defect size, such as pore size, is also controlled to some extent by the solidification rate. The influence of defects on elongation to failure and fatigue properties depends on their size, shape, distribution and fraction [8, 18].

However, the solidification rate cannot be effectively controlled in medium- and large-sized castings; hence, the chemical treatment of the molten metal becomes an essential tool for manipulating and controlling the evolution of microstructure in the slowly-solidifying regions. Sections 1.2.1 and 1.2.2 outline the roles of grain refinement and eutectic modification, respectively, in controlling the microstructural evolution of Al-Si based foundry alloys.

1.2.1. Grain refinement

Grain refinement is a common practice in foundries to obtain fine and equiaxed α-Al grains structure. The refined grain structure provides uniform mechanical properties, reduced ingot

cracking, improved feeding to eliminate shrinkage porosity, fine and homogeneous distribution of intermetallic compounds and microporosity, and also improved machinability [19].

The most common technique to promote the formation of fine and equiaxed α-Al grains is to add certain chemical elements or agents that facilitate easy nucleation of α-Al grains. Commercial Al-Ti-B based grain refiners, which are normally manufactured with more Ti amounts than that required to form TiB_2, are commonly used worldwide for the grain refinement of Al alloys [20-22]. The most widely used grain refiner for Al alloys is Al-5Ti-1B (in wt.%) master alloy, which contains excess Ti over the stoichiometric ratio of TiB_2 [23]; while insoluble TiB_2 acts as heterogeneous nucleation sites for α-Al, excess Ti provides significant constitutional undercooling at the growth front, thus enhancing the potency of TiB_2, and also slowing down the growth of α-Al [14, 23, 24]. Timelli et al. [14] reported how increasing the amount of Al-5Ti-1B grain refiners can progressively reduce the grain size of Al-7Si-3Cu-Mg alloy in the addition level of up to 0.17 wt.% Ti, while further increase of grain refiner addition level showed no apparent influence on the level of grain refinement (see Figure 3); changes in the nucleation and growth temperatures of α-Al with grain refiner addition were also observable in the cooling curves, as can be seen in Figure 4.

Although several mechanisms responsible for the grain refinement of Al alloys, induced by the addition of Al-Ti-B based grain refiners have been proposed [19, 23, 25-27], recent studies [23] claim that effective grain refinement by the Al-5Ti-1B grain refiner is directly attributed to the enhanced potency of TiB_2 particles as a result of (1) the formation of Al_3Ti two-dimensional compound (2DC) on the basal surface of TiB_2 and (2) the presence of sufficient free Ti solute in the melt. According to binary Al-Ti system, bulk Al_3Ti phase (three-dimensional) is only stable in liquid Al at Ti concentrations greater than 0.15% [23]; however, Al_3Ti 2DC may be stable at the liquid/substrate interface even at lower Ti concentrations (<0.15%) because adsorption of solute Ti atoms from the melt to the (0001) TiB_2 surface to form Al_3Ti 2DC tends to reduce interfacial energy [23].

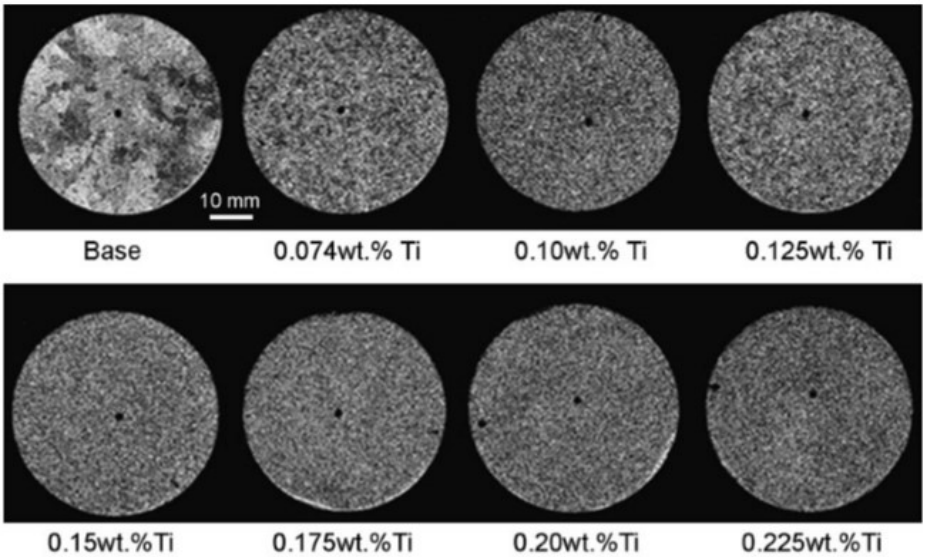

Figure 3. Effects of Al-5Ti-1B addition on the grain structure of thermal analysis test sections. The amount of Al-5Ti-1B master alloy is expressed as Ti content [14].

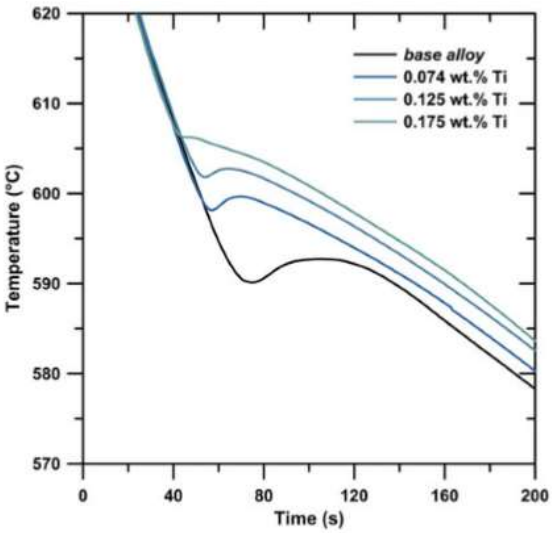

Figure 4. Cooling curves of the Al-7Si-3Cu-0.3Mg alloy in the region of primary a-Al formation at different Al-5Ti-1B levels. The amount of grain refiner is expressed as Ti content [14].

Although the Al-5Ti-1B grain refiners perform well in wrought Al alloys [28-30], their performance is limited in Al-Si foundry alloys with higher Si concentration [31, 32]. High content of Si, which leads to the formation of silicides by interacting with Ti and Al and thus severely impairs the potency of TiB_2 and Al_3Ti particles, is claimed to be responsible for the poor response of foundry Al alloys to grain refinement with Al-Ti-B master alloys [33]. Furthermore, the presence of some trace elements, such as Zr, can induce negative impact on the grain refining efficiency of Al-Ti-B master alloys and, as a result, the optimum level of grain refiners in secondary Al alloys cannot be equally achieved as compared to primary alloys [29, 34]. Zirconium is thought to poison the potency of nucleation agents, such as TiB_2 particularly at higher melt superheats, ~800 ºC [29], however, the mechanism underlying this behaviour remains unclear. Since secondary Al alloys normally contains several types of transition metals as impurities, such as Zr, V, Cr, further investigations seem still necessary to assess the grain refining efficiency of Al-Ti-B refiners.

In view of the poor grain refining performance of Al-5Ti-1B in Al-Si alloys with higher Si concentrations, there is an ongoing research to develop new types of grain refiners [35, 36]. Al-B can be a substitute for Al-Ti-B system as AlB_2 particles have been found to be highly efficient in grain refinement of Al-Si alloys with higher Si levels [36].

1.2.2. Eutectic modification

Owing to their faceted growth mode, eutectic Si particles tend to precipitate in flaky morphology under normal solidification conditions [37]. The size and morphology of eutectic Si particles have significant influence on alloy mechanical properties, particularly ductility. Coarse, flaky Si particles may act as stress concentration sites and crack propagation paths. Application of high solidification rates or solution heat treatment, and addition of certain elements, such as Sr and Na, to Al-Si alloys are the most common techniques to enable the growth of Si particles in more desirable morphology [38]. For gravity- and sand-casting processes, the addition of Sr or Na have been found to be very effective in changing the morphology of Si particles from flaky-like to fibrous-like (see Figure 5), which is referred to as the eutectic modification in the literature. In

general, modification of eutectic Si particles can be achieved by introducing a very low amount (150-300 ppm) of alloying element, such as Sr, into the melt [39-42].
The most well-accepted mechanism of eutectic Si modification by impurities has been explained by Lu and Hellawell [43, 44]; the authors reported that impurity atoms of the suitable size can force the nucleation of twins and stacking faults at the solid-liquid (eutectic Si-melt) interface. These twins create sites for atom attachment at the interface, facilitating the growth in a manner like that of an atomically rough interface. As a result, the morphology of the eutectic Si particles modifies from flakes to fibers (see Figure 6). Recently, it has been revealed that Sr-Al-Si clusters can form at the eutectic Si/liquid interface and also take part in the modification process by altering the growth of eutectic Si [45, 46].

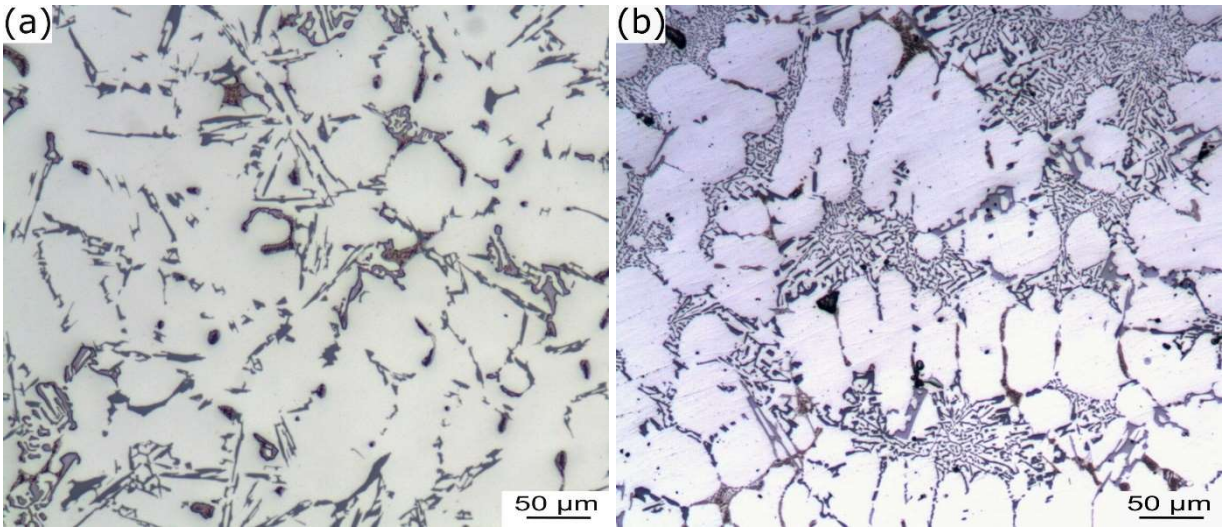

Figure 5. Comparison of the eutectic Si morphology in (a) unmodified and (b) Sr-modified (300ppm Sr) Al-7Si-3Cu-0.3Mg alloy.

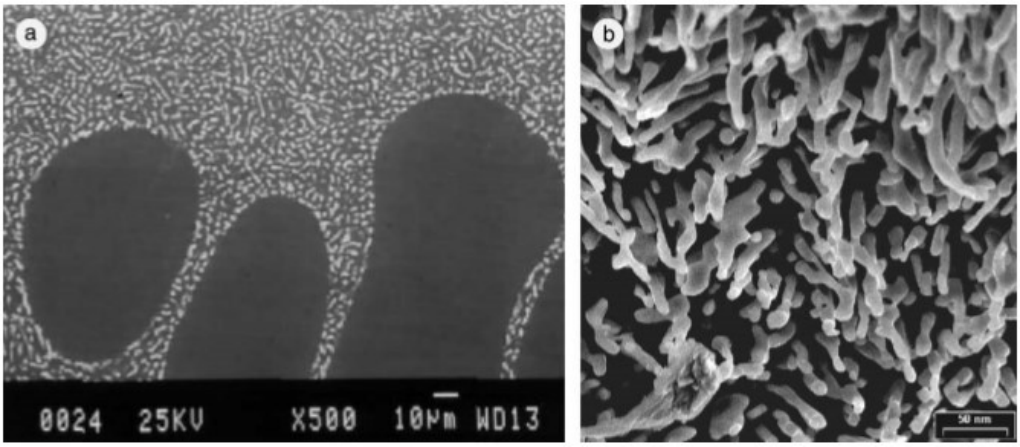

Figure 6. Microstructure of a Sr-modified Al-Si alloy (a) at low magnification, and (b) at higher magnification and deeply etched [47].

1.2.3. Formation of Fe-rich intermetallic phases

Iron is one of the most harmful impurities in Al-Si foundry alloys and its content tends to increase modestly the more frequently the metal has been recycled. Wear and tear of process equipment is the main source for the build-up of Fe impurities [48]. Owing to low solid solubility in α-Al, solute Fe tends to strongly partition into the interdendritic regions and, depending on the cooling rate and

the alloy composition, the formation of various Fe-rich compounds such as α-Al_8Fe_2Si or -$Al_{15}(FeMn)_3Si_2$, β-Al_5FeSi, δ-Al_4FeSi_2, N-Al_7Cu_2Fe and π-$Al_8Mg_3FeSi_6$ phases can occur during alloy solidification [49, 50].

The α-$Al_{15}(FeMn)_3Si_2$ and β-Al_5FeSi are the most common compounds appearing in the microstructure of Al-Si alloys. The non-faceted α-$Al_{15}(FeMn)_3Si_2$ grows more easily in irregular and curved crystal form conforming to the complicated shape of the interdendritic spaces during solidification (see Figure 7) [10]. In contrast, the growth of β-Al_5FeSi phase occurs with the twin plane re-entrant (TPRE) mechanism in a faceted mode (see Figure 8) [51, 52].

The β-Al_5FeSi is the most deleterious Fe-rich phase. The high-stress concentrations at sharp edges of β-Al_5FeSi particles as well as the weak bond between the β-Al_5FeSi phase and the Al matrix promote crack initiation, thus decreasing alloy ductility [53]. The platelet morphology of this phase creates feeding difficulties during solidification, leading to porosity formation [54]. Furthermore, the β-Al_5FeSi compounds are brittle and hard which is deleterious to the machinability of cast parts [55].

The formation of β-Al_5FeSi in the microstructure can be alleviated by various techniques: (1) alloying with transition elements such as Mn, Cr, V, Ni; (2) rapid solidification; (3) melt superheating [56]. The most common technique to neutralize/minimize the adverse effects of Fe is Mn addition and thus promotion of the formation of less harmful α-$Al_{15}(FeMn)_3Si_2$ phase during alloy solidifiication. The weight ratio between Fe and Mn, that is needed to avoid the formation of β-Al_5FeSi particles, depends on both the content of Fe and the cooling rate [57]. However, the ratio of 2:1 between Fe and Mn has been generally accepted as an optimum level.

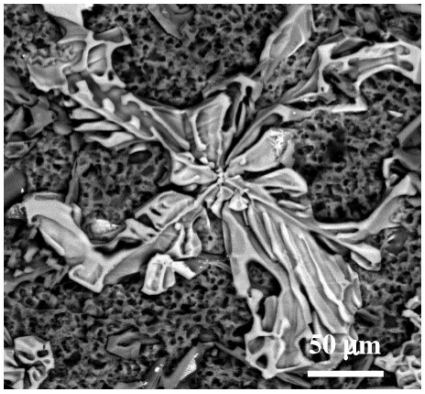

Figure 7. Morphology of α-$Al_{15}(FeMn)_3Si_2$ intermetallics in Al-Si-Cu alloy [58].

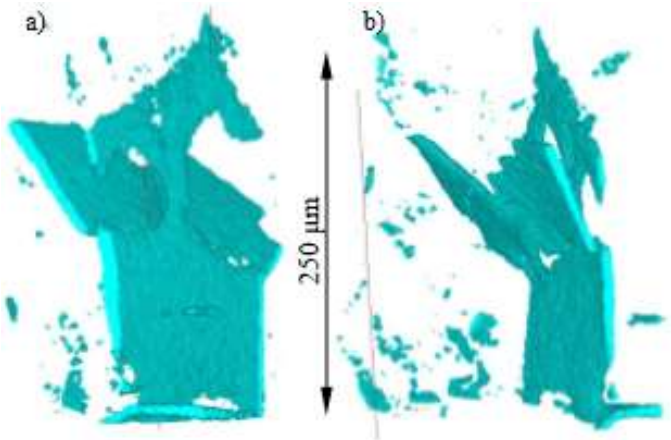

Figure 8 a and b. Two views of the same group of β-Al_5FeSi intermetallics in Al-9Si-1Fe alloy [59].

In addition, applying higher cooling rate has been reported to eliminate or reduce β-Al_5FeSi formation [60-63]. The displacement of the nucleation temperature of β-Al_5FeSi towards lower temperatures with increasing cooling rate has been observed, thus reducing the time available for the growth of β-Al_5FeSi [57]. Moreover, it is also well-known that the cooling rate can control the nucleation and growth processes, affecting both the number density and the size of microstructural features, such as β-Al_5FeSi particles [64, 65].

Several studies have focused on understanding the nucleation behaviour of β-Al_5FeSi [57, 66]. The γ-Al_2O_3 particles are believed to serve as a nucleation site for the formation of β-Al_5FeSi compounds and, in order to deactivate this nucleation site, melt superheating is proposed to transform γ-Al_2O_3 to α-Al_2O_3, which is believed to be impotent site for β-Al_5FeSi nucleation [57]. It has also been proposed that AlP, which is a potent nucleus for eutectic silicon, may also aid the nucleation of the β-Al_5FeSi [41]. Worthy to note that most of the studies over the formation of Fe-rich phases in Al-Si alloys have been conducted in non-grain-refined state; in contrast, grain refinement with Al-Ti-B is thought to affect the precipitation of Fe-rich phases and conflicting data exist in the literature in this regard. It has been stated that refinement of β-Al_5FeSi particles can occur after Al-Ti-B addition [14, 67], whereas, in other studies [68, 69], the grain refinement with Al-Ti-B exerted opposite impact. Since grain refinement of Al-Si alloys by Al-Ti-B based master alloy is a common practice in foundries to improve material performance, understanding the effect of grain refiner addition on the formation of Fe-bearing intermetallics is of great importance.

1.3. HEAT TREATMENT OF Al-Si-Cu-Mg ALLOYS

Heat treatment is an important post-solidification step for Al-Si-Cu-Mg alloys as it significantly improves alloy mechanical properties. Figure 9 shows the main heat treatment steps normally used for these alloys. Firstly, solution heat treatment is applied to an alloy at temperature just below the solidus temperature for a long enough time to enable the dissolution of the interdendritic compounds into the α-Al grains. Then, the alloy should be quenched to obtain supersaturated solid solution. In a final (aging) step, alloy is exposed to a temperature considerably lower than that used in solution heat treatment step, thus encouraging the solid-state precipitations of Cu- and/or Mg-rich particles inside α-Al matrix [8].

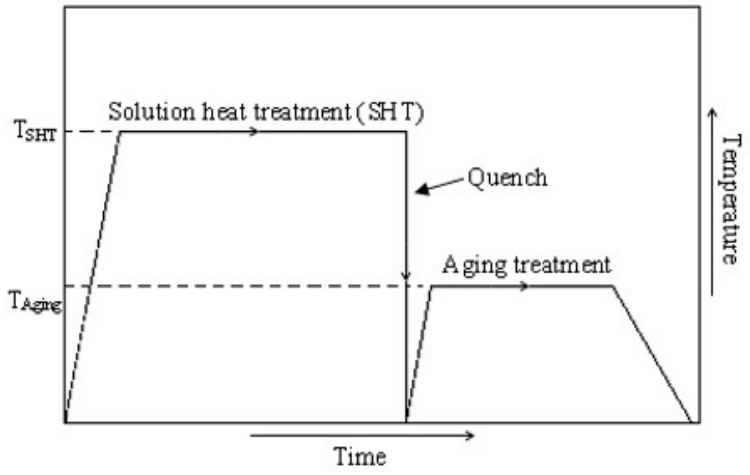

Figure 9. Diagram showing the three steps for precipitation hardening.

1.3.1. Solution heat treatment

In Al-Si-Cu-Mg alloys, the solution treatment fulfils three roles [8, 70, 71]:

- homogenization of the as-cast structure;
- dissolution of some intermetallic phases such as Al_2Cu and Mg_2Si;
- change of the size and morphology of eutectic silicon.

The time required for homogenization depends on the solution temperature and the SDAS value. In conventional solution treatment stage, the solution temperature of Al-Si-Cu-Mg alloys is maintained just below the melting temperature of the lastly-solidified phase in order to avoid its local melting, also called incipient melting [72, 73]. The time at a given solution treatment temperature must be long enough to fulfil the objectives of the solution heat treatment. In alloys with high Cu concentration, complete dissolution of the Al_2Cu phase during solution heat treatment may not take place. It has been also reported that blocky Al_2Cu particles need higher solutionizing temperature compared to the eutectic Al_2Cu particles [70, 73, 74]. Samuel et al. [75] reported that increasing Mg content in A319 Al alloy decreases the incipient melting temperature due to the formation of the Q-$Al_5Mg_8Si_6Cu_2$ phase. Heating rate to the solution treatment temperature and the solidification rate are the two parameters that can be used to determine the exact solution heat treatment temperature. Sokolowski et al. [76, 77] revealed that application of two-step solution treatment to A319 Al alloys can significantly reduce the amount of interdendritic Cu/Mg-rich phases, hence positively contributing to alloy mechanical properties.

1.3.2. Quenching

The objectives of quenching are to retain the maximum amount of the precipitation hardening elements in solution to form a supersaturated solid solution at low temperatures and introduce a large amount of lattice vacancies [8, 78].

The quench rate is a critical parameter for most Al-Si casting alloys particularly at the temperature interval between 450 °C and 200 °C because high level of supersaturation and a high diffusion rate available in this temperature range can enable the formation of precipitates very quickly. However, at higher temperatures the supersaturation level is too low, whereas at lower temperatures the diffusion rate is very limited for the precipitation to quickly take place [8, 78].

Furthermore, faster quench rate allows retaining higher vacancy concentration, thus enabling higher mobility of the elements inside α-Al matrix during aging. An optimum quench rate should yield a greater amount of lattice vacancies and low part distortion level. Lower quench rate can reduce residual stresses and distortion in the components, however, it can also exert deleterious impacts such as precipitation during quenching and reduced alloy response to aging treatment [79]. It has been stated that 4°C/s is a limiting quench rate above which the yield strength increases slowly with further increase in quench rate [8, 78]. The effectiveness of the quench is dependent upon the quench media and the quench interval. Water is the dominant quenchant for Al alloys [8].

1.3.3. Aging

With the application of solution heat treatment and quenching stages, the α-Al matrix with the high supersaturation of solute atoms and vacancies can be obtained. Guinier-Preston (GP) zones consisting of localized Cu atoms, tend to form at room temperature. At temperatures above 100

ºC, the dissolution of GP zones takes place [70] and then θ" phase tends to form in their place. A reduction in strength is seen with the dissolution of GP zones, occurring until the θ" phase starts forming. More prolonged aging leads to the transformation of θ" to the metastable θ', which is partially coherent with the α-Al matrix, and finally, to the stable θ (Al_2Cu), which is incoherent with the α-Al matrix. Maximum strength is obtained when the highest fraction of θ" phase is present [70, 80]. In the presence of Mg, various types of precipitates in different combinations have been observed in the peak-aged condition of Al-Si-Cu-Mg alloys. The type of precipitates that form depends on the alloy composition, the thermal history of the alloy and the ageing parameters applied. Examples of precipitates that can be present in the peak-aged condition are β" (Mg_2Si), θ' (Al_2Cu) and Q' ($Al_5Mg_8Si_6Cu_2$) [70, 81]. The strength obtained for quaternary Al-Si-Cu-Mg alloys after heat treatment is much higher than for the ternary Al-Si-Cu alloys [70, 82].

1.4. HIGH-TEMPERATURE STRENGTHENING IN Al-Si BASED ALLOYS VIA TRANSITION METALS ADDITION

1.4.1. Motivation

Al-Si alloys strengthened by Cu and Mg addition via precipitation hardening mechanism perform adequately at temperatures below 200 ºC [18, 47, 83, 84]. However, at higher temperatures, solute diffusion of Cu and Mg tends to be increasingly effective in promoting the precipitate coarsening within the matrix, thus contributing to the alloy softening [85-88]. Figure 10 shows how increasing the testing temperature significantly reduces the alloy strength.

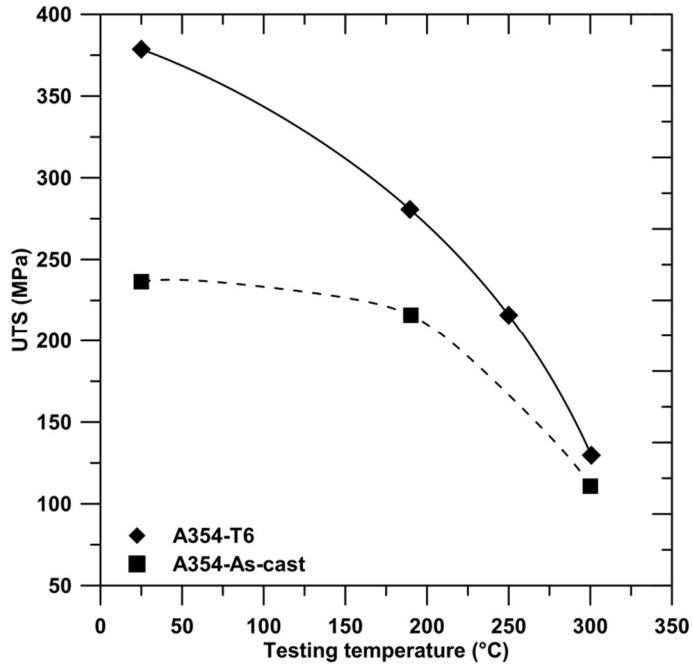

Figure 10. UTS values for an A354 alloy in as-cast and T6 heat treated states as function of testing temperature [1, 83].

The operating temperature in engine combustion chamber can often exceed 200 ºC during service [87, 89]. Moreover, a further increase of operating temperature is anticipated due to the expected engine power enhancement in near future, which indicates the necessity for the development of a new creep-resistant Al alloys [7, 87, 88].

1.4.2. Criteria for strengthening

According to equation (1), several parameters can influence the rate constant of Ostwald ripening [90]. These are the diffusivity of the rate-controlling solute (D), the precipitate-matrix interfacial free energy γ and the equilibrium solubility of the solute elements in the precipitate and matrix phases C^{β} and C^{α}

$$K \approx \frac{D\gamma}{(C^{\beta} - C^{\alpha})^2} \quad (1)$$

For creep-resistant Al alloys, the Ostwald ripening process must be slowed down. According to equation (1), the coarsening rate can be decreased when the solutes exhibit the following properties:

- ability to form high volume fraction of strengthening particles with smaller size and more homogeneous distribution;
- small diffusivity in α-Al;
- low solid solubility in α-Al;
- ability to form precipitates that possess similar crystal structure and low lattice parameter mismatch with α-Al.

Hence, to improve alloy high-temperature mechanical properties, the solid-state transformation of coarsening resistant precipitates should be encouraged. Slow-diffusing transition metals such as Zr and V can form trialuminide compounds and/or other types of precipitates containing transition metals, which all are considered as potential candidates for improving high-temperature mechanical properties of Al alloys [1, 91].

1.4.3. Theoretical background

Several studies [7, 92-95] revealed how adding certain transition elements and applying appropriate heat treatment to Al-based alloys can yield the formation of thermally stable precipitates inside α-Al grains. The peritectic-forming Zr and Sc are believed to have a notable influence on precipitation strengthening [90, 96, 97]. Although the formation of stable, coherent Al_3Sc precipitates is highly preferable, Sc is too costly to be used in Al-Si alloys [98]. Zirconium, in contrast, is relatively cheap element [98, 99]. The Zr-rich trialuminide can be as either semi-coherent tetragonal (Figure 12b,c) or coherent cubic (Figure 12a) phase; both these forms, particularly the latter one, have been found to make low energy interfaces with the matrix [90, 97]. However, low solid solubility of Zr in α-Al (see Figure 11a) restricts the formation of precipitates at high volume fraction.

Vanadium is also a slow-diffusing peritectic element, showing the maximum solid solubility (~0.4 wt.%) at the peritectic temperature of 611°C (Figure 11b) [1]. While some works showed that the formation of Al_3V or $Al_{10}V$ could be beneficial for the improvement of Al alloy performance [100], others reported how the precipitation of $Al_{10}V$ phase, particularly at grain boundaries, can deteriorate alloy mechanical properties [101]

Enriching trialuminides with other elements is considered as the promising way to further improve the precipitation strengthening of trialuminides. The lattice parameters of ($L1_2$) Al_3Zr phases could be reduced by addition of Ti, Hf, or V [72, 101, 102] and, in turn, this can lead to even greater

stability of the Al_3Zr phase by improving the lattice parameter mismatch with the α-Al solid solution. It has been also reported how the density of intradendritic Mo-rich dispersoids can be significantly raised by increasing the Mn content. Hence, it can be noted that the formation of binary dispersoids can make less contribution for the improvement of high-temperature mechanical properties mainly due to their limited volume fraction. Transforming the binary precipitates into ternary or quaternary forms by alloying with appropriate elements can contribute to an increase in volume fraction of precipitates, thus exerting better influence on alloy strength properties [58]. Therefore, further investigations in this regard might yield the possibility of the formation of a new type of dispersoids that can make significant contribution to the improvement in material high-temperature mechanical properties.

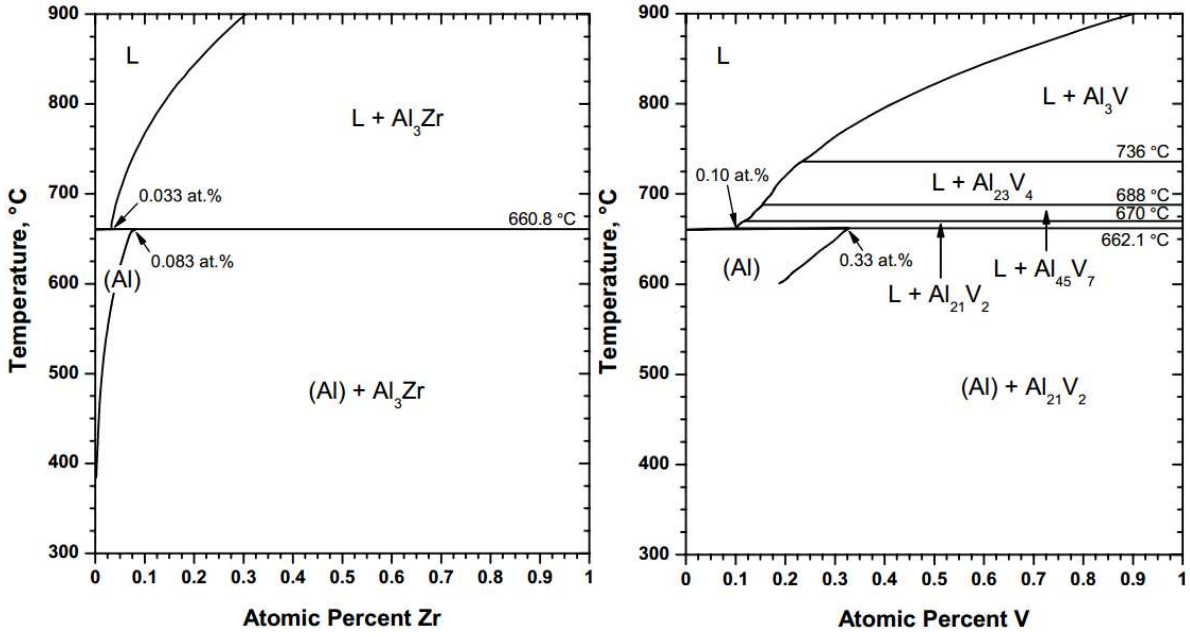

Figure 11. Phase diagrams of (a) Al-Zr and (b) Al-V systems [103].

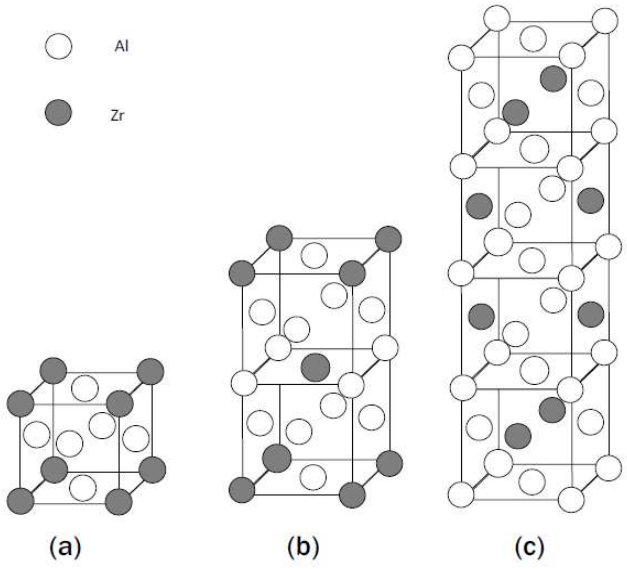

Figure 12. (a) The cubic $L1_2$, (b) tetragonal $D0_{22}$ and (c) tetragonal $D0_{23}$ crystal structures [59, 104].

Nickel is typically added to Al-Si piston alloys to improve both hardness and strength parameters at elevated temperatures as Ni-rich compounds forming during solidification are thermally resistant [84, 105]. As the solid solubility of Ni in Al is 0.04 wt.% [106], it strongly partitions to the interdendritic liquid regions during solidification, leading to the formation of various Ni-rich intermetallics. According to the equilibrium phase diagrams and experimental investigations, Ni was found to interact with Al, Cu and Fe, forming ε-Al_3Ni, δ-Al_3CuNi, γ-Al_7Cu_4Ni, T-Al_9FeNi and other complex intermetallic phases (Figure 13), which all are believed to positively contribute to alloy high-temperature strength [74, 106].

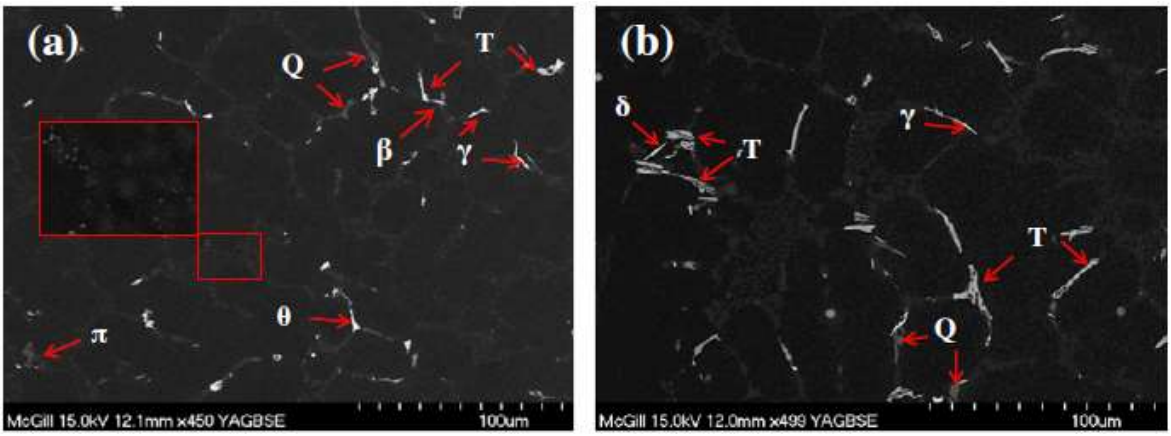

Figure 13. Microstructures of the as-cast Al-7Si-0.5Cu-Mg-(Fe) alloy with (a) 0.1 and (b) 0.3% Ni [59, 106]. The main phases are identified throughout.

1.4.4. Recent developments

Mahmudi et al. [107, 108] studied the effect of Zr on the mechanical properties of Al-Si-Cu foundry alloy and revealed that the presence of 0.15 wt.% Zr improves the hardness in both as-solutionized and age-hardened conditions (Figure 14). The improvement in hardness becomes more evident upon applying solution heat treatment for longer than 10 hours. This is attributed to the formation of intradendritic Al_3Zr precipitates (Figure 15) during solution heat treatment. Figure 14b shows the evolution of hardness as function of aging time and it is evident that Zr-added alloy exhibits higher hardness than the base alloy in all aging conditions applied.

Adding Zr and Mn caused no significant increase in the high-temperature tensile strength of A356 + 0.5Cu alloy; however, the creep resistance increased due to the precipitation of fine, thermally stable ε-AlSiZr dispersoids throughout the microstructure. In addition, Zr/Mn-added alloy also showed better ductility than the base alloy over a broad temperature range as the formation of needle-like Fe-rich compounds were suppressed in favour of script-like Fe-rich compounds [109]. Alloying Al-Si piston alloy with 0.11% Zr caused a moderate increase in alloy tensile properties at 350ºC, while 0.46% Zr addition showed opposite impact [110]; the authors associated the improvement to the strengthening effect of Zr in the alloy and the deterioration to the formation of interdendritic AlSiZr intermetallics with more harmful morphology. Higher addition levels of peritectic-forming Zr substantially increases the liquidus temperature (Figure 11a) and leads to the formation of primary, coarse Zr-rich compounds. These compounds not only reduce the precipitation strengthening effect of Zr, but also leads to an increase in fraction of interdendritic

intermetallics, which can be one of the reason for the degradation of the mechanical properties. Similar behaviour has been observed in A354 alloy with 0.4 wt.% Zr addition [18, 84].

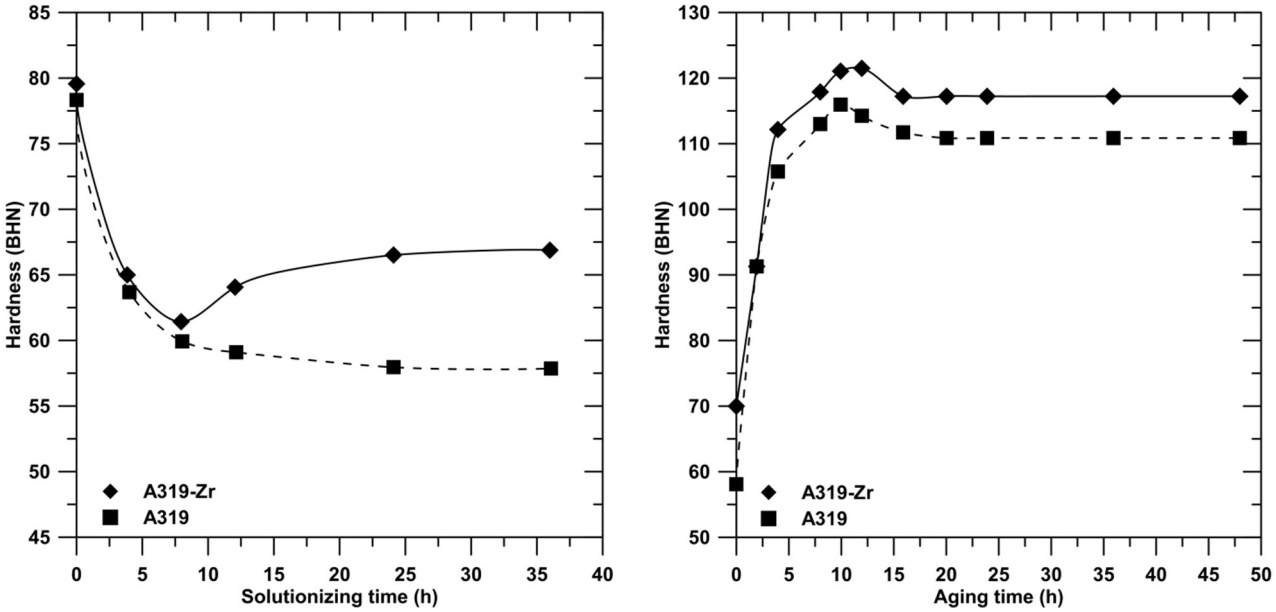

(a) (b)

Figure 14. Hardness evolution of an A319 alloy, with or without Zr addition (0.15 wt.%), as a function of (a) solution heat treatment time and (b) aging time after 24h solution treatment [58, 107, 108].

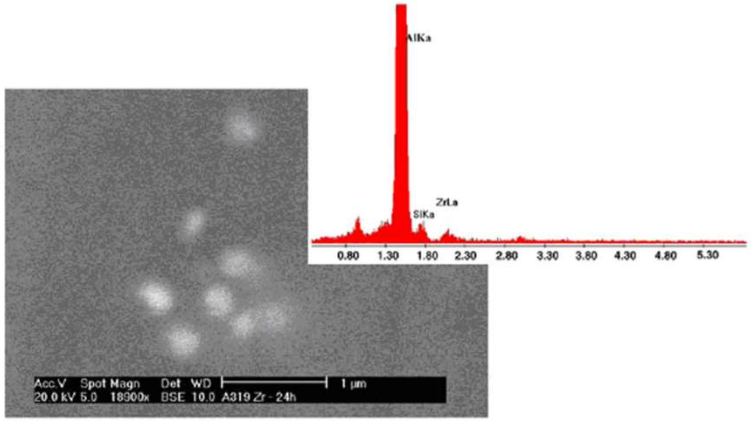

Figure 15. SEM micrograph of heat treated A319-Zr alloy indicating the presence of Zr-bearing precipitates as confirmed by EDS spectrum [59, 107, 108].

Addition of 0.2 wt.% Ni and/or 0.2 wt.% Zr exerted no statistically significant influense on the room- and high-temperature tensile properties of heat-treated A354 (Al-Si-Cu-Mg system) alloy [18, 84]. The same behaviour has been seen in case of A356 (Al-Si-Mg system) alloy with additions of 600 ppm Ni and 1000 ppm V [89]. However, as shown in Figure 16a, at 300 °C testing temperature, there is a slight increase in UTS and YS of Ni- and Zr-containing alloys in the heat-treated condition if compared to the base alloy. A significant UTS improvement has been observed in the alloys containing 0.2 wt.% Ni and 0.2 wt.% Zr in the as-cast condition with respect to the base alloy (Figure 16b), and this was attributed to the formation of Ni- and Zr-rich intermetallics (Figure 17), which can obstruct further development of cracks [18, 84, 111].

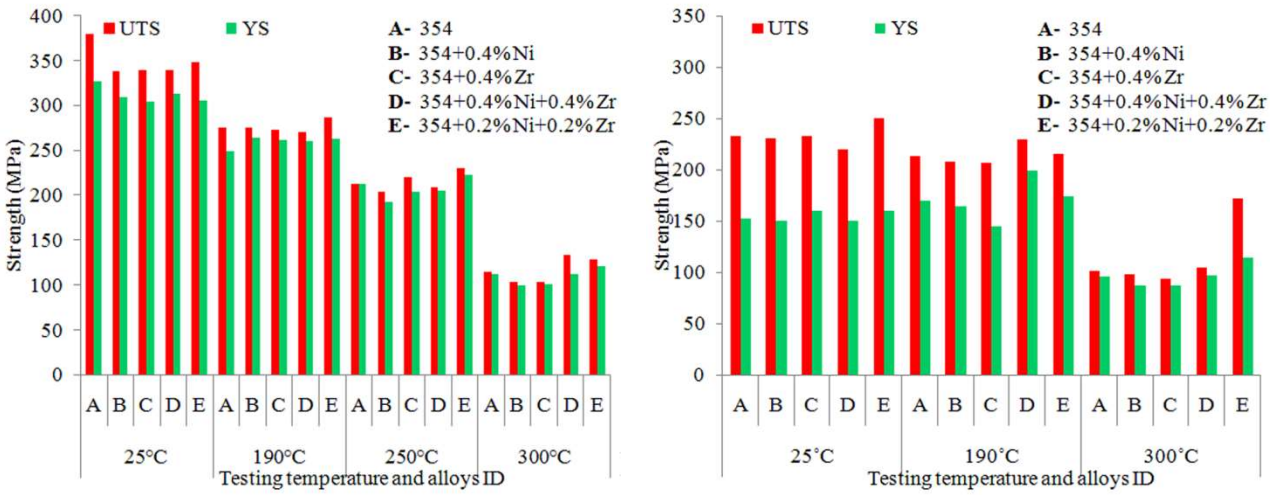

Figure 16. UTS and YS values of Ni/Zr-containing A354 alloys in (a) heat treated and (b) as-cast conditions as function of the testing temperature [59, 83].

Li et al. [112] found that among various Ni-rich intermetallic compounds, the δ-Al_3CuNi phase possesses the most efficient contribution to high temperature strength of Al-Si piston alloys due to its strip-like interconnected morphology, which is consistent with [106] too. The Al_9FeNi phase is very brittle even at elevated temperatures and its fracture at the early stage of creep deformation was found to reduce the creep resistance of the alloy. Modification of Al_9FeNi particles with Mn appears to prevent cracking of these compounds and increase the creep resistance [113].

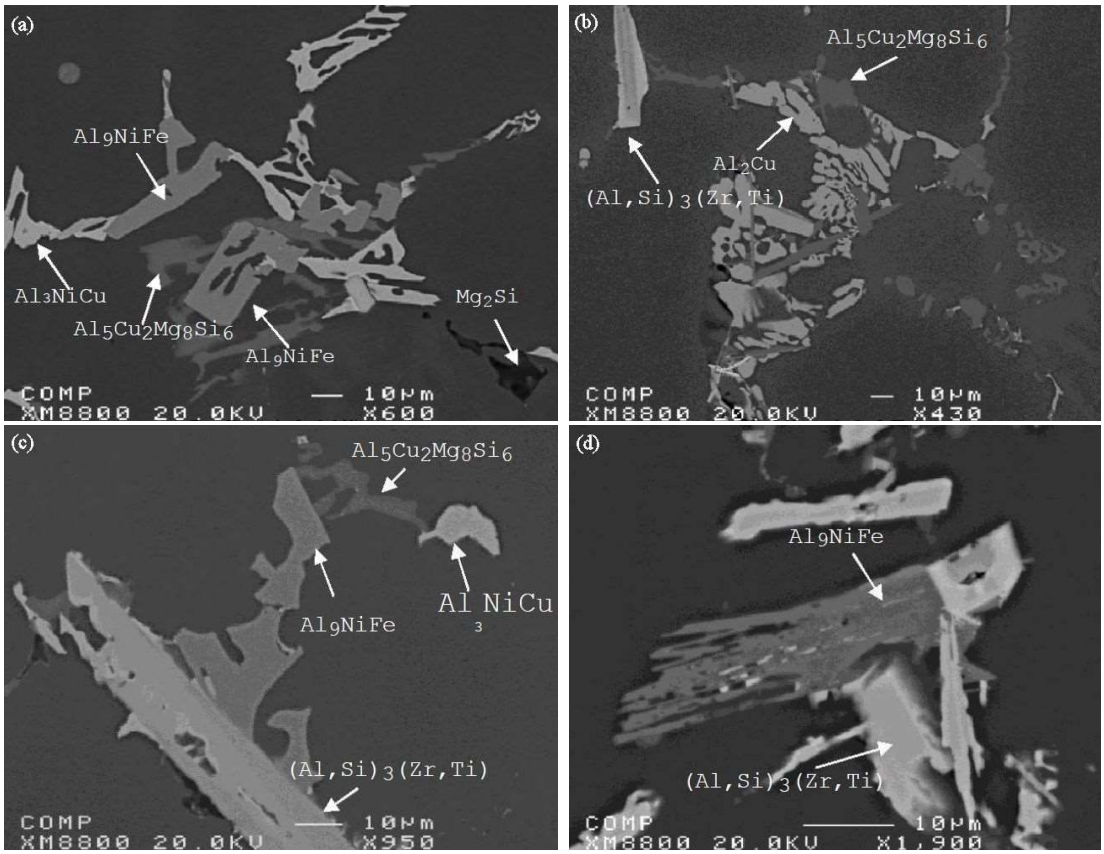

Figure 17. SEM microstructures of as-cast A354 alloy containing about (a) 0.4% Ni, (b) 0.4% Zr, (c) 0.2% Zr and 0.2% Ni, and (d) 0.4% Zr and 0.4% Ni; the different intermetallic compounds are indicated [83].

The room- and high-temperature tensile properties of Al-9Si-1Cu alloy considerably increased upon the addition of 0.2 wt.% Mn and 1 wt.% Ni (Figure 18) [114]. The effect of Ni addition on high-temperature fatigue toughness and fracture mechanisms of A357 alloy was evaluated [115] and it has been observed how the high-temperature tensile strength and cyclic fatigue are definitely increased. It is worthy to note that high Ni content in the Al foundry alloys seems not to be practical, mainly because it would increase the cost of the alloy too much [83].

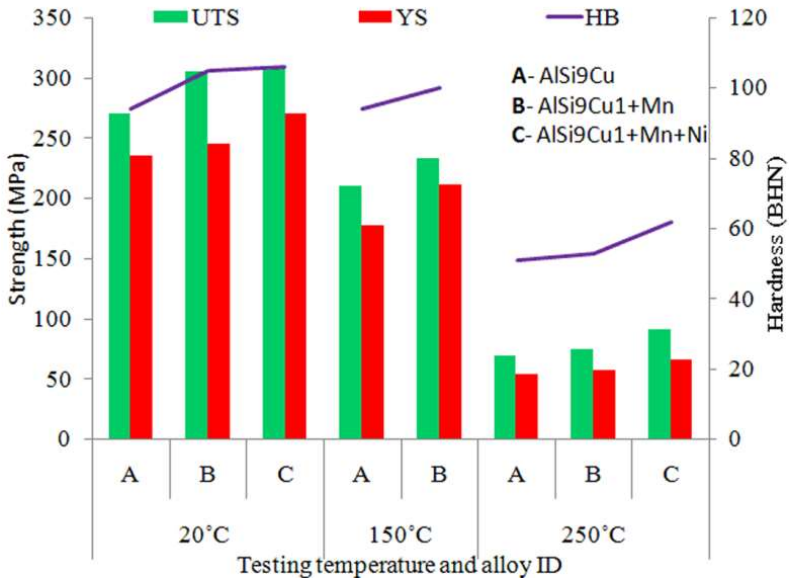

Figure 18. UTS, YS and Brinell hardness values of Mn- and Ni-containing Al-9Si-Cu alloys as function of testing temperature. Before tensile testing, the specimens were pre-conditioned for 500 hours at the corresponding test temperature [114].

The formation of Al(FeMo)Si dispersoids in the microstructure of Mo-containing Al-Si7-Cu0.5-Mg0.3 alloy effectively hindered the dislocation motions, leading to a significant increase in the elevated temperature strength and creep resistance [87]. Further addition of Mn to Mo-containing alloy caused an increase in the density of secondary precipitates and decrease in their average size, which leads to further improvement in high temperature mechanical properties. However, higher amount of Mn than the critical level increased the volume fraction of interdendritic intermetallics, thus deteriorating alloy ductility [88].

The modification of a new Mg-free A319 Al alloy with Zr and V additions showed negligible influence on alloy tensile properties at room temperature, however appreciable positive effect was observable at high temperature [23]. Adding combined Zr and V to an A356 alloy enhanced yield point and cyclic yield strength, while UTS remained almost constant (Figure 19a); in addition, hardness of Zr/V-modified alloy was higher in the range of temperatures between 150 and 250 °C, and also 350 and 450 °C (Figure 19b) [116]. The fatigue behaviour of A356 alloy with combined addition of V and Zr improved with respect to the alloy containing only Zr and the base A356 alloy [7, 92, 95]. This improvement was attributed to the increased volume fraction of Zr/V-rich dispersoids. Furthermore, activation energy of the plastic deformation of Zr/V-modified A356 alloy increased, which is an indication of the beneficial role of transition elements on improving the alloy high-temperature performance [117].

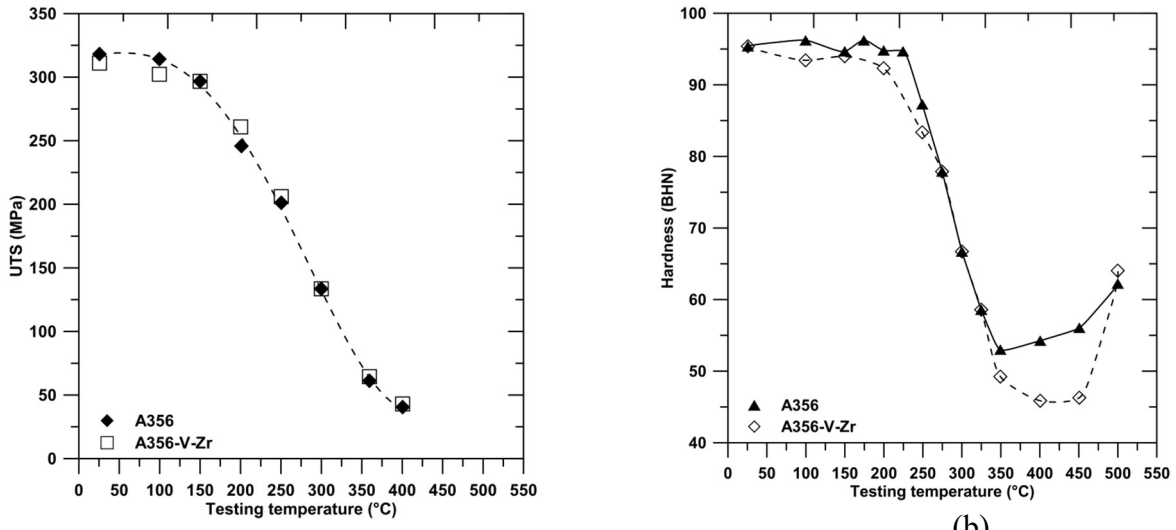

(a) (b)

Figure 19. Evolution of (a) hardness and (b) UTS in as-cast A356 base alloy and after Zr and V addition as a function of testing temperature [116].

Additions of Zr, V and Ti resulted in the formation of coarse and complex $Al_3Si_{26}TiV_{10}Fe$ and $Al_{13}Si_2Ti_3Zr$ phases, and the solution heat treatment caused only partial dissolution of these particles (Figure 20). Their partial dissolution indicates that some concentrations of Zr and V are available for further secondary precipitation [116]. However, the steep α-Al solvus line in Al-Zr phase diagram (Figure 11a) indicates how the solubility of Zr in conventional heat treatment temperature ranges is considerably limited, thus reducing the possibility of obtaining the α-Al solid solution with high Zr concentration.

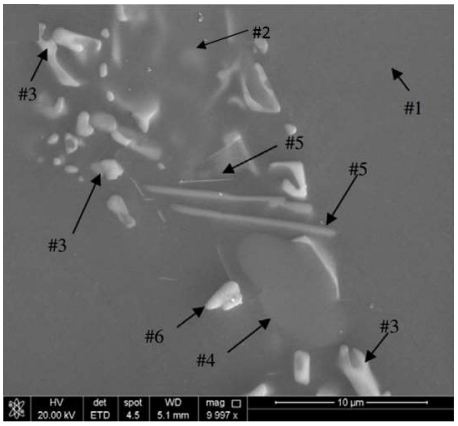

Figure 20. Microstructures of Zr- and V-containing alloy in the T6 heat treated condition: a) and b) SEM/BSE images under various magnifications. (#1 α-Al matrix; #2 Al-Si eutectic; #3 Al_2Cu; #4 $Al_8FeMg_3Si_6$; #5 $Al_{27}SiTiZr_9$; #6 AlSiTiVFe) [116].

The presence of Zr and V containing secondary precipitates in the microstructure (Figure 21) is confirmed by TEM characterization combined with EDS and diffraction analysis [116]. They are identified as rod-shaped stable $Al_3(ZrVTi)$ trialuminides with tetragonal structure. It should be noted that these precipitates are also found in smaller sizes (below 50 nm) with an $L1_2$ type structure.

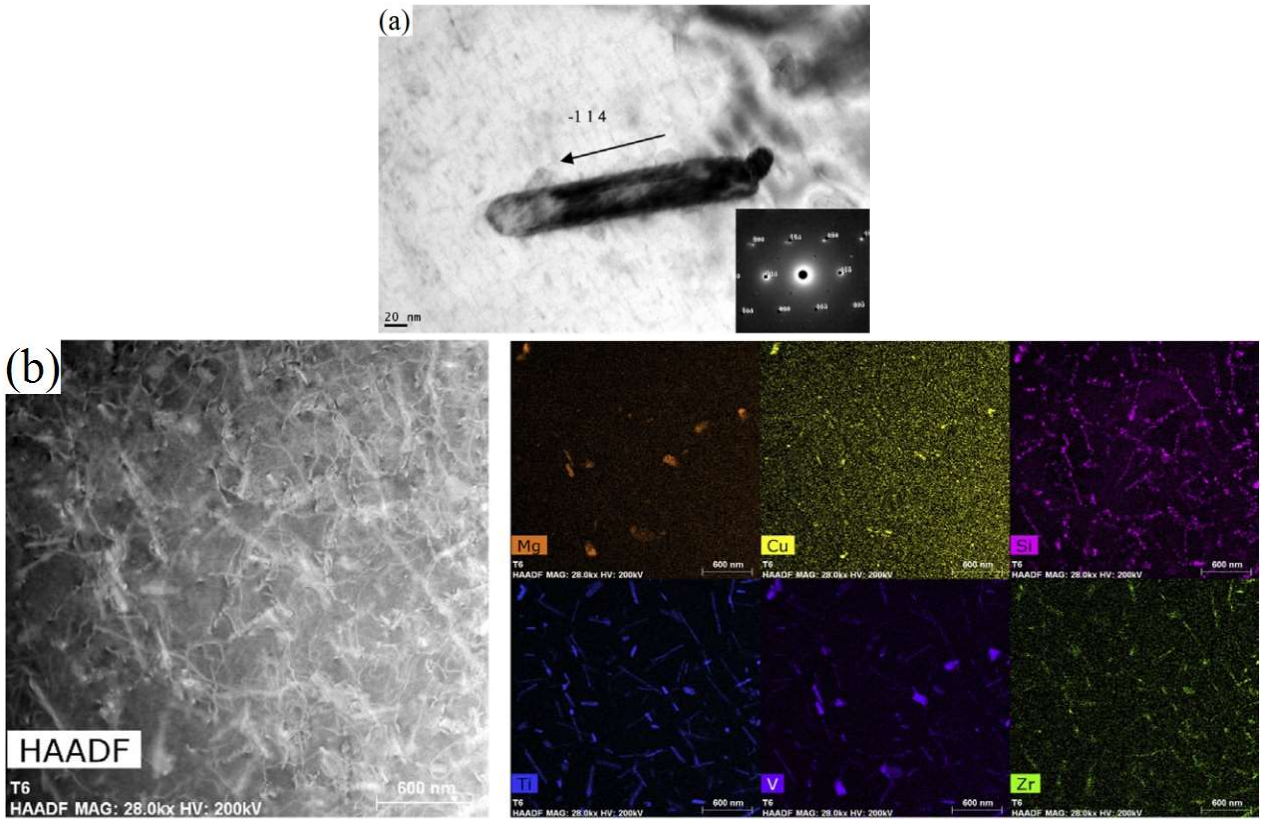

Figure 21. TEM observations of secondary precipitates in the microstructure of A356 alloy in T6 + holding at 475ºC for 128 h condition. (a) Bright field image of an $Al_3(ZrVTi)$ precipitate and the corresponding SAED pattern (inset). (b) Z-contrast high angle annular dark field image (HAADF) of the secondary precipitate structure along with elemental maps showing the two types of Al_2CuMg (S-phase) secondary precipitates and nano-rods of $Al_3(ZrVTi)$ covered by Si and Cu nano-particles [116].

1.4.5. Manufacturing issues

Several studies indicate how to attain the maximum beneficial effect of transition elements on precipitation strengthening of Al-Si alloys, it is necessary to apply the processing route that can yield the formation of nano-sized and homogenously dispersed precipitates throughout the microstructure. Considering that the post-solidification homogenization is limited due to steep α-Al solvus in binary Al-Zr, Al-Ti and Al-V equilibrium phase diagrams (Figure 11), the supersaturated Zr, Ti and V amounts in solid solution of α-Al matrix should be achieved during solidification. Therefore, by applying subsequent heat treatment, the solid-state precipitation of transition metals-rich phases can occur, thus exerting better influence on alloy high-temperature mechanical properties. However, there are several other factors which should be also considered in maximizing the precipitation hardening effects of peritectic-forming transition metals:

- Several transition metals such as Ti, V and Zr Al have peritectic phase diagram with Al and form primary trialuminide at hyperperitectic concentrations [104]. Since the liquidus temperature increases with increasing the solute concentrations in the peritectic systems (Figure 11), it necessitates to raise melt holding and pouring temperatures to obtain single liquid phase. However, too high melt temperature is not preferable in foundry industries as it leads to high energy consumption and reduced tool life. If the pouring temperature is not enough high, then, during pouring and mould cavity filling, the melt loses its temperature, giving rise to the formation of coarser and heterogeneously distributed primary precipitates.

- Moreover, in the presence of higher concentrations of peritectic-forming transition metals than their solubility limit in α-Al, the solidification starts with the crystallization of pro-peritectic Al_3M (M is a peritectic-forming transition metal) phase in equilibrium or near-equilibrium solidification conditions. The more solute content in the alloy, the coarser and insoluble intermetallics containing transition metals tend to form during early stage of solidification. These insoluble compounds significantly limit the precipitation strengthening effects of the transition metals and therefore, it is necessary to apply proper solute concentrations and cooling conditions to maximize the amount of supersaturated transition metals in solid solution of α-Al matrix directly during alloy solidification.
- It is known that Al-Ti-B based master alloys are typically used to obtain fine and equiaxed α-Al grains in Al alloys. The marked grain refinement is generally attributed to the presence of Al_3Ti and TiB_2 particles, which act as heterogeneous nuclei for α-Al during alloy solidification [23]. However, in the combined presence of Al-Ti-B based grain refiners and peritectic-forming transition metals such as Zr, interaction of transition metals with Al_3Ti and TiB_2 particles occurs [28, 29], yielding neither effective grain refinement nor the formation of the microstructure favourable for high-temperature applications.
- Silicon is known to have negative influence on the formation of trialuminides containing transition metals [33] because it lowers solid solubility of peritectic-forming transition metals in α-Al matrix [118-120], and it also decreases their ability to form more favourable dispersoids. Si can incorporate into the structure of trialuminides, negatively affecting their coarsening resistance [104, 121]. This behaviour limits the critical content of transition elements in the Al alloys which can make the best contribution to dispersion hardening.
- Recently, it has been observed how the primary and interdendritic Zr-rich phases formed during solidification can undergo partial dissolution upon applying solution heat treatment [116]. The presence of Zr in the alloy can increase the optimum solutionizing time of the alloy [108] as the solid-state precipitation of Zr/V-rich particles occurs directly during solution heat treatment process, but not during aging. It has been stated that the temperature range of 495-530°C is needed to enable the formation of Al_3Zr precipitates [122]. It is worthy to note that under certain solution heat treatment conditions, the cubic $L1_2$ Zr-rich precipitates (Figure 12a) can transform into complex tetragonal $D0_{22}$ or $D0_{23}$ structures (Figure 12b and c). The precipitates with $D0_{22}$ and $D0_{23}$ structures are semi-coherent with the α-Al matrix. As a result, the coherency strengthening diminishes when these precipitates form at the expense of the $L1_2$ precipitates. The loss of coherency between the precipitate and the matrix accelerates the Ostwald ripening of the precipitate and the alloy will lose some part of the strengthening effect [83]. Therefore, for the alloys containing transition elements, the heat treatment parameters should be carefully set to ensure the adequate microstructure refinement and the activation of Zr and/or V enriched secondary precipitates.

2. RESEARCH APPROACH

CHAPTER INTRODUCTION

This chapter describes the research methodology used in this study. First, the aim, scope and the research questions of the present study are described, and then, the summary of research activity and methodology used in this study are presented; thorough experimental details can be found in research papers appended to this thesis.

2.1. AIM AND SCOPE

Secondary Al-Si-Cu-Mg based foundry alloys are increasingly used in automotive industry, particularly in the fabrication of engine components. One issue which is still a subject of ongoing investigations in secondary Al-Si alloys is the presence of several types of *transition metal impurities*, such as Fe, Mn, Cr, Ti, V, Ni and Zr, in trace amounts. Intermetallic compounds formed from these elements during solidification tend to degrade alloy mechanical properties, particularly ductility. Considering the difficulty or too costly route of the removal of some trace elements, such as Fe, from Al-Si alloys, considerable research activities have been conducted in recent years to favour the formation of more desirable type of intermetallic compounds at the expense of deleterious ones. Although phases formation involving these transition metal impurities in non-grain-refined Al-Si alloys has been extensively studied [55, 62, 66, 123, 124], role of chemical grain refinement in microstructural evolution of secondary Al-Si-Cu-Mg alloys needs further investigations since grain refinement is considered as one of the critical melt treatment operations. This work primarily aims to characterize the formation of intermetallic phases containing transition metal impurities in both non-grain-refined and grain-refined Al-Si alloys and contribute to the understanding of the mechanisms underlying the microstructural changes occurring with the addition of grain refiner. Another issue to consider is the limited thermal stability of Al-Si-Cu-Mg alloys at temperatures above 200 ^{o}C. It has been reported [87, 89] how the operating temperature in engine combustion chamber can often exceed 200 ^{o}C during service. Moreover, a further increase of operating temperature is anticipated due to the expected engine power enhancement in near future, which indicates the necessity for the development of a new creep-resistant Al alloys [7]. *Deliberate addition of transition metals* is believed to yield a new heat-resistant alloy as induced by the solid-state formation of thermally stable dispersoids inside α-Al grains [125]. This study thus also attempted to investigate the effect of adding transition metals Zr, V and Ni on the solidification processing, microstructural evolution and room/high-temperature tensile properties of secondary Al-Si-Cu-Mg alloys, with the aim of estimating the feasibility of the enhancement of high-temperature strength properties of secondary (recycled) Al-Si-Cu-Mg foundry alloys via transition metals addition.

2.2. RESEARCH DESIGN

2.2.1. Research perspective

The flow chart, shown in Figure 22, illustrates the research approach adopted in this study. Initially, the topics of interest were defined considering some metallurgical issues commonly encountered in the fabrication and use of secondary Al-Si-Cu-Mg alloys. Comprehensive literature survey was conducted on selected research topics. The online library search engines, such as Scopus, Science Direct, Springer Link and Google Scholar, were used to conduct comprehensive bibliographic search in the topics of interest. The review of relevant literature allowed to critically summarize the current knowledge in the selected area of research and define the research questions. The experiment was designed to address the research questions. The results obtained from the experimental activities were analysed, evaluated and compared with the findings available in the literature.

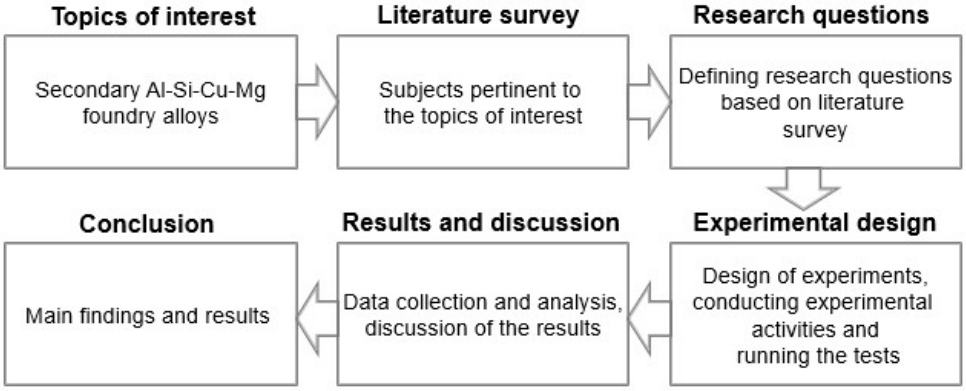

Figure 22. Schematic illustration of the research approach used in the present work.

The present study investigated the role of (a) transition metal impurities (research phases I – III) and (b) deliberately added transition metals (research phases IV and V) on the solidification path, microstructural evolution and mechanical properties of secondary Al-7Si-3Cu-0.3Mg alloys.

- **Phase I – Grain refinement, eutectic modification and intermetallics formation in secondary Al-Si-Cu-Mg alloys: role of transition metal impurities.** The roles of impurity (trace) elements and melt superheat in the efficiency of grain refinement with Al-5Ti-1B, eutectic modification by Al-10Sr and the precipitation behaviour of intermetallic phases in secondary Al-7Si-3Cu-0.3Mg alloy were investigated. The findings of this study can facilitate foundries and alloy development communities to optimize the grain refiner addition level more effectively by considering the contribution of transition metal impurities, such as Zr and V.
- **Phase II – Fe-rich intermetallics in secondary Al-Si-Cu-Mg alloys: role of Al-5Ti-1B grain refiner.** The influence of adding Al-5Ti-1B and Al-10Ti grain refiners on the precipitation of Fe-rich compounds in secondary Al-7Si-3Cu-0.3Mg alloy was investigated. The findings of this study can contribute to an understanding of the mechanisms underlying the influence of grain refiner on the formation of Fe-rich intermetallics. Moreover, the obtained results stimulate foundries and alloy development communities to develop more effective grain refining master alloys having no deleterious impact on the formation of Fe-rich intermetallic phases.

- **Phase III – Fe-rich intermetallics in secondary Al-Si-Cu-Mg alloys: a comparison of the roles of Al-5Ti-1B and Al-5B grain refiners.** The effects of cooling rate and adding varying levels of Al-5B and Al-5Ti-1B grain refiners on the formation of Fe-rich intermetallics in secondary Al-7Si-3Cu-0.3Mg alloy were investigated. This study compares two different grain refining master alloys (Al-5Ti-1B and Al-5B) in terms of their influence on the precipitation of Fe-rich intermetallic compounds in secondary Al-Si-Cu-Mg alloys.
- **Phase IV – Solidification processing and microstructural evolution of secondary Al-Si-Cu-Mg alloys: Role of Zr, V and Ni additions.** The effect of individual and combined Ni, V and Zr additions on macro- and microstructural features, such as the grain refinement level and the characteristics (size, morphology, chemical composition and crystal structure) of phases forming during solidification was investigated. The findings of this study can allow gaining further understanding of the role of deliberately-added transition metals in the possibility of developing a new generation of heat-resistant Al-Si based foundry alloys.
- **Phase V – Microstructural evolution and tensile properties of secondary Al-Si-Cu-Mg alloys: Role of Zr and V addition.** The effect of Zr and V additions and heat treatment on microstructural evolution and tensile properties of secondary Al-7Si-3Cu-0.3Mg alloy was investigated, with the aim of revealing a new type of thermally stable, intradendritic precipitates having greater potential in high-temperature strengthening of Al-Si based alloys. The findings of this study can estimate the feasibility of high-temperature strengthening in secondary Al-Si alloys via transition metals addition.

2.2.2. Research questions

Several research questions have been raised and addressed during each phase of this study. The main questions can be categorized into two main groups and are addressed in the indicated Supplements:

- Transition metal impurities, which are commonly present in secondary Al alloys;
  - Do transition metal impurities, such as Zr and V, have an influence on the efficiency of grain refinement and eutectic modification of secondary Al-Si-Cu-Mg alloys? Is the observed effect dependent on the level of melt superheat? (Supplement I)
  - What is the role of transition metal impurities, such as Zr, V, Mn and Fe, in the formation of intermetallic compounds during solidification of secondary Al-Si-Cu-Mg alloys? (Supplements I, II and III)
  - Does grain refinement have an influence on the formation of Fe-rich intermetallic phases in secondary Al-Si-Cu-Mg alloys? Is the observed effect dependent on the solidification rate? (Supplements II and III)
  - How do two different grain refining master alloys (Al-5Ti-1B and Al-5B) perform in terms of their influence on the formation of Fe-rich phases in secondary Al-Si-Cu-Mg alloys? Is the observed effect dependent on the solidification rate? (Supplement III)
  - Is the ratio between Mn and Fe contents a deciding factor in suppressing the crystallization of needle-like, deleterious β-Al_5FeSi compounds via stabilization of more desirable, script-like α-$Al_{15}(FeMn)_3Si_2$ phase during solidification of secondary Al-7Si-3Cu-0.3Mg alloys? (Supplements II and III)

- Deliberate addition of transition metals Zr, V and Ni;
    - What is the effect of adding transition metals (Zr, V and Ni) individually or in combination on the solidification path and microstructural evolution of secondary Al-Si-Cu-Mg alloys? (Supplement IV)
    - What is the effect of adding transition metals (Zr, V and Ni) individually or in combination on the grain refinement of secondary Al-Si-Cu-Mg alloys? (Supplement IV)
    - Do adding Zr and V promote the formation of thermally stable precipitates inside α-Al matrix during heat treatment of secondary Al-Si-Cu-Mg alloys? (Supplement V)
    - Does the interaction between transition metal impurities and deliberately added Zr and V increase the formation of thermally stable precipitates inside α-Al matrix? (Supplement V)
    - What is the effect of adding Zr and V on room- and high-temperature static tensile properties of secondary Al-Si-Cu-Mg alloys? (Supplement V)

2.3. MATERIALS AND EXPERIMENTAL PROCEDURE

2.3.1. Materials and melt processing

In this work, Al-7Si-3Cu-0.3Mg alloy (equivalent to the US designation A320) was used as a baseline material. The base material was supplied by Raffineria Metalli Capra and Raffmetal Spa in the form of commercial foundry ingots produced by recycling of scrap aluminium. The master alloys used to modify the alloy chemistry are Al-10Sr, Al-5Ti-1B, Al-10Ti, Al-10Zr, Al-10V, Al-25Ni and Al-5B (in wt.%). This work is divided into five research phases (see Section 2.2.1. for the objectives of each phase) and the chemical composition of the alloys investigated at different research phases and the corresponding melt processing conditions are presented in the following sub-sections. Research phases I, II and III describe the experimental activities concerning the investigations of the role of transition metal impurities in solidification path and microstructural evolution of secondary Al-7Si-3Cu-0.3Mg alloy before and after melt chemical treatment, and the research phases IV and V present the experimental activities related to the investigations of the role of deliberate addition of transition metals in solidification path, microstructural evolution and tensile properties of secondary Al-7Si-3Cu-0.3Mg alloy.

2.3.1.1. Phase I – Grain refinement, eutectic modification and intermetallics formation in secondary Al-Si-Cu-Mg alloys: role of transition metal impurities

In this research phase, metallographic and thermal analysis techniques were used to quantitatively examine the macro- and microstructural changes occurring with increasing the pouring temperature of the melt (700, 750 and 800 ºC), before and after the combined addition of modifier and grain refiner to the base alloy. The chemical composition of the base alloy investigated in this research phase and referred to as *untreated alloy* is presented in Table 2. Al-5Ti-1B and Al-10Sr master alloys were respectively used for grain refinement and eutectic modification and the prepared alloy is referred to as *treated alloy* (see Table 2 for treated alloy composition). Ingots were initially melted in a SiC crucible in an electric (muffle) furnace at 700 ºC. The melt was poured into a boron-nitride coated cylindrical steel cup to perform thermal analysis. Figure 23

shows schematic illustration of the thermal analysis set-up with the cup and thermocouple. To perform thermal analysis at higher pouring temperatures (750 and 800 ºC), the melt temperature was raised and was held for at least 30 min at a given temperature prior to pouring. For treated alloys, the melt was treated with grain refiner and modifier with a contact time of at least 15 min, and then, thermal analysis of treated alloy was also carried out at three different pouring temperatures (700, 750 and 800 ºC) following the same melt processing route used for untreated alloy. Prior to pouring, the melt was stirred, and surface skimmed to remove the dross. Three series of thermal analysis experiments were conducted for each condition. A temperature difference of 50 ºC between melt pouring temperature and steel cup temperature was maintained at different melt superheat levels. Average value of SDAS in the resulting microstructure near the tip of thermocouple was about 60 µm in both untreated and treated alloys.

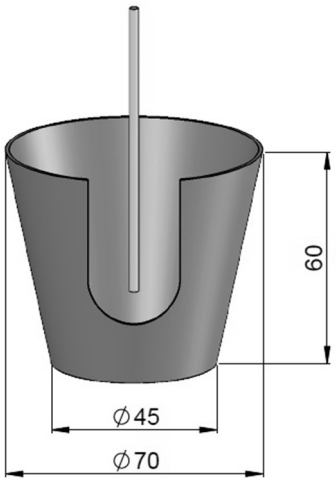

Figure 23. Schematic illustration of the thermal analysis set-up with steel cup and thermocouple. All dimensions are in mm (Courtesy of Dr. G. Basso).

Table 2. Chemical composition of the alloys investigated in this research phase (wt. %).

Alloy	Si	Fe	Cu	Mn	Mg	Zn	Cr	Ni	Ti	Pb	Sr	V	Zr	B	Al
Untreat	7.7	0.44	3	0.23	0.3	0.7	0.04	0.02	0.10	0.03	0.000	0.01	0.01	0	bal.
Treated	7.4	0.44	3	0.22	0.3	0.7	0.04	0.02	0.17	0.03	0.013	0.01	0.01	0.02	bal.

2.3.1.2. Phase II – Fe-rich intermetallics in secondary Al-Si-Cu-Mg alloys: role of Al-5Ti-1B grain refiner

In this research phase, the metallographic and thermal analysis techniques were used to investigate the role of grain refinement in the solidification path and microstructural evolution of secondary Al-7Si-3Cu-0.3Mg alloys.

Thermal analysis (Figure 23) experiments were performed for non-grain-refined (base) alloy and the alloys separately refined by Al-5Ti-1B and Al-10Ti master alloys. Table 3 presents the chemical composition of the studied alloys. Melting of ingots was conducted in a SiC crucible in an electric (muffle) furnace at 750 ºC. Contact time of grain refining master alloy with the molten metal was at least 15 min. The melt was stirred, and surface skimmed to remove the dross. Then the melt was poured into the boron-nitride coated cylindrical steel cup preheated to 700 ºC.

Average SDAS value in the resulting microstructure near the tip of thermocouple was about 60 µm in all studied alloys.

Step castings (Figure 24) were produced from two different alloys: (1) non-grain-refined (base) alloy and (2) alloy grain refined by Al-5Ti-1B master alloy. The base material was melted in an electrical resistance furnace at 750 ± 5 ºC. After having complete liquid phase, the melt was stirred and surface skimmed. Then the melt was poured into the cavity of steel mould preheated to 390 ºC. The remaining liquid metal was then treated with Al-5Ti-1B master alloy with a contact time of at least 20 min prior to pour. Chemical composition results were similar with that of the corresponding alloys produced for thermal analysis experiments (see Table 3).

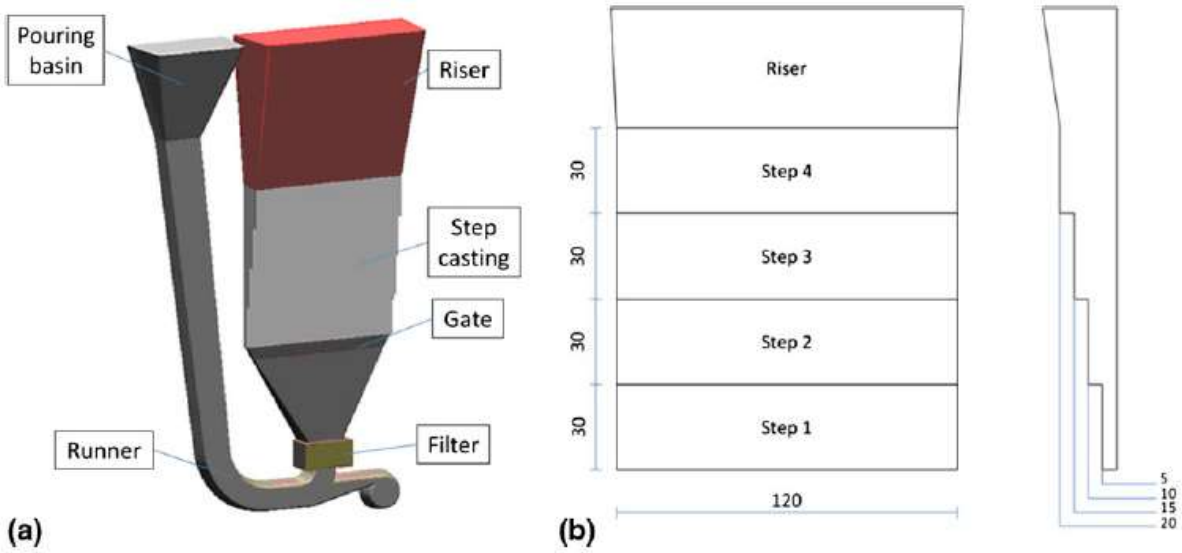

Figure 24. (a) Step casting CAD 3D geometry with (b) front and side views (dimensions in mm) [14].

Table 3. Chemical composition of the alloys investigated in this research phase (wt. %).

Alloy	Si	Fe	Cu	Mn	Mg	Zn	Cr	Ni	Zr	V	Ti	B	Al
Base alloy	7.57	0.44	3.1	0.23	0.3	0.7	0.04	0.02	0.01	0.01	0.1	0.001	bal
Base alloy + Al-5Ti-1B	7.42	0.43	3.0	0.22	0.3	0.7	0.04	0.02	0.01	0.01	0.14	0.017	bal
Base alloy + Al-10Ti	7.29	0.43	3.0	0.22	0.3	0.7	0.04	0.02	0.01	0.01	0.14	0.001	bal

2.3.1.3. Phase III – Fe-rich intermetallics in secondary Al-Si-Cu-Mg alloys: a comparison of the roles of Al-5Ti-1B and Al-5B grain refiners

In this research phase, the Al-7Si-3Cu-0.3Mg-0.44Fe-0.24Mn-0.7Zn-0.02Ti (equivalent to the US designation A320) was used as the base alloy. The material also contained other elements such as Zr, V, Ca, Bi, P and Sb in amounts less than 0.01 wt.% as impurities. In comparison to the base alloy used in other research phases (Table 2 and Table 3), the base alloy of the present research phase contains very limited amounts of diboride-forming Ti, which enables to analyse and compare the performance of Al-B and Al-Ti-B based master alloys more effectively.

The base alloy ingots were melted in a SiC crucible in an electric (muffle) furnace at 750°C. After complete dissolution, the melt was stirred and surface skimmed, followed by a 10 min of holding. The molten metal was then cast into the boron nitride-coated steel cup (Figure 23) and mould (Figure 25), both preheated at 550°C. The remaining liquid was grain refined by Al-5Ti-1B master alloy to produce alloys with greater B (40 and 80 ppm) and Ti (400 and 600 ppm) levels. Similarly,

a separately-melted base alloy was treated by Al-5B master alloy to produce alloys with greater B levels (400 and 800 ppm). The molten metal was stirred 5 min after metal treatment and the holding time between stirring and pouring stages was 20 min. The measured Ti and B contents in alloys refined by Al-5Ti-1B were similar to the target values; however, while the measured B level in alloys refined by Al-5B was lower than the target concentrations, the Ti, V and Zr levels in the alloys refined by Al-5B dropped to zero. This is due to the formation and then removal of cluster of diborides (TiB_2, ZrB_2 and VB_2) via settlement. Average SDAS in the investigated specimens extracted from large- and small-diameter moulds were about 60 and 20 µm, respectively.

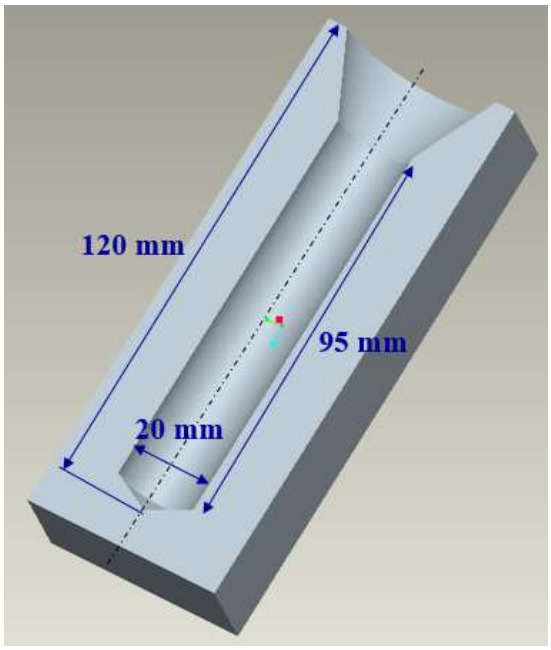

Figure 25. Schematic section of the steel mould [126].

2.3.1.4. Phase IV – Solidification processing and microstructural evolution of secondary Al-Si-Cu-Mg alloys: role of Zr, V and Ni additions

The effect of individual and combined Zr, V and Ni additions on solidification path and microstructural evolution of secondary Al-7Si-3Cu-0.3Mg alloy were investigated using microscopy and thermal analysis techniques. Schematic illustration of thermal analysis set-up is shown in Figure 23. The chemical composition of alloy used as the base material in this study is presented in Table 4. Table 5 lists the concentration of Ni, V and Zr obtained in the studied alloys. Ceramic crucible (SiC) was used to melt the material in an electrical (muffle) furnace at 760 ºC. After complete dissolution, the melt was stirred and surface-skimmed to remove the dross, followed by pouring the melt into the boron nitride-coated cylindrical steel cup preheated to 700 ºC. The Al-10Zr, Al-10V and Al-25Ni master alloys were used to increase the concentrations of Zr, V and Ni, respectively, in secondary Al-7Si-3Cu-0.3Mg alloy. Average SDAS value in the resulting microstructure near the tip of thermocouple was about 60 µm in all studied alloys.

Table 4. Chemical composition of the base alloy (wt. %).

Alloy	Si	Fe	Cu	Mn	Mg	Zn	Cr	Ni	Ti	V	Zr	Al
Al-7Si-3Cu-0.3Mg	7.68	0.44	3.02	0.23	0.31	0.78	0.04	0.02	0.1	0.01	0.01	bal.

Table 5. The achieved Ni, V and Zr contents in the alloys prepared for this study (wt. %).

Elem.	Alloys							
	A (Al-7Si-3Cu-0.3Mg)	A+V	A+Ni,V	A+Zr	A+Zr,V	A+Ni	A+Ni,Zr	A+Ni,V,Zr
Ni			0.25			0.25	0.25	0.25
V		0.25	0.25		0.25			0.25
Zr				0.12	0.12		0.12	0.12

2.3.1.5. Phase V – Microstructural evolution and tensile properties of secondary Al-Si-Cu-Mg alloys: role of Zr and V additions

In this research phase, the effects of Zr and V microalloying additions and heat treatment on the microstructure and mechanical properties of secondary Al-7Si-3Cu-0.3Mg alloy were investigated. Table 6 lists the chemical composition of the alloys investigated in this study. Hereafter, the new alloy prepared for this study is referred to as a (Zr/V-) modified alloy. The melting of the base alloy ingots was conducted in an electrical-resistance furnace at 760 ºC. The Al-10Zr and Al-10V master alloys were added to the melt to increase Zr and V contents. The melt was stirred, and surface skimmed 15 min prior to pour. A steel mould was used to produce castings (see Figure 26 for the 3D CAD design of casting). The boron nitride was used to coat the mould inner surfaces. The temperature was monitored by means of thermocouples embedded in the die to insure a good reproducibility of the tests. The working temperature of the die was in the range of 390-450ºC. Average SDAS value at the cross section of tensile specimen gauge length was ~15 μm.

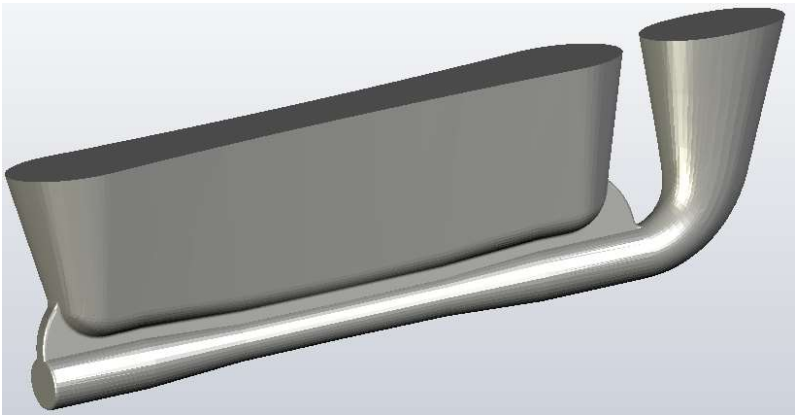

Figure 26. Tensile test casting CAD 3D geometry.

Table 6. The chemical composition of the base and Zr/V-modified alloys (wt. %).

Alloy type	Si	Fe	Cu	Mn	Mg	Zn	Cr	Ni	Ti	Pb	V	Zr	Al
Base	7.8	0.46	3.1	0.23	0.3	0.78	0.040	0.02	0.1	0.03	0.01	0.01	bal.
Modified	7.6	0.45	3.0	0.22	0.3	0.76	0.037	0.02	0.1	0.03	0.30	0.15	bal.

2.3.2. Heat treatment

The age-hardening heat treatment (T6 state) of some selected tensile test bars (research phase V) was performed in an air-circulating furnace; the solution heat treatment was performed at 485 ºC for 24 h and then quenched in water at room temperature, followed by aging at 180 ºC for 8 hours. The temperature for solution heat treatment was selected based on the results from differential

scanning calorimetry (DSC) analyses performed in research phase IV. Longer solutionizing time was applied to enable the precipitation reactions involving Zr and V inside α-Al matrix [107].

2.3.3. Sample preparation

2.3.3.1. Thermal analysis

For DSC measurements performed in research phase IV, cylindrical-shaped discs weighing about 35 mg were drawn from the specimens produced for chemical composition analyses.

2.3.3.2. Microstructural analysis

Thermal analysis (Figure 23) samples were cut through the central axis. Samples for macro- and microstructural investigations were sectioned near the tip of the thermocouples to correlate the solidification parameters obtained from thermal analysis with the metallographic observations.
Samples for microstructural investigations of cylindrical-shaped small-diameter castings (Figure 25) were sectioned at 25 mm from the bottom surface.
Step castings (Figure 24b) were halved along the main axis and the specimens representing the central part of each step was extracted for microstructural analyses.
Samples for microstructural analyses of tensile test bars (Figure 26) representing the base and Zr/V-modified alloys both in the as-cast and heat-treated states were sectioned from the cross-section of the gauge length.
The specimens obtained were mounted, grinded and polished following the standard techniques.

2.3.3.3. Tensile testing

All the as-cast and heat-treated tensile test bars were machined to produce specimens with the total length of 175 mm, a gauge length of 65 mm, and a diameter of 10 mm.

2.3.4. Characterization methods

2.3.4.1. Solidification path

The traditional thermal analysis and differential scanning calorimetry (DSC) were used for thermal analysis studies.
In case of traditional thermal analysis (see Figure 23), K-type thermocouples fixed at the lid of the cup and covered with tightly fitting steel tubes, were inserted into the melt on the central axis at depth of 30 mm. The temperature and time were collected by means of the data acquisition system with a sampling rate of 0.25 s^{-1}, analog-to-digital converter accuracy of 0.1ºC, and connected to a personal computer. The system was given to cool in air and gave a cooling rate of 0.17 ± 0.1 °C/s in the solidification interval. For each set of temperature/time relations in the centre of the sample, the cooling curves and the corresponding derivative curves were plotted to determine the characteristic temperatures related to the formation of phases based on the first derivative cooling curve approach [127]. Figure 27 and Table 7 show the definition method and the description of thermal analysis parameters, respectively, used in the present work.

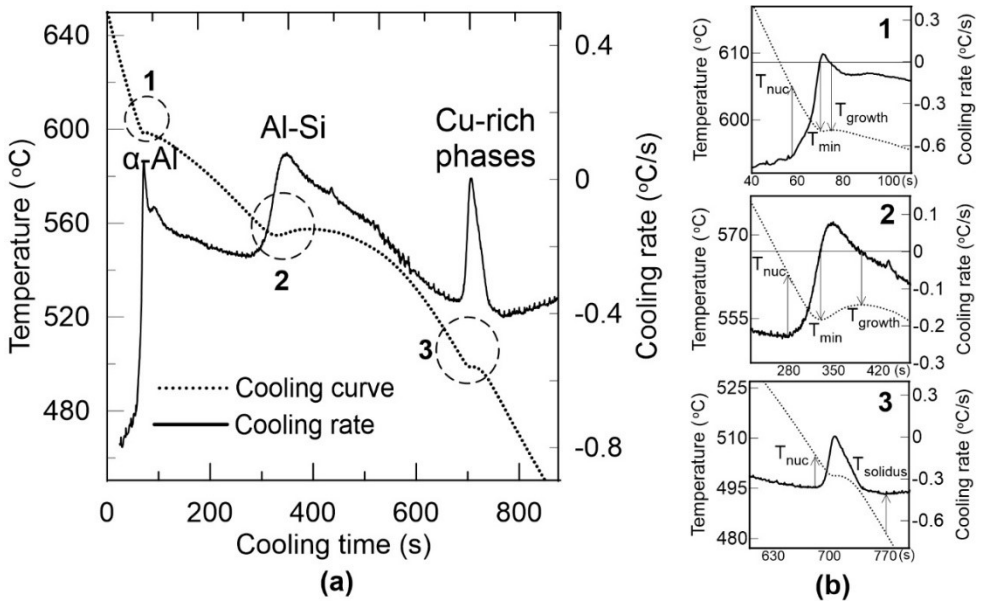

Figure 27. (a) Cooling curve and first derivative of Al-7Si-3Cu-0.3Mg alloy indicating three main phase reactions, (b) magnified plots of three phase reactions showing the method used to determine the characteristic points, such as T_{Nuc}, T_{Growth}, T_{Min} and $T_{Solidus}$.

Table 7. Definition of the characteristic temperatures from Figure 27.

Symbol	Description
T_{nuc}	Nucleation temperature of a phase, such as α-Al, Al-Si eutectic and Al-Cu eutectic
T_{min}	Minimum temperature of a phase, such as α-Al, Al-Si eutectic and Al-Cu eutectic; latent heat amount balances the heat amount of the system
T_{growth}	Growth temperature of a phase, such as α-Al, Al-Si eutectic and Al-Cu eutectic
T_{NG}	The difference between the nucleation and growth temperatures ($T_{NG} = T_{nuc}$-T_{growth})
T_{rec}	Recalescence undercooling of a phase, such as α-Al and Al-Si eutectic ($T_{rec}=T_{growth}$-T_{min})
$T_{solidus}$	Solidus temperature; marks the end of the solidification

The DSC measurements were carried out in a dynamic argon atmosphere (70 mL min^{-1}) by using a Setaram Labsys Evo equipment. The cell was heated up to 760 C at 5 ºC/min and then equilibrated at this temperature for 15 min before cooling at 5 ºC/min to room temperature.

2.3.4.2. Microstructure

Optical microscope (OM), scanning electron microscope (SEM) equipped with energy-dispersive (EDS), wavelength-dispersive spectrometers (WDS) and electron backscattered diffraction (EBSD) and transmission electron microscopy (TEM) equipped with EDS were used to characterize the type and morphology of the phases precipitated during solidification and heat treatment of studied alloys.

Some microstructural features, such as the size and morphology of Si particles and Fe-rich compounds, were quantitatively analysed using an image analyser. Several micrographs were captured from each specimen to obtain a statistical average of the analysed parameters.

To quantitatively calculate the grain size, the polished specimens were etched in concentrated Keller's reagent (7.5 ml HNO_3, 2.5 ml HF, 5 ml HCl and 35 ml H_2O). The grain size was measured using the intercept method, according to the ASTM standard E112-12 [129]. To highlight Fe-rich

compounds in the microstructure, the surfaces of some samples were etched in a mixture of H_2O and H_2SO_4, preheated to 70 ºC.

2.3.4.3. Tensile properties

The tensile tests were conducted at MTS 810 tensile testing machine at a strain rate of 10^{-3} s^{-1}. The strain was measured using a 25-mm extensometer. The as-cast specimens were only tested at room temperature (20 ºC), whereas the heat-treated specimens were tested at both room (20 ºC) and high temperatures (200 and 300 ºC). For the cases of high-temperature tests, the tensile specimens were held at testing temperature for 30 min before starting the test. At least four tensile tests were conducted for each condition. Experimental data were collected and processed to provide yield strength (YS), ultimate tensile strength (UTS) and elongation to failure (% El).

3. SUMMARY OF RESULTS AND DISCUSSION

CHAPTER INTRODUCTION

This chapter presents and summarizes main results of this work. More detailed discussion of the findings is provided in the appended Supplements. Each Supplement addresses the research questions posed to various degrees. This chapter comprises two research topics: (1) investigation of the role of transition metal impurities in solidification path and microstructural evolution of secondary Al-7Si-3Cu-0.3Mg alloys (phases I, II and III), and (2) investigation of the effects of deliberate addition of some transition metals on solidification path, microstructural evolution and mechanical properties of secondary Al-7Si-3Cu-0.3Mg alloys (phases IV and V).

3.1. Phase I – Grain refinement, eutectic modification and intermetallics formation in secondary Al-Si-Cu-Mg alloys: role of transition metal impurities

In this research phase, metallographic and thermal analysis techniques were used to quantitatively examine the macro- and microstructural changes occurring in secondary Al-7Si-3Cu-0.3Mg alloy before and after the melt chemical treatment (modification with Al-10Sr and grain refinement by Al-5Ti-1B) at various pouring temperatures (700, 750 and 800 ºC).

3.1.1. Solidification path and general microstructure

Figure 28 shows the solidification path of untreated and treated Al-7Si-3Cu-0.3Mg alloy; three different peaks associated with the formation of α-Al, Al-Si eutectic and Cu-rich phases (Al_2Cu and $Al_5Si_6Cu_2Mg_8$) are revealed in the derivative curve of the untreated alloy (Figure 28a), whereas, in addition to the above-mentioned phases, the α-$Al_{15}(FeMn)_3Si_2$ reaction gave a rise of a small peak in the first derivative of the treated alloy (see Figure 28b). The precipitation sequence observed in this study agrees well with Refs. [10, 130]. Application of thermal analysis technique to study the role of melt chemical treatment by Al-Ti-B and Al-Sr based master alloys in the nucleation and growth of α-Al and Al-Si eutectic is well studied and the changes occurred in the regions of α-Al and Al-Si eutectic formation in the cooling curves upon the melt chemical treatment is in consistency with the literature [127, 131].

Figure 29 shows the typical microstructures observed in the studied alloys; in general, the microstructures consist of α-Al matrix, eutectic Si network, Cu- and Fe-rich phases. It is worth noting that, in addition to the observed eutectic modification and grain refinement, which are discussed in detail in the following sections, the melt chemical treatment also rendered some changes in the phases formation sequence during alloy solidification. Iron, which is present as an impurity was bound to α-$Al_{15}(FeMn)_3Si_2$ in untreated alloy, whereas the treated alloy microstructure exhibits both α-$Al_{15}(FeMn)_3Si_2$ and β-Al_5FeSi phases. In addition, the flaky-like

AlSiTi compounds were only observable in the microstructure of the treated alloy (see Figure 30). Lack of the relative peaks in the cooling and derivative curves is likely due to the heat amount generated during the formation of these phases, which is below the resolution limit of the thermal analysis technique used [130, 131]. Since both AlSiTi and β-Al_5FeSi are considered as deleterious intermetallics [130, 132, 133], this research work contributed a great deal to characterize some metallurgical parameters having an influence on the formation behaviour of these intermetallics.

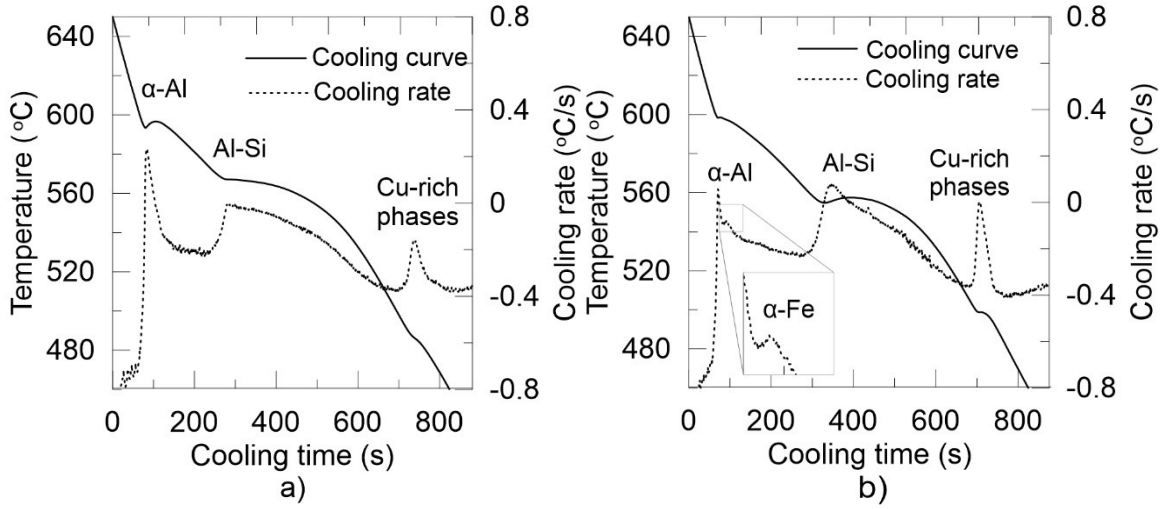

Figure 28. Cooling curves of (a) untreated and (b) treated Al-7Si-3Cu-0.3Mg alloy. The corresponding first derivatives are plotted.

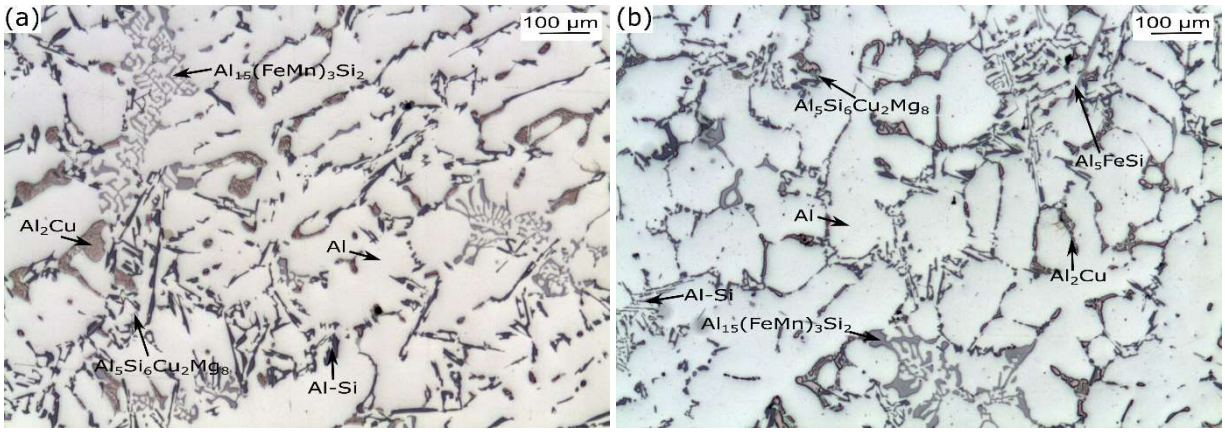

Figure 29. Optical micrographs from a) untreated and b) treated Al-7Si-3Cu-0.3Mg alloys. The main phases are indicated throughout.

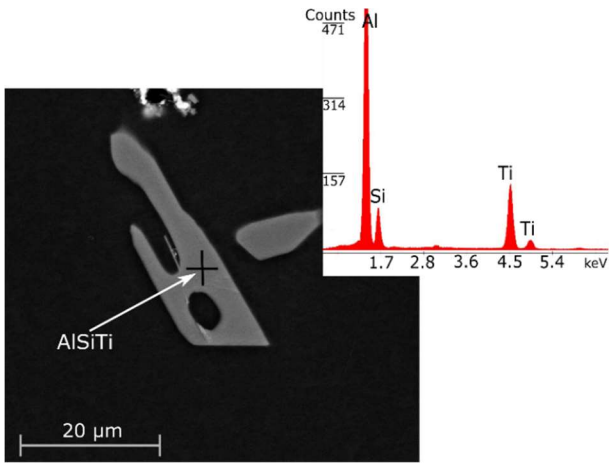

Figure 30. BSE image showing the AlSiTi particle with the corresponding EDS spectra.

3.1.2. α-Al grains refinement

Both macrostructural (Figure 31) and thermal (Figure 28) analyses confirm a notable grain refinement achieved upon the addition of Al-5Ti-1B master alloy to the base alloy. With the Al-5Ti-1B addition, the average grain size and the corresponding standard deviation decreased by about 5 and 10 times, respectively (see Figure 32). In addition, it can be seen from Figure 32 that the pouring temperature shows no apparent influence on grain refinement level in the present experimental conditions. It is known from the literature how some transition metals, such as Zr and V, can negatively affect the efficiency of Al-Ti-B based grain refiners due to their interaction with TiB_2 or Al_3Ti grain refining substrates, thus reducing their potency to nucleate α-Al [28, 29, 32, 134]. The deactivation of TiB_2 particles by Zr were found to be more evident at higher melt holding temperatures, ~ 800 ºC [29, 32]. However, in the present study, no evidence of the poisoning effect of Zr on grain refining efficiency of Al-5Ti-1B master alloys was observed. Since the base (untreated) alloy contains low Zr concentration (~ 100 ppm), its interaction with TiB_2 particles seems to be insignificant.

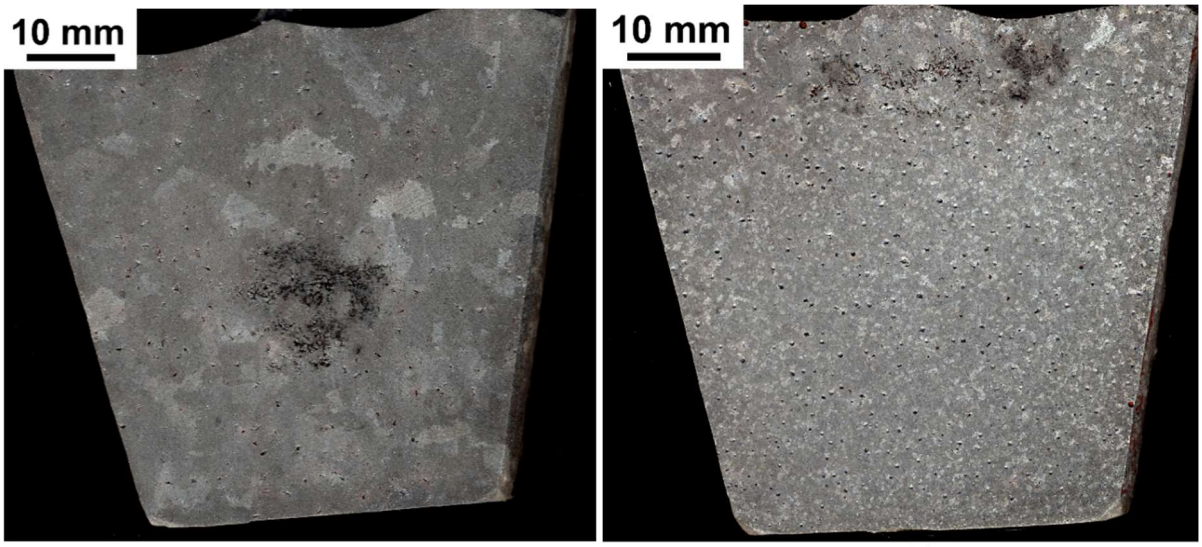

Figure 31. Grain structure of (a) untreated and (b) treated Al-7Si-3Cu-0.3Mg alloys.

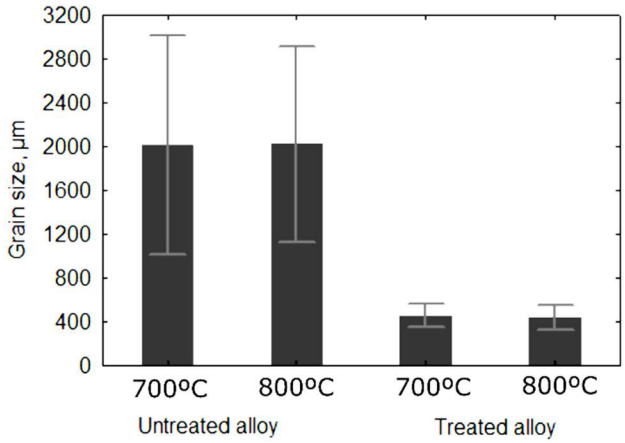

Figure 32. The evolution of α-Al grains in untreated and treated Al-7Si-3Cu-0.3Mg alloys as a function of the pouring temperature. The standard deviations are given as error bars.

However, in the present study, several transition metal impurities, such as Zr, V and Mn, showed a tendency to accumulate into the primary AlSiTi intermetallics (Figure 33). As noted earlier, the

AlSiTi compounds appeared only in the microstructure of the treated alloy (Figure 29); the precipitation of these deleterious intermetallic compounds are more likely promoted by the increased Ti content (see Table 2) which exceeds its max solid solubility limit in the α-Al [135]. It has been recently stated that, in the presence of sufficient amount of Si and Ti in Al-Si alloy, the interaction of Si with Ti can occur directly in the melt, forming AlSiTi intermetallics [33].

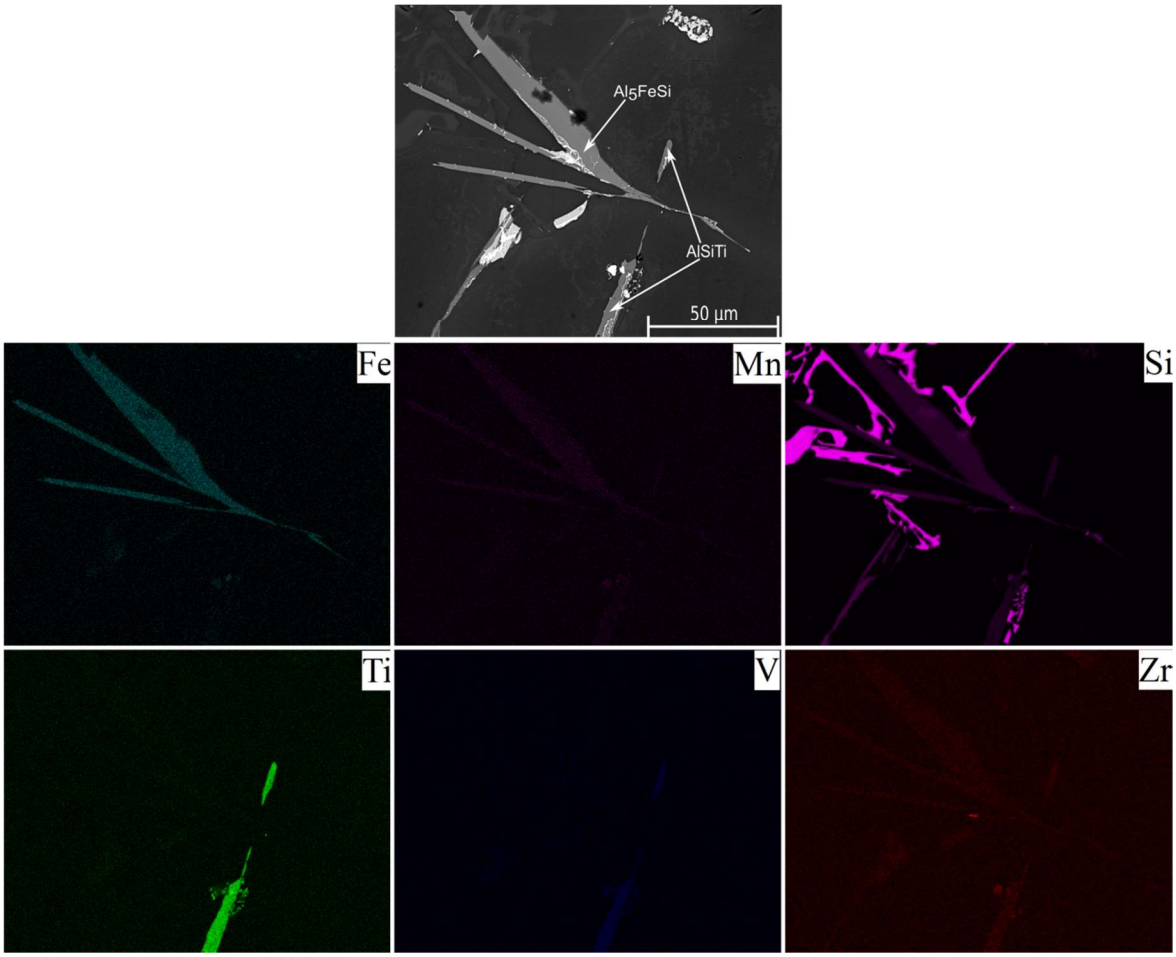

Figure 33. Backscattered electron image of AlSiTi and Al_5FeSi particles with the corresponding EDS composition maps, showing the distributions of Ti, V, Zr, Fe, Mn and Si elements.

Although the solubility of V and Zr into the AlSiTi particles in Al-Si alloy containing Zr and V as the alloying elements has been previously confirmed [136], the present study also revealed how, in addition to impurity elements Zr and V, some Mn can also incorporate into AlSiTi particles (Figure 33). It can be thus noted that transition metal impurities Zr, Mn and V tend to further promote the formation of undesired AlSiTi intermetallics in secondary Al alloys refined by Al-Ti-B based master alloys. The precipitation of these primary compounds causes not only casting defects formation due to their flaky-like morphology, but also reduction of the degree of constitutional undercooling in front of growing α-Al; it is known that Ti possess the highest growth restriction factor in Al. It can be thus inferred that the optimization of grain refiner addition level in secondary Al foundry alloys, containing Ti, V and Zr as impurities, is more complicated than the process optimization in primary alloys.

It has been recently reported [137] how V tends to dissolve into β-Al_5FeSi phase, thereby showing no apparent influence on the evolution of alloy grain structure; however, according to the findings

of the present study, vanadium more preferentially accumulates into primary Ti-bearing compounds than the β-Al_5FeSi phase (Figure 33).

3.1.3. Al-Si eutectic modification

The characteristic temperatures related to the formation of eutectic Si were extracted using the derivatives and cooling curves and compared between untreated and treated alloys, processed at different melt superheats (see Figure 34a). Varying the pouring temperature showed no influence on the eutectic reaction of untreated alloy, e.g. T_{growth} remained almost constant around 566 ºC (see Figure 34a). Depression of the eutectic formation temperature observed in the treated alloy (see Figure 34a) is an indication of the eutectic Si structure modification [138], which was also verified by the microstructural investigation of the size and morphology of eutectic Si particles (see Figure 34b). A slight increase in the nucleation and minimum temperatures of the eutectic reaction with increasing the pouring temperature in treated Al-7Si-3Cu-0.3Mg alloy (see Figure 34a) is due to Sr fading in the molten bath as melt oxidation occurs upon prolonged holding time at higher temperature.

It has been reported that some trace elements such as Bi and B can induce a negative impact on the efficiency of Sr modification [139-141]. However, low content of trace elements present in the base alloy seems to result in no interactions of trace elements, such as B and Bi with Sr [142, 143]. Moreover, transition metal impurities present in the base alloy showed no impact on the occurrence of eutectic reaction in the present study.

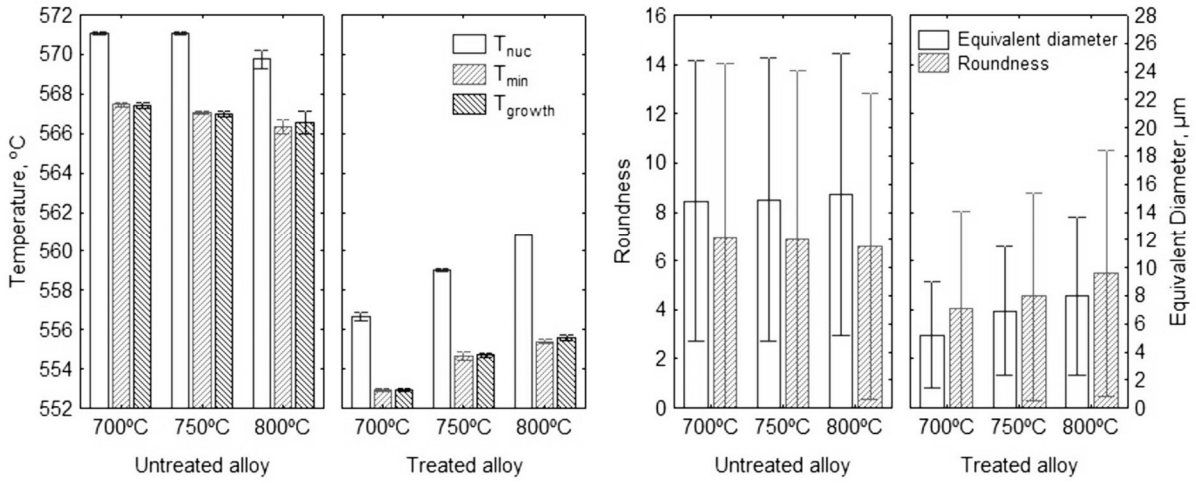

Figure 34. (a) The solidification characteristics of eutectic Si over different pouring temperatures and chemical treatment level; (b) evolution of average roundness and equivalent diameter of eutectic Si particles as function of pouring temperature and chemical treatment.

3.2. Phase II – Fe-rich intermetallics in secondary Al-Si-Cu-Mg alloys: role of Al-5Ti-1B grain refiner

In this research phase, thermal and metallographic analysis techniques were used to investigate the influence of Al-5Ti-1B and Al-10Ti grain refiner additions on the precipitation of Fe-rich compounds in secondary Al-7Si-3Cu-0.3Mg alloys. In addition, step casting (see Figure 26) production route was employed to investigate the influence of cooling rate on the formation of Fe-

rich compounds in secondary Al-7Si-3Cu-0.3Mg alloy, before and after grain refinement with Al-5Ti-1B.

3.2.1. Thermal analysis

Figure 35 shows the cooling curves and corresponding first derivatives of the studied alloys in the region of primary α-Al formation. The recalescence, which has been effectively used to assess the grain refinement level [144], clearly indicates higher grain refining efficiency of Al-5Ti-1B compared to that of Al-10Ti master alloys [145].

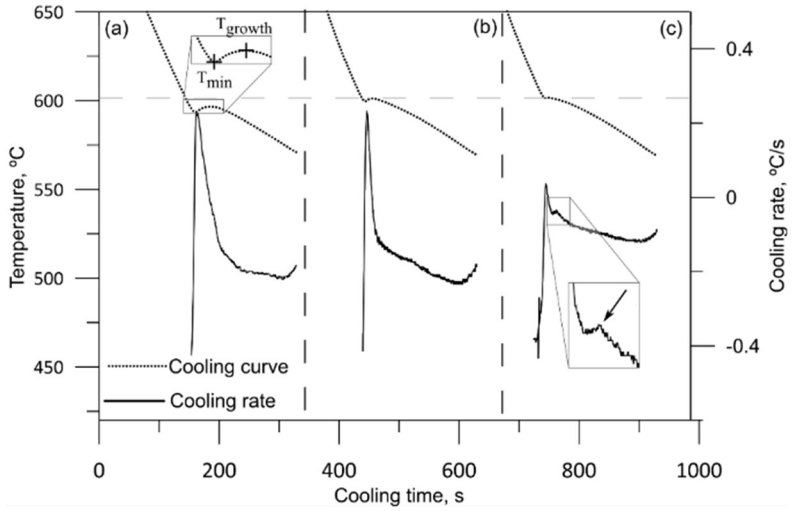

Figure 35. Cooling curves of Al-7Si-3Cu-0.3Mg alloy (a) before the grain refinement, after addition of (b) Al-10Ti and (c) Al-5Ti-1B grain refiners. The corresponding first derivatives are also presented.

Typical microstructures obtained from Al-7Si-3Cu-0.3Mg alloy with different melt chemical treatment levels are shown in Figure 36. In all the studied alloys, the α-$Al_{15}(FeMn)_3Si_2$ appears as a dominant Fe-rich phase in the microstructure. Needle-like β-Al_5FeSi particles appeared only in the microstructure of the alloy refined by Al-5Ti-1B master alloy (Figure 36c). No β-Al_5FeSi reaction was detected in the base alloy and the alloy refined by Al-10Ti master alloys.

The derivative curve related to the alloy refined by Al-5Ti-1B exhibits a small peak indicated by arrow in Figure 35c; this peak is thought to be the consequence of α-Fe reaction. Since the growth of primary α-Al takes longer time in non-grain-refined alloy and the alloy refined by Al-10Ti, as compared to the alloy refined by Al-5Ti-1B, the peak indicating the formation of α-$Al_{15}(FeMn)_3Si_2$ in the two former alloys can be overlapped by the neighbouring peak representing primary α-Al formation. The precipitation of β-Al_5FeSi has been reported to occur mainly by two sequences: (1) pre-eutectic i.e. prior to the (Al)-Si eutectic reaction, in the form of two phases (Al)- $Al_9Fe_2Si_2$ eutectic reaction, and (2) co- or post (Al)-Si eutectic in the form of three phases (Al)-Si-$Al_9Fe_2Si_2$ eutectic reaction [146]. Simplified Al-Si-Fe-Mn phase diagram (see Figure 37) suggests the occurrence of both pre-eutectic and co-eutectic reactions involving β-Al_5FeSi in the presently studied alloys. However, as β-Al_5FeSi formation occurred only in the Al-7Si-3Cu-0.3Mg alloy refined by Al-5Ti-1B and remained unfavourable during solidification of both non-refined alloy and the alloy refined with Al-10Ti, it is thus believed that some metastable α-Fe continues to form in preference to β-Al_5FeSi phase during solidification of non-refined alloy and the alloy grain refined by Al-10Ti. The fact that the occurrence of β-Al_5FeSi reaction during solidification of the base alloy and the alloy refined by Al-10Ti remained unfavourable, can be due to absence of potent

nucleation site in the melt, which in turn, leads to a greater melt undercooling for the nucleation of β-Al_5FeSi phase to occur; however, before certain solid particle in the interdendritic liquid region becomes active for β-Al_5FeSi phase nucleation during solidification, the nucleation of metastable α-$Al_{15}(FeMn)_3Si_2$ seems to occur more easily. It has been stated that several particles such as Al_2O_3 and Al_3Ti particles can act as nucleation sites for the formation of α-Fe phase [124]. The present study revealed that α-$Al_{15}(FeMn)_3Si_2$ phase can also nucleate on primary AlSiTi compounds (see Figure 38).

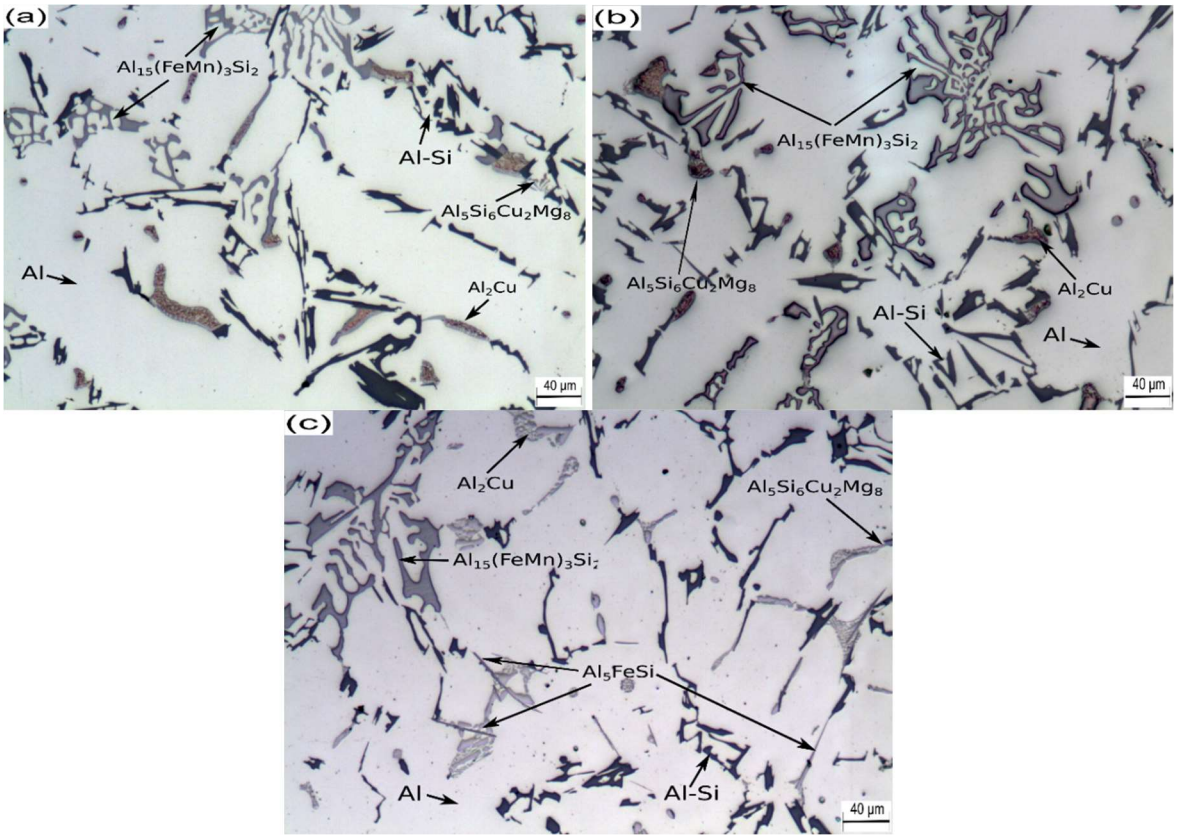

Figure 36. Typical microstructures of Al-7Si-3Cu-0.3Mg alloy (a) before grain refinement, (b) after grain refinement by Al-10Ti and (c) after grain refinement by Al-5Ti-1B master alloy.

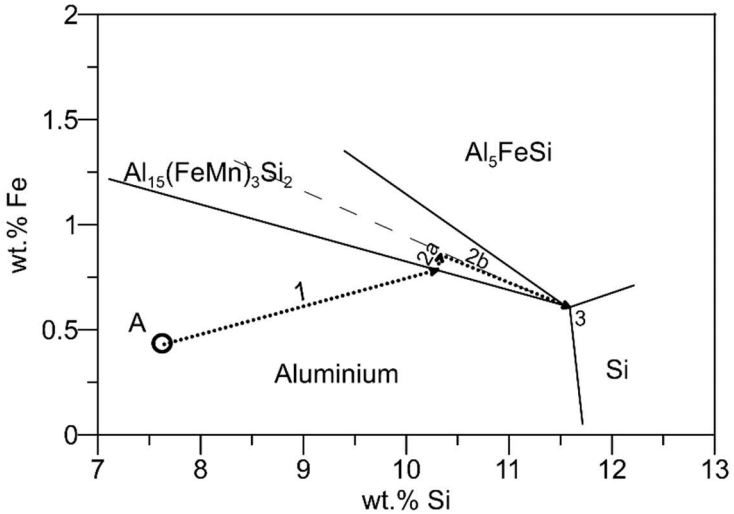

Figure 37. Simplified Al-Si-Fe-Mn phase diagram at 0.2 wt.% Mn level [10]. The composition of the base material investigated in this study is indicated by the point A.

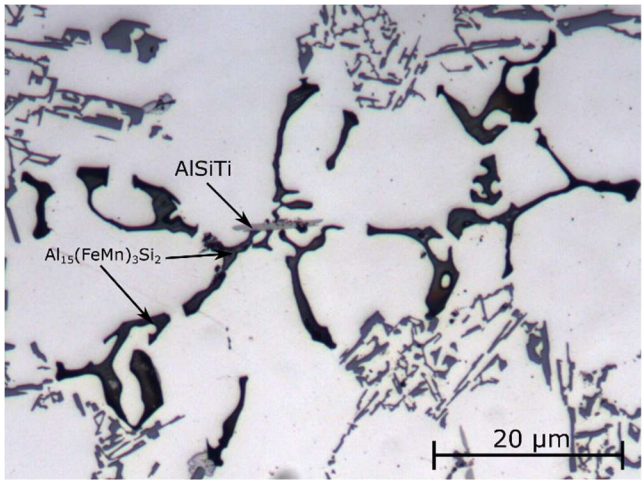

Figure 38. Optical micrograph showing the α-$Al_{15}(FeMn)_3Si_2$ phase precipitated on the surface of AlSiTi particles. The sample surface is etched for easy visualisation.

3.2.2. Influence of cooling rate

The cooling rates in the different steps of the casting (Figure 24) were estimated by the secondary dendrite arm spacing, SDAS, according to the empirical equation (2) [147]:

$$SDAS = 39.4R^{-0.317} \quad (2)$$

where *R* represents the mean cooling rate of the primary α-Al dendrites during solidification. Table 8 lists the average SDAS values with corresponding standard deviations and the estimated cooling rates.

Table 8. Average secondary dendrite arm spacing, SDAS, measured in different steps (with corresponding standard deviations) and the corresponding cooling rates calculated according to equation (2) are reported.

Step thickness (mm)	SDAS (µm)	Cooling rate (°C/s)
5	18 (2.5)	11.8
10	23 (3.4)	5.1
15	25 (3.9)	4.1
20	31 (4.8)	2.1

Typical microstructures representing non-refined alloy are shown in Figure 39a,b; α-$Al_{15}(FeMn)_3Si_2$ accounts for the major portion of Fe-rich phases, competing only with a small-sized π-$Al_8Mg_3FeSi_6$ particles in limited numbers. The β-Al_5FeSi formation remained unfavourable during solidification of non-refined alloy, regardless of cooling rate (Figure 39a,b). Figure 39c,d display typical microstructures observed in the alloy refined by Al-5Ti-1B master alloy. It is clearly evident from Figure 39 that after the grain refinement, the formation of β-Al_5FeSi phase becomes favourable and both α-$Al_{15}(FeMn)_3Si_2$ and β-Al_5FeSi phases formed during alloy solidification, which agrees with the results of thermal analysis samples in terms of the precipitation sequence of Fe-rich phases during solidification (Figure 36). However, it is worth noting that at high cooling rates i.e. in the microstructures from the step casting, the fraction of needle-like β-Al_5FeSi compounds was increased at the expense of α-$Al_{15}(FeMn)_3Si_2$ phase, i.e. more amount of Fe was involved in the formation of β-Al_5FeSi if compared to the microstructure

representing thermal analysis samples. This is inconsistent with Refs. [60-63], where it has been reported that higher cooling rate can exert positive influence on β-Al_5FeSi to α-$Al_{15}(FeMn)_3Si_2$ transformation; on the contrary, higher cooling rates (~ 12 ºC), in the present study, favoured the crystallization of β-Al_5FeSi over α-$Al_{15}(FeMn)_3Si_2$ phase. It is thus can be noted that grain refinement of secondary Al alloys can exert a notable influence on the precipitation kinetics of Fe-rich phases.

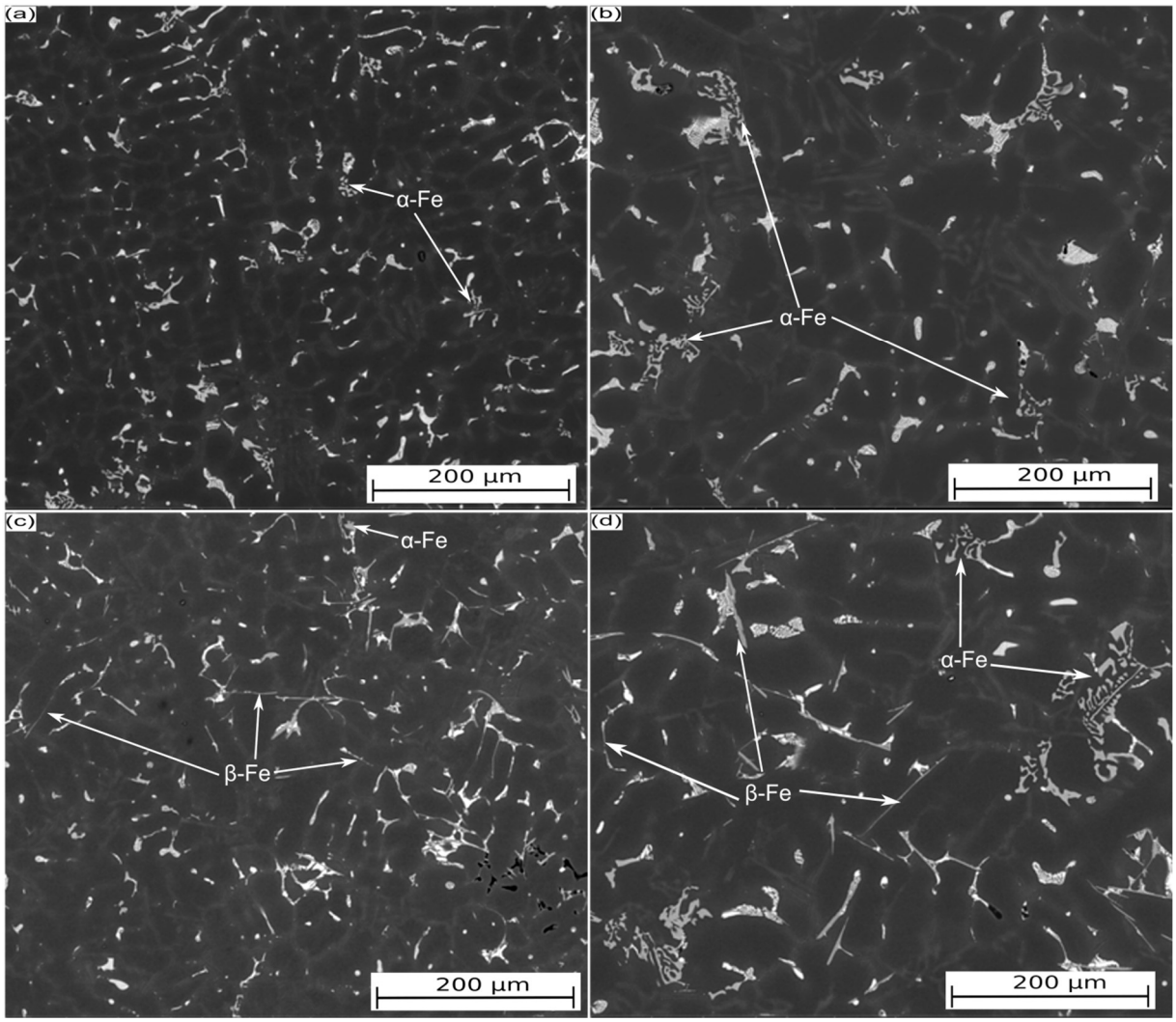

Figure 39. BSE images taken from (a,c) 5 mm and (b,d) 20 mm steps of step casting. The micrographs corresponds to (a,b) non-grain refined alloy and (c,d) grain refined alloy with Al-5Ti-1B.

Higher cooling rate reduced the average length of β-Al_5FeSi particles (Figure 40a), also accompanied by the increased number density (Figure 40b). Similar findings have been reported in Ref. [57], where increasing the cooling rate is found to displace the nucleation temperature of β-Al_5FeSi to lower temperatures, hence shortening the time available for the growth of β-Al_5FeSi. Moreover, it is also well-known that the cooling rate can control the nucleation and growth processes, thus affecting both the number density and the size of microstructural features, such as β-Al_5FeSi particles [64, 65].

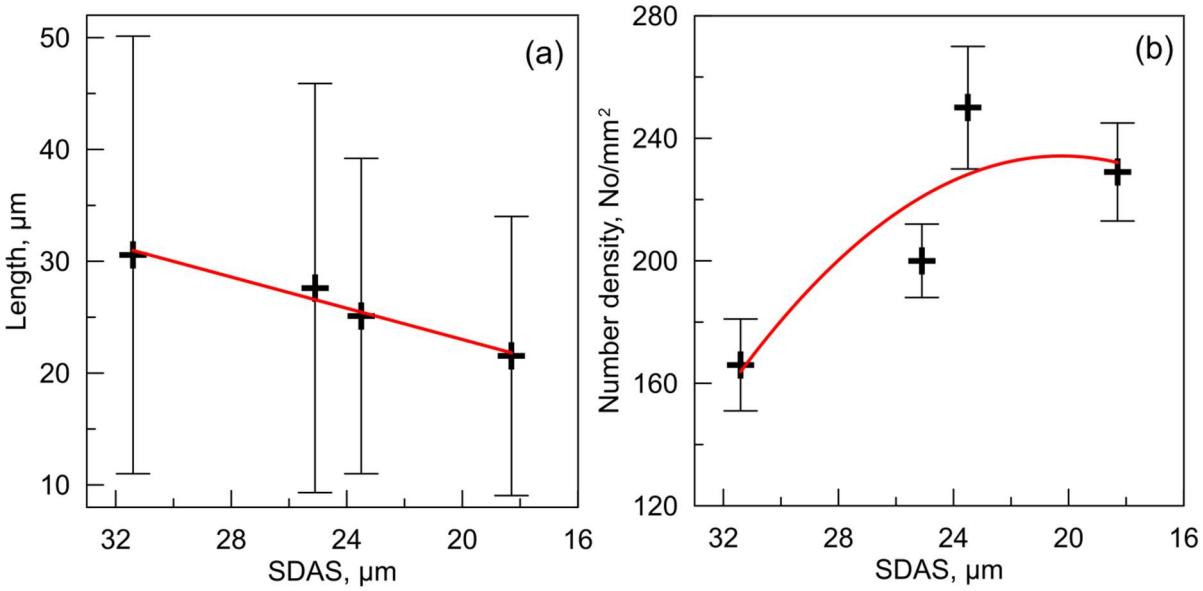

Figure 40. BSE image of Al_5FeSi particles with corresponding WDS composition maps, showing the distributions of Ti and B elements.

3.2.3. Precipitation of β-Al_5FeSi particles

Since needle-like β-Al_5FeSi compounds are known to degrade material mechanical properties, suppressing β-Al_5FeSi reaction by promoting the crystallization of less-deleterious α-$Al_{15}(FeMn)_3Si_2$ phase during alloy solidification is a well-diffused practice in Al foundries and this is normally achieved by adding Mn in the level of about half of Fe content. Hwang et al. [148] stated that in the presence of sufficient Mn amounts in Al-Si alloy, the β-Al_5FeSi formation can be completely suppressed; on the contrary, it has been also reported how even high Mn addition levels yield incomplete β-Al_5FeSi to α-$Al_{15}(FeMn)_3Si_2$ transformation [60]. It is thus worthy to note that in addition to the ratio between Fe and Mn contents in the alloy, the nucleation and growth kinetics of the phases, such as α-Fe and β-Al_5FeSi, can play a decisive role in promoting the formation of a certain phase during alloy solidification.

The present study revealed that the precipitation of β-Al_5FeSi particles occurs only after the grain refinement of Al-7Si-3Cu-0.3Mg alloy by Al-5Ti-1B. Although according to phase diagram presented in Figure 37, the precipitation of β-Al_5FeSi during solidification of the alloy is also expectable, no evidence of β-Al_5FeSi formation was observed in non-grain-refined alloy and the alloy refined with Al-10Ti.

The nucleation of Fe-rich phases, particularly β-Al_5FeSi phase is generally thought to take place on Al_2O_3 and/or AlP particles, which are normally present in Al alloys, particularly in secondary materials [41, 57, 149, 150], however, these phases appear not to favour the nucleation of β-Al_5FeSi phase during solidification of the base material in the present investigation conditions.

The α-$Al_{15}(FeMn)_3Si_2$ phase has a non-faceted growth mode, which allows the α-$Al_{15}(FeMn)_3Si_2$ phase to grow more easily in irregular shape [10]. On the contrary, the growth of β-Al_5FeSi phase occurs by the twin plane re-entrant (TPRE) mechanism in a lateral or faceted mode and contains multiple (001) growth twins parallel to the growth direction [51, 52], and thus, there is no need to nucleate a new plane. A high lateral growth rate of β-Al_5FeSi phase has been recently observed by means of in situ microtomography using high-energy X-rays synchrotron [130, 150]. The growth disadvantage of the faceted over non-faceted phases can be explained by the difficulty in atomic attachment in former case. In other words, at high cooling rates, and hence reduced time for

growth, a greater degree of undercooling is required to overcome the barrier to atomic attachment to (and hence growth of) the faceted phase than to the non-faceted morphology [151]. Therefore, increasing the cooling rate is reported to promote the formation of a metastable α-$Al_{15}(FeMn)_3Si_2$ phase at the expense of stable β-Al_5FeSi particles [10], which agrees well with Ref. [151], where it has been demonstrated how the faceted Al_6Fe phase can be replaced by non-faceted Al_3Fe at higher solidification front velocities. However, this behaviour seems to be relevant in the case when there is a competition between the growth rates of two phases. However, for the competitive growth theory to become applicable, both the stable and metastable phases must nucleate easily. Considering that in the present study, the β-Al_5FeSi phase dominates at high cooling rates of the alloy grain refined by Al-5Ti-1B, as can be observed by comparing Figure 36c with Figure 39c,d it can be thus noted that the role of the competitive nucleation is more relevant than the competitive growth theory in understanding non-equilibrium solidification of the investigated alloys.

The lack of β-Al_5FeSi reaction during solidification of the base alloy can be explained by a greater undercooling needed for the nucleation of β-Al_5FeSi phase; in contrast, the nucleation of α-Fe seems to occur more easily on certain substrate in the undercooled melt, and thus the formation of some metastable α-Fe remains still favourable for nucleation and growth, thus avoiding the precipitation of β-Al_5FeSi in the microstructure. In other words, once the segregation line, presented in Figure 37, reaches line 2a, α-$Al_{15}(FeMn)_3Si_2$ phase becomes thermodynamically stable phase and continues to form until the segregation line crosses the line 2b, where the precipitation of both α-$Al_{15}(FeMn)_3Si_2$ and β-Al_5FeSi is expected to occur; however, due to lack of a potent nucleation site for β-Al_5FeSi, nucleation of stable and even some metastable α-Fe seems to occur more easily.

In contrast, solidification of the alloy refined with Al-5Ti-1B proceeds by involving both α-$Al_{15}(FeMn)_3Si_2$ and β-Al_5FeSi reactions. This suggests the melt contains certain particles which facilitate nucleation of β-Al_5FeSi at low undercooling. The TiB_2 particles released into the melt upon the addition of Al-5Ti-1B master alloys, are known to act as heterogeneous nucleation for α-Al and thus play an important role in grain refinement of Al alloys [152]. However, the majority of TiB_2 particles added into the melt does not contribute to the nucleation of α-Al grains, and, as a result, these particles can be pushed to interdendritic liquid, where they can be active to nucleate certain eutectic phases. The EDS and WDS investigations also revealed the presence of TiB_2 particles adjacent to β-Al_5FeSi compounds (Figure 41 and Figure 42). It is, therefore, proposed that the TiB_2 particles promoted the crystallization of β-Al_5FeSi over α-$Al_{15}(FeMn)_3Si_2$ by acting as potent nucleation site. Sha et al. [153], demonstrated by using transmission electron microscopy (TEM) how TiB_2 can nucleate β-Al_5FeSi in 6xxx series wrought Al alloys due to low lattice mismatch. Similar results have also been reported in Ref. [154]. This finding could also explain why the addition of Al-Ti-B grain refiner caused a thickening of β-Al_5FeSi, as reported in Ref. [68], and precipitation of β-Al_5FeSi at earlier stages of solidification [136]. The TiB_2 seems to promote the nucleation of β-Al_5FeSi without any need for greater undercooling, and as a result, thickening and branching of β-Al_5FeSi occurs due to the increased solidification range of β-Al_5FeSi.

The chemical compositions of α-$Al_{15}(FeMn)_3Si_2$ and β-Al_5FeSi phases, analysed by EDS, are presented in Table 9; it is evident that Mn has also a strong solubility in β-Al_5FeSi phase, indicating that the local chemistry is favourable for the occurrence of both α-$Al_{15}(FeMn)_3Si_2$ and β-Al_5FeSi reactions.

Table 9. Average EDS results of α-$Al_{15}(FeMn)_3Si_2$ and β-Al_5FeSi phases (at.%).

Alloy	Al	Si	Fe	Mn	Cr	Cu
α-$Al_{15}(FeMn)_3Si_2$	73	11	11	2	0.14	bal.
β-Al_5FeSi	70	17	10	1	-	bal.

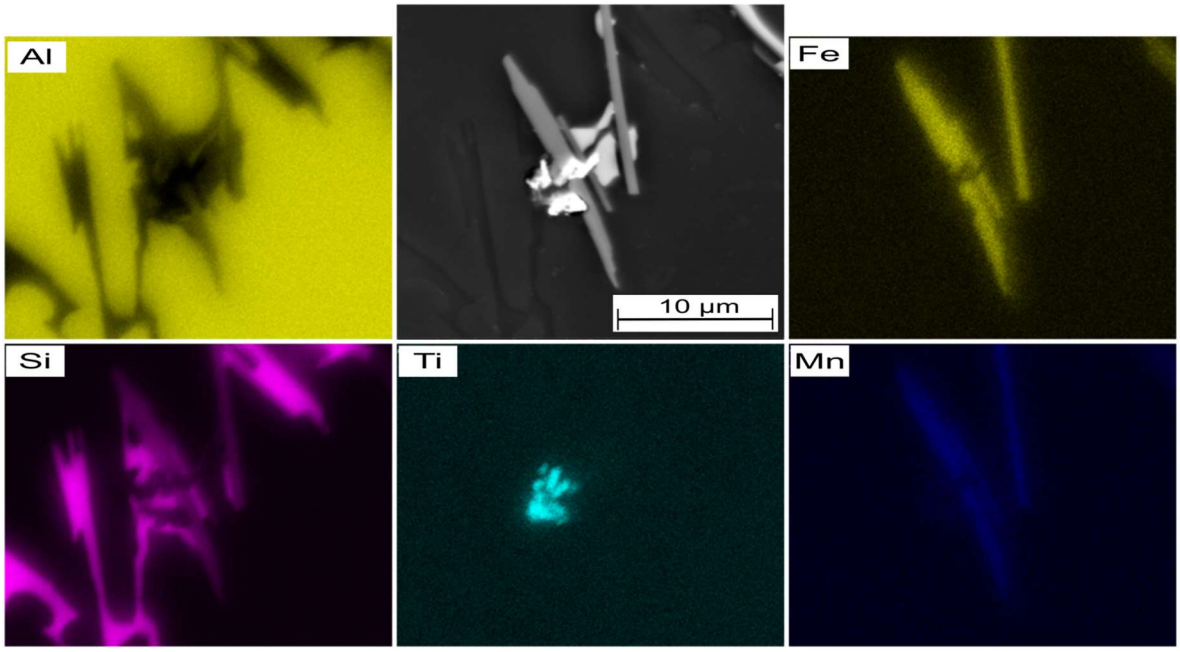

Figure 41. Backscattered electron image of β-Al_5FeSi phase with corresponding EDS composition maps, showing the distributions of Al, Fe, Mn, Si and Ti elements.

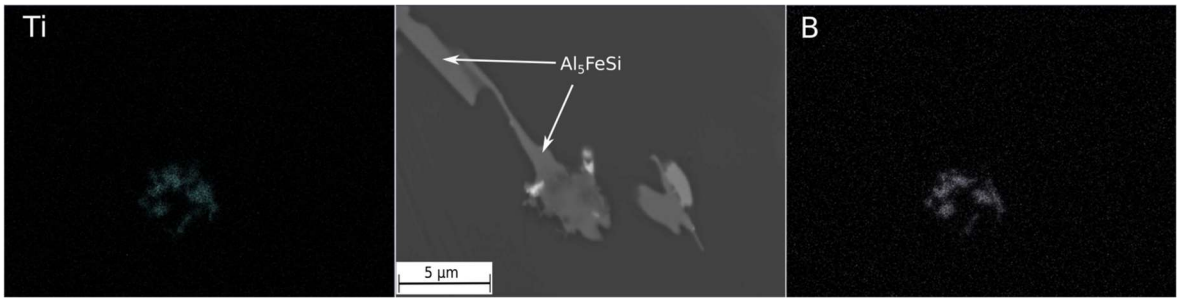

Figure 42. Backscattered electron image of β-Al_5FeSi particles with corresponding WDS composition maps, showing the distributions of Ti and B elements.

Another interesting finding of this study is the impact of higher cooling rate in further promoting the precipitation of β-Al_5FeSi phase at the expense of α-Fe in the alloy grain refined with Al-5Ti-1B. Higher cooling rate tends to further promote β-Al_5FeSi formation in the material refined with Al-5Ti-1B; β-Al_5FeSi needles become the dominant Fe-rich phase largely replacing α-$Al_{15}(FeMn)_3Si_2$ in the microstructure. Greater thermal undercooling provided by higher cooling rates causes the solidification to quickly proceed through the line 2a (see Figure 37), thus involving only a small amount of Fe in the crystallization of α-$Al_{15}(FeMn)_3Si_2$ phase. As a result, the remaining Fe in liquid region beocmes available to solidify through the line 2b, where the precipitation of β-Al_5FeSi compounds occurs more favourably due to the presence of potent substrates, TiB_2, for their nucleation. A similar observation has been reported in Ref. [66], where the β-Al_5FeSi has been found to nucleate more efficiently on TiB_2 particles in the alloy containing higher solute concentrations, in contrast to the alloys with less alloying elements, where the TiB_2

appears to be inactive for β-Al_5FeSi nucleation. This behaviour shows the role of constitutional undercooling in improving the potency of the nucleation sites.

3.3. Phase III – Fe-rich intermetallics in secondary Al-Si-Cu-Mg alloys: a comparison of the roles of Al-5Ti-1B and Al-5B grain refiners

In this research phase, two different castings: (1) cylindrical-shaped castings (SDAS ~20 µm) (see Figure 25) and (2) cup castings (SDAS ~60 µm) of thermal analysis (see Figure 23), were produced to analyse and compare the effects of adding varying levels of Al-B and Al-Ti-B based grain refining master alloys and the cooling rate on the solidification of Fe-rich intermetallic phases.

3.3.1. Grain refinement with Al-5Ti-1B master alloy

Table 10 lists the average grain size measured in the studied alloys; greater Ti and B levels induced more effective grain refinement [14].

Table 10. Average grain size and corresponding standard deviation (in mm) measured in base alloy (0 ppm B) and after metal treatment with Al-5Ti-1B (40 and 80 ppm B) and Al-5B (400 and 800 ppm).

Alloy	**Base alloy**	**Base alloy + Al-5Ti-1B**		**Base alloy + Al-5B**	
B content (ppm)	**0**	**40**	**80**	**400**	**800**
Grain size (mm)	2.1 (0.8)	0.6 (0.2)	0.44 (0.1)	0.8 (0.2)	0.41 (0.1)

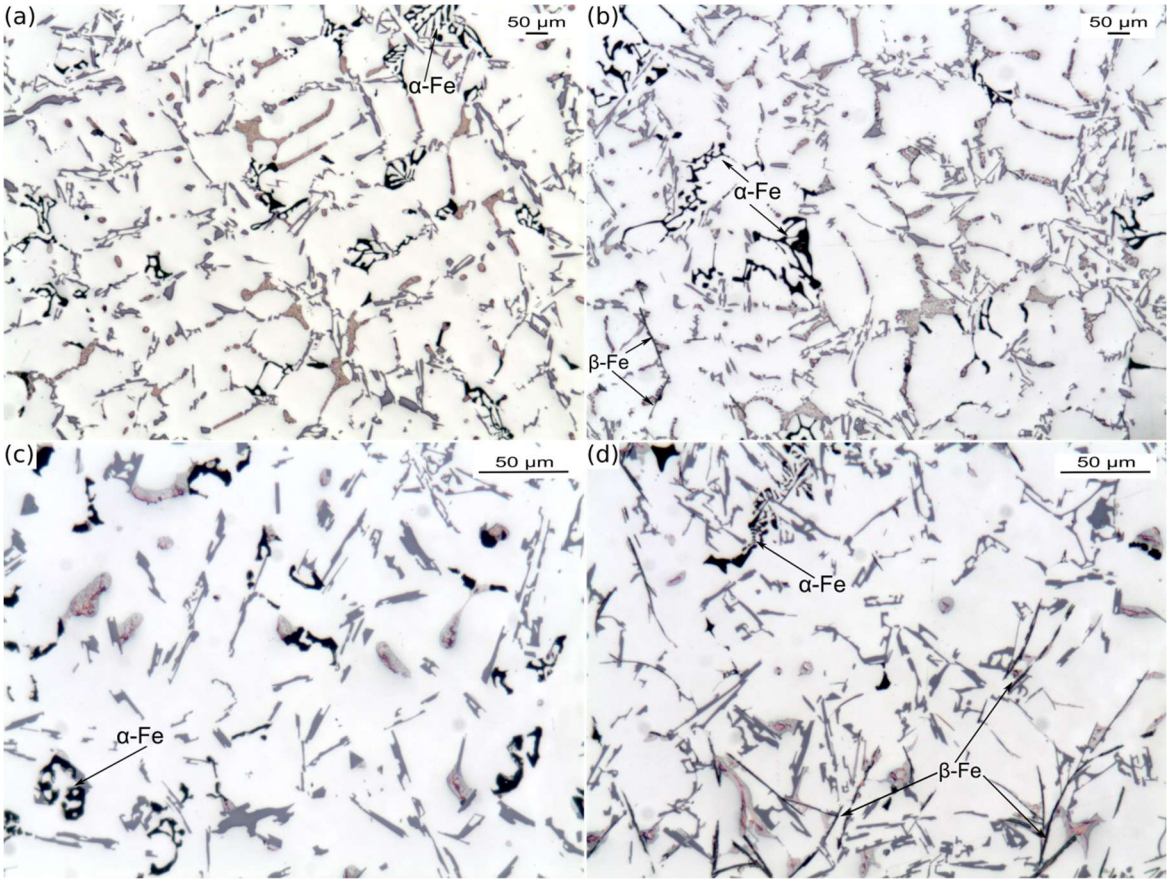

Figure 43. Typical microstructures representing (a,c) the base alloy and (b,d) the alloy refined with Al-5Ti-1B (80 ppm B). The micrographs correspond to specimens produced with (a,b) large-diameter mould (60 µm SDAS) and (c,d) small-diameter mould (20 µm SDAS). The samples were etched to highlight Fe-rich compounds.

In the previous research phase (see Section 3.2), it has been demonstrated how the addition of Al-5Ti-1B grain refiner (170 ppm B) induces the precipitation of deleterious β-Al_5FeSi compounds at the expense of α-$Al_{15}(FeMn)_3Si_2$ phase. The results of the present investigations indicate that the grain refinement of Al alloy by Al-5Ti-1B master alloy at even low addition levels can induce and promote the formation of β-Al_5FeSi phase (Figure 43). It is also found that increasing Al-5Ti-1B grain refiner addition level enhances the nucleation rate of β-Al_5FeSi particles (Table 11). Consistent with results of the previous research phase, higher cooling rate (SDAS ~ 20 µm) further promoted the β-Al_5FeSi formation during solidification of the alloy refined by Al-5Ti-1B (Table 11). It is also worth noting that higher cooling rate shows a significant influence on the activation of β-Al_5FeSi phase nucleation in the alloy refined by Al-5Ti-1B.

Table 11. Average area fraction (%) of β-Al_5FeSi phase observed in the base alloy (0 ppm B) and after grain refinement with Al-5Ti-1B (40 and 80 ppm B) and Al-5B (400 and 800 ppm), cast in large-diameter (60 µm SDAS) and small-diameter (20 µm SDAS) moulds.

Alloy	**Base alloy**	**Base alloy + Al-5Ti-1B**		**Base alloy + Al-5B**	
B content (ppm)	**0**	**40**	**80**	**400**	**800**
SDAS ~ 60	-	0.15	0.2	-	-
SDAS ~ 20	-	0.31	0.47	-	-

- Not revealed from optical microscopy analysis

3.3.2. Grain refinement with Al-5B

Table 10 clearly indicates how Al-5B grain refiner (800 ppm B) exerts a demonstrable role in refining the grain structure of the alloy and the average grain size achieved by Al-5B addition is notably comparable with that obtained upon Al-5Ti-1B grain refiner addition. It must be also noted that the presence of some transition metals, such as Ti, Zr and V, which are present in the base alloy as trace elements (impurities) leads to the consumption of some B amount to form transition metal diborides (TiB_2, ZrB_2 and VB_2) directly in the melt. In-situ formation of these diborides in the melt also leads to their clustering, which then leads to their rapid removal from the melt via settlement. Formation of these transition metal diborides is more favourable than AlB2 due to their lower free energy [155]. Therefore, effective grain refinement of secondary Al alloys by Al-B based master alloys is only achievable upon the addition of sufficient amount of Al-B master alloy which releases enough B amount for effective grain refinement, in addition to those involved in the formation of transition metal diborides [156]. In the present study, adding 400 ppm B resulted in relatively poor grain refinement level (see Table 10); boron released into the melt appears to be mainly bound to transition metal diborides and thus lesser amount of B remains available for the formation of AlB_2 necessary for alloy grain refinement. In contrast, adding 800 ppm B effectively refined the grain structure of the alloy, occurring in addition to the complete removal of transition metal diborides from the melt via settlement.

Typical microstructures representing the alloy refined by Al-5B master alloy and solidified at two different rates are shown in Figure 44. It is evident that α-$Al_{15}(FeMn)_3Si_2$ appears to be again as a sole Fe-rich phase in the microstructure regardless of the cooling rate. This implies that unlike Al-5Ti-1B master alloy, the Al-5B grain refiner tends not to promote the formation of β-Al_5FeSi phase during alloy solidification. To be more exact, the AlB_2 particles forming during solidification and contributing to the alloy grain refinement appear to be kinetically inactive to nucleate β-Al_5FeSi, even though AlB_2 is isomorphous with TiB_2. This can be due to either larger lattice mismatch between

AlB_2 and β-Al_5FeSi or the formation of an Al overlay or else on the AlB_2 compounds, thus deactivating the nucleation of β-Al_5FeSi. The formation of SiB_6 [31] and Al [157] layers on AlB_2 have been reported in the literature to explain the mechanisms responsible for the grain refinement of Al-Si alloys with Al-B master alloys.

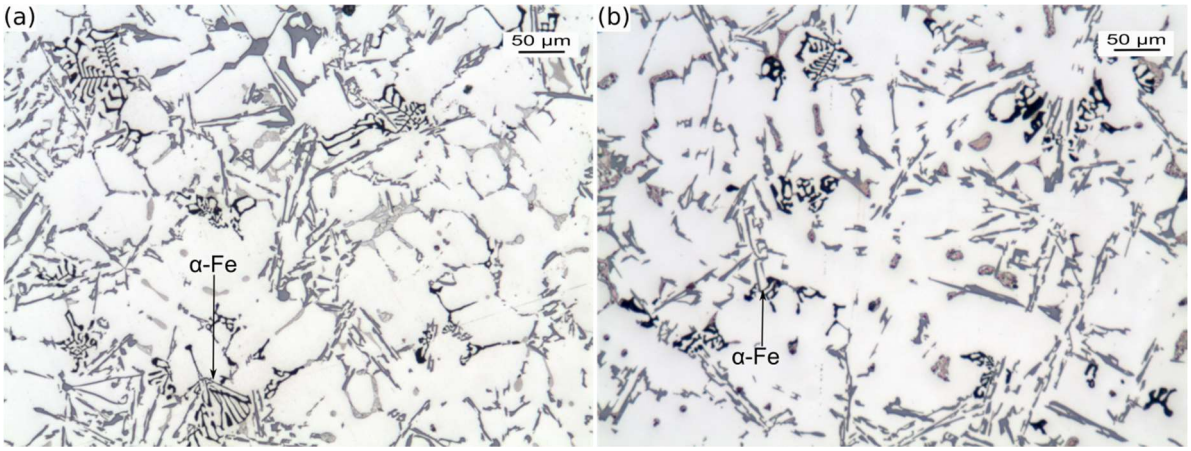

Figure 44. Typical microstructures of alloy refined with Al-5B (800 ppm B), and cast in (a) large diameter mould (60 µm SDAS) and (b) small diameter mould (20 µm SDAS). The samples were etched to highlight Fe-rich compounds.

3.4. Phase IV – Solidification processing and microstructural evolution of secondary Al-Si-Cu-Mg alloys: role of Zr, V and Ni additions

The effects of individual and combined Zr, V and Ni (0.12, 0.25 and 0.25 wt.% respectively) additions on solidification path and microstructural evolution of secondary Al-7Si-3Cu-0.3Mg alloy with SDAS of ~ 60 µm were investigated using microscopy and thermal analysis techniques.

3.4.1. Thermal Analysis

Figure 45 shows the cooling curves and the associated first derivatives related to Al-7Si-3Cu-0.3Mg and Al-7Si-3Cu-0.3Mg+Ni,V,Zr alloys. Formation of several phases, such as α-Al, eutectic Si and Cu-rich compounds, gave rise to the evident peaks during thermal analysis, which is consistent with Reference [10]. Adding alloying elements Ni, V and Zr individually or in combination altered the formation temperatures of primary α-Al and post-eutectic Cu-rich compounds. Although the formation of phases containing Ni, V and Zr is expectable during solidification [106, 107], the cooling curves and the associated first derivatives of the studied alloys revealed no peak related to their formation, which can be due to a limited fraction of Ni/V/Zr-rich phases forming during solidification.

In comparison, the heating and cooling traces obtained from the DSC measurements revealed an additional peak occurring due to post-eutectic reaction only in Ni-added alloys (see Figure 45b); thus, this can be described by the formation of Ni-rich intermetallic compounds [106]. The formation temperatures of the main phases, such as α-Al, Al-Si eutectic and Cu-rich compounds are also observable in the heating and cooling traces obtained from the DSC measurements (see Figure 45b). Like traditional thermal analysis, comparison of the cooling curves of the studied alloys obtained from the DSC measurements also confirmed how adding Ni, V and Zr induces changes in the precipitation kinetics of primary α-Al and the Cu-rich compounds.

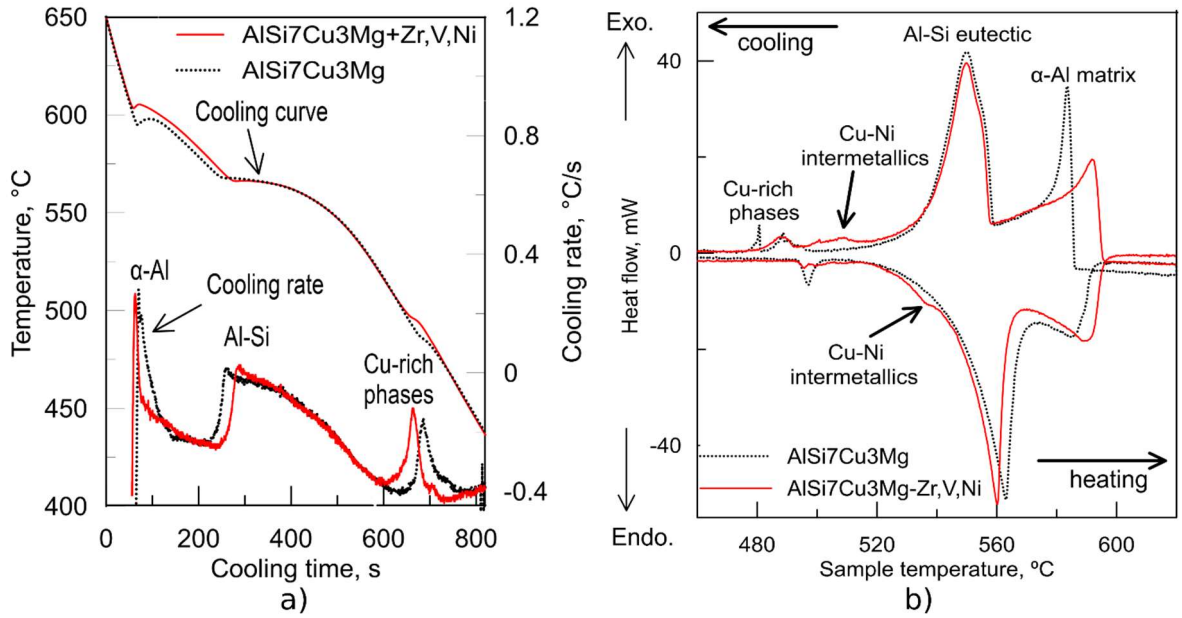

Figure 45. (a) Cooling curves and corresponding first derivatives obtained from thermal analysis of Al-7Si-3Cu-0.3Mg alloy before and after 0.25% Ni, 0.25% V and 0.12% Zr additions; (b) heating and cooling DSC curves obtained from the same alloys.

Comparison of the cooling traces related to primary α-Al reaction and obtained from the DSC measurements of the studied alloys (see Figure 46) indicate that while Ni addition exerted no apparent influence, adding Zr and V individually or in combination shifted the formation temperature of α-Al towards higher temperatures, which can be attributed to the peritectic nature of added transition metals. As can be seen in Figure 46 and Table 12, the liquidus temperature, T_{liq}, which is determined from the extrapolated finish point of the endothermic peak on the heating curves of the studied alloys, increases with Zr and/or V addition. The nucleation temperatures, T_{nuc}, of the studied alloys are also determined from the extrapolated onset point of the exothermic peak on the cooling curves (see Figure 46) and listed in Table 12. The undercooling degrees, ΔT, required for the initiation of primary α-Al in the studied alloys and calculated according to the equation (3)

$$\Delta T = T_{liq} - T_{nuc} \qquad (3)$$

where T_{liq} is the liquidus temperature and T_{nuc} is the nucleation temperature, both determined from the DSC heating and cooling curves respectively, are listed in Table 12. It can be seen from Table 12 that while Ni addition causes no apparent changes on ΔT, adding Zr and V individually or in combination led to a reduction in ΔT value, particularly in Zr-added alloys. This implies that with the addition of Zr and/or V, primary α-Al tends to nucleate more easily on certain substrate, which is elaborated in detail in section 3.4.2.

Although Ni addition showed no impact on the formation of primary α-Al, it influenced the sequence and kinetics of post-eutectic reactions. In addition to observed peak associated with the formation of Ni-rich compounds during DSC analyses, the solidification reaction involving Cu-rich compounds occurred at higher temperatures (see Figure 45).

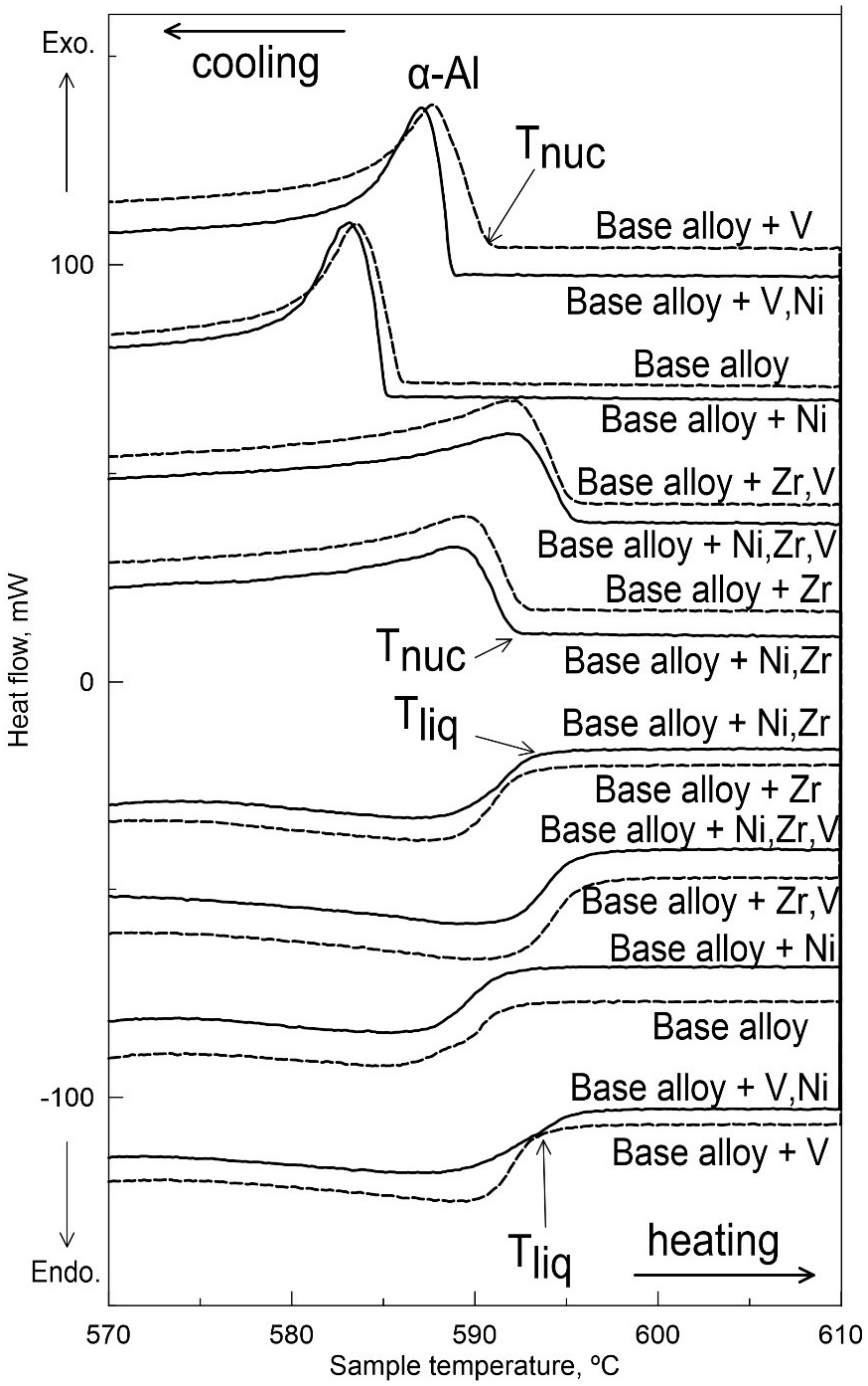

Figure 46. Comparison of the cooling curves in the formation region of α-Al phase from all the experimental alloys. Time-scale in the horizontal axis is adjusted for easy observation.

Table 12. Characteristic temperatures on DSC curves and the estimated nucleation undercooling of studied alloys (°C).

Alloys	T_{liq}, ºC	T_{nuc}, ºC	ΔT, ºC
Base alloy	593.1	586.2	6.9
Base alloy + Ni	592.2	585.5	6.7
Base alloy + V	596.0	591.5	4.5
Base alloy + Ni, V	596.0	590.7	4.7
Base alloy + Zr	593.8	593.1	0.7
Base alloy + Zr, Ni	593.8	592.4	1.4
Base alloy + V, Zr	596.6	595.6	1.0
Base alloy + Ni, Zr, V	597.5	595.6	1.9

3.4.2. Solidification macrostructure

Figure 47 shows the evolution of the grain structure in the studied alloys with different Zr and V additions. It is evident from Figure 47 that varying the alloying addition levels influenced the formation of α-Al grains. Both V and Zr additions contributed to the refinement of the grain structure, reducing the average grain size from ~1200 μm in the base alloy to ~700 μm in the alloy with individual V or Zr addition. The combined V and Zr additions showed stronger grain refinement level than the individual V or Zr additions; the average grain size was decreased to ~500 μm.

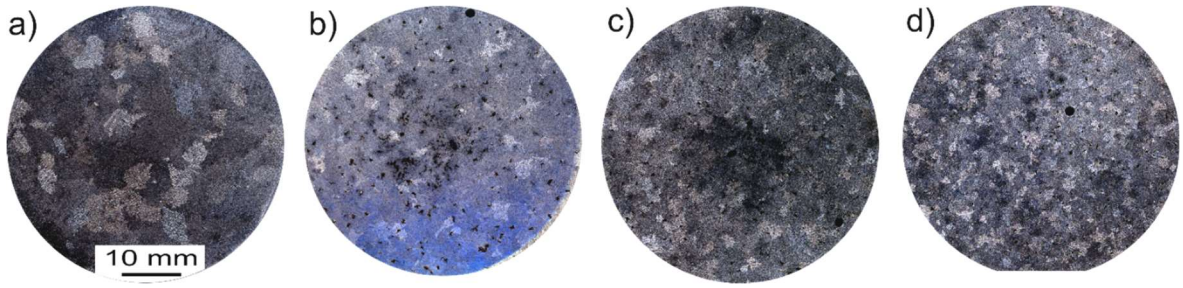

Figure 47. Grain structures of Al-7Si-3Cu-0.3Mg alloy from thermal analysis test sections; the macrographs refer to (a) the base alloy and after (b) 0.12% Zr, (c) 0.25% V, and (d) 0.12% Zr and 0.25% V additions.

It is known that adding Zr beyond its max solubility in α-Al matrix leads to the precipitation of primary pro-peritectic particles prior to the formation of primary α-Al. Microstructural investigations revealed that Zr-rich particle appearing inside α-Al grain (see Figure 48) only contains Zr and Al as constituent elements (see Figure 48). Therefore, based on the EDS results (Figure 48) and the equilibrium Al-Zr system (see Figure 11a), the particle appearing in the centre of α-Al grain is believed to be the Al_3Zr phase, which has been found as potent nucleation site for the primary α-Al [30, 97, 158]. A significant reduction in the degree of undercooling, ΔT, observed in Zr-added alloys (Table 12) also indicates how these Zr-rich particles can effectively nucleate α-Al at lower undercoolings. The mechanism of grain refinement by Zr addition in Al alloys is well discussed in Reference [30]. Moreover, the presence of pro-peritectic Al_3Zr within α-Al grain also implies that the peritectic reaction remained incomplete during solidification due to relatively higher cooling rate than the equilibrium condition.

Although V addition caused grain refinement of the alloy (see Figure 47), no any intradendritic V-rich particle that would be responsible for the grain refinement was revealed in the present investigation. According to the equilibrium Al-V system (see Figure 11b), several V-rich pro-peritectic phases, such as $Al_{21}V_2$ and Al_3V, are expected to precipitate [159]; both these V-rich particles were found to possess low interfacial energy with α-Al [91]. However, the V-rich pro-peritectic particles are more likely not forming during alloy solidification, which can be due to lower V addition level to the base alloy or more preferential involvement of V in the formation of $(AlSi)_2(VTiMn)$ and α-$Al_{15}(FeMn)_3Si_2$ phases, as discussed in more detail in section 3.4.3. As both $(AlSi)_2(VTiMn)$ and α-$Al_{15}(FeMn)_3Si_2$ compounds form by pre-eutectic reaction during alloy solidification, the role of V is believed to be significant in enhancing the growth restriction factor (Q), which is a parameter used to measure the effect of solute on grain refinement [21]

$$Q = mc_0(k-1) \qquad (3)$$

where m is the gradient of the liquidus, c_0 is the alloy composition, k is the partitioning coefficient. For multicomponent alloys, the Eq. 3 is extended to include the contribution of each alloying element [22]. Although the concentration of V is quite low, 0.25 wt. %, the $m(k-1)$ factor is quite high in comparison to the other elements such as Si, Mg, Cu, etc; hence, the presence of V in the alloy can significantly contribute to constitutional undercooling of the liquid in the solidifying front, leading to the activation of certain heterogeneous nuclei present in the liquid.

The effect of V on grain refinement of Al-Si alloys is disputed in the literature. While some researches [160, 161] stated that V addition can markedly refine the grain structure of Al alloys, other investigations [162, 163] revealed no apparent influence; the presence of Si in Al alloys is believed to avoid the formation of pro-peritectic V-rich precipitate needed for effective grain refinement [163]. Considering the grain refinement attained in the present study upon V addition, it can be argued that V addition can significantly contribute to restricting the growth of α-Al crystals and activating certain solid particles to nucleate α-Al phase.

Further grain refinement level achieved upon combined Zr and V additions can be mainly attributable to the increased number of potent nucleation sites due to the enrichment of V in Zr-rich particles (see Figure 49).

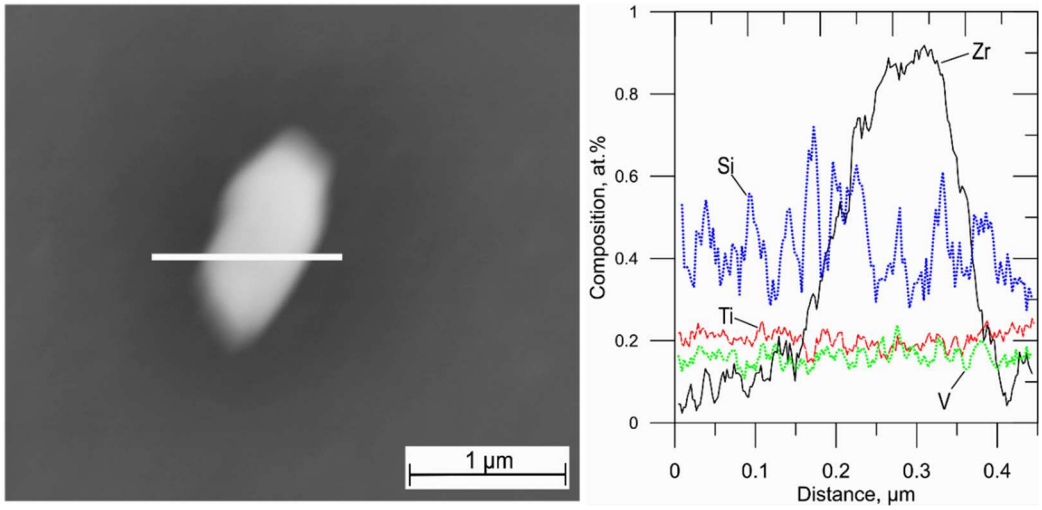

Figure 48. SEM image of Zr-rich phase in Al-7Si-3Cu-0.3Mg+Zr alloy with corresponding EDS line-scan, showing the distributions of Ti, Si, V and Zr elements.

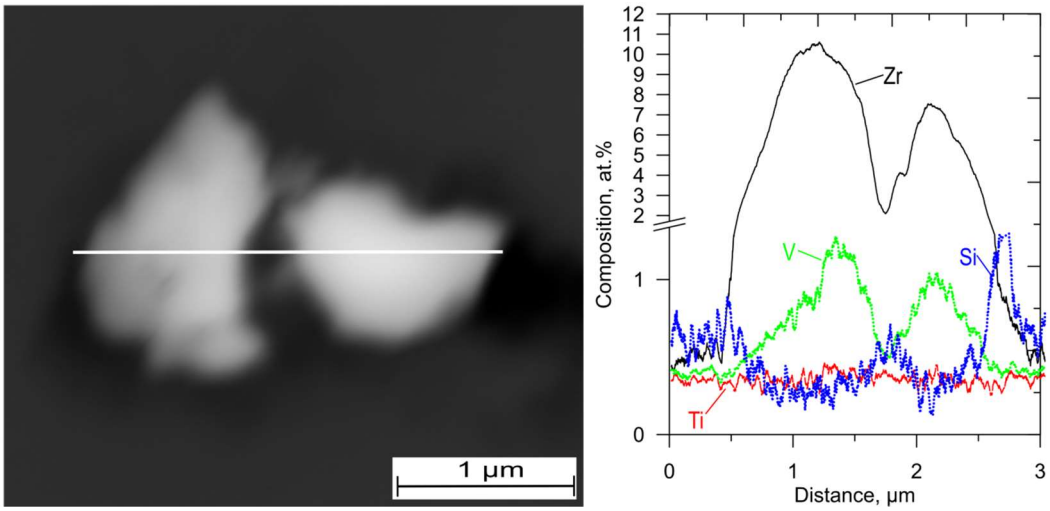

Figure 49. SEM image of Zr-rich phase in Al-7Si-3Cu-0.3Mg + Zr,V alloy with corresponding EDS line-scan, showing the distributions of Ti, Si, V and Zr elements.

3.4.3. Solidification microstructure

In general, transition metals, such as Zr and V, are added to improve the material high-temperature mechanical properties [84, 109, 110, 164]. Applying heat treatment promotes solid-state transformation of phases involving Zr and V in α-Al grain interiors; the precipitates enriched with slow-diffusers are thought to strengthen the material. However, their low diffusivity complicates both homogenization of transition metals throughout microstructure and dissolution of primary, interdendritic compounds containing transition metals into α-Al matrix during conventional heat treatment; hence, the role of solidification microstructure in defining the alloy mechanical properties is significant.

Figure 50 shows typical microstructures representing Al-7Si-3Cu-0.3Mg and Al-7Si-3Cu-0.3Mg+Zr,V,Ni alloys. The microstructure of the base alloy exhibits α-Al matrix, Al-Si eutectic, Al_2Cu, $Al_5Si_6Cu_2Mg_8$, $Al_{15}(FeMn)_3Si_2$ phases (Figure 50a). Adding V, Zr and Ni to Al-7Si-3Cu-0.3Mg alloy induced the formation of V-, Zr- and Ni-rich intermetallic compounds in addition to the phases observed in the base material (Figure 50b).

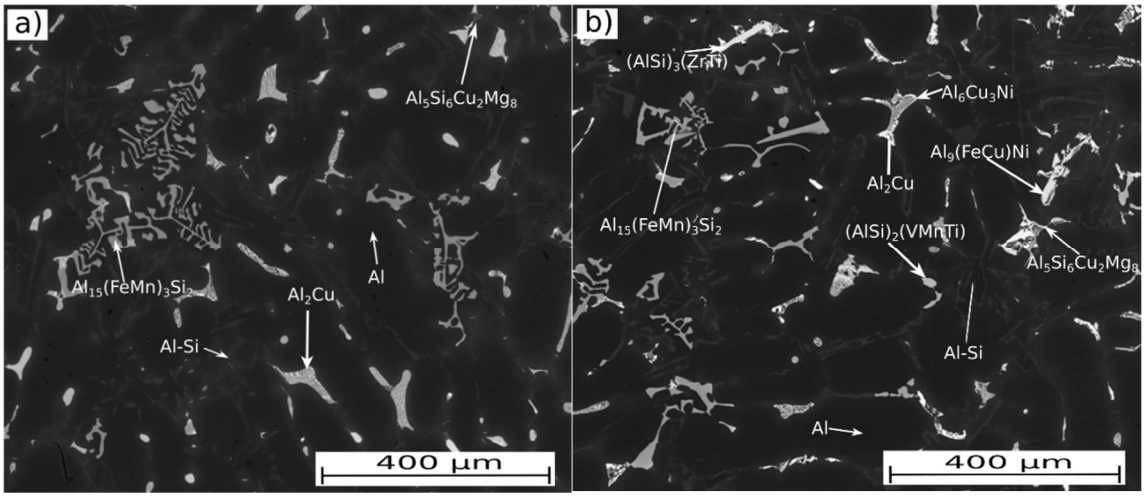

Figure 50. SEM micrographs obtained from (a) Al-7Si-3Cu-0.3Mg, and (b) Al-7Si-3Cu-0.3Mg+Ni,Zr,V alloys. The different phases are indicated by arrows throughout.

In addition to some intradendritic Al_3Zr particles (see Figure 48), interdendritic Al-Si-Zr-Ti compounds (see Figure 51), which are referred as $(AlSi)_3(TiVZr)$ phase in the literature [94], formed during the early stage of solidification of Zr-added alloys; however, in the present study, V appears to be slightly soluble in $(AlSi)_3(TiVZr)$, reaching up to 0.5 at.% in the alloys with combined Zr and V additions (see Figure 51). The $(AlSi)_3(TiVZr)$ particles were scarce in the microstructure, appearing with flaky morphology and in the size range of 15-70 µm. It has been reported how the Zr-rich compounds appearing in the interdendritic regions with flaky morphology tend to deteriorate casting soundness and alloy mechanical properties [18, 84, 110]. It can be thus inferred that the level of Zr should not be too high than its max solid solubility in α-Al to avoid the formation of a large volume fraction of insoluble and deleterious intermetallics.

Moreover, primary $(AlSi)_3(TiVZr)$ particles seem to act as the preferential nucleation sites for the formation of α-Fe-rich compounds (see Figure 52). The AlSiTi compounds, which are structurally similar to $(AlSi)_3(TiVZr)$ phase, were also found as potent nucleation sites for α-Fe compounds (see Figure 38). Although this observation may not contribute to the development of high-temperature resistant Al alloy, it can allow us to enlarge our fundamental understanding of the role of

heterogeneous nucleation in the formation of intermetallic compounds containing transition metal impurities, e.g. Fe-rich phases during Al alloy solidification. As it is discussed in Sections 3.2 and 3.3, the role of heterogeneous nucleation appears to be significant in controlling the formation of Fe-rich compounds in Al-Si alloys.

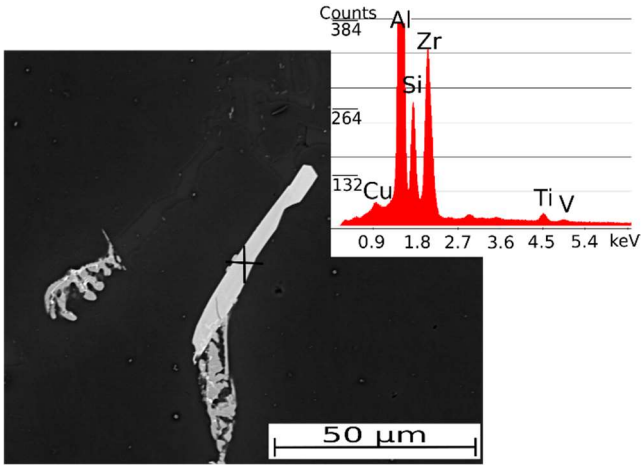

Figure 51. SEM micrograph showing an AlSiZrTi particle with the corresponding EDS spectra in the Zr-containing alloy (Al-7Si-3Cu-0.3Mg+Zr).

Since primary, interdendritic Zr/V-rich compounds cannot easily dissolve into the α-Al matrix during solution heat treatment due to low diffusivity of Zr and V in α-Al, the supersaturation of Zr and V in solid solution of α-Al should be achieved during non-equilibrium solidification to maximize their dispersion hardening effect. The distribution of Zr, V, Ti and Mn elements over the cross section of α-Al grain observed in Al-7Si-3Cu-0.3Mg+Zr,V alloy is shown in Figure 53. The α-Al grain core exhibits positive segregation of V and Ti, whilst another peritectic-forming element, Zr, appears to be uniformly distributed across the α-Al grain (see Figure 53); this can be due to the involvement of Zr in the formation of primary $(AlSi)_3(TiVZr)$ and Al_3Zr particles, which causes the remaining liquid to become less-enriched with Zr. This clearly indicates how the dispersion hardening effect of Zr in Al-Si alloys is limited; however, the V, Ti and Mn show higher solubility in α-Al matrix, which can allow the solid-state precipitation of V/Ti-rich phases at relatively higher volume fractions, thus contributing better to alloy strengthening.

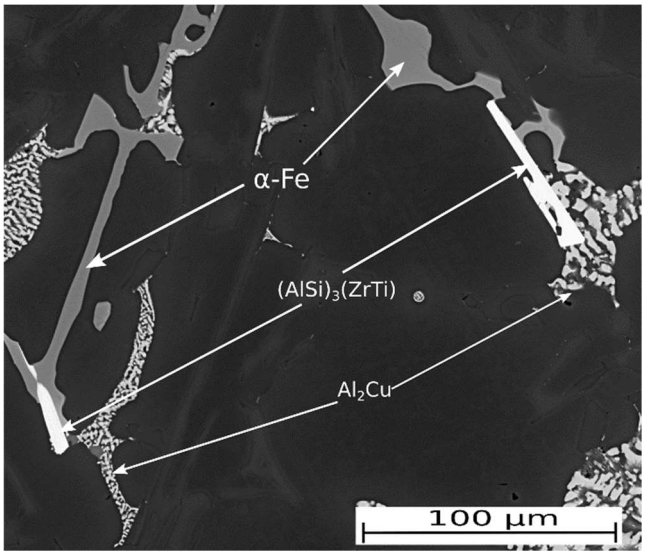

Figure 52. SEM micrograph showing the nucleation of Cu- and Fe-rich phases on $(AlSi)_3(ZrTi)$ particles.

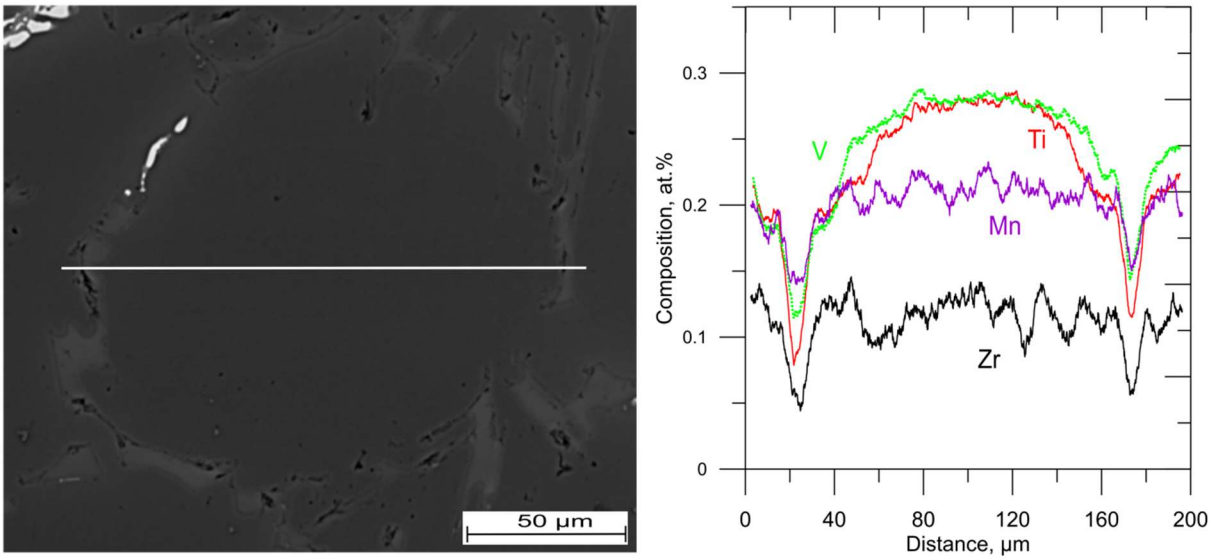

Figure 53. SEM image of α-Al grain in Al-7Si-3Cu-0.3Mg+Zr,V alloy with corresponding EDS line-scan, showing the distributions of Zr, V, Ti and Mn elements.

As previously mentioned, pro-peritectic V-rich precipitates remained unfavourable to form during solidification of V-added alloys. Excess V beyond saturation limit in α-Al matrix was involved in the crystallisation of polyhedral-shaped $(AlSi)_2(VTiMn)$ phase, appearing in interdendritic regions with the average size of ~15 µm. This phase is rarely observable throughout the microstructure. The phase is well indexed with hexagonal $CrSi_2$ (Figure 54), which is isomorphous with Si_2V phase [165]. While Al can easily substitute Si in this phase due to similarity in their atomic radius [166], the Cr, Mn and Fe are more likely incorporating into Si_2V by substituting V. Enabling the solid-state precipitation of a phase containing both V and Mn can be beneficial due to their opposite partitioning behaviour in α-Al, which can lead to a reduction of dispersoid free zones in the α-Al grains. As can be seen in Figure 53, the distribution of Mn over the cross section of α-Al grain is homogeneous as its partitioning coefficient is almost equal to unity, while V tends to segregate to grain core/centre during alloy solidification.

Some part of V segregated to interdendritic liquid during solidification were found to be bound to $Al_{15}(FeMn)_3Si_2$ phase (see Figure 55) [161, 163].

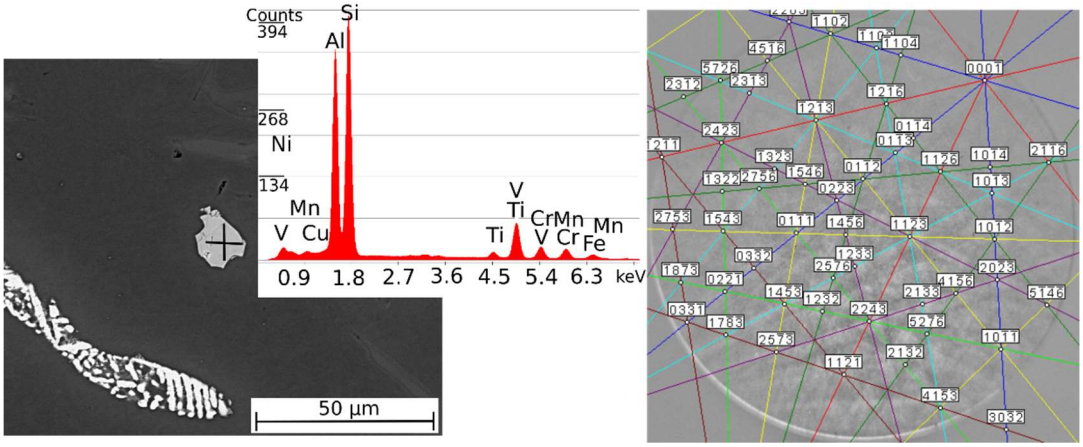

Figure 54. SEM micrograph showing hexagonal $(AlSi)_2(VTiMn)$ particle in V-containing Al-7Si-3Cu-0.3Mg alloy, with corresponding EDS spectra and indexed EBSD pattern.

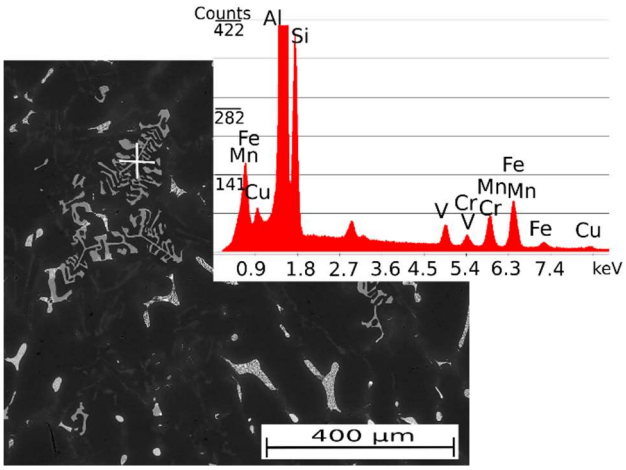

Figure 55. SEM micrograph showing the presence of V in $Al_{15}(FeMn)_3Si_2$ particle in Al-7Si-3Cu-0.3Mg+V alloy.

Due to low solid solubility of Ni in α-Al matrix, almost all Ni added to the alloy were involved in the formation of interdendritic intermetallic compounds. Microstructural investigation revealed two different Ni-rich phases: $Al_9(FeCu)Ni$ and Al_6Cu_3Ni, as identified by the analysis of chemical composition and crystallographic structure (Figure 56 and Figure 57). The monoclinic $Al_9(FeCu)Ni$ phase appears in microstructure in flaky morphology (see Figure 56) [105], whilst the compounds formed with bone-like morphology was identified as the cubic Al_6Cu_3Ni phase (see Figure 57).
Both Al_6Cu_3Ni and $Al_9(FeCu)Ni$ compounds were reported to positively contribute to alloy high-temperature strength properties [106, 114, 115]. It has been stated that Ni-rich intermetallics can also maintain the interconnectivity of the eutectic network [96]. However, flaky morphology of $Al_9(FeCu)Ni$ compounds with the sharp edges seems undesirable as they can act as crack initiation points. In contrast, the cubic Al_6Cu_3Ni phase with bone-like morphology can be preferable type of Ni-rich phase. The similarity in crystallographic structure of the adjacent phases is thought to maintain their coherency at elevated temperature expositions, contributing to higher creep resistance of the material.

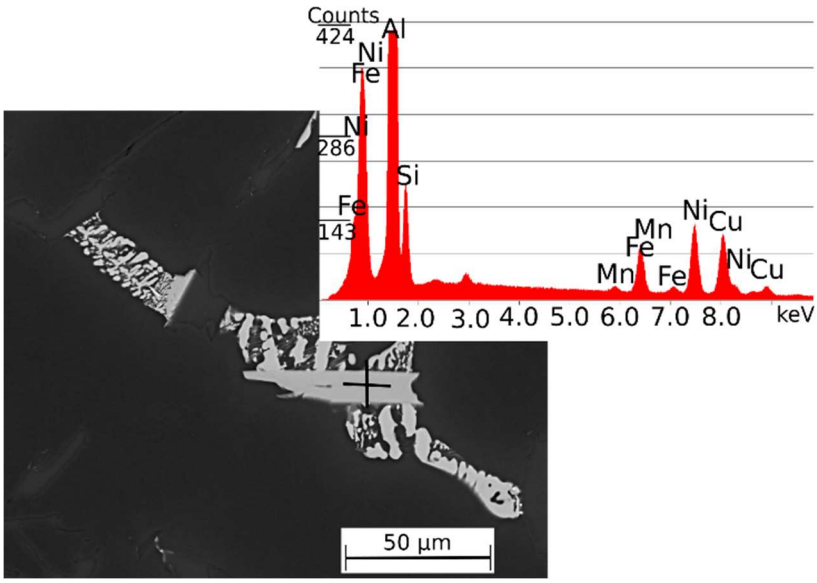

Figure 56. SEM micrographs showing $Al_9(CuFe)Ni$ phase, with corresponding EDS spectra.

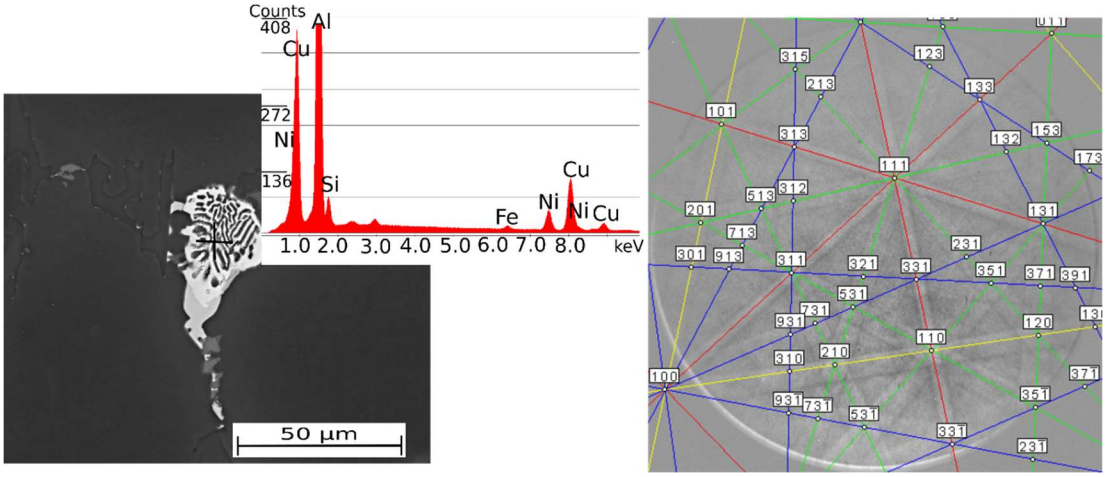

Figure 57. SEM micrographs showing cubic Al_6Cu_3Ni, as revealed by EDS spectra and indexed EBSD patterns.

3.5. Phase V – Microstructural evolution and tensile properties of secondary Al-Si-Cu-Mg alloys: role of Zr and V additions

In this research phase, the effects of Zr and V microalloying additions and heat treatment on microstructure and static tensile properties of secondary Al-7Si-3Cu-0.3Mg alloy with SDAS of ~ 15 µm were investigated.

3.5.1. General microstructure of as-cast alloys

The typical as-cast microstructures representing the base and Zr/V-modified alloys are shown in Figure 58. The main phases present in the microstructure of the base alloy are α-Al matrix, eutectic Si, $Al_{15}(FeMn)_3Si_2$ and Cu-rich compounds (see Figure 58a). The presence of (0.15 %) Zr yielded the formation of primary $(AlSi)_3(ZrTi)$ compounds during solidification of Zr/V-modified alloy (Figure 58b). These interdendritic $(AlSi)_3(ZrTi)$ compounds having the length of ~10 µm were observed throughout the microstructure in flaky- and plate-like morphology. The majority of V added to the alloy were retained inside α-Al matrix during solidification (Figure 60); owing to its peritectic nature, V tends to segregate to the core of growing α-Al grains during non-equilibrium solidification. Excess V beyond its solubility in α-Al was found incorporated into pro-eutectic α-$Al_{15}(FeMn)_3Si_2$ phase (see Figure 59), thus slightly increasing the fraction of Fe-rich intermetallic compounds from 0.4 % in the base alloy to 0.5 % in the Zr/V-modified alloy. At low cooling rate corresponding to the SDAS of ~65 µm (see Figure 55 in research phase II), in addition to the enrichment of V in α-$Al_{15}(FeMn)_3Si_2$ phase, rarely observable $(AlSi)_2(VTiMn)$ compounds were also present in the interdendritic regions. In the present study, however, higher cooling rate corresponding to the SDAS of ~15 µm seems to increase the solid solubility of V in α-Al matrix, thus making pro-eutectic $(AlSi)_2(VMn)$ reaction unfavourable during alloy solidification.

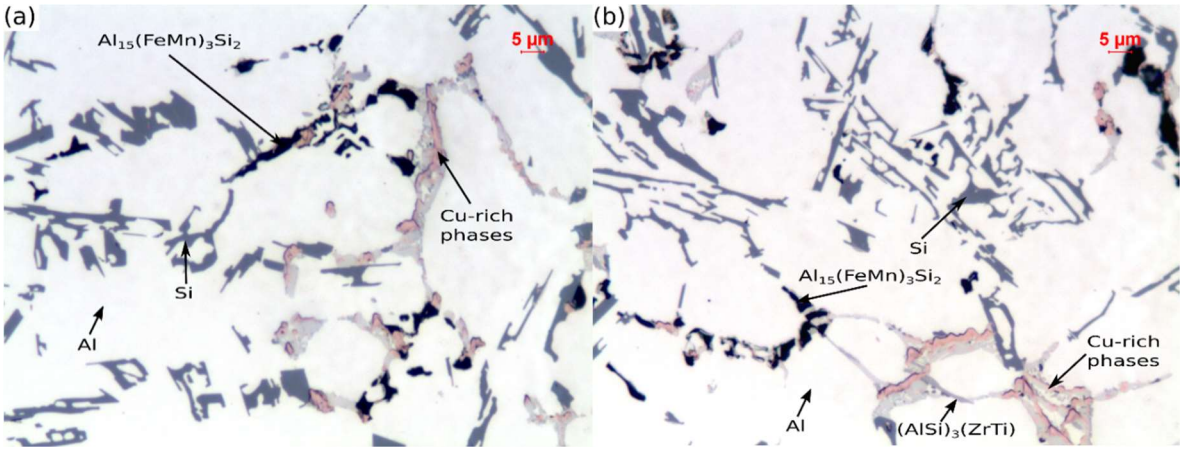

Figure 58. Typical microstructures of the (a) base and (b) Zr/V-modified alloys in as-cast states. The samples were etched in a mixture of H_2O and H_2SO_4, preheated to 70 °C to highlight Fe-rich compounds.

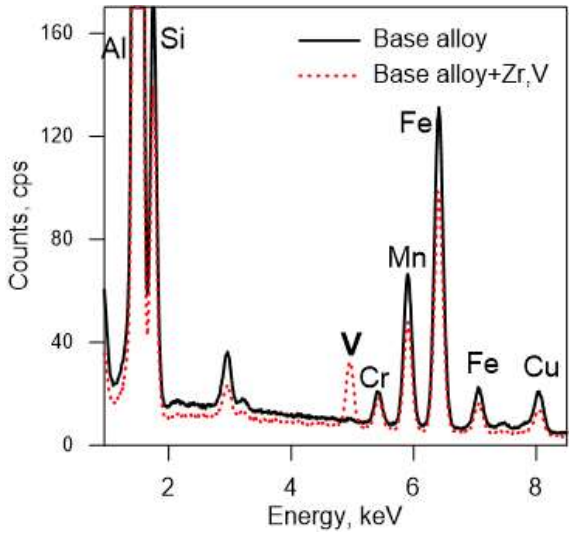

Figure 59. Typical EDS spectra of α-$Al_{15}(FeMn)_3Si_2$ phase observed in the (a) base and (b) Zr/V-modified alloys in as-cast states.

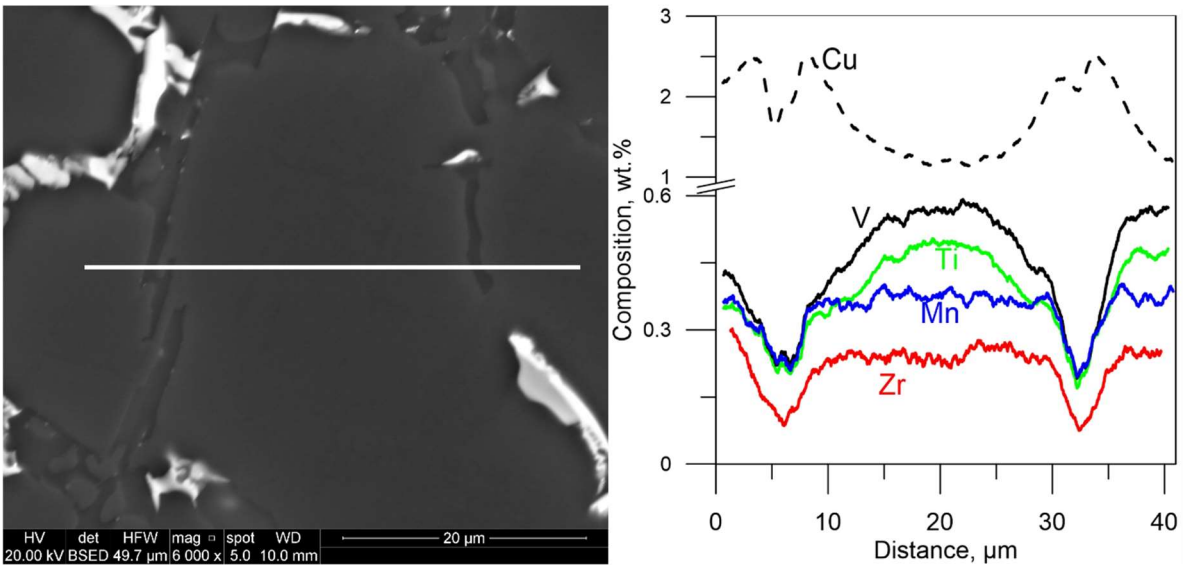

Figure 60. SEM image of α-Al grain in Zr/V-modified alloy with corresponding EDS line-scan, showing the distributions of Zr, V, Ti, Mn and Cu elements.

3.5.2. General microstructure of heat-treated alloys

Figure 61 shows the typical microstructures of both the base and Zr/V-modified alloys after T6 heat treatment. In contrast to the microstructures of the as-cast alloys, the microstructures representing the heat-treated alloys exhibit finer and more rounded Si particles; the roundness of Si particles was reduced from ~5 in the as-cast state to ~ 2 in the heat-treated state, which indicates how applying heat treatment yields the fragmentation and spheroidization of eutectic Si particles [70]. Moreover, heat treatment is known to solubilize interdendritic Cu/Mg-rich compounds into α-Al matrix; however, some Cu-rich compounds were found to be present in interdendritic regions of the heat-treated alloys (see Figure 61). According to the compositional mapping analyses performed on heat-treated alloys (Figure 62 and Figure 63), the undissolved Cu-rich particles appear to be $Al_5Si_6Cu_2Mg_8$ and some blocky Al_2Cu phases, which seem to require higher solutionizing temperature for their effective dissolution into the α-Al matrix. Moreover, although Ni is present in the alloy as impurity (~200 ppm), it formed some interdendritic intermetallics based on Al-Ni-Cu system, showing no dissolution tendency into the α-Al matrix during solution heat treatment (Figure 63). Similarly, the interdendritic α-$Al_{15}(FeMn)_3Si_2$ and $(AlSi)_3(ZrTi)$ phases also remained undissolved into the α-Al matrix during solution heat treatment (Figure 61 and Figure 62).

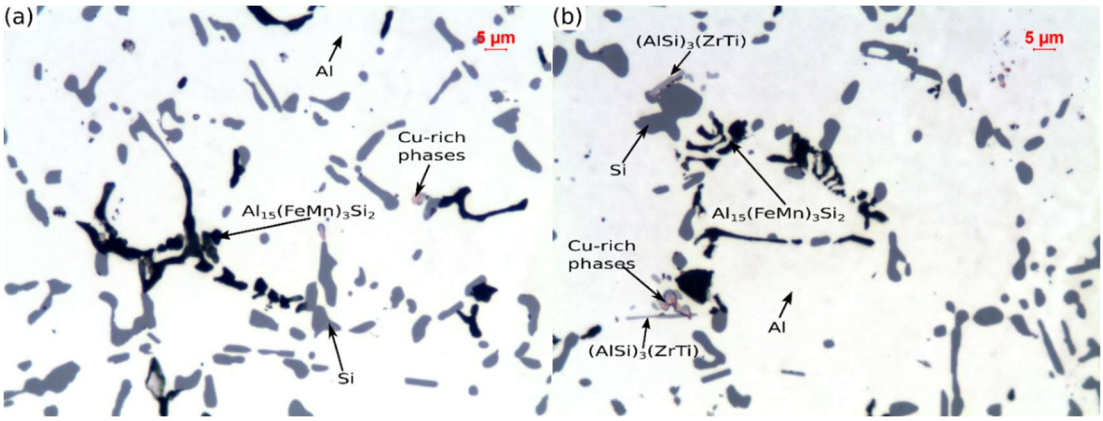

Figure 61. Typical microstructures of the (a) base, and (b) Zr/V-modified alloys in the heat-treated states. The samples were etched in a mixture of H_2O and H_2SO_4, preheated to 70 °C to highlight Fe-rich compounds.

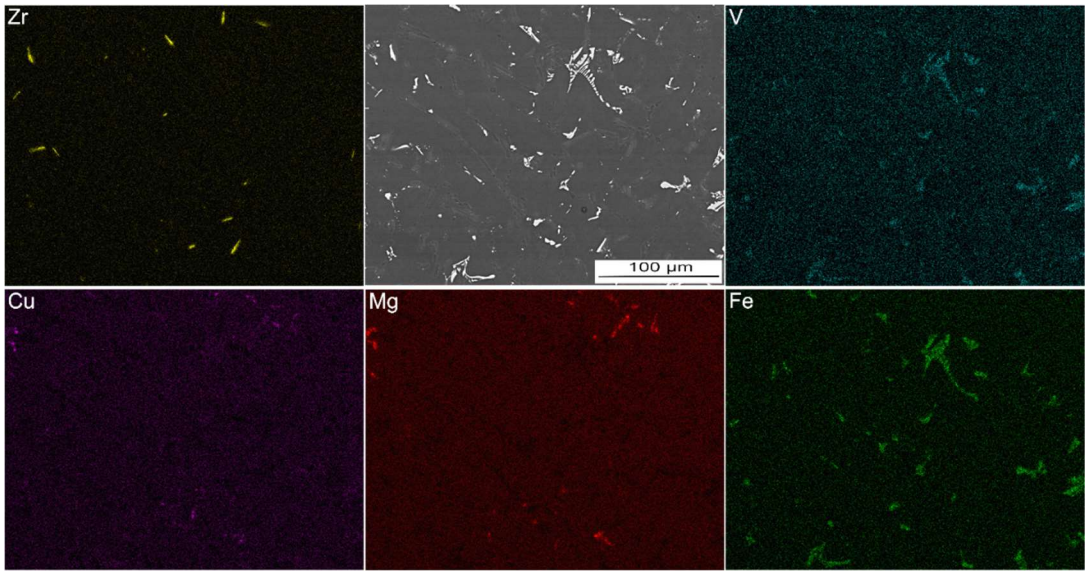

Figure 62. Backscattered electron image of a typical microstructure of Zr/V-modified alloy after T6 heat treatment with corresponding EDS composition maps, showing the distributions of Zr, V, Cu, Mg and Fe elements.

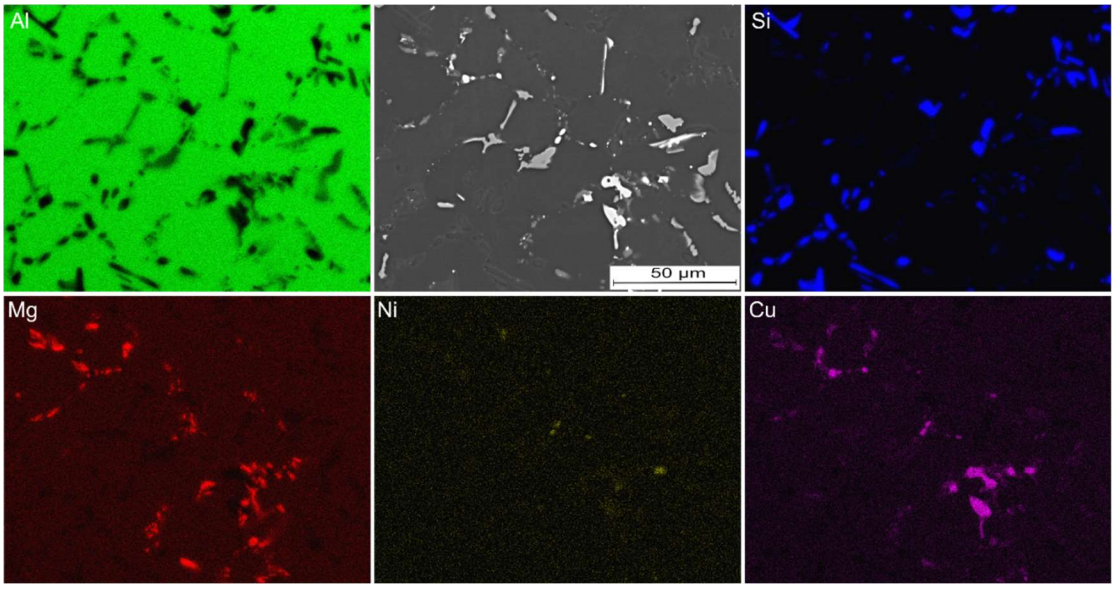

Figure 63. Backscattered electron image of a typical microstructure of Zr/V-modified alloy after T6 heat treatment with corresponding EDS composition maps, showing the distributions of Al, Si, Mg, Ni and Cu elements.

3.5.3. Solid-state phase transformations in heat-treated alloys

Figure 64 presents bright field (BF) TEM micrographs displaying the solid-state precipitation occurred inside α-Al matrix during T6 heat treatment. The dominant needle-like precipitates (see Figure 64) are believed to be θ′ phase [46]. Detailed characterization of the solid-state precipitation reactions involving Cu and Mg in Al-Si-Cu-Mg alloys can be found elsewhere [46, 167, 168]. Microstructural investigation of Zr/V-modified alloy revealed nano-sized Zr/V-rich precipitates inside α-Al matrix.

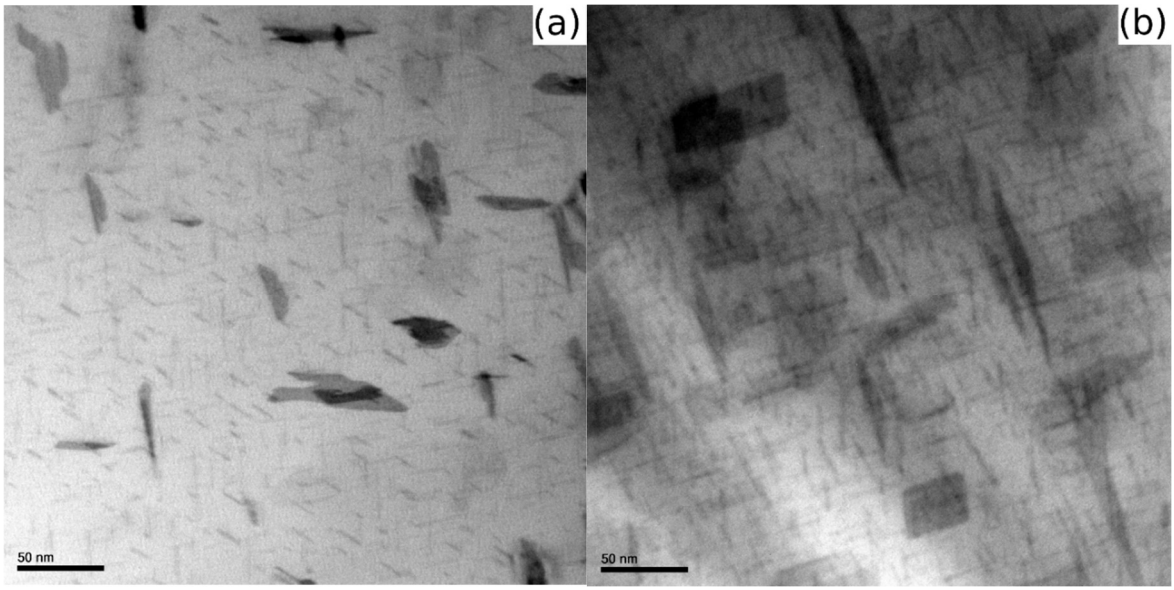

Figure 64. BF TEM micrographs showing the precipitation observed after T6 heat treatment in the (a) base and (b) Zr/V-modified alloys.

As the precipitation reactions involving Zr and V is expected to occur during solutionizing stage (see the following section for the precipitation behaviour of Zr/V-rich particles), the TEM investigations was also carried out on the samples extracted from the solution heat-treated and as-quenched alloys. Figure 65 shows optical micrographs (Figure 65a,b) and BF TEM micrographs (Figure 65c,d)

displaying the precipitation occurred in the α-Al grain interiors of the studied alloys during solution heat treatment. Substantially more precipitates can be seen in the Zr/V-modified alloy (Figure 65b,d) compared to the base alloy (Figure 65a,c). According to the EDS analysis of intradendritic precipitates formed during solution heat treatment of the base alloy (see Figure 66), the precipitates are believed to be of α-Al(MnFe)Si type [6, 169]. In the case of Zr/V-modified alloy, three different types of intradendritic phases containing transition metals tended to precipitate during solutionizing stage (Figure 67). The precipitate numbered 1 in Figure 67a is believed to be the α-Al(MnVFe)Si phase, which has been also revealed in the base alloy (Figure 66) and several other studies in the form of α-Al(MnFe)Si [169-171]. In the present study, the α-Al(MnVFe)Si particles were observed in plate-like morphology with the average size of ~ 100 nm and accounted for a major part of precipitates formed during solution heat treatment of the Zr/V-modified alloy. Vanadium was found to significantly promote the precipitation of α-Al(MnFe)Si by substituting Mn in this phase. The flaky-like Zr-rich precipitates numbered 2 in Figure 67a and identified as $(AlSi)_3(ZrTi)$ in Ref. [116] are rarely observable in the α-Al grain interiors, which can be due to the low solid solubility of both Zr and Ti in α-Al. The irregular-shaped V-rich precipitate numbered 3 in Figure 67a is believed to be an $(AlSi)_2(VCr)$ phase according to its composition; however, further TEM investigations seem necessary to conduct crystallographic studies of this phase. This precipitate is also hardly apparent in the microstructure (grain interiors) since V was mainly bound to intradendritic α-Al(MnVFe)Si phase.

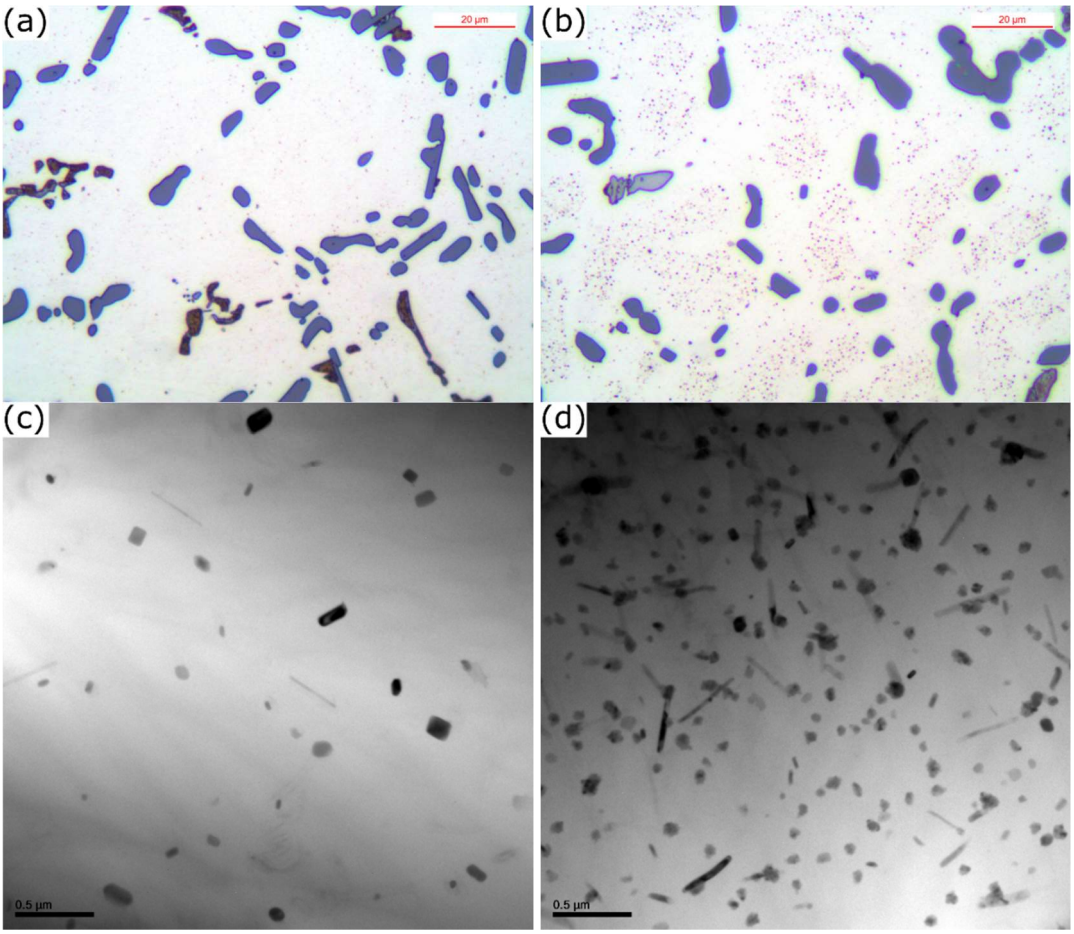

Figure 65. (a,b) Optical micrographs and (c,d) BF TEM micrographs showing the precipitates formed during solution heat treatment of the (a,c) base and (b,d) Zr/V-modified alloys. Optical micrographs were obtained from the samples etched in 1% HF for 30 s to reveal secondary precipitates.

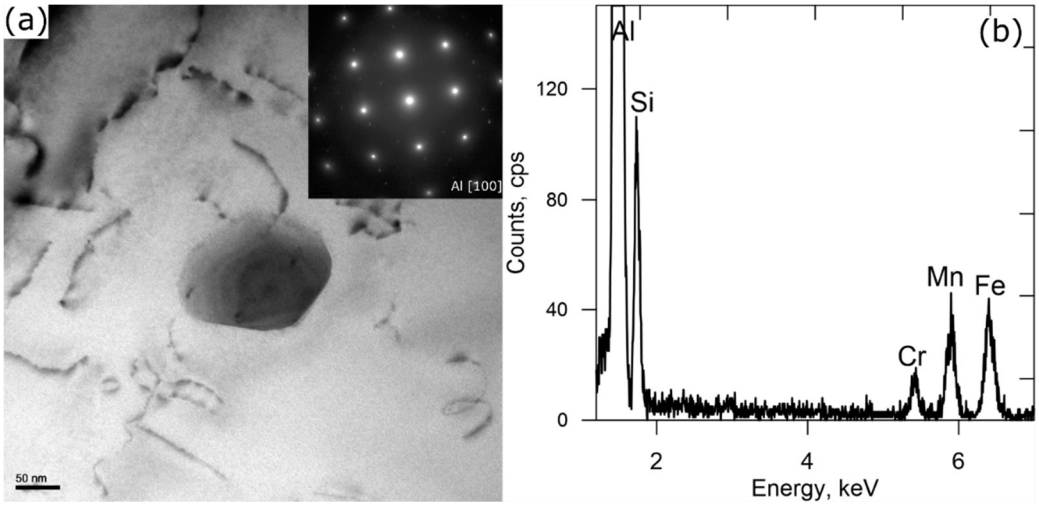

Figure 66. (a) BF TEM micrograph showing the α-Al(MnFe)Si precipitate formed in α-Al grain interior during solution heat treatment of the base alloy, and (b) EDS spectrum of α-Al(MnFe)Si precipitate shown in Figure 66a.

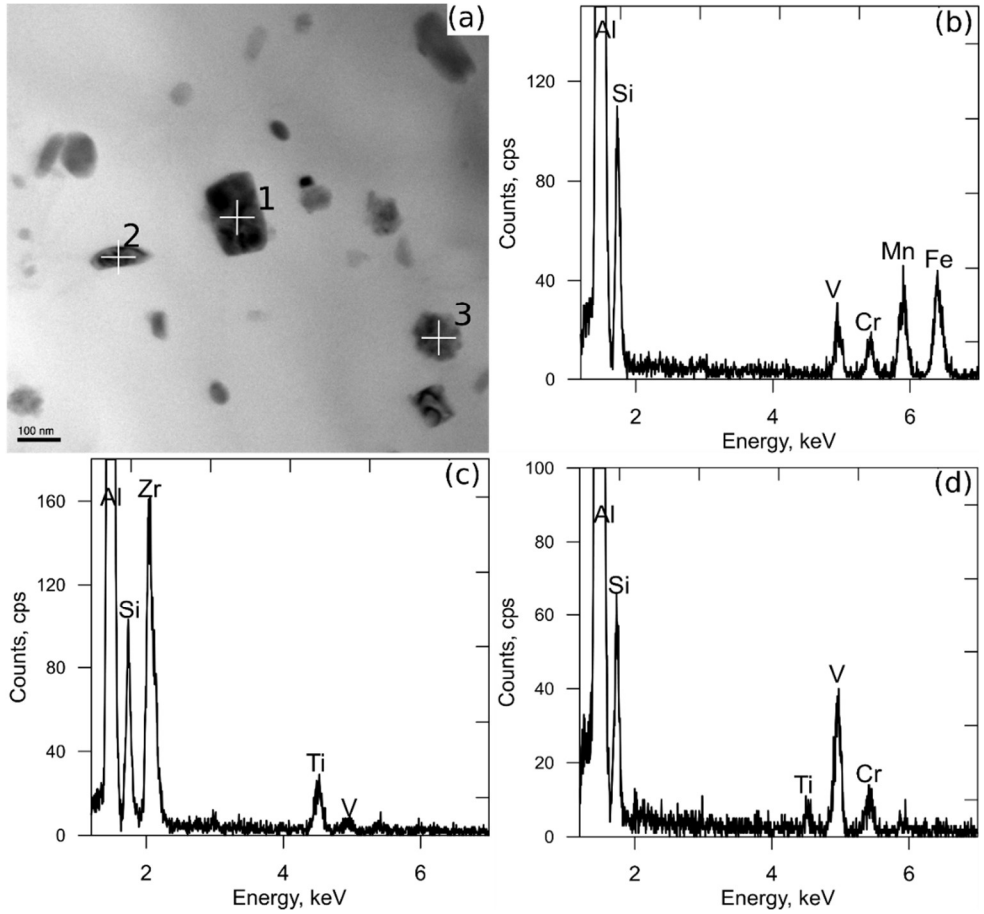

Figure 67. (a) BF TEM micrograph showing the precipitates formed in α-Al grain interiors at solution heat treatment stage of Zr/V-modified alloy; (b) EDS spectrum of Al(MnVFe)Si precipitate numbered 1 in Figure 67a; (c) EDS spectrum of $(AlSi)_3(ZrTi)$ precipitate numbered 2 in Figure 67a; (d) EDS spectrum of $(AlSi)_2(VCr)$ precipitate numbered 3 in Figure 67a.

3.5.3.1. Precipitation behaviour of intradendritic Zr/V-rich particles

Solution treatment is the initial stage of the T6 heat treatment process used to primarily dissolve interdendritic Cu- and Mg-rich compounds into the α-Al matrix, and also spheroidize/fragmentize the eutectic Si particles [44, 47, 70]; however, the present study also revealed that the solutionizing stage

induces solid-state precipitation reactions involving slow-diffusing transition metals (see Figure 65). As the peritectic-forming Zr and V elements tended to mainly concentrate inside α-Al matrix during solidification (see Figure 60), a slight amount of these elements were rejected into the interdendritic liquid by the growing dendrites. Therefore, the contribution of Zr and V to the evolution of insoluble and interdendritic intermetallics was insignificant (see Figure 61 and Figure 62). Based on these observations, we can also infer that only the supersaturated Zr and V amounts in solid solution of α-Al obtained during non-equilibrium solidification can be involved in the solid-state precipitation occurring inside α-Al matrix. As mentioned earlier, a very limited amount of α-Al(MnFe)Si precipitates formed in α-Al grain interiors of the base alloy after solution heat treatment (see Figure 65a). Since Mn is normally added to promote the formation of α-$Al_{15}(MnFe)_3Si_2$ over β-Al_5FeSi during solidification [172], some part of Mn can be also retained inside Al matrix during solidification (see Figure 60). Non-equilibrium solidification, in turn, can also facilitate the supersaturation of Mn, Cr and Fe in α-Al solid solution and when the alloy is exposed to a higher temperature for a certain period of time, e.g. at solution heat treatment stage, the diffusion of transition metals becomes active, which causes the supersaturated transition metals in α-Al solid solution to decompose and precipitate inside in α-Al matrix.

As stated in Section 3.1, adding Zr and V significantly increased the fraction of α-Al(MnFe)Si precipitates in α-Al grain interiors (see Figure 65), which can be described by the peritectic nature of V, more shallow solvus line in Al corner of Al-V phase diagram (Figure 11b) and the ability of V to substitute Mn in α-Al(MnFe)Si phase.

Another interesting feature observed in Figure 65a,b was the presence of α-Al matrix zones free from precipitates; the Zr/V-rich precipitates are mainly concentrated in the core regions of α-Al grains. This behavior is the direct consequence of the solidification microstructure. As shown in Figure 60, inhomogeneous distribution of transition metals over the cross section of α-Al grain matrix is obtained during non-equilibrium solidification and due to their slow diffusivity in α-Al matrix, applying solution heat treatment cannot yield homogeneous distribution of transition metals inside α-Al matrix. However, the interaction between V and Mn to form a single phase in the α-Al grain interiors is highly beneficial; the partitioning behaviour of V during solidification is opposite to that of Mn, which can lead to a more uniform distribution of the precipitates and the reduction of the precipitates free zones. Moreover, both Mn and V are the slow-diffusing elements, with relatively high solid solubility in α-Al, which can promote the solid-state precipitation of α-Al(MnVFe)Si phase at relatively high volume fractions.

It can be also noted that the size of precipitates is in the order of 100 nm (see Figure 65), which is significantly larger than the Cu-rich strengthening precipitates formed during aging (see Figure 64). Optimization of solution heat treatment parameters of Zr/V-modified Al-7Si-3Cu-0.3Mg alloy may maximize the dispersion hardening effects of α-Al(MnVFe)Si, contributing better to the high-temperature strengthening in Al-Si alloys. The α-Al(MnFe)Si dispersoids have been recently shown to be partly coherent with the Al matrix [8].

The solutionizing stage also caused the α-Al solid solution supersaturated with Zr to decompose and precipitate inside the α-Al matrix in the form of $(AlSi)_3(ZrTi)$ phase in limited amounts and with the average length of around 100 nm. Gao et al. [21] have reported how Ti and V can accumulate into Al_3Zr phase [133]; however, in the present study, only Ti, which is present in the alloy as a trace element, tended to substitute Zr, whereas V showed no tendency to contribute to the formation of $(AlSi)_3(ZrTi)$ phase. This can be due to a more favourable involvement of V in the formation of α-Al(MnVFe)Si phase. Sepehrband et al. [107] revealed that solution heat treatment of A319 alloy

containing Zr, at 505 ºC for 24 h caused the precipitation of Al_3Zr particles with the length of around 210-250 nm in α-Al grain interiors. The smaller size of these rod-like precipitates observed in the present study can be due to lower solutionizing temperature 485 ºC applied. In a recent study, the $(AlSi)_3(ZrTi)$ precipitates have been shown to be partly coherent with the Al matrix [116].

3.5.4. Room- and high-temperature tensile properties of the alloys

Table 13 presents the averaged room-temperature tensile properties of the studied alloys in the as-cast and heat-treated states. Applying T6 heat treatment significantly enhanced the strength properties of the studied alloy. While the yield strength (YS) and ultimate tensile strength (UTS) of the base alloy increased from 155 and 248 MPa in the as-cast state to 364 and 415 MPa in T6 heat-treated states, respectively, the elongation to failure (% El) remained almost constant in the range of ~ 2 % in both the as-cast and heat-treated states of the studied alloys. The effect of adding Zr and V can be characterized by a slight increase of YS in both the as-cast and heat-treated states (see Table 13).

Table 13. Tensile properties with corresponding standard deviation (in parentheses) of the base and Zr/V-modified alloys before and after T6 heat treatment at room temperature.

Alloy type	As-cast			T6 treatment		
	YS	UTS	% El	YS	UTS	% El
base	155 (5.2)	248.2 (2.8)	1.95 (0.20)	364.4 (2.8)	415.2 (4.6)	1.98 (0.26)
modified	158.6 (0.3)	248.8 (1.5)	1.77 (0.12)	368.8 (2.1)	414.8 (3.5)	1.70 (0.30)

Figure 68 shows the tensile properties of the base and Zr/V-modified alloys after T6 heat treatment as function of testing temperature. It is evident that tensile properties is progressively reduced by increasing the testing temperature (see Figure 68) [18]; the YS and UTS of the base alloy decreased from approximately 364 and 415 MPa at room temperature to about 262 and 271 MPa at 200 ºC, followed by a further decrease to 83 and 86 MPa at 300 ºC testing temperatures respectively, whereas the elongation increased from ~2% at 20 ºC to approximately 2.5% at 200 ºC, and 8% at 300 ºC. As testing temperature increases, the effect of Zr and V addition became more evident; the Zr/V-modified alloy showed higher strength properties at 300 ºC testing temperature by ~ 20 % compared to the base alloy. The achieved improvement, however, was also followed by a slight reduction of % El (Figure 68c).

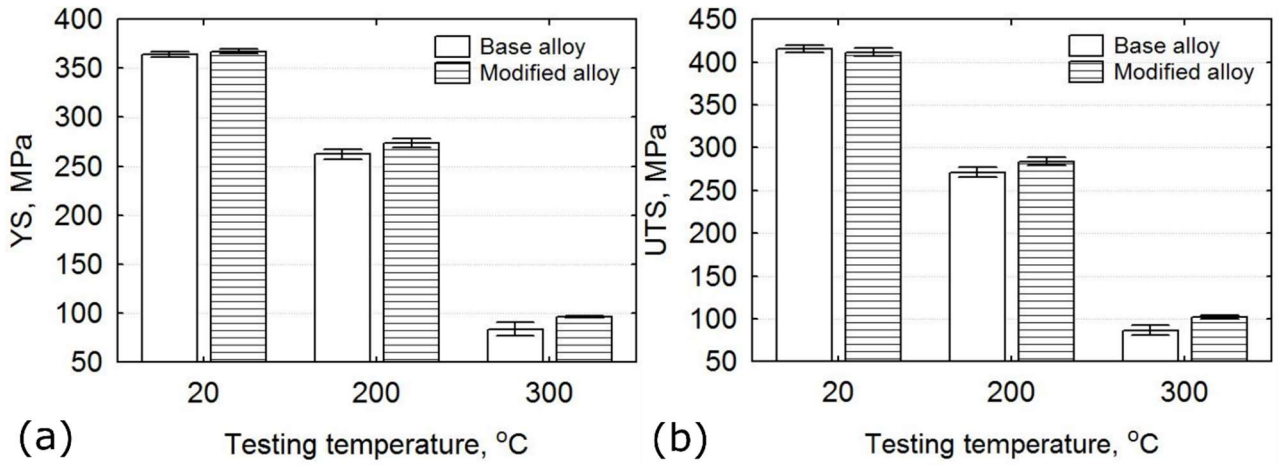

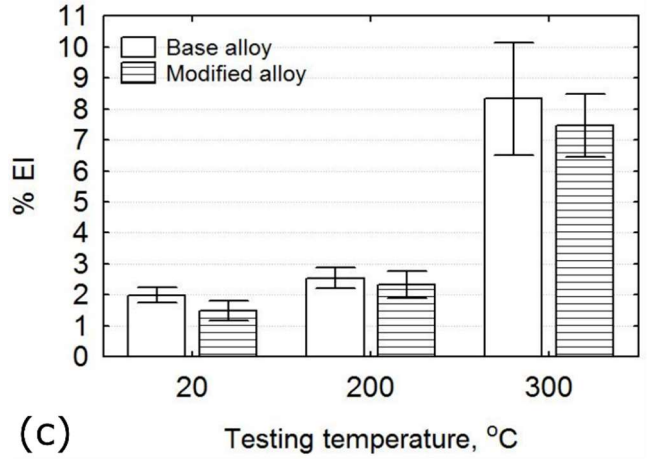

Figure 68. A comparison of the tensile properties of the base and Zr/V-modified alloys after T6 heat treatment, obtained at different testing temperatures: (a) yield strength, (b) ultimate tensile strength and (c) elongation to failure.

3.5.5. Tensile fracture surfaces

The typical examples of fractured surfaces of the studied alloys observed by SEM fractographs are shown in Figure 69. The presence of casting defects, such as oxide inclusions and shrinkage, appear to govern the fracture of the tensile-tested specimens; these casting defects can act as preferable sites for crack initiation [8]. These defects can be also credited for the scattering of elongation to failure of the studied alloys, particularly at high-temperature tensile testings (Figure 68c). When the damage is initiated by the casting defects, then the propagation occurs by cracking of interdendritic, brittle phases, such as eutectic Si and Fe/Cu-rich intermetallic particles, (see Figure 70 and Figure 71) due to the development of internal stresses in the particles by plastic deformation. Microcracks originated in those interdendritic, brittle intermetallics propagate through the a-Al matrix and subsequently connect to each other to produce the main crack.

As can be seen in Figure 70, the main fracture profile line of the base and Zr/V-modified alloys in as-cast state reflects the shape of the dendritic structure. The cleavage fracture of eutectic Si and Cu/Fe-rich intermetallics are evident. The plastically deformed microregions (micronecks) of the a-Al dendrites are also noticed in both the base and Zr/V-modified alloys. Therefore, the fracture mode observed in both alloys was a mixed interdendritic-transdendritic. The SEM fractograph representing Zr/V-modified alloy in as-cast state also shows the tear ridges and fractured brittle phases, such as Si and Cu/Fe-rich intermetallics (Figure 72a). Since the α-Al matrix is relatively soft and ductile, the stress incompatibilities evolved at the particle/matrix interfaces favour cracking of brittle, interdendritic phases, thus dominating the fracture mode [85].

Applying T6 heat treatment showed no significant influence on the fracture profile of the alloys tested at room temperature (see Figure 71). Although solutionizing stage caused spheroidization of eutectic Si particles, some Si particles still remained elongated and coarser and these particles crack more easily as they possess lower fracture stress [173-175]. Although more spheroidized Si particles in heat-treated alloys would contribute to higher elongation to failure, the hardening of α-Al matrix induced by T6 heat treatment restrains the plastic deformation of α-Al matrix. These microstructural changes can be responsible for having nearly the same elongation to failure observed in both the as-cast and heat-treated states of the studied alloys.

The fracture profile of the studied alloys tested at 200 ºC remained without any significant changes compared to the alloys tested at room temperature (see Figure 71); however, the development of some

dimples at fracture surfaces of the alloy tested at 200 ºC indicates a slight plastic deformation of α-Al matrix occurred during tensile testing (Figure 72c); measurement of the tensile properties of the studied alloys also show a slightly higher elongation to failure of the alloys tested at 200 ºC compared to the alloys tested at room temperature (Figure 68c). The absence of significant number of dimples on the fracture surfaces of the alloys tested at 20 and 200 ºC temperatures (Figure 72a,b,c) is an indication of the brittle fracture mode that was operative in these investigation conditions.
Further increase of the testing temperature to 300 ºC resulted in brittle-to-ductile transition of fracture mode in both alloys (see Figure 69). Although interdendritic particles cracking and micronecks can be also seen on the fractured surfaces (see Figure 71c,f), the fracture path mainly follows the sheared α-Al matrix (see Figure 69). Fracture of the alloys tested at 300 ºC was dominated by ductile dimple fracture with the cavities containing multiple fragmented intermetallic phases (Figure 72d) [85, 176]. Note that at low temperatures, a single dominant cleavage crack of brittle, interdendritic phases was observable on the fracture surfaces (Figure 72a,b,c). When the testing temperature is raised to 300 ºC, the α-Al matrix becomes much softer than at room temperature, thus increasing the plasticity of the alloys.

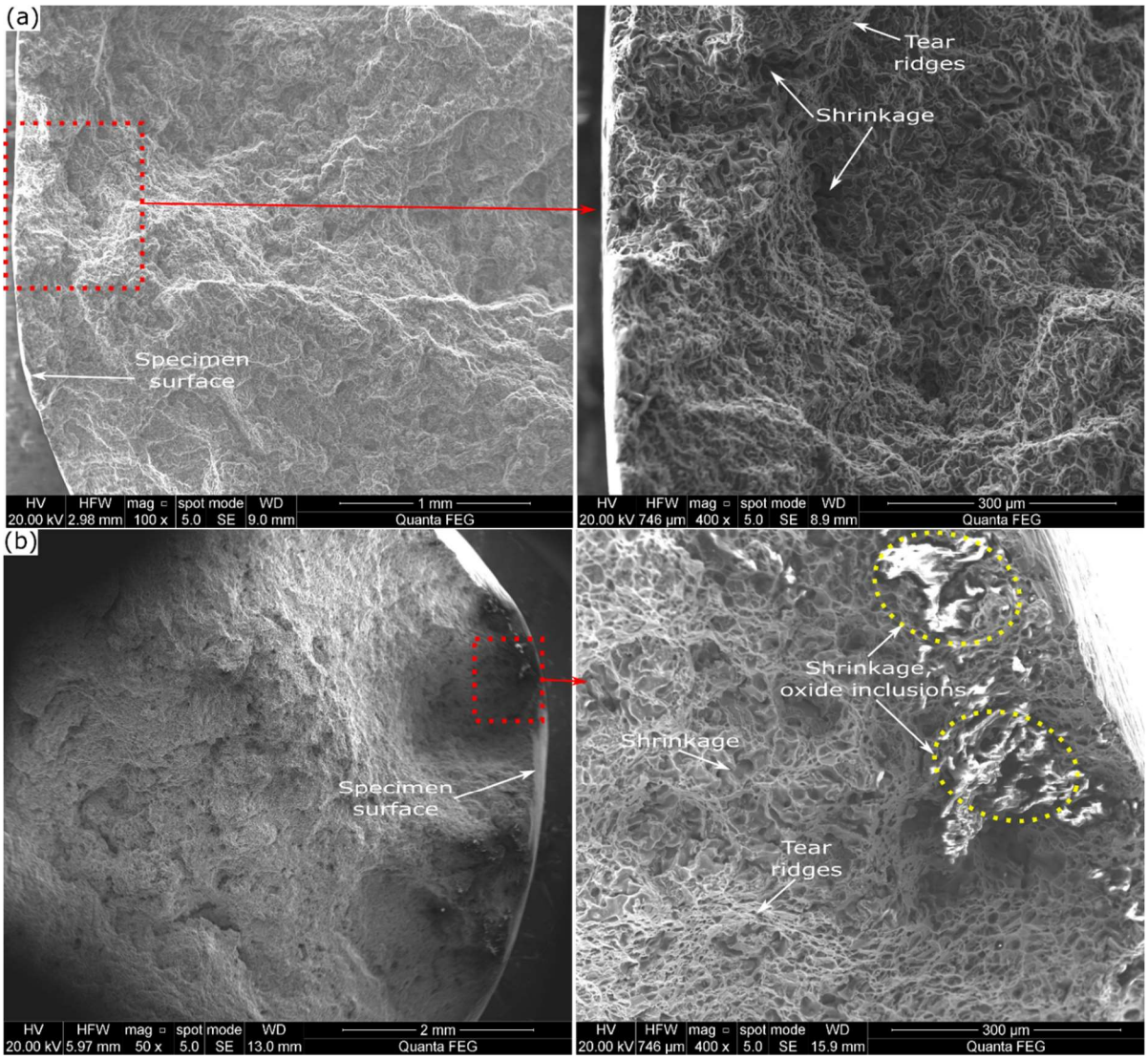

Figure 69. Secondary electron micrographs showing the fracture surfaces of Zr/V-modified Al-7Si-3Cu-0.3Mg alloy in T6 heat-treated state and tested at (a) 20 and (b) 300 ºC temperatures. The location of crack initiation, and the casting defects, such as shrinkage and oxide inclusions, that initiated the crack can be seen.

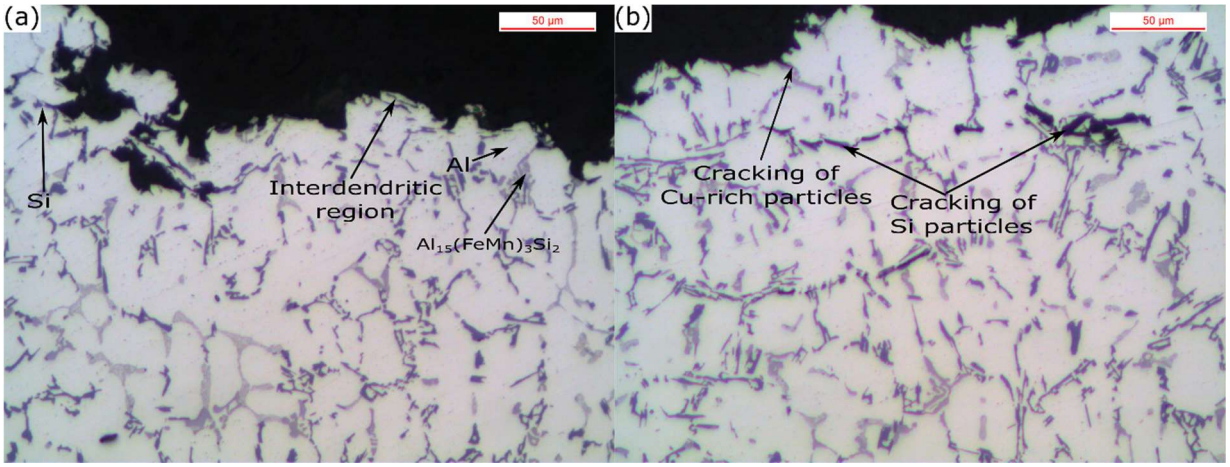

Figure 70. Optical micrographs of fracture profiles, showing a mixed transdendritic-interdendritic fracture on (a) the base and (b) Zr/V-modified alloys.

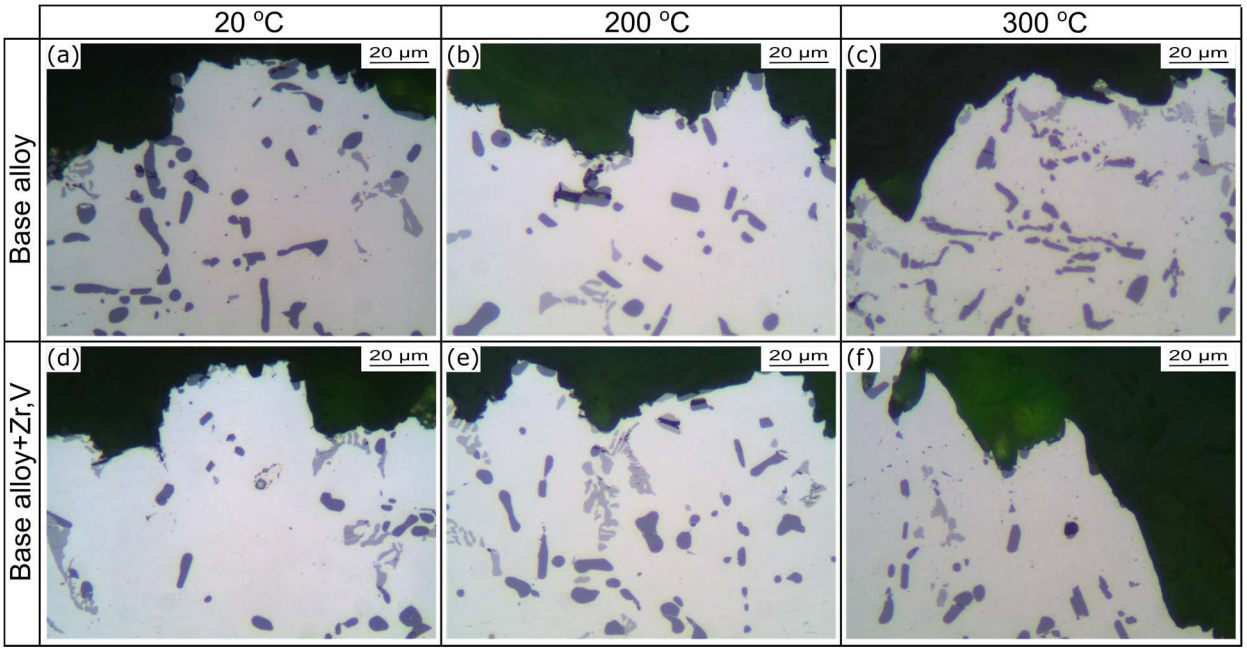

Figure 71. Optical micrographs of the tensile fracture profile of the (a,b,c) base and (d,e,f) Zr/V-modified alloys tested at (a,d) 20, (b,e) 200 and (c,f) 300 °C temperatures.

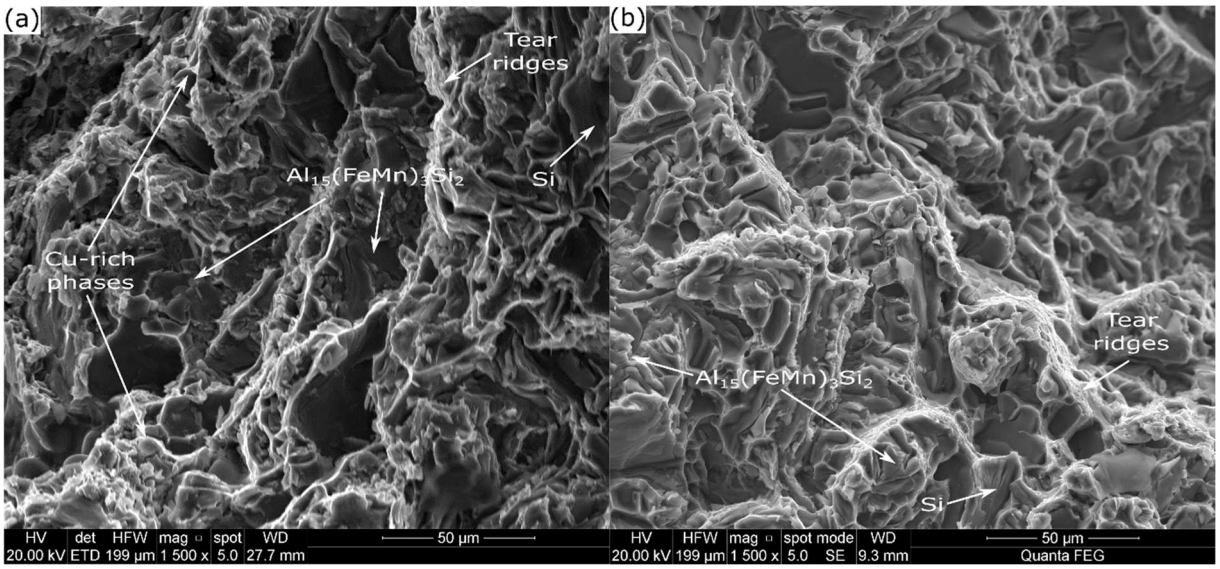

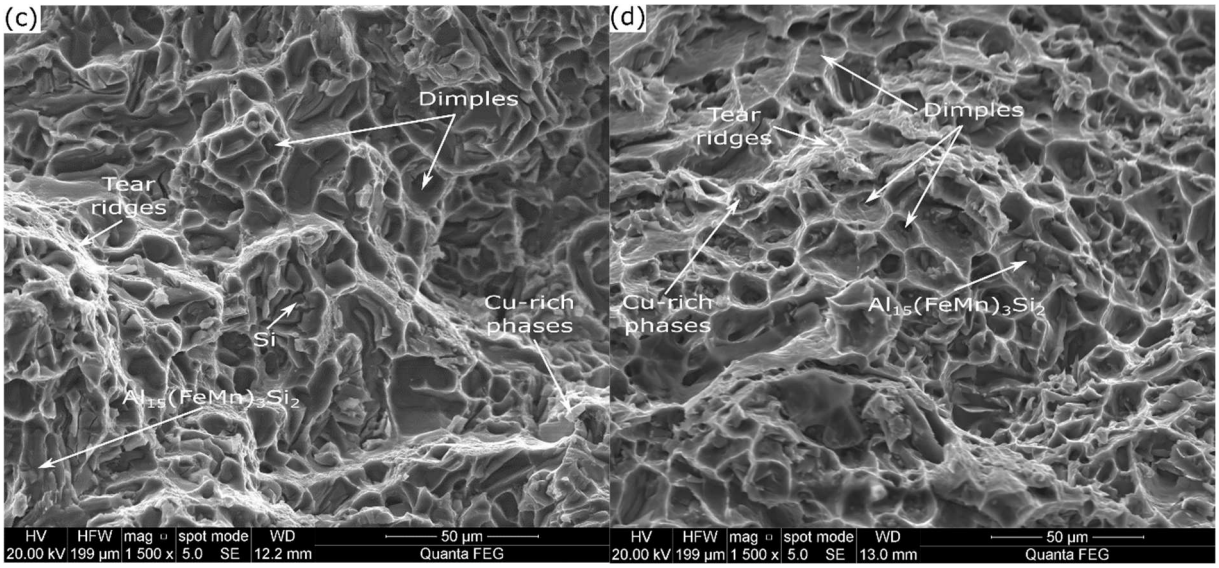

Figure 72. Secondary electron micrographs of fractured surfaces of Zr/V-added Al-7Si-3Cu-0.3Mg alloy in (a) as-cast and (b,c,d) T6 heat-treated states and tested at (a,b) 20, (c) 200 and (d) 300 ºC temperatures.

3.5.6. Microstructure - property relationship

Adding Zr and V exerted a slight influence on tensile properties of as-cast Al-7Si-3Cu-0.3Mg alloy; an increase of YS by ~5 MPa was observed upon Zr and V addition, however, this improvement was achieved at the expense of alloy ductility. Since majority of added Zr and V were retained in α-Al solid solution during solidification (see Figure 60), a slight increase in YS parameter can be attributed to the solid solution strengthening effects of alloying additions [177]. The poor ductility of Al-Si based alloys has been mainly attributed to the internal damage dominated by cracking of insoluble Cu/Fe-rich intermetallics and eutectic Si particles [13, 15, 89]. It is also worthy to note that the levels of deliberately-added transition metals should be strictly controlled to avoid further increase of the volume fraction and size of brittle, interdendritic intermetallics, such as α-$Al_{15}(FeMn)_3Si_2$ phase in secondary Al-Si foundry alloys.

The role of T6 heat treatment in the strengthening of the Al-Si-Cu-Mg based alloys is well-known [70]. The solid-state precipitation reactions involving Cu and Mg can provide significant strengthening by precipitation hardening mechanism [70]; comparison of the tensile properties of the base and Zr/V-modified alloys revealed a slight improvement of YS by ~4 MPa after Zr and V addition. It can be thus implied that the enhanced properties of both alloys upon T6 heat treatment is primarily the consequence of intradendritic Cu/Mg-rich precipitates while the influence of intradendritic Zr/V-rich particles on alloy strength properties at room-temperature is insignificant.

Increasing the testing temperature decreased the tensile properties of both alloys (Figure 68a,b). It is also observed (Figure 68a,b) that UTS parameter is more sensitive to thermal exposure compared to the YS of the alloys [42]. With increasing the temperature, the cross slips are thermally activated by climbing of dislocations resulting in the degradation of material strength [4, 18, 40, 84]. In addition, the solute diffusion of Cu and Mg becomes increasingly effective in promoting precipitate coarsening within the α-Al matrix, hence further contributing to the alloy softening [13, 18]. Comparison of the tensile properties of the alloys as function of the testing temperature (Figure 68a,b) indicates that the effect of Zr and V additions seem to be more evident at high temperatures; both the YS and UTS parameters of the Zr/V-modified alloy are higher by ~ 20% with respect to the strength properties of the base alloy. This improvement is attributed to the presence of intradendritic V/Zr-rich precipitates, which are thermally more stable compared to Cu/Mg-rich precipitates.

Both alloys remained inherently brittle as the elongation to failure remained relatively low at 20 and 200 ºC testing conditions (see Figure 68c). However, the alloy ductility become significant at 300 ºC (see Figure 68c). These findings are consistent with Reference [13], where a temperature of 300 ºC is arbitrarily chosen to indicate a transition from stress controlled to strain dominated fracture behaviour in Al-Si-Cu-Mg alloys. The effect of adding Zr and V on elongation to failure remains almost negligible (see Figure 68c), which can be explained by the fact that both Zr and V tended to concentrate mainly in grain interiors during solidification, and showed less impact on the evolution of insoluble, interdendritic intermetallics.

4. CONCLUDING REMARKS

CHAPTER INTRODUCTION

This chapter summarizes the highlighted conclusions which were drawn from this study.

The primary objective of this study was to characterize the formation of intermetallic phases containing transition metals in secondary Al-Si-Cu-Mg foundry alloys before and after grain refinement by different master alloys (Al-5Ti-1B, Al-10Ti and Al-5B) and contribute to the understanding of the mechanisms underlying the microstructural changes occurring with the addition of grain refiner. Another objective of this study was to investigate the effect of deliberate transition metals addition on the solidification path, microstructural evolution and room/high-temperature tensile properties of secondary Al-7Si-3Cu-0.3Mg alloy, with the aim of estimating the feasibility of the enhancement of the material high-temperature strength properties. The main conclusions are presented for each aspect of this work.

4.1. Transition metal impurities

- The impurities, such as Zr (~ 100 ppm), showed no apparent influence on the grain refining efficiency of Al-5Ti-1B master alloy, regardless of the pouring temperature applied.
- The transition metal impurities, Zr, V and Mn, were found to be more favourably soluble into primary AlSiTi particles, thus contributing to further stabilization and increased fraction of undesired AlSiTi phase. This behavior can further limit the critical Ti content needed for effective grain refinement, thus complicating the optimization of grain refinement process in secondary Al-Si alloys.
- The transition metal impurities exerted no any apparent contaminating influence on the effectiveness of Sr-modification.
- Iron, which is the most common and harmful impurity in Al alloys, only formed script-like α-$Al_{15}(FeMn)_3Si_2$ phase during solidification of the base alloy. This is due to (1) the presence of sufficient amount of Mn in the base material that promotes the formation of α-$Al_{15}(FeMn)_3Si_2$ over undesired β-Al_5FeSi compounds, and (2) the fact that competitive nucleation during later stages of solidification appears to be in favour of α-$Al_{15}(FeMn)_3Si_2$ over β-Al_5FeSi, i.e. lack of potent nucleation site for β-Al_5FeSi in the interdendritic liquid regions of solidifying alloy causes the nucleation and then growth of some metastable α-$Al_{15}(FeMn)_3Si_2$ in preference to β-Al_5FeSi. In contrast, Fe tended to solidify as both α-$Al_{15}(FeMn)_3Si_2$ and β-Al_5FeSi phases during solidification of the alloy treated by Sr-modifier and Al-5Ti-1B grain refiner. The TiB_2 particles released into the melt upon Al-5Ti-1B grain refiner addition seem to promote the nucleation of β-Al_5FeSi at lower undercooling by acting as heterogeneous nucleation site.
- Iron available in the alloy as impurity was again involved in the formation of both α-$Al_{15}(FeMn)_3Si_2$ and β-Al_5FeSi phases during solidification of the alloy with Al-5Ti-1B grain refiner, however without Sr-modifier, thus verifying the role of Al-5Ti-1B grain refiner in having significant influence on the formation of Fe-rich phases. At low cooling rates corresponding to the SDAS of ~60 μm, β-Al_5FeSi particles are rarely observed in the microstructure as

significantly more Fe was bound to α-$Al_{15}(FeMn)_3Si_2$ phase; on the contrary, at higher cooling rates corresponding to the SDAS of ~20 μm, the β-Al_5FeSi becomes largely dominating Fe-rich phase in the microstructure, i.e. Fe largely prefers to solidify as β-Al_5FeSi phase even though the Fe to Mn ratio (~0.6) is still favourable to avoid β-Al_5FeSi reaction.

- The precipitation sequence of Fe-rich phases in the alloy refined by Al-5Ti-1B master alloys showed no dependence of Al-5Ti-1B grain refiner level; however, both the high cooling rates and higher grain refiner addition levels tended to increase the volume fraction of β-Al_5FeSi at the expense of α-$Al_{15}(FeMn)_3Si_2$.
- No changes in the phase formation sequence of Fe-rich compounds were observed upon grain refinement of the alloy by Al-5B master alloy. The α-$Al_{15}(FeMn)_3Si_2$ again becomes the sole Fe-rich phase in the microstructure, regardless of the cooling rate. Although AlB_2 and TiB_2 are isomorphous and possess similar lattice parameters, AlB_2 appears not to promote the nucleation of β-Al_5FeSi phase; this can be due to the existence of Al-AlB_2 eutectic reaction during the early stages of solidification, which may deactivate the nucleating potency of AlB_2 particles.
- Nickel present in the alloy as impurity in trace amount (~200 ppm) tended to segregate to interdendritic region during solidification and interact with Cu to form insoluble Al-Cu-Ni intermetallics, thus diminishing the precipitation strengthening effect of Cu to a certain extent.

4.2. Deliberately-added transition metals

- Individual Zr (0.12 wt. %) addition to secondary Al-7Si-3Cu-0.3Mg alloy caused the precipitation of primary pro-peritectic Al_3Zr particles during solidification, which led to a considerable refinement of α-Al grains. However, few numbers of Al_3Zr particles precipitating in very early stages of solidification appear to interact with Si and Ti to form $(AlSi)_3(ZrTi)$ compounds, which are not effective nuclei for α-Al. The formation of $(AlSi)_3(ZrTi)$ compounds causes α-Al matrix to become less-enriched with Zr, reducing its dispersion hardening contribution. Therefore, the content of Zr in the alloy needs to be properly established by considering the alloy composition and solidification conditions to avoid the formation of primary, undesired $(AlSi)_3(ZrTi)$ platelets.
- Individual V (0.25 wt. %) addition showed similar grain refining efficiency to that of Zr addition. However, the role of V appears to be significant in increasing the growth restriction factor, thus providing greater level of constitutional undercooling, causing certain solid particles to become active for the nucleation of α-Al. Excess V beyond its supersaturation limit in α-Al matrix was bound to polyhedral-shaped $(AlSi)_2(VMnTi)$ and α-Fe compounds.
- Combined V and Zr addition yielded greater level of grain refinement of the alloy if compared to the individual Zr and V additions. This is mainly attributable to the fact that some V accumulated into Al_3Zr particles, increasing the number density of Zr-rich trialuminides, and also to the role of V in increasing the level of constitutional undercooling.
- Nickel addition, individually or in combination with Zr and/or V, only influenced the kinetics and sequence of post-eutectic reactions; during alloy solidification, Ni solidified as Al_6Cu_3Ni and $Al_9(CuFe)Ni$ phases, precipitating prior to Al_2Cu and $Al_5Si_6Cu_2Mg_8$ intermetallics. These Ni-rich intermetallics not only consumed some amount of Cu, but also acted as nucleation site for Al_2Cu and $Al_5Si_6Cu_2Mg_8$ particles, thus decreasing the freezing range of the alloy. Cubic Al_6Cu_3Ni phase appears in Chinese-script morphology, thus can be a preferable Ni-rich phase, compared to the other Ni-rich compounds, such as platelet-like $Al_9(FeCu)Ni$ phase.

- Addition of Zr (0.15 wt.%) and V (0.30 wt.%) induced the formation of flaky-like, interdendritic $(AlSi)_3(ZrTi)$ compounds, and a slight increase in the fraction of interdendritic $Al_{15}(MnFe)_3Si_2$ phase due to enrichment of V.
- The interdendritic intermetallics containing Zr and V, such as $(AlSi)_3(ZrTi)$ and $Al_{15}(FeMnV)_3Si_2$ compounds remained undissolved into the α-Al matrix during solution heat treatment. The supersaturated Zr and V in solid solution of α-Al, obtained during non-equilibrium solidification, tended to decompose and precipitate inside α-Al grains during solution heat treatment stage. The interaction between the deliberately-added Zr and V, and impure (trace) Mn, Fe, Ti and Cr elements promoted the formation of a substantial volume fraction of multiple intradendritic, nano-sized precipitates: the blocky-like α-Al(MnVFe)Si, the flaky-like $(AlSi)_3(ZrTi)$ and the irregular-shaped $(AlSi)_2(VCr)$ phases. The α-Al(MnVFe)Si accounted for the major part of the thermally stable phases formed during solutionizing stage; the interaction between peritectic-forming V and eutectic-forming Mn to form the α-Al(MnVFe)Si precipitate is believed to be highly beneficial due to their opposite partitioning behavior, as well as their higher solubility and lower diffusivity in α-Al matrix.
- Adding Zr and V showed no significant influence on alloy tensile properties in both as-cast and heat-treated states at room temperature; however, an increase of the UTS and YS of Zr/V-modified alloy with respect to the base alloy at elevated temperatures by ~ 20 % are attributed to the presence of thermally stable Zr/V-rich precipitates formed during solution heat treatment inside α-Al matrix.

5. FUTURE WORKS

CHAPTER INTRODUCTION

This chapter describes the suggestions for future works

Based on the findings derived from the experimental investigations of the role of (a) transition metal impurities and (b) deliberately added transition metals in solidification processing, microstructural evolution and tensile properties of secondary Al-Si-Cu-Mg alloys, the following suggestions can be proposed for future works. The main suggestions are presented for each aspect of this work.

5.1. Transition metal impurities

- The TEM crystallographic investigations of the interface between TiB_2 and β-Al_5FeSi phases can help gain further understanding of the role of heterogeneous nucleation in intermetallic phases selection during alloy solidification.
- Since Al-5B grain refiner showed comparable grain refining performance to that of Al-5Ti-1B master alloy, without any deleterious influence on the formation of Fe-rich intermetallics, further investigations of the grain refining performance of Al-B based master alloys in Al-Si alloys may reveal further insights.

5.2. Deliberately-added transition metals

- As the solid-state precipitation reactions involving Zr and V occurred during solution heat treatment, the optimization of solutionizing time and temperature by considering not only the dissolution kinetics of interdendritic Cu/Mg-rich intermetallics, spheroidization and fragmentation of eutectic Si particles, but also maximum dispersion hardening effect of Zr and V may enable the development of more heat resistant Al alloy.

REFERENCES

[1] J. Rakhmonov, G. Timelli, F. Bonollo, Adv. Eng. Mater., 18 (2016) 1096-1105.

[2] A.S.J. Green, Aluminum Recycling and Processing for Energy Conservation and Sustainability, ASM International, Materials Park, Ohio 2007.

[3] U.M.J. Boin, M. Bertram, JOM, 57 (2005) 26-33.

[4] J.G. Kaufman, E.L. Rooy, Aluminum Alloy Castings: Properties, Processes, and Applications, ASM International, Materials Park, 2004.

[5] H.Z. Ye, J. Mater. Eng. Perform., 12 (2003) 288-297.

[6] S. Shankar, Y.W. Riddle, M.M. Makhlouf, Metall. Mater. Trans. A, 35A (2004) 3038-3043.

[7] S.K. Shaha, F. Czerwinski, W. Kasprzak, J. Friedman, D.L. Chen, Metall. Mater. Trans. A, 46 (2015) 3063-3078.

[8] A.M.A. Mohamed, F.H. Samuel, A Review on the Heat Treatment of Al-Si-Cu/Mg Casting Alloys, Heat Treatment, in: F. Czerwinski (Ed.) Heat Treatment - Conventional and Novel Applications, InTech, 2012.

[9] D. Stefanescu, Casting, ASM International, 1988.

[10] L. Backerud, G. Chai, J. Tamminen, Solidification Characteristics of Aluminum Alloys, AFS/ScanAluminium, Oslo, 1990.

[11] M. Tupaj, A.W. Orlowicz, M. Mroz, A. Trytek, O. Markowska, Arch. Foundry Eng., 16 (2016) 125-128.

[12] M. Zamani, S. Seifeddine, E. Ghassemali, Metall. Ital., (2016) 29-32.

[13] S.W. Choi, Y.M. Kim, K.M. Lee, H.S. Cho, S.K. Hong, Y.C. Kim, C.S. Kang, S. Kumai, J. Alloys Compd., 617 (2014) 654-659.

[14] G. Timelli, G. Camicia, S. Ferraro, J. Mater. Eng. Perform., 23 (2014) 611-621.

[15] S. Saleem, H. Fredriksson, Mater. Sci. Forum, 765 (2013) 135-139.

[16] O. El Sebaie, A.M. Samuel, F.H. Samuel, H.W. Doty, Mater. Sci. Eng. A, 486 (2008) 241-252.

[17] I. Aguilera-Luna, M.J. Castro-Román, J.C. Escobedo-Bocardo, F.A. García-Pastor, M. Herrera-Trejo, Mater. Charact., 95 (2014) 211-218.

[18] A.M.A. Mohamed, F.H. Samuel, S. Al Kahtani, Mater. Sci. Eng. A, 577 (2013) 64-72.

[19] P.S. Mohanty, J.E. Gruzleski, Acta Metall. Mater., 43 (1995) 2001-2012.

[20] M. Easton, D. StJohn, Metall. Mater. Trans. A, 30 (1999) 1613-1623.

[21] M. Easton, D. StJohn, Metall. Mater. Trans. A, 36A (2005) 1911-1920.

[22] D.H. StJohn, A. Prasad, M.A. Easton, M. Qian, Metall. Mater. Trans. A, 46A (2015) 4868-4885.

[23] Z. Fan, Y. Wang, Y. Zhang, T. Qin, X.R. Zhou, G.E. Thompson, T. Pennycook, T. Hashimoto, Acta Mater., 84 (2015) 292-304.

[24] G. Timelli, G. Camicia, S. Ferraro, R. Molina, Met. Mater. Int., 20 (2014) 677-686.

[25] I. Maxwell, A. Hellawell, Acta Metall., 23 (1975) 229-237.

[26] I.G. Davies, J.M. Dennis, A. Hellawell, Metall. Trans., 1 (1970) 275-280.

[27] M. Vader, J. Noordegraaf, P.C. van Wiggen, Light Met., (1991) 1123-1130.

[28] D. Qiu, J.A. Taylor, M.X. Zhang, Metall. Mater. Trans. A, 41A (2010) 3412-3421.

[29] A.M. Bunn, P. Schumacher, M.A. Kearns, C.B. Boothroyd, A.L. Greer, Mater. Sci. Technol., 15 (1999) 1115-1123.

[30] F. Wang, D. Qiu, Z.L. Liu, J.A. Taylor, M.A. Easton, M.X. Zhang, Acta Mater., 61 (2013) 5636-5645.

[31] Z. Chen, H. Kang, G. Fan, J. Li, Y. Lu, J. Jie, Y. Zhang, T. Li, X. Jian, T. Wang, Acta Mater., 120 (2016) 168-178.

[32] A.L. Greer, Philos. Trans. R. Soc. London, Ser. A, 361 (2003) 479-494.

[33] T.E. Quested, A.T. Dinsdale, A.L. Greer, Mater. Sci. Technol., 22 (2006) 1126-1134.

[34] J.A. Spittle, S. Sadli, Mater. Sci. Technol., 11 (1995) 533-537.

[35] Y. Birol, Mater. Sci. Technol., 30 (2014) 1154-1161.

[36] Y. Birol, Mater. Sci. Technol., 28 (2012) 363-367.

[37] A. Mazahery, M.O. Shabani, JOM, 66 (2014) 726-738.

[38] L. Lu, A.K. Dahle, Mater. Sci. Eng. A, 435 (2006) 288-296.

[39] A.K. Dahle, K. Nogita, J.W. Zindel, S.D. McDonald, L.M. Hogan, Metall. Mater. Trans. A, 32 (2001) 949-960.

[40] A.K. Dahle, K. Nogita, S.D. McDonald, C. Dinnis, L. Lu, Mater. Sci. Eng. A, 413 (2005) 243-248.

[41] Y.H. Cho, H.C. Lee, K.H. Oh, A.K. Dahle, Metall. Mater. Trans. A, 39 (2008) 2435-2448.

[42] Y. Sun, S.P. Pang, X.R. Liu, Z.R. Yang, G.X. Sun, Trans. Nonferrous Met. Soc. China, 21 (2011) 2186-2191.

[43] S.Z. Lu, A. Hellawell, Metall. Trans. A, 20 (1989) 1288-1290.

[44] S.Z. Lu, A. Hellawell, Metall. Trans. A, 18 (1987) 1721-1733.

[45] M. Timpel, N. Wanderka, R. Schlesiger, T. Yamamoto, N. Lazarev, D. Isheim, G. Schmitz, S. Matsumura, J. Banhart, Acta Mater., 60 (2012) 3920-3928.

[46] J. Barrirero, J.H. Li, M. Engstler, N. Ghafoor, P. Schumacher, M. Oden, F. Mucklich, Scripta Mater., 117 (2016) 16-19.

[47] M.M. Makhlouf, H.V. Guthy, J. Light Met., 1 (2001) 199-218.

[48] A.S.J. Green, in, ASM International, Materials Park, Ohio 2007, pp. 267.

[49] M. Javidani, D. Larouche, X.G. Chen, Metall. Mater. Trans. A, 46A (2015) 2933-2946.

[50] W. Khalifa, F.H. Samuel, J.E. Gruzleski, Metall. Mater. Trans. A, 34A (2003) 807-825.

[51] S.K. Tang, T. Sritharan, Mater. Sci. Technol., 14 (1998) 738-742.

[52] B. Closset, F. Paray, J. Gruzleski, H. Mulazimoglu, Light Metals 1996, (1996) 737-744.

[53] S. Murali, K.S. Raman, K.S.S. Murthy, Mater. Sci. Eng. A, 151 (1992) 1-10.

[54] A. Pennors, A.M. Samuel, F.H. Samuel, H.W. Doty, Trans Amer. F., 106 (1998) 251-264.

[55] X.J. Cao, J. Campbell, Mater. Trans., 47 (2006) 1303-1312.

[56] G. Timelli, E. Fiorese, Metall. Ital., (2011) 9-23.

[57] L.A. Narayanan, F.H. Samuel, J.E. Gruzleski, Metall. Mater. Trans. A, 25 (1994) 1761-1773.

[58] L. Hurtalova, E. Tillova, M. Chalupova, Metallography Xv, 782 (2014) 359-364.

[59] P. Mikołajczak, L. Ratke, Arch. Foundry Eng., 2013, pp. 79.

[60] S. Seifeddine, S. Johansson, I.L. Svensson, Mater. Sci. Eng. A, 490 (2008) 385-390.

[61] Z. Ma, E. Samuel, A.M.A. Mohamed, A.M. Samuel, F.H. Samuel, H.W. Doty, Mater. Des., 31 (2010) 3791-3803.

[62] K. Liu, X. Cao, X.G. Chen, Metall. Mater. Trans. B, 43 (2012) 1231-1240.

[63] A. Hernandez-Rodriguez, M.D.J. Castro-Roman, M. Herrera-Trejo, S. Belmares-Perales, P. Orozco-Gonzalez, Metalurgija, 53 (2014) 314-316.

[64] P. Ashtari, H. Tezuka, T. Sato, Mater. Trans., 44 (2003) 2611-2616.

[65] R. Chen, Y.-F. Shi, Q.-Y. Xu, B.-C. Liu, Trans. Nonferrous Met. Soc. China (English Edition), 24 (2014) 1645-1652.

[66] W. Khalifa, F.H. Samuel, J.E. Gruzleski, H.W. Doty, S. Valtierra, Metall. Mater. Trans. A, 36A (2005) 1017-1032.

[67] S. Haro-Rodriguez, R.E. Goytia-Reyes, D.K. Dwivedi, V.H. Baltazar-Hernandez, H. Flores-Zuniga, M.J. Perez-Lopez, Mater. Des., 32 (2011) 1865-1871.

[68] A.M. Samuel, F.H. Samuel, H.W. Doty, J. Mater. Sci., 31 (1996) 5529-5539.

[69] D. Casari, M. Merlin, G.L. Garagnani, J. Mater. Sci., 48 (2013) 4365-4377.

[70] E. Sjolander, S. Seifeddine, J. Mater. Process. Technol., 210 (2010) 1249-1259.

[71] E. Sjolander, S. Seifeddine, Metall. Mater. Trans. A, 45A (2014) 1916-1927.

[72] Y.C. Chen, M.E. Fine, W. Jr, Acta Metall. Mater., 38 (1990) 771-780.

[73] A.M. Samuel, J. Gauthier, F.H. Samuel, Metall. Mater. Trans. A, 27 (1996) 1785-1798.

[74] Z. Li, A.M. Samuel, F.H. Samuel, C. Ravindran, S. Valtierra, J. Mater. Sci., 38 (2003) 1203-1218.

[75] F.H. Samuel, J. Mater. Sci., 33 (1998) 2283-2297.

[76] J.H. Sokolowski, X.C. Sun, G. Byczynski, D.O. Northwood, D.E. Penrod, R. Thomas, A. Esseltine, J. Mater. Process. Technol., 53 (1995) 385-392.

[77] J.H. Sokolowski, M.B. Djurdjevic, C.A. Kierkus, D.O. Northwood, J. Mater. Process. Technol., 109 (2001) 174-180.

[78] D.L. Zhang, L. Zheng, Metall. Mater. Trans. A, 27 (1996) 3983-3991.

[79] J.T. Staley, Mater. Sci. Technol., 3 (1987) 923-935.

[80] G.Q. Wang, L. Yan, G.C. Ren, Z.K. Zhao, Adv Mater Res-Switz, 146-147 (2011) 1667-1670.

[81] H.L. Yang, S.X. Ji, W.C. Yang, Y. Wang, Z.Y. Fan, Mater. Sci. Eng. A, 642 (2015) 340-350.

[82] P. Ouellet, F.H. Samuel, J. Mater. Sci., 34 (1999) 4671-4697.

[83] J.H. Sandoval, PhD thesis, University of Quebec, Chicoutimi, 2010.

[84] J. Hernandez-Sandoval, G.H. Garza-Elizondo, A.M. Samuel, S. Valtiierra, F.H. Samuel, Mater. Des., 58 (2014) 89-101.

[85] E. Rincon, H.F. Lopez, M.M. Cisneros, H. Mancha, Mater. Sci. Eng. A, 519 (2009) 128-140.

[86] M. Javidani, D. Larouche, Int. Mater. Rev., 59 (2014) 132-158.

[87] A.R. Farkoosh, X. Grant Chen, M. Pekguleryuz, Mater. Sci. Eng. A, 620 (2014) 181-189.

[88] A.R. Farkoosh, X. Grant Chen, M. Pekguleryuz, Mater. Sci. Eng. A, 627 (2015) 127-138.

[89] M.T. Di Giovanni, E. Cerri, D. Casari, M. Merlin, L. Arnberg, G.L. Garagnani, Metall. Mater. Trans. A, 47 (2016) 2049-2057.

[90] K.E. Knipling, D.C. Dunand, D.N. Seidman, Acta Mater., 56 (2008) 1182-1195.

[91] K.E. Knipling, D.C. Dunand, D.N. Seidman, Int. J. Mater. Res., 97 (2006) 246-265.

[92] S.K. Shaha, F. Czerwinski, W. Kasprzak, J. Friedman, D.L. Chen, Int. J. Fatigue, 70 (2015) 383-394.

[93] S.K. Shaha, F. Czerwinski, W. Kasprzak, J. Friedman, D.L. Chen, Mater. Sci. Eng. A, 636 (2015) 361-372.

[94] S.K. Shaha, F. Czerwinski, W. Kasprzak, J. Friedman, D.L. Chen, Thermochim. Acta, 595 (2014) 11-16.

[95] S.K. Shaha, F. Czerwinski, W. Kasprzak, D.L. Chen, Mater. Des., 59 (2014) 352-358.

[96] F. Stadler, H. Antrekowitsch, W. Fragner, H. Kaufmann, P.J. Uggowitzer, Int. J. Cast Met. Res., 25 (2012) 215-224.

[97] K.E. Knipling, D.C. Dunand, D.N. Seidman, Acta Mater., 56 (2008) 114-127.

[98] N.A. Belov, A.N. Alabin, D.G. Eskin, V.V. Istomin-Kastrovskii, J. Mater. Sci., 41 (2006) 5890-5899.

[99] N.A. Belov, A.N. Alabin, I.A. Matveeva, D.G. Eskin, Trans. Nonferrous Met. Soc. China, 25 (2015) 2817-2826.

[100] Y. Meng, J.Z. Cui, Z.H. Zhao, Y.B. Zuo, J. Alloys Compd., 573 (2013) 102-111.

[101] Y.C. Chen, M.E. Fine, J.R. Weertman, R.E. Lewis, Scripta Metall. Mater., 21 (1987) 1003-1008.

[102] M.S. Zedalis, M.E. Fine, Metall. Trans. A, 17 (1986) 2187-2198.

[103] H. Okamoto, Phase Diagrams of Dilute Binary Alloys, ASM International, Materials Park, 2002.

[104] K.E. Knipling, PhD thesis, Northwestern University, Evanston, 2006.

[105] J. Hernandez-Sandoval, A.M. Samuel, S. Valtierra, F.H. Samuel, Metallography, Microstructure, and Analysis, 3 (2014) 408-420.

[106] A.R. Farkoosh, M. Javidani, M. Hoseini, D. Larouche, M. Pekguleryuz, J. Alloys Compd., 551 (2013) 596-606.

[107] P. Sepehrband, R. Mahmudi, F. Khomamizadeh, Scripta Mater., 52 (2005) 253-257.

[108] R. Mahmudi, P. Sepehrband, H.M. Ghasemi, Mater. Lett., 60 (2006) 2606-2610.

[109] M. Garat, G. Laslaz, AFS trans., 07-002 (2007) 1-8.

[110] T. Gao, D. Li, Z. Wei, X. Liu, Mater. Sci. Eng. A, 552 (2012) 523-529.

[111] J.H. Sandoval, A.M.A. Mohamed, S. Valtierra, F.H. Samuel, in: 14th International Conference on Aluminium Alloys, ICAA 2014, June 15, 2014 - June 19, 2014, Trans Tech Publications Ltd, Trondheim, Norway, 2014, pp. 489-494.

[112] Y.G. Li, Y. Yang, Y.Y. Wu, L.Y. Wang, X.F. Liu, Mater. Sci. Eng. A, 527 (2010) 7132-7137.

[113] A.R. Farkoosh, M. Pekguleryuz, Mater. Sci. Eng. A, 582 (2013) 248-256.

[114] R. Molina, P. Amalberto, M. Rosso, Metall. Sci. Technol., 29 (2011) 5-15.

[115] X.-G. Dong, J. Zhou, Y.-J. Jia, B. Liu, Trans. Nonferrous Met. Soc. China (English Edition), 22 (2012) s661-s667.

[116] W. Kasprzak, B.S. Amirkhiz, M. Niewczas, J. Alloys Compd., 595 (2014) 67-79.

[117] S.K. Shaha, F. Czerwinski, W. Kasprzak, D.L. Chen, J. Alloys Compd., 593 (2014) 290-299.

[118] L.F. Mondolfo, Aluminum Alloys, Butterworth-Heinemann, 1976.

[119] L.F. Mondolfo, Al–Si–Ti Aluminum–Silicon–Titanium system, in: Aluminum Alloys, Butterworth-Heinemann, 1976, 614-615.

[120] L.F. Mondolfo, Al–Si–Zr Aluminum–Silicon–Zirconium system, in: Aluminum Alloys, Butterworth-Heinemann, 1976, 618-619.

[121] N.Q. Vo, D.C. Dunand, D.N. Seidman, Mater. Sci. Eng. A, 677 (2016) 485-495.

[122] A. Waheed, G.W. Lorimer, J. Mater. Sci. Lett., 16 (1997) 1643-1646.

[123] X. Cao, N. Saunders, J. Campbell, J. Mater. Sci., 39 (2004) 2303-2314.

[124] K. Liu, X. Cao, X.G. Chen, Metall. Mater. Trans. A, 42A (2011) 2004-2016.

[125] J. Rakhmonov, G. Timelli, F. Bonollo, Adv. Eng. Mater., 18 (2016) 1096-1105.

[126] G. Timelli, P. Ferro, F. Bonollo, La metal. ital., (2010) 1-11.

[127] M.B. Djurdjevic, I. Vicario, G. Huber, Rev. Metal., 50 (2014).

[128] J. Rakhmonov, G. Timelli, F. Bonollo, Metall. Mater. Trans. A, 47 (2016) 5510-5521.

[129] A.S.f.T. Materials, in, ASTM International, 2013, pp. 9-11.

[130] C. Puncreobutr, A.B. Phillion, J.L. Fife, P. Rockett, A.P. Horsfield, P.D. Lee, Acta Mater., 79 (2014) 292-303.

[131] S. Farahany, A. Ourdjini, M.H. Idris, S.G. Shabestari, J. Therm. Anal. Calorim., 114 (2013) 705-717.

[132] C. Puncreobutr, PhD thesis, Imperial College London, 2013, pp. 173.

[133] T. Gao, X. Liu, J. Mater. Sci. Technol., 29 (2013) 291-296.

[134] W.D. Kang, H.G. Park, Korean J. Met. Mater., 49 (2011) 619-627.

[135] X.G. Chen, Fortier, M, J. Mater. Process. Technol., 210 (2010) 1780-1786.

[136] B. Suarez-Pena, J. Asensio-Lozano, Scripta Mater., 54 (2006) 1543-1548.

[137] T.H. Ludwig, P.L. Schaffer, L. Arnberg, Metall. Mater. Trans. A, 44A (2013) 3783-3796.

[138] A. Manente, G. Timelli, Metall. Ital., (2008) 37-50.

[139] S. Farahany, A. Ourdjini, M.H. Idris, L.T. Thai, Trans. Nonferrous Met. Soc. China, 21 (2011) 1455-1464.

[140] L.M. Lu, A.K. Dahle, Light Met., (2006) 807-812.

[141] S. Farahany, A. Ourdjini, T.A. Abu Bakar, M.H. Idris, Thermochim. Acta, 575 (2014) 179-187.

[142] S. Ferraro, G. Timelli, A. Fabrizi, Mater. Sci. Forum, 765 (2013) 59-63.

[143] K. Nogita, S.D. McDonald, A.K. Dahle, Mater. Trans., 44 (2003) 692-695.

[144] Q. Wang, Y.X. Li, X.C. Li, Metall. Mater. Trans. A, 34A (2003) 1175-1182.

[145] E. Samuel, B. Golbahar, A.M. Samuel, H.W. Doty, S. Valtierra, F.H. Samuel, Mater. Des., 56 (2014) 468-479.

[146] C.M. Dinnis, J.A. Taylor, A.K. Dahle, Mater. Sci. Eng. A, 425 (2006) 286-296.

[147] Q.G. Wang, D. Apelian, D.A. Lados, J. Light Met., 1 (2001) 85-97.

[148] J.Y. Hwang, H.W. Doty, M.J. Kaufman, Mater. Sci. Eng. A, 488 (2008) 496-504.

[149] J.A. Taylor, G.B. Schaffer, D.H. StJohn, Metall. Mater. Trans. A, 30 (1999) 1657-1662.

[150] S. Terzi, J.A. Taylor, Y.H. Cho, L. Salvo, M. Suery, E. Boller, A.K. Dahle, Acta Mater., 58 (2010) 5370-5380.

[151] C.M. Allen, K.A.Q. O'Reilly, B. Cantor, P.V. Evans, Prog. Mater Sci., 43 (1998) 89-170.

[152] G.K. Sigworth, T.A. Kuhn, Int. J. Metalcast., 1 (2007) 31-40.

[153] G. Sha, K. O'Reilly, B. Cantor, R. Hamerton, J. Worth, Mater. Sci. Forum, 331 (2000) I/.

[154] T. Smith, K. O'Reilly, S. Kumar, I. Stone, Metall. Mater. Trans. A, 44 (2013) 4866-4871.

[155] A. Khaliq, M.A. Rhamdhani, G.A. Brooks., J. Grandfield, Thermodynamic Analysis of Ti, Zr, V and Cr Impurities in Aluminum Melt, in: S.J. Lindsay (Ed.) Light Metals 2011, Springer International Publishing, Cham, 2016, pp. 751-756.

[156] Y. Birol, Mater. Sci. Technol., 30 (2014) 465-470.

[157] Y. Liu, C. Ding, Y.-X. Li, Trans. Nonferrous Met. Soc. China (English Edition), 21 (2011) 1435-1440.

[158] F. Wang, D. Qiu, Z.L. Liu, J. Taylor, M. Easton, M.X. Zhang, Trans. Nonferrous Met. Soc. China, 24 (2014) 2034-2040.

[159] B. Huber, K.W. Richter, J. Alloys Compd., 493 (2010) L33-L35.

[160] W.M. Edwards, R.C. Thomson, S.J. Barnes, S.I. Barnes, Mater. Sci. Forum, 396-4 (2002) 625-630.

[161] A.K.P. Rao, Trans. Indian Institute Met., 64 (2011) 447-451.

[162] R. Cook, M.A. Kearns, P.S. Cooper, J. Light Met., (1997) 809-814.

[163] T.H. Ludwig, P.L. Schaffer, L. Arnberg, Light Metals, 2013, 1023-1028.

[164] G. Tong, L. Dakui, W. Zuoshan, L. Xiangfa, Evolution, microhardness of ZrAISi intermetallic and its impact on the elevated-temperature properties in Al-Si alloys, Elsevier, Kidlington, Royaume-Uni, 2012.

[165] W.B. Pearson, Chapter VI - crystallographic data on “strukturbericht” types, A Handbook of Lattice Spacings and Structures of Metals and Alloys, Pergamon, 1958, 79-121.

[166] B. Huber, H.S. Effenberger, K.W. Richter, Intermetallics, 18 (2010) 606-615.

[167] H.M. Medrano-Prieto, C.G. Garay-Reyes, C.D. Gómez-Esparza, I. Estrada-Guel, J. Aguilar-Santillan, M.C. Maldonado-Orozco, R. Martínez-Sánchez, Mater. Charact., 120 (2016) 168-174.

[168] S. Capuzzi, G. Timelli, A. Fabrizi, F. Bonollo, in: 7th International Light Metals Technology Conference, LMT 2015, July 27, 2015 - July 29, 2015, Trans Tech Publications Ltd, Port Elizabeth, South africa, 2015, pp. 212-218.

[169] Y.J. Li, A.M.F. Muggerud, A. Olsen, T. Furu, Acta Mater., 60 (2012) 1004-1014.

[170] M. Tocci, R. Donnini, G. Angella, A. Pola, Mater. Charact., 123 (2017) 75-82.

[171] H.-W. Huang, B.-L. Ou, Mater. Des., 30 (2009) 2685-2692.

[172] J. Rakhmonov, G. Timelli, F. Bonollo, L. Arnberg, Int. J. Metalcast., (2016) 1-11.

[173] Q.G. Wang, C.H. Caceres, J.R. Griffiths, Metal. Mat. Trans. A, 34 (2003) 2901-2912.

[174] W.H. Hunt, J.R. Brockenbrough, P.E. Magnusen, Scripta Metal. Mater., 25 (1991) 15-20.

[175] M. Zamani, S. Seifeddine, A.E.W. Jarfors, Mater. Des., 86 (2015) 361-370.

[176] G. Rajaram, S. Kumaran, T.S. Rao, Mater. Sci. Eng. A, 528 (2010) 247-253.

[177] D. Casari, T.H. Ludwig, M. Merlin, L. Arnberg, G.L. Garagnani, Mater. Sci. Eng. A, 610 (2014) 414-426.

APPENDED PAPERS

Supplement I

J. Rakhmonov, G. Timelli and F. Bonollo, Influence of melt superheat and Sr modifier and Al-5Ti-1B grain refiner on microstructural evolution of secondary Al-Si-Cu alloys, Metallurgical and Materials Transactions A, 2016 (47A), 5511-5521

Supplement II

J. Rakhmonov, G. Timelli, F. Bonollo and L. Arnberg, Influence of grain refiner addition on the precipitation of Fe-rich phases in secondary AlSi7Cu3Mg alloy, International journal of metal-casting, 2017 (11), 294-304

Supplement III

J. Rakhmonov, G. Corradin, G. Timelli and H. Liu, Comparison of the effects of Al-5B and Al-5Ti-1B grain refiners on the formation of Fe-rich phases in secondary Al-7Si-3Cu-0.3Mg alloys, Proceedings of the 6th Decennial International Conference on Solidification Processing, Old Windsor, 2017, 162-165

Supplement IV

J. Rakhmonov, G. Timelli and F. Bonollo, Characterization of the effects of Zr, V and Ni on solidification path and microstructural evolution of secondary AlSi7Cu3Mg alloy, Material characterization, 2017 (128), 100-108

Supplement V

J. Rakhmonov, G. Timelli, A. Fabrizi and F. Bonollo, Effect of V and Zr Microalloying and Heat Treatment on Microstructure and Mechanical Properties of Secondary Al-7Si-3Cu-0.3Mg Alloy, submitted for publication in Metallurgical and materials transaction A, 2017

SUPPLEMENT 1

Influence of melt superheat, Sr modifier, and Al-5Ti-1B grain refiner on microstructural evolution of secondary Al-Si-Cu alloys

J. Rakhmonov, G. Timelli and F. Bonollo, Metallurgical and materials transactions A, 2016 (47A), 5511-5521

Influence of Melt Superheat, Sr Modifier, and Al-5Ti-1B Grain Refiner on Microstructural Evolution of Secondary Al-Si-Cu Alloys

JOVID RAKHMONOV, GIULIO TIMELLI, and FRANCO BONOLLO

The role of impurity elements and melt superheat on the efficiency of Sr modification, grain refinement with Al-Ti-B and the precipitation behavior of intermetallic phases in a secondary Al-7Si-3Cu-0.3Mg alloy were investigated. Metallographic and thermal analysis techniques were used to quantitatively examine the macro- and microstructural changes occurring with modifier and grain refiner additions at various pouring temperatures. The results indicate how the Sr modification and grain refinement with Al-Ti-B can be effective enough despite the presence of impurity elements in the material and the variation of pouring temperature. A slight poisonous effect of impurities, in particular, Zr and V, in the grain refinement efficiency can be eventually induced due to their action in promoting the formation of primary AlSiTi compounds. Moreover, grain refiner addition exerted a pronounced influence on the precipitation sequence of Fe-rich phases. The TiB_2 particles appeared to promote the formation of Al_5FeSi during solidification by acting as a favorable nucleation site.

DOI: 10.1007/s11661-016-3716-z

I. INTRODUCTION

ALUMINUM-SILICON-BASED alloys can be considered as the most important foundry alloys for the production of automotive engine components equipping light duty vehicles, like personal cars and light commercial vehicles, due to their good ratio between weight and mechanical properties, and excellent casting characteristics.

The secondary Al process is highly attractive because it requires significantly less energy and emits less CO_2 to the atmosphere compared to the primary route. Over 90 pct of the aluminum used in transportation industry comes from secondary sources, *i.e.*, recycled material.[1] However, secondary Al alloys usually contain several types of impurity elements in small amounts, which can exert negative effects on the mechanical properties and the final quality of the cast components.[2]

The mechanical properties of Al casting alloys are strongly dependent on the macro- and microstructural features, such as the size, morphology, and the distribution of α-Al dendrites, eutectic Si, and intermetallic compounds, which form during solidification.[3] Some features, such as the grain size, level of eutectic Si modification, dendrite coherency point can be quantified online by using an accurate thermal analysis system.[4]

The chemical grain refinement and eutectic modification are two critical stages in melt chemical treatments. The grain size and the Si modification level can be significantly improved by introducing a certain amount of Al-Ti-B grain refiner and Sr modifier into the melt. Several research activities have been conducted to understand the effects of chemical grain refinement on the α-Al dendrite features and modification on eutectic Si structure.[5,6] Most studies, however, have focused on primary Al alloys. Investigations on the grain refinement of secondary Al-Si alloys are rather limited.[7] On the other hand, the optimum level of grain refiners in secondary alloys cannot be equally achieved as compared to primary alloys due to the presence of some trace elements that can induce a negative impact on the grain refinement efficiency.[8,9] Zirconium was found to poison the potency of nucleation agents, such as TiB_2, particularly at higher melt superheats, ~1073 K (800 °C).[8] Furthermore, the grain refinement level can be deteriorated by varying pouring temperatures.[10,11]

The effects of Al-Ti-B on the precipitation behavior of Fe-bearing compounds are disputed and still not well understood.[12–14] Iron is considered as one of the most deleterious impurities in secondary Al-Si alloys and due to low solid solubility in the α-Al phase, the Fe-rich compounds precipitate in the microstructure during solidification. The formation of Fe-rich particles, particularly β-Al_5FeSi platelets, is usually undesired since the mechanical properties of the alloy can be negatively affected.[15,16]

The aim of this study is to investigate the role of impurity elements and the melt superheat on the efficiency of Sr modification, grain refinement with Al-5Ti-1B, and the precipitation behavior of intermetallic phases in secondary Al-7Si-3Cu-0.3Mg alloys.

JOVID RAKHMONOV, Ph.D. Student, GIULIO TIMELLI, Assistant Professor, and FRANCO BONOLLO, Full Professor, are with the Department of Management and Engineering, University of Padova, Stradella S. Nicola, 3 36100 Vicenza, Italy. Contact email: rakhmonov@gest.unipd.it.
Manuscript submitted February 19, 2016.
Article published online August 15, 2016

II. EXPERIMENTAL METHODS

A. *Materials and Processing*

Al-7Si-3Cu-0.3Mg alloy (equivalent to the US designation A320) was used as a baseline material which was supplied by Raffineria Metalli Capra in the form of commercial foundry ingots produced by recycling scrap aluminum. The Al-5Ti-1B and Al-10Sr rod-shaped master alloys (in wt pct) were, respectively, used for grain refinement and eutectic modification.

Thermal analysis was carried out for both untreated (base) and treated (modified and grain refined) alloys at three different pouring temperatures [973 K, 1023 K, and 1073 K (700 °C, 750 °C, and 800 °C)].

Experimental activities on untreated alloy started with melting of about 2.3 kg of supplied material in a SiC crucible inside an electrically heated, air-circulating chamber furnace at 973 K (700 °C). Then the melt was stirred and the surface skimmed to remove the dross, after which the melt is poured into a cylindrical steel cup preheated at 923 K (650 °C) for thermal analysis. Then the melt temperature was increased up to 1023 K (750 °C) and further to 1073 K (800 °C) to perform thermal analyses at these pouring temperatures. Prior to each set of thermal analysis experiments, the temperature of the melt was checked and the melt was held at a temperature of interest for 30 minutes. At higher melt superheat, the steel cup temperature was increased to maintain a temperature difference of 50 K (50 °C) between pouring and cup temperatures.

The experimental activities used for untreated alloys were repeated to analyze the solidification path of Al-7Si-3Cu-0.3Mg alloy after treatment with Al-5Ti-1B grain refiner and Al-10Sr modifier. About 0.035 kg of Al-5Ti-1B and 0.0033 kg of Al-10Sr slices were added to the molten bath for about 15 minutes before pouring the molten metal at 973 K (700 °C). With increasing pouring temperature which also results in the prolonged holding time, a reduction of Sr concentration in the alloy took place due to melt oxidation. As a result, the content of Sr decreased from 0.015 wt pct at 973 K (700 °C) to 0.013 and then to 0.011 wt pct at 1023 K and 1073 K (750 °C and 800 °C) experimental conditions, respectively.

The samples for chemical analysis were poured prior to each set of thermal analysis experiments. The averaged chemical composition of the experimental alloys, measured by optical emission spectrometry, is shown in Table I. Other elements such as Bi, Sb, P, Ca, and Sn were present in amounts less than 0.01 wt pct and these elements are not included in Table I. In the present work, all elements, other than Al, Si, Cu, and Mg, were considered as impurities.

B. *Thermal Analysis*

Thermal analysis was carried out with two K-type thermocouples of 1.5 mm diameter. A boron-nitride-coated cylindrical steel cup with the dimensions of the outer diameter of 45 mm, height of 60 mm, and a uniform wall thickness of 3 mm was used for thermal analysis. The area of thermocouples contacting with the melt was protected in tightly fitting steel tubes to allow the same thermocouples to be used throughout the experimental plan. The data were collected using a high-speed data acquisition system with a sampling rate of 0.02 s^{-1}, analog-to-digital converter accuracy of 0.1 K (0.1 °C), and linked to a personal computer. Two thermocouples were inserted into the melt, one in the center and one adjacent to the wall, 30 mm down from the top part of the sample. The system was allowed to cool in air at a cooling rate of 0.17 ± 0.1 K/s. The thermocouples were calibrated against the melting point of pure aluminum, assuming a melting point of 933 K (660.0 °C). A minimum of two thermal analyses were carried out for each condition. For each set of temperature/time relations in the center of the sample, the cooling curves and the corresponding derivative curves were plotted to determine the nucleation temperature T_{nuc}, minimum T_{min}, and growth T_{growth} temperatures for primary α-Al, Al-Si eutectic, and Cu-rich compounds formation, based on the first derivative cooling curve approach.[4] Figure 1 and Table II show the definition method and the description of thermal analysis parameters, respectively, used in the present work.

C. *Macro- and Microstructural Characterization*

Samples for macro- and microstructural investigations were sectioned longitudinally near the tip of the thermocouples in order to correlate the solidification parameters from thermal analysis with the metallographic observations. Then the samples were mounted, ground, and polished using standard polishing techniques.

Optical microscope (OM), scanning electron microscope (SEM) equipped with energy-dispersive (EDS), and wavelength-dispersive spectrometers (WDS) were used to characterize the type and morphology of the phases precipitated during solidification, as well as the distribution of alloying and trace elements in the microstructure. A total of at least 2000 eutectic Si particles were measured for each sample in OM coupled with an image analyzer.

To quantitatively calculate the grain size, the polished specimens were etched in concentrated Keller's reagent (7.5 ml HNO_3, 2.5 ml HF, 5 ml HCl, and 35 ml H_2O). The grain size was measured using the intercept method, according to the ASTM standard E112-12.[17]

Table I. The Chemical Composition of the Experimental Alloys (Weight Percent)

Alloy	Si	Fe	Cu	Mn	Mg	Zn	Cr	Ni	Ti	Pb	Sr	V	Zr	B	Al
Untreated	7.68	0.444	3.02	0.229	0.311	0.778	0.0394	0.0219	0.010	0.034	0.0001	0.011	0.010	0.0009	bal.
Treated	7.36	0.439	3.11	0.221	0.312	0.757	0.0384	0.0252	0.170	0.049	0.0130	0.010	0.010	0.0200	bal.

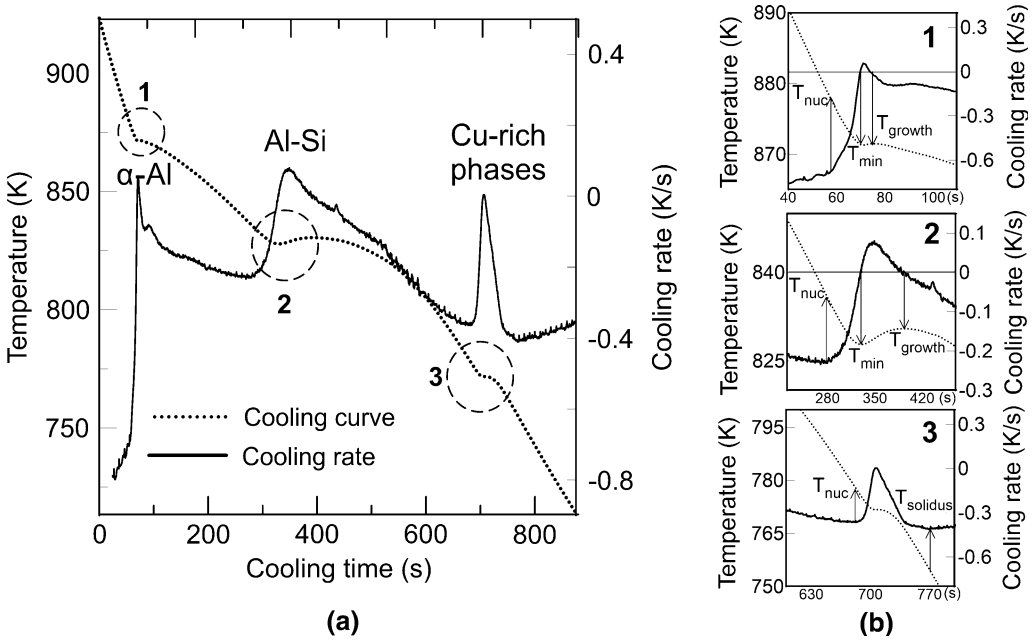

Fig. 1—(*a*) Cooling curve and first derivative of Al-7Si-3Cu-0.3Mg alloy indicating three main phase reactions, (*b*) magnified plots of three phase reactions showing the method used to determine the characteristic points, such as T_{Nuc}, T_{Growth}, T_{Min}, and $T_{Solidus}$.

Table II. Definition of the Characteristic Temperatures from Fig. 1

Symbol	Description
T_{nuc}	Nucleation temperature of a phase, such as α-Al, Al-Si eutectic, and Al-Cu eutectic
T_{min}	Minimum temperature of a phase, such as α-Al, Al-Si eutectic, and Al-Cu eutectic; latent heat amount balances the heat amount of the system
T_{growth}	Growth temperature of a phase, such as α-Al, Al-Si eutectic, and Al-Cu eutectic
T_{NG}	The difference between the nucleation and growth temperatures ($T_{NG} = T_{nuc} - T_{growth}$)
T_{rec}	Recalescence undercooling of a phase, such as α-Al and Al-Si eutectic ($T_{rec} = T_{growth} - T_{min}$)
$T_{solidus}$	Solidus temperature; marks the end of the solidification

III. RESULTS AND DISCUSSIONS

A. *Thermal Analysis*

The solidification path of both untreated and treated Al-7Si-3Cu-0.3Mg alloys remained apparently unaffected with the variation of pouring temperature. However, after the treatment of melt with Al-Ti-B and Al-Sr, significant changes took place in the solidification path, as shown in Figure 2, which displays the typical cooling curves and the corresponding first derivative curves. The derivative curve of the untreated alloy (Figure 2(a)) reveals three different peaks associated with the formation of α-Al, Al-Si eutectic, and Cu-rich phases (Al_2Cu and $Al_5Si_6Cu_2Mg_8$), while Figure 2(b) represents the solidification path of treated alloy where four different peaks corresponding to the precipitation of α-Al, Al-Si eutectic, Cu-rich intermetallics (Al_2Cu and $Al_5Si_6Cu_2Mg_8$), and α-$Al_{15}(Fe,Mn)_3Si_2$ particles were identified.[18,19] Changes in the formation temperature of the main phases are discussed in detail in the next sections.

B. *General Microstructure*

Microstructural investigations confirm the presence of the phases detected by thermal analysis, and additionally, the α-$Al_{15}(FeMn)_3Si_2$, Q-$Al_5Si_6Cu_2Mg_8$, and AlSiTi compounds, as well as Bi-Sb and Pb-rich particles were detected (see Figures 3 and 4). The lack of the relative peaks in the cooling and derivative curves is likely due to the heat amount generated during the formation of these phases, which is below the resolution limit of the thermal analysis technique used.[20]

The microstructural characterization also indicates that the AlSiTi and β-Al_5FeSi phases existed only in the case of treated alloy, regardless of the pouring temperature. No evidence of the precipitation of these compounds was observed in untreated alloy. It was also observed that the pouring temperature exerted no influence on the type of phases forming during solidification in the case of both untreated and treated alloys.

The π-$Al_8Mg_3FeSi_6$, AlSiTi compounds, and Bi-Sb and Pb-rich particles, as revealed by SEM investigation (Figure 4), appeared in the interdendritic regions. The Bi-Sb and Pb-rich particles were in the size range of few μm with rounded or blocky morphologies.

The precipitation characteristics of various phases observed in the microstructure are elaborated and discussed in detail in the next sections.

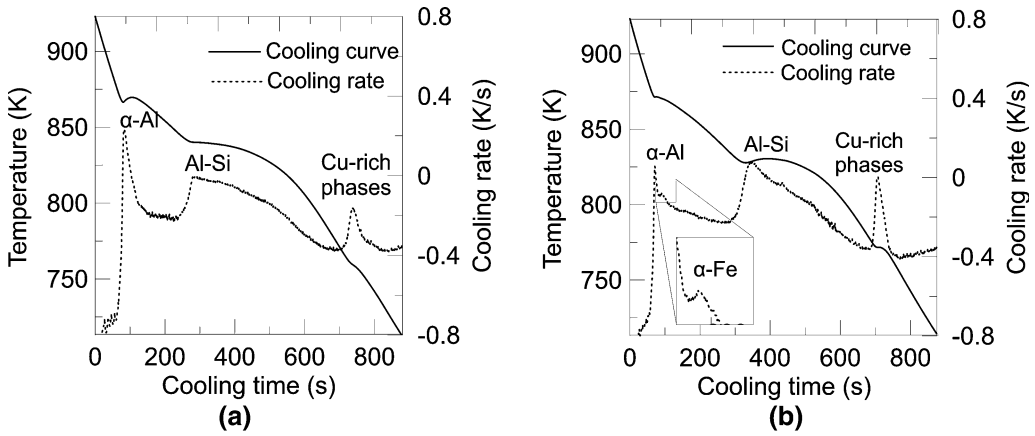

Fig. 2—Cooling curves of Al-7Si-3Cu-0.3Mg alloy in (*a*) untreated state and (*b*) after Al-5Ti-1B and Sr treatment. The corresponding first derivatives are plotted.

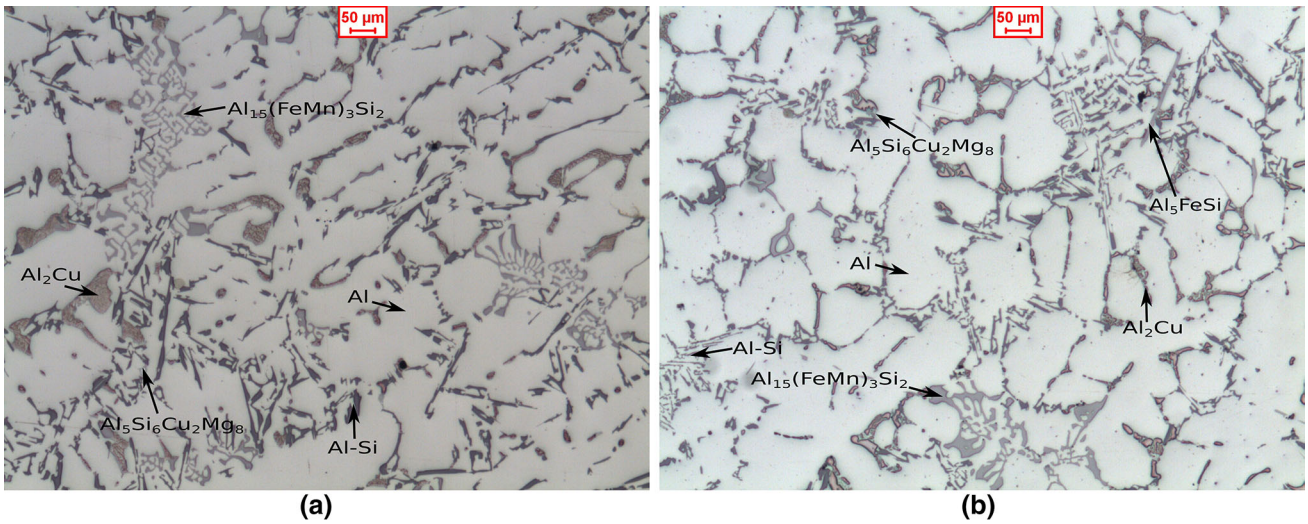

Fig. 3—Optical micrographs from (*a*) untreated and (*b*) treated Al-7Si-3Cu-0.3Mg alloys. The main phases are indicated throughout.

C. *Primary α-Al Phase*

The characteristic temperatures obtained from the cooling curves and referred to the formation of the α-Al are plotted in Figure 5. The variation in the pouring temperature had no significant influence in the nucleation and growth temperatures of α-Al in both untreated and treated Al-7Si-3Cu-0.3Mg alloys. After Al-5Ti-1B grain refiner addition, the nucleation and growth of α-Al phase occurred at the early stage of solidification, *i.e.*, at higher temperatures by about 6 K (6 °C) compared to the untreated molten bath. This is due to heterogeneous nucleation during solidification, resulting from the presence of Ti atoms for growth restriction and Al_3Ti, TiB_2 particles that act as nucleating sites for α-Al.[21,22]

It has been reported how the recalescence parameters, t_{rec}, which is the duration of the recalescence period ($t_{rec} = t_{growth} - t_{min}$), and T_{rec}, which is the difference between α-Al growth and minimum temperatures ($T_{rec} = T_{growth} - T_{min}$), can yield the best correlation with the grain size.[21,23] The recalescence parameters significantly decreased with Al-5Ti-1B grain refiner addition in current investigations (Figure 5); this further evidences an improvement in the efficiency of grain refinement.

It is also known how the difference in the nucleation and growth temperatures ($T_{NG} = T_{nuc} - T_{growth}$) has been used to assess the grain refinement efficiency.[7] If the nucleation of primary α-Al dendrites starts at or above the steady-state growth temperature, or $T_{NG} \geq 0$, new α-Al crystals can form not only from the regions in contact with die walls but also directly in the liquid mass ahead of the growing crystal front throughout the casting section.[24] In the present work, T_{NG} was observed to be positive in all studied conditions (Figure 5). This is an indication of how the initial Ti content in the base alloy can induce a rough and partial grain refinement of the material.[7]

A significant refinement of the grain structure with the addition of grain refiner was also confirmed by macrostructural investigations, as shown in Figure 6.

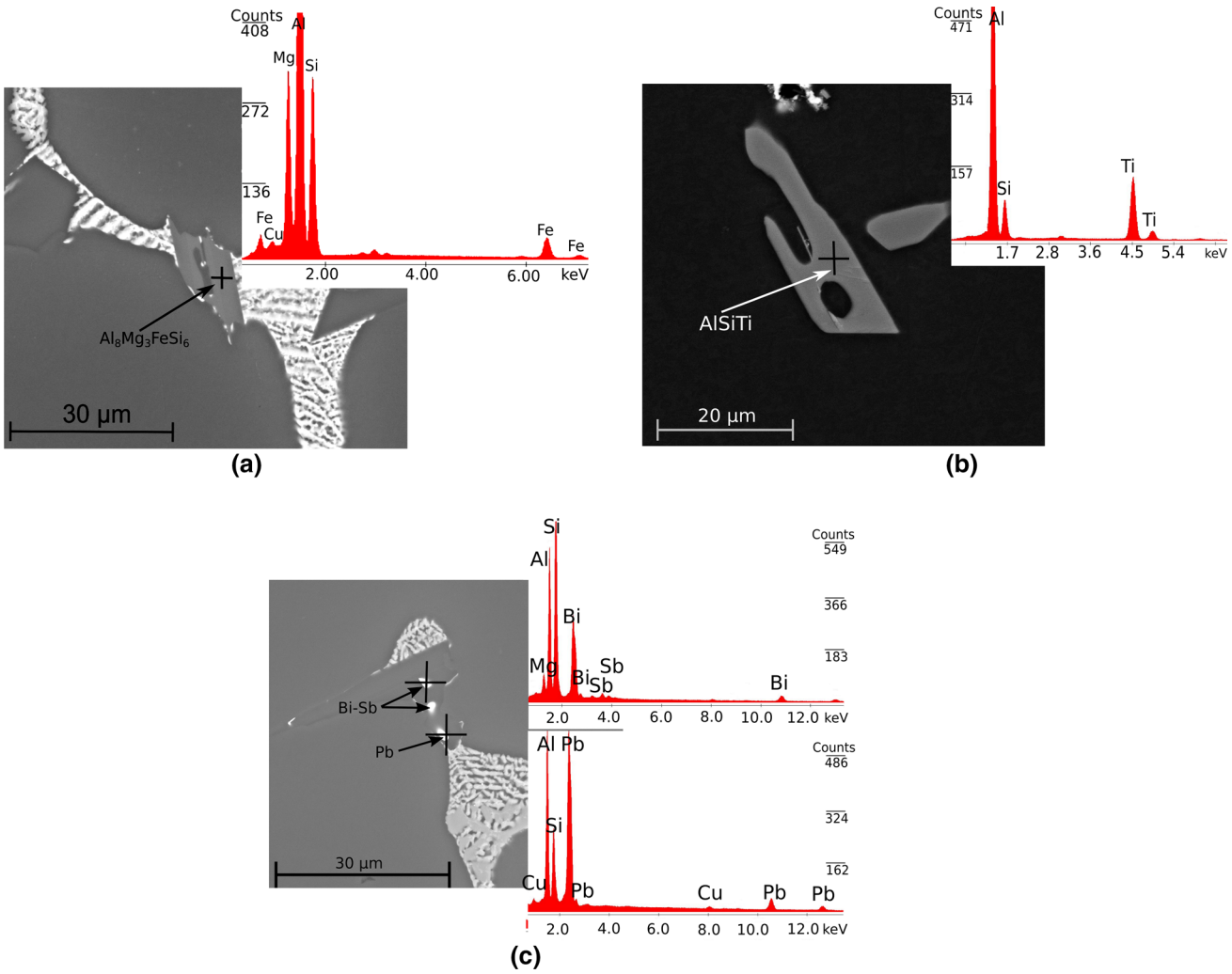

Fig. 4—Backscattered electron images indicating the (*a*) $Al_8Mg_3FeSi_6$, (*b*) AlSiTi, (*c*) Bi-Sb and Pb-rich particles with the corresponding EDS spectra.

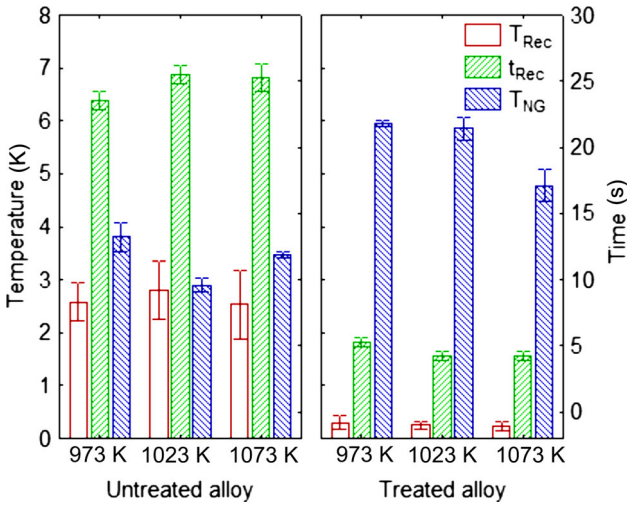

Fig. 5—Main solidification parameters of α-Al phase obtained from the cooling curves in the analyzed conditions.

The untreated alloy exhibits coarse and a mixture of columnar and equiaxed grains, whereas a finer equiaxed and homogeneous grain structure was observed in the grain-refined material.

The influence of pouring temperature was revealed as being insignificant in grain evolution in the present experimental conditions. The average grain size in the untreated conditions is about 1600 μm with a standard deviation of about 900 μm. After the Al-5Ti-1B addition, the average grain size and the corresponding standard deviation reduced by about 5 and 10 times, respectively (see Figure 7). The present results seem to be inconsistent with References 10, 11, and 25, where the pouring temperature is believed to affect the stability and the number density of nucleating substrates. Both thermal and macrostructural results confirm here how the grain refinement efficiency remained apparently unaffected by the variation of pouring temperature.

It has been reported how Zr and V can replace some atoms of Ti in TiB_2 or Al_3Ti due to their similarity in

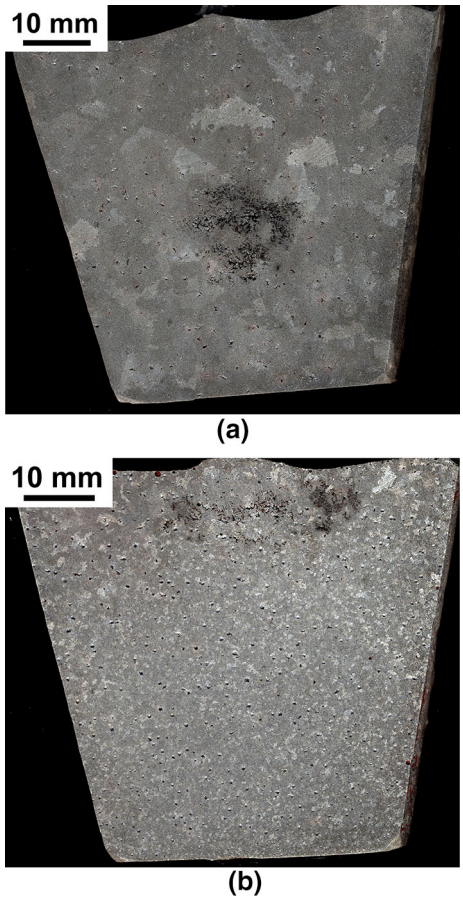

Fig. 6—Grain structure in (*a*) untreated and (*b*) treated Al-7Si-3-Cu-0.3Mg alloys.

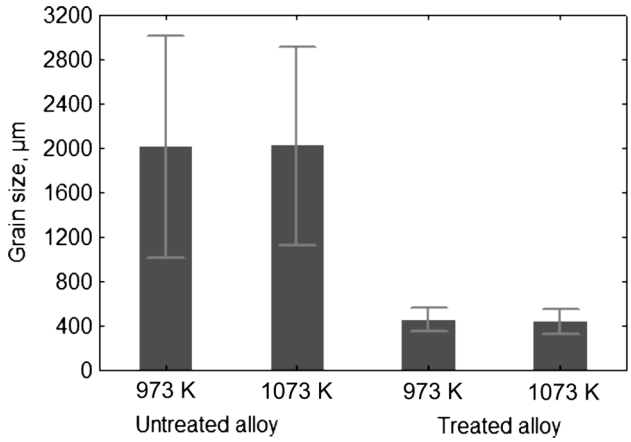

Fig. 7—The evolution of α-Al grains in untreated and treated Al-7-Si-3Cu-0.3Mg alloys as a function of the pouring temperature. The standard deviations are given as error bars.

atomic radius, and thus, reduce the potency of substrates.[8,26–28] The role of Zr (0.05 wt pct) in deactivating TiB_2 particles appears to be significant especially at higher melt superheats, ~1073 K (800 °C).[8,28] However, no evidence of the poisoning effect of Zr, which is present as an impurity in the supplied material, was observed in the present work. This behavior can be explained by the low amount of Zr (see Table I) in the initial alloy, which does not significantly interact with TiB_2 particles.

Zirconium tended to dissolve more favorably into Al_3Ti particles together with Si, V, and Mn, contributing to the formation of undesired and primary AlSiTi particles in the microstructure (Figure 8). Microstructural analysis reveals the presence of primary AlSiTi intermetallic compounds only in the treated Al-7Si-3-Cu-0.3Mg alloy (Figure 8). This is likely due to the increased Ti level in the treated alloy that exceeds the solubility limit in the α-Al solid solution.[29] It has been stated how the interaction of Si with Ti can take place directly in the melt at certain Si and Ti concentrations in Al alloy.[30] Although the solubility of V and Zr into the AlSiTi particles has been previously confirmed and documented in the literature,[31] the solubility of Mn in AlSiTi particles was revealed for the first time to the best knowledge of authors. It can be noted that the existence of Zr, Mn, and V as impurities in the material can result in further stabilization of undesired AlSiTi phase in the microstructure, *i.e.*, the formation of primary AlSiTi particles can be further promoted or the number density and size of AlSiTi particles can be enhanced, leading to the deterioration of the material's performance.

Considering these aspects, the optimization of grain refiner's level in secondary Al foundry alloys, containing Ti, V, and Zr as impurities, appears to be much more complicated than the process optimization in primary alloys.

It has been also shown how V can dissolve into β-Al_5FeSi phase and it has no apparent influence on the grain size;[32] however, in the present study, vanadium accumulates more preferably into primary Ti-bearing precipitates rather than to the β-Al_5FeSi phase (Figure 8). This behavior can be due to the low level of V in the present experimental alloy (Table I).

D. *Al-Si Eutectic*

The characteristics of the Al-Si eutectic reaction were also determined from the thermal analysis and are shown in Figure 9(a), which clearly illustrates how varying the pouring temperature tends not to cause any remarkable changes in the eutectic reaction of untreated alloy; thus, T_{growth} remained almost constant around 839 K (566 °C). In the treated Al-7Si-3Cu-0.3Mg alloy, the lower the pouring temperature, the more depression in the nucleation and growth temperatures of eutectic was observed. It is well known how the depression in the eutectic temperature can be used as an indicator of the extent of Si structure modification expected in the casting: lower eutectic temperature indicates greater modification effect.[33] The Sr modification in present study caused a drastic reduction of the eutectic temperature by ~10 K (10 °C). A slight increase in the nucleation and minimum temperatures of the eutectic reaction with increasing the pouring temperature in treated Al-7Si-3Cu-0.3Mg alloy (see Figure 9(a)) is due to Sr fading in the molten bath, as a result of melt oxidation upon prolonged holding time at higher temperature. This behavior is explained earlier in detail in Section II–A.

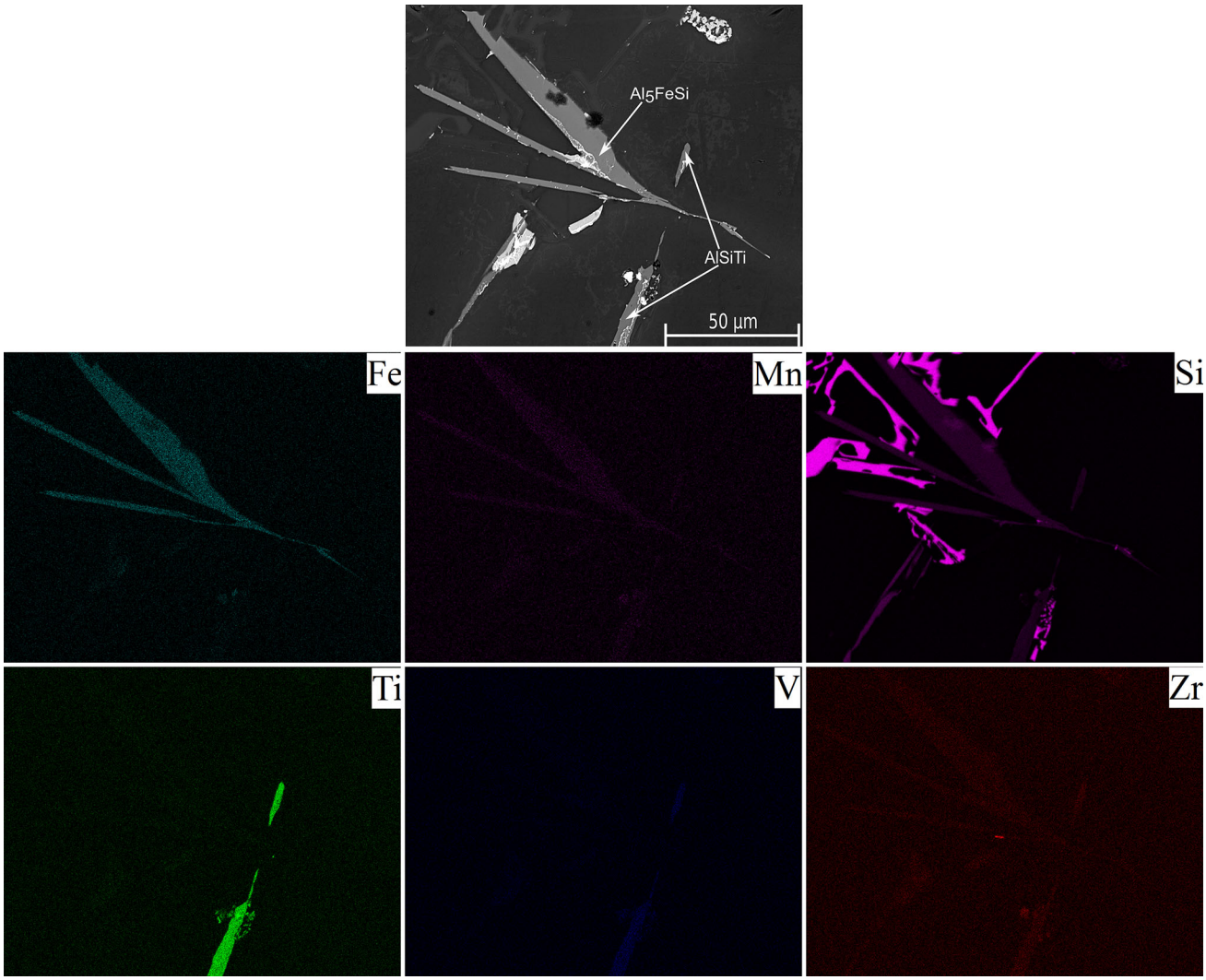

Fig. 8—Backscattered electron image of AlSiTi and Al_5FeSi particles with the corresponding EDS composition maps, showing the distributions of Ti, V, Zr, Fe, Mn, and Si elements.

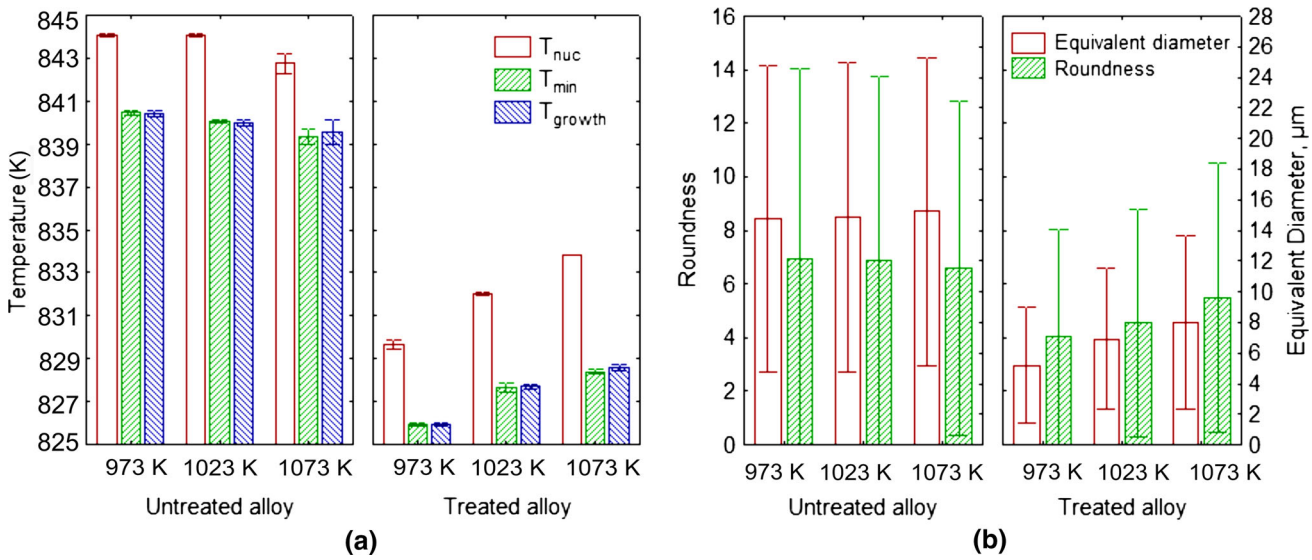

Fig. 9—(*a*) The solidification characteristics of eutectic Si over different pouring temperatures and chemical treatment level; (*b*) evolution of average roundness and equivalent diameter of eutectic Si particles as function of pouring temperature and chemical treatment.

The extent of Si particles' modification was also assessed by the microstructural investigation. It can be seen in Figures 3 and 9(b) how the Sr addition changed the size and morphology of eutectic Si. The treated samples exhibit a partially modified microstructure, with regions of refined and fibrous eutectic silicon. This behavior is more likely due to poor Sr addition and low cooling rate during thermal analysis.[33]

Several trace elements such as Bi and B can induce a negative impact on the efficiency of Sr modification.[34–36] However, no interactions of trace elements, such as B and Bi with Sr were detected in the present study. This could be due to a low content of trace elements that do not react with Sr.[37,38]

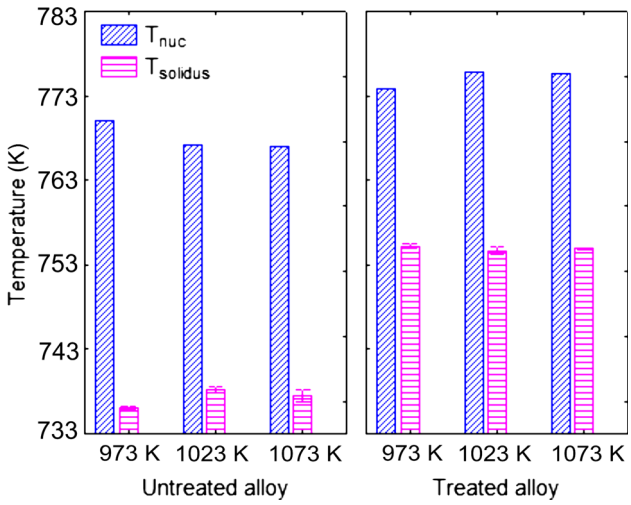

Fig. 10—The effect of pouring temperature on the solidification characteristics of Cu-rich precipitates in Al-7Si-3Cu-0.3Mg alloy before and after combined Sr modification and grain refinement with Al-Ti-B.

Table III. Average EDS Results of the Different Fe-Intermetallic Phases (Atmospheric Percent)

Alloy	Al	Si	Fe	Mn	Cr	Mg	Cu
$Al_{15}(Fe,Mn)_3Si_2$	73	11	11	2	0.14	—	bal.
Al_5FeSi	70	17	10	1	—	—	bal.
$Al_8Mg_3FeSi_6$	61	23	3.5	—	—	10	bal.

IV. CU-RICH COMPOUNDS

Two different types of Cu-rich phases were observed in the microstructure: θ-Al_2Cu and Q-$Al_5Si_6Cu_2Mg_8$. The Al_2Cu phase appeared as a predominant Cu-rich phase in the microstructure. It seems that the both Al_2Cu and $Al_5Si_6Cu_2Mg_8$ particles crystallized sequentially or at the same time; thus, the relative peak of $Al_5Si_6Cu_2Mg_8$ phase in the first derivative of the cooling curve was more likely overlapped by the peak associated with the formation of Al_2Cu compounds. Therefore, in this study, the evolution of a relative peak in the first derivative of cooling curves (Figure 2) seems to be the result of a mutual contribution of Al_2Cu and $Al_5Si_6Cu_2Mg_8$ phases. A sketch of the solidification characteristics of Cu-rich compounds in the alloys investigated is given in Figure 10. The impact of pouring temperature on the solidification parameters of Cu-rich compounds seems to be negligible, whereas the chemical treatment of the base material with Al-Sr and Al-Ti-B shifted the nucleation temperature of Cu-rich particles to higher temperatures by about 5 K (5 °C) compared to an untreated alloy. Since the solidification of the present alloy conditions ends with the precipitation of Cu-rich particles, the solidus temperature was treated as one of the solidification parameters of Cu-rich compounds in

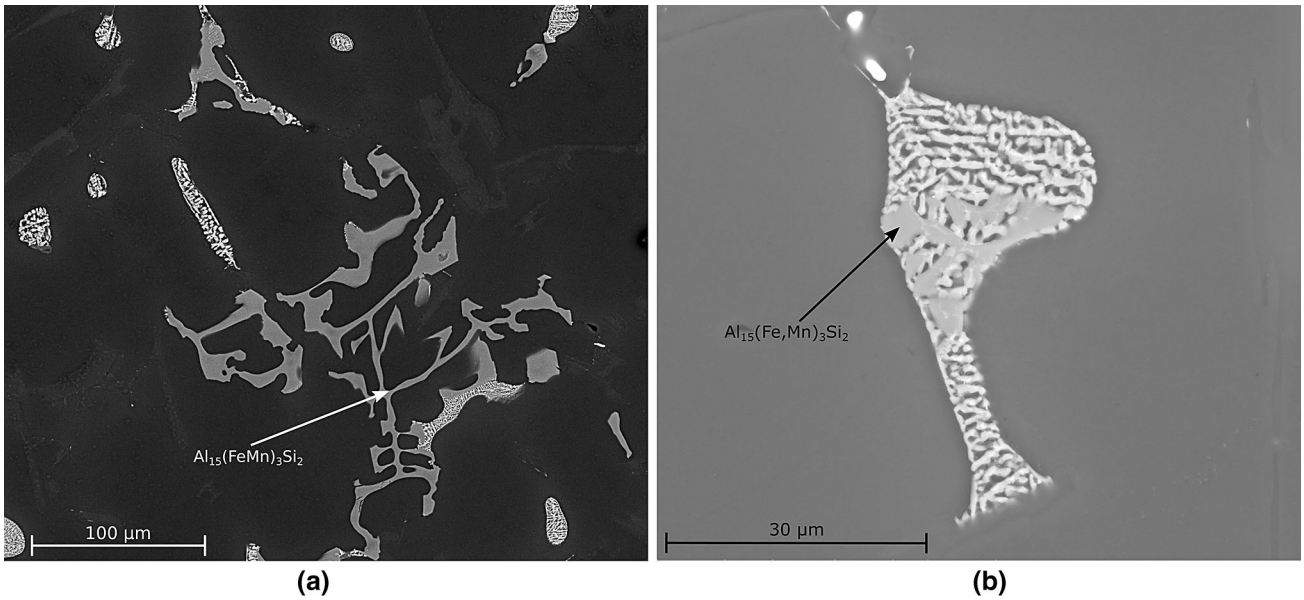

Fig. 11—Backscattered electron micrographs showing (*a*) coarse primary α-$Al_{15}(Fe,Mn)_3Si_2$ particle, and (*b*) fine secondary α-$Al_{15}(Fe,Mn)_3Si_2$ particle.

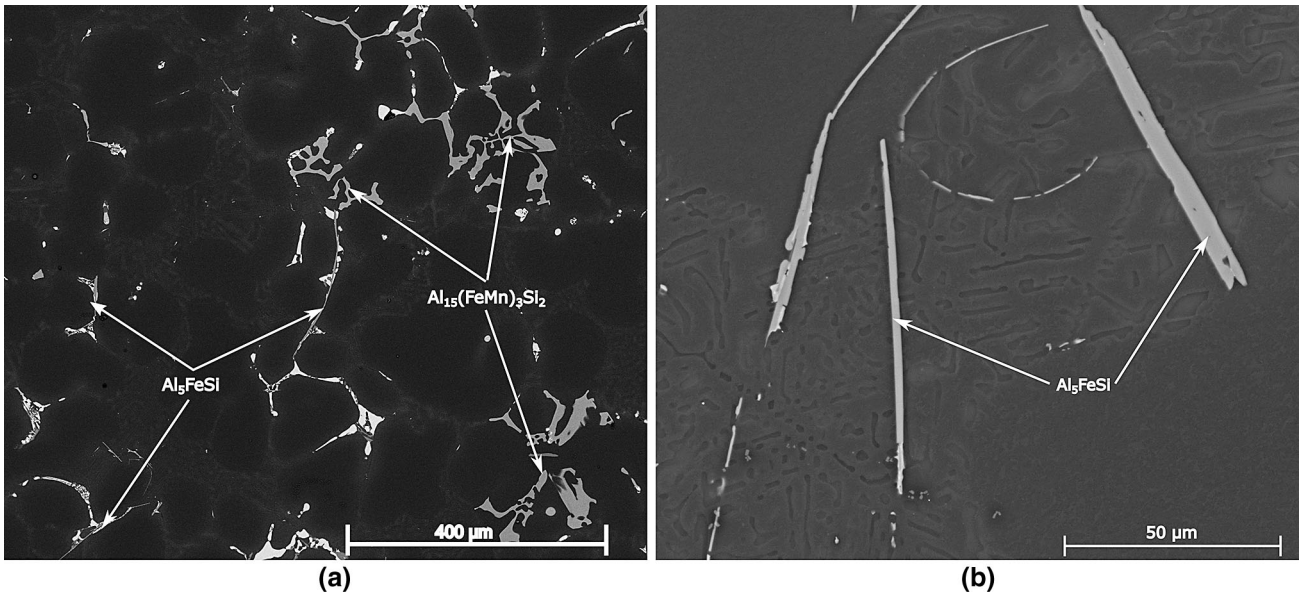

Fig. 12—Backscattered electron micrographs showing (*a*) coarse α-$Al_{15}(Fe,Mn)_3Si_2$ compounds and secondary β-Al_5FeSi particles, and (*b*) the distribution of β-Al_5FeSi particles in eutectic colonies.

the present study. Figure 10 shows how a solidus temperature shifted upward by ~20 K (20 °C) after Sr modification and grain refinement with Al-Ti-B, leading to a reduction of solidification interval. This behavior seems to be due to segregation of Cu in the regions away from the Al-Si eutectic colonies after Sr addition.[39]

A. *Fe-Rich Compounds*

As aforementioned, the Fe-rich compounds precipitated in the untreated alloy are α-$Al_{15}(Fe,Mn)_3Si_2$ and π-$Al_8Mg_3FeSi_6$ phases, whereas the β-Al_5FeSi compounds were revealed in addition to the previous phases after Sr modification and grain refinement with Al-5Ti-1B. The α-$Al_{15}(Fe,Mn)_3Si_2$ phase accounts for the major portion of the Fe-rich phases in both untreated and treated alloys, while the small-sized π-phase was rarely observed (Figure 4). Table III shows the average EDS results of the different Fe-rich phases precipitated during solidification. The microstructural investigation reveals that the precipitation behavior of the α-$Al_{15}(Fe,Mn)_3Si_2$ phase in treated alloys differs from the untreated condition.

The untreated alloy exhibits coarse α-$Al_{15}(Fe,Mn)_3Si_2$ compounds appearing with Chinese-script morphology in the microstructure (Figure 11(a)), as well as finer α-$Al_{15}(Fe,Mn)_3Si_2$ particles in more irregular shape, formed within the interdendritic channels (Figure 11(b)).

The treated alloy indicates the presence of only initially precipitated α-$Al_{15}(Fe,Mn)_3Si_2$ compounds. Small-scale α-$Al_{15}(Fe,Mn)_3Si_2$ particles were not observed after the addition of Sr modifier and Al-5Ti-1B grain refiner. Instead, β-Al_5FeSi needles appeared to be a predominant Fe-rich phase in the interdendritic channels (Figure 12). It was also observed how some α-$Al_{15}(Fe,Mn)_3Si_2$ particles can nucleate on primary AlSiTi compounds (Figure 13).

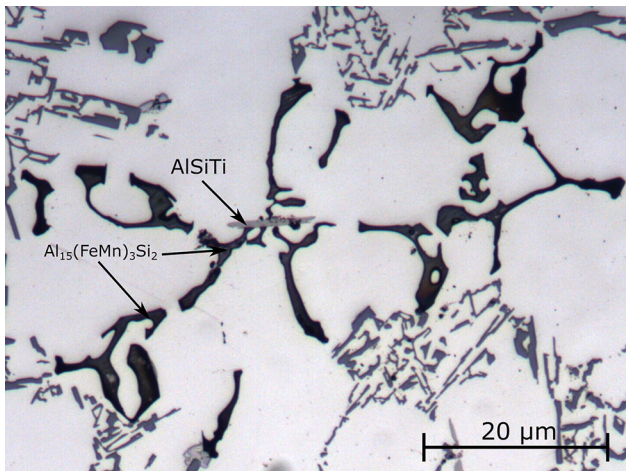

Fig. 13—Optical micrograph showing the α-$Al_{15}(Fe,Mn)_3Si_2$ phase nucleated on AlSiTi particles. The sample surface is etched for easy visualization.

The β-Al_5FeSi particles distributed unevenly in the microstructure, mostly appearing at eutectic colony boundaries (Figure 12). No evident peak associated with the precipitation of β-Al_5FeSi in the derivative curves was observed. This can be explained by a limited fraction of β-Al_5FeSi in the microstructure, as well as their nucleation occurring over a wide temperature range.[19]

Microstructural investigations show the existence of TiB_2 particles lying adjacent to β-Al_5FeSi compounds (Figures 14 and 15). Considering that this behavior was observed in many cases, it is, therefore, proposed that the TiB_2 particles promoted the formation of β-Al_5FeSi compounds over α-$Al_{15}(Fe,Mn)_3Si_2$ phase by acting as a favorable nucleation site, which seems to be consistent with Reference 40, where it has been demonstrated by using transmission electron microscopy how TiB_2 can

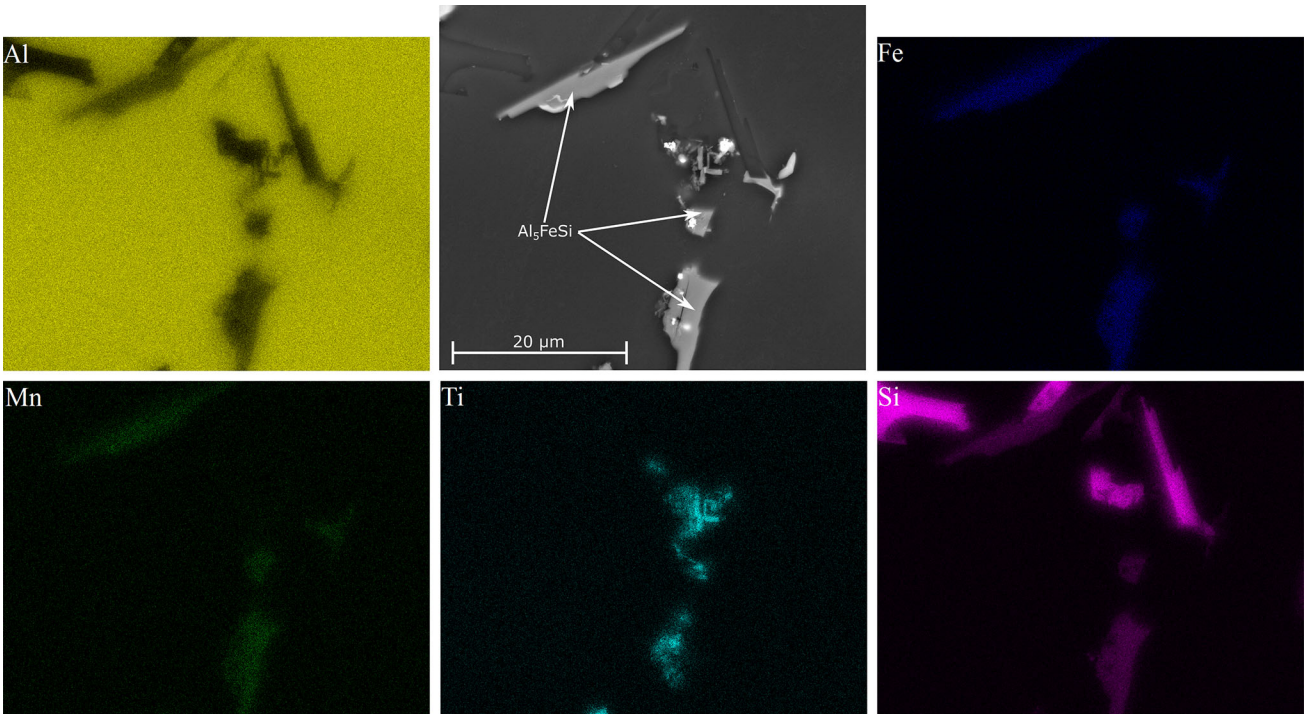

Fig. 14—Backscattered electron image of β-Al_5FeSi phase with corresponding EDS composition maps, showing the distributions of Al, Fe, Mn, Si, and Ti elements.

Fig. 15—Backscattered electron image of β-Al_5FeSi phase with corresponding WDS composition maps, showing the distributions of Ti and B elements.

nucleate β-Al_5FeSi in 6xxx series wrought Al alloys due to low lattice mismatch. Similar results have also been reported in Reference 41.

According to Al-Si-Fe-Mn phase diagram presented in Figure 16, the occurrence of both α-$Al_{15}(Fe,Mn)_3Si_2$ and β-Al_5FeSi involving reactions can be expected in the present study. The fact that the Al_5FeSi involving reaction remained unfavorable during solidification of untreated alloy can be due to a greater undercooling needed for nucleation of β-Al_5FeSi phase, whereas nucleation of α-$Al_{15}(Fe,Mn)_3Si_2$ seems to be more favorable on certain substrate in the undercooled melt, thus avoiding the precipitation of β-Al_5FeSi in the microstructure. In other words, once the segregation line, presented in Figure 16, crosses line 2a, the α-$Al_{15}(Fe,Mn)_3Si_2$ phase starts to form. This phase continues to crystallize until the segregation line reaches the line 2b, where the precipitation of both

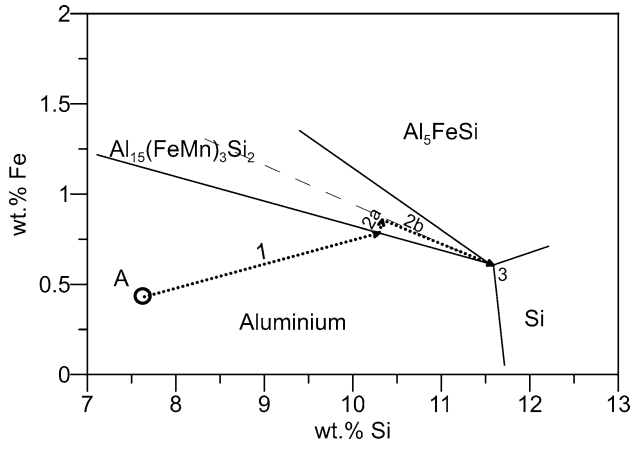

Fig. 16—Simplified Al-Si-Fe-Mn phase diagram at 0.2 wt pct Mn level.[18] The composition of the base material investigated in this study is indicated by the point A.

α-$Al_{15}(Fe,Mn)_3Si_2$ and β-Al_5FeSi is expected to occur; however, due to lack of a potent nucleation site for β-Al_5FeSi, nucleation of α-$Al_{15}(Fe,Mn)_3Si_2$ seems to occur more easily. In contrast, in the case of treated alloy, when the solidification proceeds through the line 2b, the precipitation of β-Al_5FeSi was more favorable due to the presence of TiB_2 particles, which act as an effective nucleation site for their formation.

V. CONCLUSIONS

The role of impurity elements and melt superheat on the efficiency of Sr modification, grain refinement with Al-5Ti-1B and the precipitation behavior of intermetallic phases in a secondary Al-7Si-3Cu-0.3Mg alloy were investigated and the following conclusions can be drawn.

- The variation of pouring temperature had no apparent influence on the efficiency of grain refinement by Al-Ti-B, indicating how the grain-refining inoculants remain stable within the studied range of pouring temperature, and the potency of TiB_2 particles remains unaffected by impurities such as Zr at certain melt superheats.
- Vanadium and Zirconium were found to be more favorably soluble into primary AlSiTi particles, contributing to a further stabilization and the increased volume fraction of undesired AlSiTi phase. This behavior can further limit the critical Ti content needed for effective grain refinement, complicating the optimization of grain refinement process in secondary Al-Si alloys.
- The crystallization of primary AlSiTi compounds in the microstructure can lead to a depletion of solute content needed for grain growth restriction and the formation of casting defects due to their coarse and flaky morphology.
- The effectiveness of Sr modification remained without any apparent contaminating influence of impurity elements.
- The presence of sufficient amount of Mn in base material completely avoided the formation of undesired β-Al_5FeSi compounds by promoting the crystallization of α-$Al_{15}(Fe,Mn)_3Si_2$ particles throughout the microstructure. Competitive nucleation during later stages of solidification in the case of untreated alloy was also in favor of α-$Al_{15}(Fe,Mn)_3Si_2$ over β-Al_5FeSi. However, after Sr modification and grain refinement with Al-Ti-B, the β-Al_5FeSi phase also appeared in the microstructure nucleating on TiB_2 particles.

ACKNOWLEDGMENTS

This work was developed within the ERASMUS MUNDUS Project (Silkroute—Strand 1/ Lot L09, Project n. 545765). The author would like to thank Raffineria Metalli Capra Spa (Brescia, Italy) for the experimental support to the research. Many thanks are also due to Mr. L. Mariani (Media System Lab Srl) and Dr. F. Reinauer (AMETEK EDAX BU) for their support with WDS analysis.

REFERENCES

1. U.M.J. Boin and M. Bertram: *JOM*, 2005, vol. 57, pp. 26–33.
2. A.S.J. Green: *Aluminum Recycling and Processing for Energy Conservation and Sustainability*, ASM International, Materials Park, 2007, pp. 125–30.
3. M.J. Caton, J.W. Jones, J.M. Boileau, and J.E. Allison: *Metall. Mater. Trans. A*, 1999, vol. 30A, pp. 3055–68.
4. M.B. Djurdjevic, I. Vicario, and G. Huber: *Rev. Metal.*, 2014, vol. 50 (1), pp. 1–12.
5. G.S.V. Kumar, B.S. Murty, and M. Chakraborty: *J. Alloys Compd.*, 2009, vol. 472, pp. 112–20.
6. M. Timpel, N. Wanderka, R. Schlesiger, T. Yamamoto, N. Lazarev, D. Isheim, G. Schmitz, S. Matsumura, and J. Banhart: *Acta Mater.*, 2012, vol. 60, pp. 3920–28.
7. G. Timelli, G. Camicia, and S. Ferraro: *J. Mater. Eng. Perform.*, 2014, vol. 23, pp. 611–21.
8. A.M. Bunn, P. Schumacher, M.A. Kearns, C.B. Boothroyd, and A.L. Greer: *Mater. Sci. Technol.*, 1999, vol. 15, pp. 1115–23.
9. J.A. Spittle and S. Sadli: *Mater. Sci. Technol.*, 1995, vol. 11, pp. 533–37.
10. B. Zhang, M. Garro, and C. Tagliano: *Metall. Sci. Technol.*, 2003, vol. 21, pp. 3–9.
11. J. Pavlovic-Krstic: PhD Thesis, University of Magdeburg, Magdeburg, 2010, p. 150.
12. F.H. Samuel, A.M. Samuel, H.W. Doty, and S. Valtierra: *Metall. Mater. Trans. A*, 2001, vol. 32A, pp. 2061–75.
13. L. Lu and A.K. Dahle: *Metall. Mater. Trans. A*, 2005, vol. 36A, pp. 819–35.
14. W. Khalifa, A.M. Samuel, F.H. Samuel, H.W. Doty, and S. Valtierra: *Int. J. Cast Met. Res.*, 2006, vol. 19, pp. 156–66.
15. M. D. Ferdian: PhD thesis, Institut National Polytechnique de Toulouse, Toulouse, 2014, p. 247.
16. G. Timelli and E. Fiorese: *Metall. Ital.*, 2011, vol. 103, pp. 9–23.
17. American Society for Testing Materials: *American Society for Testing Materials*, ASTM International, West Conshohocken, 2013, pp. 9–11.
18. L. Backerud, G. Chai, and J. Tamminen: *Solidification Characteristics of Aluminum Alloys*, Oslo, AFS/ScanAluminium, 1990, vol. 2, pp. 72–95.
19. C. Puncreobutr, A.B. Phillion, J.L. Fife, P. Rockett, A.P. Horsfield, and P.D. Lee: *Acta Mater.*, 2014, vol. 79, pp. 292–303.
20. S. Farahany, A. Ourdjini, M.H. Idris, and S.G. Shabestari: *J. Therm. Anal. Calorim.*, 2013, vol. 114, pp. 705–17.
21. D G Ibarra: PhD Thesis, McGill University, Montreal, 1999, pp. 123–28.
22. G. Timelli, G. Camicia, S. Ferraro, and R. Molina: *Met. Mater. Int.*, 2014, vol. 20, pp. 677–86.
23. Q. Wang, Y.X. Li, and X.C. Li: *Metall. Mater. Trans. A*, 2003, vol. 34A, pp. 1175–82.
24. L. Lu and A.K. Dahle: *Mater. Sci. Eng. A*, 2006, vol. 435, pp. 288–96.
25. H.U. Xiaowu, A.I. Fanrong, and Y. Hong: *Acta Metall. Sin.(Engl. Lett.)*, 2012, vol. 25, pp. 272–78.
26. D. Qiu, J.A. Taylor, and M.X. Zhang: *Metall. Mater. Trans. A*, 2010, vol. 41A, pp. 3412–21.
27. W.D. Kang and H.G. Park: *Korean J. Met. Mater.*, 2011, vol. 49, pp. 619–27.
28. A.L. Greer: *Philos. Trans. R. Soc. Lond. Ser. A*, 2003, vol. 361, pp. 479–94.
29. X.G. Chen and M. Fortier: *J. Mater. Process. Technol.*, 2010, vol. 210, pp. 1780–86.
30. T.E. Quested, A.T. Dinsdale, and A.L. Greer: *Mater. Sci. Technol.*, 2006, vol. 22, pp. 1126–34.
31. B. Suarez-Pena and J. Asensio-Lozano: *Scripta Mater.*, 2006, vol. 54, pp. 1543–48.
32. T.H. Ludwig, P.L. Schaffer, and L. Arnberg: *Metall. Mater. Trans. A*, 2013, vol. 44A, pp. 3783–96.

33. A. Manente and G. Timelli: *Metall. Ital.*, 2008, vol. 100, pp. 37–50.
34. S. Farahany, A. Ourdjini, M.H. Idris, and L.T. Thai: *Trans. Nonferrous Met. Soc. China*, 2011, vol. 21, pp. 1455–64.
35. L. M. Lu and A. K. Dahle: *Light Met.*, 2006, pp. 807–12.
36. S. Farahany, A. Ourdjini, T.A. Abu Bakar, and M.H. Idris: *Thermochim. Acta*, 2014, vol. 575, pp. 179–87.
37. S. Ferraro, G. Timelli, and A. Fabrizi: *Mater. Sci. Forum*, 2013, vol. 765, pp. 59–63.
38. K. Nogita, S.D. McDonald, and A.K. Dahle: *Mater. Trans.*, 2003, vol. 44, pp. 692–95.
39. Z. Li, A.M. Samuel, F.H. Samuel, C. Ravindran, and S. Valtierra: *J. Mater. Sci.*, 2003, vol. 38, pp. 1203–18.
40. G. Sha, K. O'Reilly, B. Cantor, R. Hamerton, and J. Worth: *Mater. Sci. Forum*, 2000, vol. 331, pp. 253–58.
41. T. Smith, K. O'Reilly, S. Kumar, and I. Stone: *Metall. Mater. Trans. A*, 2013, vol. 44, pp. 4866–71.

SUPPLEMENT 2

Influence of grain refiner addition on the precipitation of Fe-rich phases in secondary AlSi7Cu3Mg alloys

J. Rakhmonov, G. Timelli, F. Bonollo and L. Arnberg, International journal of metalcasting, 2017 (11), 294-304

INFLUENCE OF GRAIN REFINER ADDITION ON THE PRECIPITATION OF Fe-RICH PHASES IN SECONDARY AlSi7Cu3Mg ALLOYS

Jovid Rakhmonov, Giulio Timelli, and Franco Bonollo
Department of Management and Engineering, University of Padova, Stradella S. Nicola, 3, 36100 Vicenza, Italy

Lars Arnberg
Department of Materials Science and Engineering, NTNU, Trondheim, Norway

DOI 10.1007/s40962-016-0076-9

Abstract

The effect of grain refiner addition on the precipitation of Fe-rich compounds in secondary AlSi7Cu3Mg has been studied. Thermal and metallographic analysis techniques have been used to examine the formation of Fe-bearing intermetallics. The results show that grain refinement with AlTi5B1 can alter the precipitation sequence of Fe-rich phases. In non-grain refined alloy and grain-refined alloy with AlTi10, two different Fe-rich phases, α-$Al_{15}(Fe,Mn)_3Si_2$ and π-$Al_8Mg_3FeSi_6$, form, whereas, with AlTi5B1 addition, the β-Al_5FeSi phase also tends to crystallize, nucleating on TiB_2 particles. It has also been demonstrated how at high cooling rates, the β-Al_5FeSi-involved reactions occur more preferentially, when compared to α-$Al_{15}(Fe,Mn)_3Si_2$ phase. This crystallization behaviour is explained in terms of phase diagram relationship and the nucleation kinetics of competing α-$Al_{15}(Fe,Mn)_3Si_2$ and β-Al_5FeSi phases.

Keywords: *Al–Si alloys, grain refinement, microstructure, thermal analysis, Fe-rich intermetallics, cooling rate*

Introduction

Al–Si alloys are widely used in the automotive industry due to their attractive strength to weight ratio as well as superior casting characteristics. In addition, the excellent recyclability of Al–Si alloys favours massive use of secondary (recycled) alloys in the foundry industry, as secondary Al alloys production has significant cost advantages in comparison with primary Al alloys. However, the presence of several impurity elements in recycled materials can lead to the deterioration of mechanical properties, as well as the final quality of cast components.

Iron is one of the most harmful impurities in Al–Si foundry alloys. Due to its low solid solubility in α-Al, strong segregation of Fe into the interdendritic regions occurs during solidification, leading to the formation of various Fe-rich phases, such as α-Al_8Fe_2Si or α-$Al_{15}(Fe,Mn)_3Si_2$, β-Al_5FeSi, δ-Al_4FeSi_2, N-Al_7Cu_2Fe and π-$Al_8Mg_3FeSi_6$ phases, depending on the cooling rate and the alloy composition.[1,2]

Among various Fe-rich phases, β-Fe is considered to be the most undesired one. The high-stress concentrations located near sharp edges of β-Fe particles as well as the weak bond between the β-Fe phase and the Al matrix promote crack initiation, thus decreasing the ductility of the castings.[3] The platelet morphology of this phase creates feeding difficulties during solidification, leading to porosity formation.[4] Furthermore, the β-Fe compounds are brittle and hard which is deleterious to the machinability of cast parts.[5]

The formation of β-Fe in the microstructure can be avoided by various techniques: (1) alloying with transition elements such as Mn, Cr, V, Ni; (2) alloying with Sr; (3) rapid solidification; (4) melt superheating.[6]

The most common technique to neutralize/minimize the adverse effects of Fe is Mn addition. The weight ratio between Fe and Mn, that is needed to avoid the formation of β-Fe particles, depends on both the content of Fe and the cooling rate.[7] However, the ratio of 2:1 between Fe and Mn has been generally accepted as an optimum level.

Several studies have focused on understanding the metallurgical parameters affecting the precipitation behaviour of β-Fe.[7,8] Recently, the nucleation mechanisms and growth kinetics of β-Fe phase have been thoroughly assessed by means of real-time in situ synchrotron X-ray tomography.[9] However, it seems that the role of grain refinement with Al–Ti–B on the formation of Fe-rich phases is not well understood and conflicting data exist in the literature. It has been stated that refinement of β-Fe particles can occur after Al–Ti–B addition,[10,11] whereas, in other studies,[12,13] the grain refinement with Al–Ti–B exerted opposite impact. Since grain refinement is a common practice in foundries to improve the material's performance, understanding the effect of grain refiner addition on the formation of Fe-bearing intermetallics is of great importance.

The aim of this study is to investigate the influence of AlTi5B1 and AlTi10 grain refiner additions on the precipitation of Fe-rich compounds in secondary AlSi7Cu3Mg alloys under different cooling conditions.

Experimental Details

Thermal Analysis

A secondary AlSi7Cu3Mg (wt%) alloy, supplied by Raffineria Metalli Capra, was adopted as a baseline material. AlTi5B1 rods and AlTi10 waffles were used to grain-refine the material. Although Sr modification is a well-accepted practice for AlSi7Cu3Mg alloys in Al foundry, this step was not carried out in the preset study as Sr itself has an apparent influence on the formation of Fe-rich phases.[14,15]

Thermal analysis experiments were conducted for three different alloy combinations: non-grain-refined (as supplied), AlTi5B1- and AlTi10-grain-refined AlSi7Cu3Mg alloys. The melting of the material was performed in a SiC crucible in a resistance-heated furnace at 750 °C (1382 °F). The molten metal was held for at least 120 min to obtain homogeneous liquid phase. Then, the melt was stirred and skimmed to remove dross prior to pouring into a boron nitride-coated cylindrical steel cup (outer diameter 45 mm, height 60 mm and a uniform wall thickness of 3 mm) preheated to 700 °C (1292 °F). A minimum of two thermal analyses were made for each alloy condition. Samples for chemical analysis were poured prior to each set of thermal analysis experiments. The chemical composition of the experimental alloys, measured by optical emission spectrometry, is shown in Table 1. Other elements such as Zr, V, Ca, Sn, Bi, P and Sb are present in amounts less than 0.01 wt% and are not included in Table 1.

The two-thermocouple method was used for thermal analysis experiments. The tips of the thermocouples in contact with the melt were covered with tightly fitting steel tubes. The data were collected using a data acquisition system with a sampling frequency of 4 s^{-1}, analogue-to-digital converter accuracy of 0.1 °C (32.18 °F). Two thermocouples were inserted into the melt, one in the centre and one adjacent to the wall, 30 mm below the surface of the sample. The system was allowed to air cool and gave an average cooling rate of 0.17 ± 0.1 °C/s (32.306 ± 32.18 °F/s) in the solidification interval. Cooling curves and corresponding derivatives were used to determine the characteristic temperatures related to the formation of phases based on the first derivative cooling curve approach.[16]

Step Casting

The base material was melted in an electrical resistance furnace and heated to 750 ± 5 °C (1382 ± 41 °F/s). The melt was held at this temperature for about 120 min in order to ascertain that all phases were completely melted and that the melt was homogeneous. The melt was then stirred and surface-skimmed, followed by pouring into the cavity of the preheated die. The remaining molten metal was grain-refined by AlTi5B1 with a contact time of at least 20 min prior to pour. Chemical analysis was performed after each pour and the results obtained were similar to those, observed in the case of thermal analysis experiments for both non-grain refined alloy and grain-refined alloy with AlTi5B1, shown in Table 1.

The geometry of the step casting used in the present study is presented in Reference 10. The AISI H11 die used in this study is designed to make castings with four different thicknesses ranging between 5 and 20 mm. Al_2O_3 foam filters (30 ppi) were used for each casting to allow a smooth flow of the molten metal into the die cavity. A layer of boron nitride coating was sprayed at 200 °C (392 °F) on the inner die surfaces. Before pouring, the temperature of the die was increased to 390 ± 10 °C (734 ± 50 °F). The temperature was monitored by means of thermocouples embedded in the die to ensure a good reproducibility of the tests. The working temperature of the die was in the range of 390–450 °C (734–842 °F).

Metallographic Characterization

Thermal analysis samples were cut along the central axis of the cylinder. Samples for microstructure analysis were sectioned near the tip of the thermocouples in order to correlate the thermal analysis parameters with the microscopic observations. Step castings were halved along the main axis. Then, all samples were mounted, ground and polished using the standard procedure. Optical microscopy (OM), scanning electron microscopy (SEM) coupled with energy-dispersive (EDS) and wavelength-dispersive spectrometry (WDS) were used to characterize the type and morphology of Fe-rich phases in as-cast microstructure.

Table 1. Chemical Composition of the Experimental Alloys (wt%)

Alloy	Si	Fe	Cu	Mn	Mg	Zn	Cr	Ni	Ti	Pb	B	Al
A (AlSi7Cu3Mg)	7.57	0.44	3.1	0.23	0.31	0.77	0.04	0.02	0.01	0.04	0.001	bal
A + AlTi5B1	7.42	0.43	3.0	0.22	0.30	0.72	0.04	0.02	0.14	0.04	0.017	bal
A + AlTi10	7.29	0.43	3.0	0.22	0.31	0.76	0.04	0.02	0.14	0.04	0.001	bal

Several backscattered electron (BSE) images, representing a total area of 10 mm^2, were captured from each step of casting to investigate the distribution of β-Fe particles in the microstructure.

Results and Discussion

Thermal Analysis

The cooling curves of both non-grain-refined and grain-refined alloys in the region of primary α-Al formation (Figure 1) clearly show the effect of the grain refinement. It is known that the recalescence, which is the difference between growth and minimum temperatures, can be strongly correlated with the grain refinement level.[17] It can be seen in Figure 1c that the recalescence is almost zero in alloy grain-refined with AlTi5B1, indicating an important role of TiB_2 particles for the grain refinement. The influence of AlTi10 addition on refining α-Al grains is also clearly evident from the corresponding cooling curve (Figure 1b); however, the AlTi10 appears not to be as efficient as AlTi5B1 (Figure 1c).[18]

Typical microstructures obtained from non-grain-refined and grain-refined alloys are shown in Figure 2. In general, the microstructure consists of α-Al matrix, eutectic Si network, Cu- and Fe-rich phases. In both non-grain-refined and grain-refined alloys, the α-$Al_{15}(Fe,Mn)_3Si_2$ accounts for the major portion of the Fe-rich phases. A limited number of π-$Al_8Mg_3FeSi_6$ particles in a size range of few microns were observed in all alloy conditions. Needle-like β-Fe particles appear in the microstructure of alloy grain-refined with AlTi5B1, whereas no evidence of β-Fe phase formation is observed in non-grain-refined and AlTi10-grain-refined structures (Figure 2). Figure 3 shows the morphology and the EDS analysis results of three different Fe-rich phases.

From the cooling curves and the associated first derivatives, no evident peak related to the formation of Fe-rich phases was detected; however, a small peak indicated by arrow in Figure 1c appears only after grain refinement with AlTi5B1 and this is thought to be consequence of α-Fe formation. The absence of similar peaks in the cooling curves of both non-refined alloy and grain-refined alloy with AlTi10 (Figure 1) can be due to overlapping by the neighbouring peak indicating the formation of α-Al, since the growth of primary α-Al takes longer time in these two alloys, as compared to grain-refined alloy with AlTi5B1 (see Figure 1). The simplified Al–Si–Fe–Mn phase diagram at constant Mn level (0.2 wt%) and the solidification

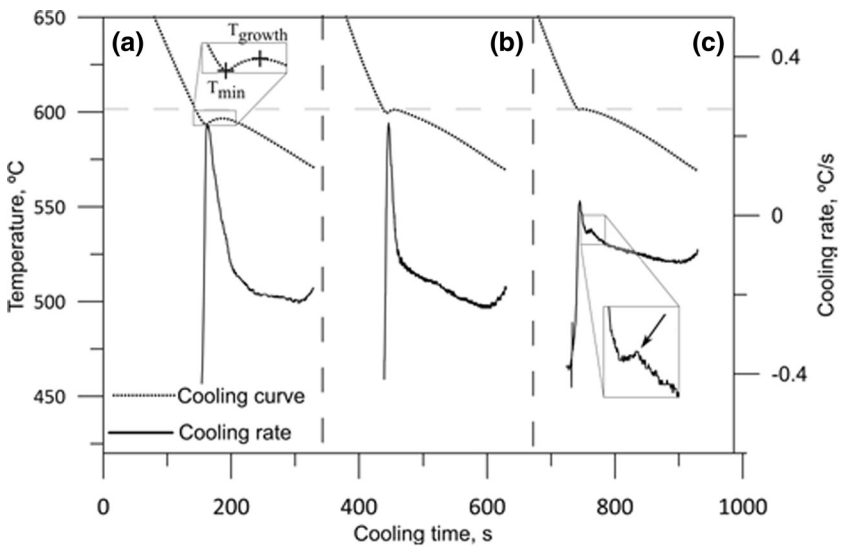

Figure 1. Cooling curves of AlSi7Cu3Mg alloy (a) before the grain refinement, after addition of (b) AlTi10 and (c) AlTi5B1 grain refiners. The corresponding first derivatives are also presented.

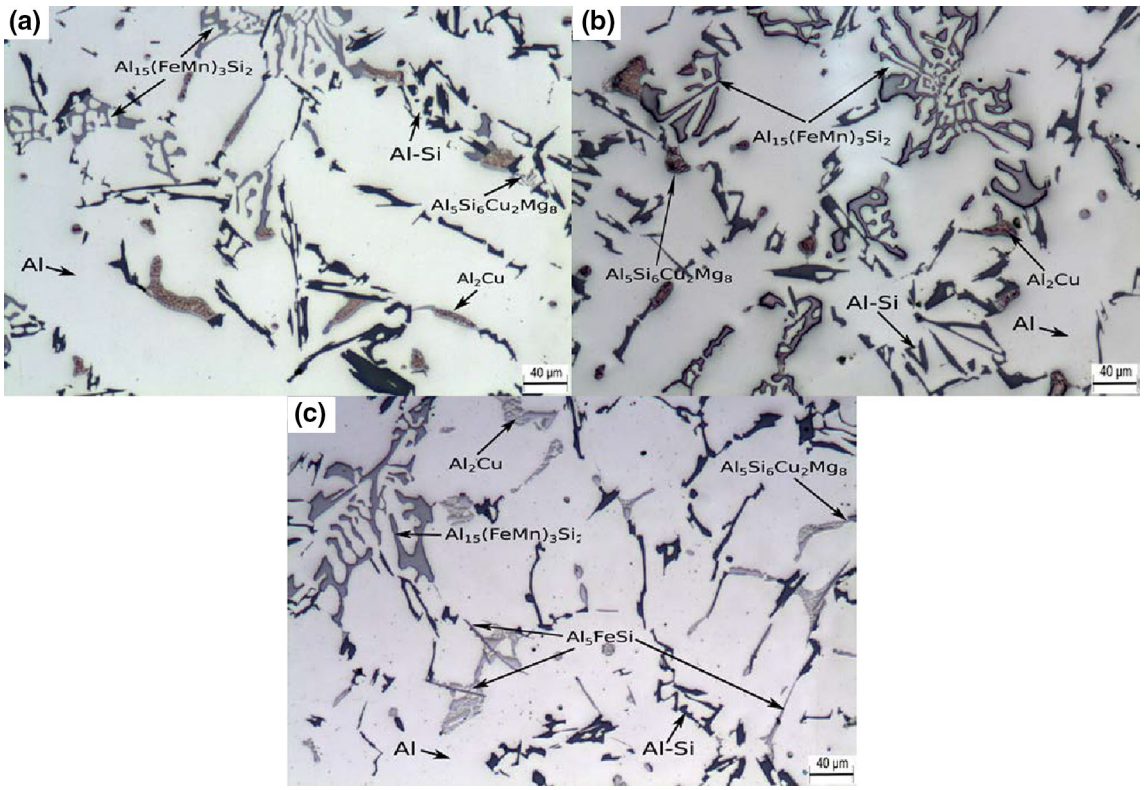

Figure 2. Typical microstructures of (a) non-grain-refined, (b) AlTi10- and (c) AlTi5B1-grain-refined AlSi7Cu3Mg alloy.

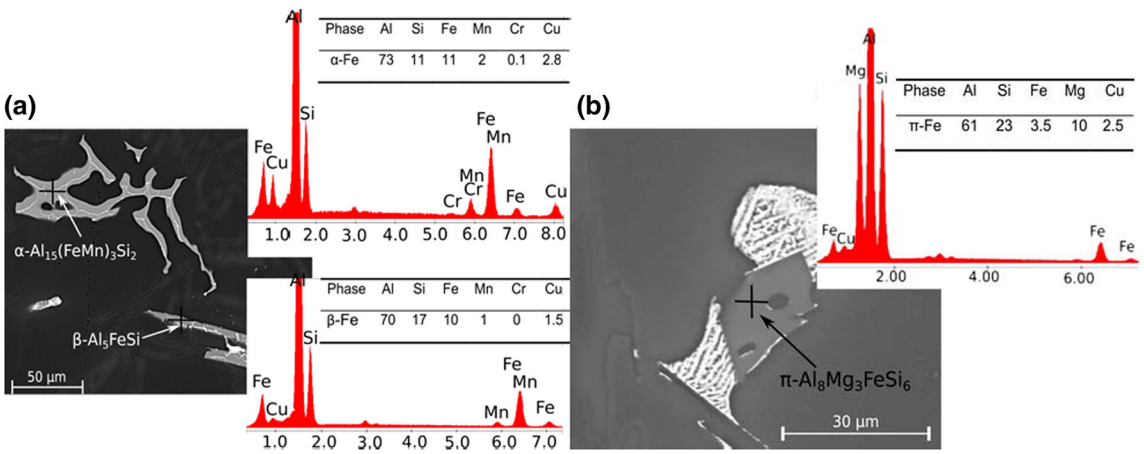

Figure 3. Backscattered electron images showing (a) $Al_{15}(FeMn)_3Si_2$ and Al_5FeSi phases, and (b) $Al_8Mg_3FeSi_6$ compounds with the corresponding EDS spectra and composition (in at.%).

path depicted on the Al-rich corner (Figure 4) show how α-Fe phase is expected to solidify by following the primary α-Al phase.

Although the microstructural investigation of the alloy grain-refined with AlTi5B1 revealed the existence of β-Fe intermetallics throughout the microstructure (Figure 2c), no peak associated with their formation in the cooling curve and the first derivative was observed. This can be explained by a limited fraction of β-Fe in the microstructure, as well as their nucleation occurring over a wide temperature range.[9] The precipitation of β-Fe is mainly classified by a two sequences: (1) pre-eutectic, i.e. prior to the (Al)–Si eutectic reaction, in the form of a two-phase (Al)–β-$Al_9Fe_2Si_2$ eutectic reaction, and (2) co- or post-(Al)–Si eutectic in the form of a three-phase (Al)–Si–β-$Al_9Fe_2Si_2$ eutectic reaction.[19] According to the Al–Si–Fe–Mn phase diagram presented in Figure 4, the occurrence of both β-Fe reactions can be expected in the present study. Considering that β-Fe formation occurs only in the

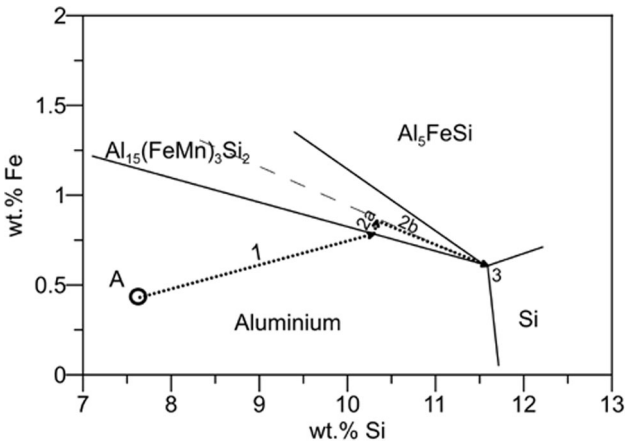

Figure 4. Simplified Al–Si–Fe–Mn phase diagram at 0.2 wt% Mn level.[31] The composition of the base material investigated in this study is indicated by the point A.

Table 2. Average Secondary Arm Spacing, λ_2, Measured in Different Steps (with Corresponding Standard Deviations) and the Corresponding Cooling Rates Calculated According to Eqn. 1 are Reported

Step thickness (mm)	λ_2 (μm)	Cooling rate (°C/s)
5	18 (2.5)	11.8
10	23 (3.4)	5.1
15	25 (3.9)	4.1
20	31 (4.8)	2.1

case of alloy grain-refined with AlTi5B1 and not in the cases of non-refined alloy and grain-refined alloy with AlTi10, it is believed that some α-Fe particles appearing in the microstructure of non-refined alloy and grain-refined alloy with AlTi10 are in metastable state, forming in preference to β-Fe phase. The precipitation kinetics of Fe-rich phases (α-Fe and β-Fe) is discussed in detail in the next sections.

Influence of Cooling Rate

The cooling rates in the different steps of the casting were estimated by the secondary dendrite arm spacing, λ_2, according to the empirical equation[20]:

$$\lambda_2 = 39.4R^{-0.317} \qquad \text{Eqn. 1}$$

where R represents the mean cooling rate of the primary α-Al dendrites during solidification. The average λ_2 values with corresponding standard deviations and the estimated cooling rates are listed in Table 2.

Typical microstructures obtained from the step castings produced from non-refined alloy are shown in Figures 5a, b and 6a, b. In the non-refined alloy, α-Fe appears to be a dominating Fe-rich phase (Figures 5a, b, 6a, b), competing only with a small-sized π-$Al_8Mg_3FeSi_6$ particles in a limited numbers. No reaction involving β-Fe phase took place during solidification (Figures 5a, b, 6a, b), being consistent with what was observed in the microstructure of thermal analysis samples processed from non-refined alloy (Figure 2c). Increasing the cooling rate up to ~12 °C/s (53.6 °F/s) shows no influence on the precipitation sequence of Fe-rich phases (Figures 3a, 5a, b, 6a, b), which seems to agree with Reference 7, where it has been stated how α-Fe phase appears as a sole Fe-rich phase in Mn-containing A319 alloy at the cooling rates of up to 10 °C/s (50 °F/s). However, it has been also demonstrated how further increase in the cooling rate to 20 °C/s (68 °F/s) causes the formation of β-Fe compounds in addition to α-Fe phase throughout the microstructure.[7] At low cooling rates (up to 10 °C/s (50 °F/s)), almost all Fe atoms are bound in crystallization of the α-Fe phase before reaching line 2b in Figure 4, whereas at high cooling rates (20 °C/s (68 °F/s)), Fe is partially consumed until the solidification reaches the line 2b in Figure 4; hence, the remaining Fe is available to form in a mixture of the α-Fe and β-Fe phases.[7]

Figures 5c, d and 6c, d display the typical microstructures from AlSi7Cu3Mg alloy grain-refined with AlTi5B1 master alloy. After the grain refinement with AlTi5B1, the β-Fe particles appear to be formed in addition to α-Fe, which is in agreement with the results of thermal analysis samples with respect to the precipitation sequence of Fe-rich phases. However, at high cooling rates, i.e. in the microstructures from the step casting, needle-like β-Fe appears to be the dominating Fe-rich phase, followed by the α-Fe and few π-Fe particles (Figures 5c, d, 6c, d). Qualitative comparison of the microstructures representing the thermal analysis sample (Figure 2c) and the step casting (Figure 5c, d) suggests that at high cooling rates, more Fe seems to be bound to the β-Fe phase. This implies that no evidence of the positive effect of increasing cooling rate in terms of the transformation of β-Fe into α-Fe has been observed in the present study. Instead, at higher cooling rates the α-Fe compounds tend to rarely appear in the microstructure. This behaviour is in disagreement with References 21–24, where a higher cooling rate is reported to eliminate or reduce β-Fe formation; thus, it can be noted that the influence of grain refinement with AlTi5B1 on the nucleation kinetics of β-Fe phase seems to be significant. This behaviour is elaborated in the next section.

Quantitative analysis of β-Fe particles shows a decreasing average length parameter with increasing cooling rate (Figure 7a); however, high cooling rates also cause the number density of β-Fe needles to rise (Figure 7b). Similar results have been presented in Reference 7, and this behaviour has been attributed to the displacement of the nucleation temperature of β-Fe towards lower temperatures with increasing cooling rate, thus reducing the time available for the growth of β-Fe. Moreover, it is also well known that the cooling rate can control the nucleation and growth processes, affecting both the number

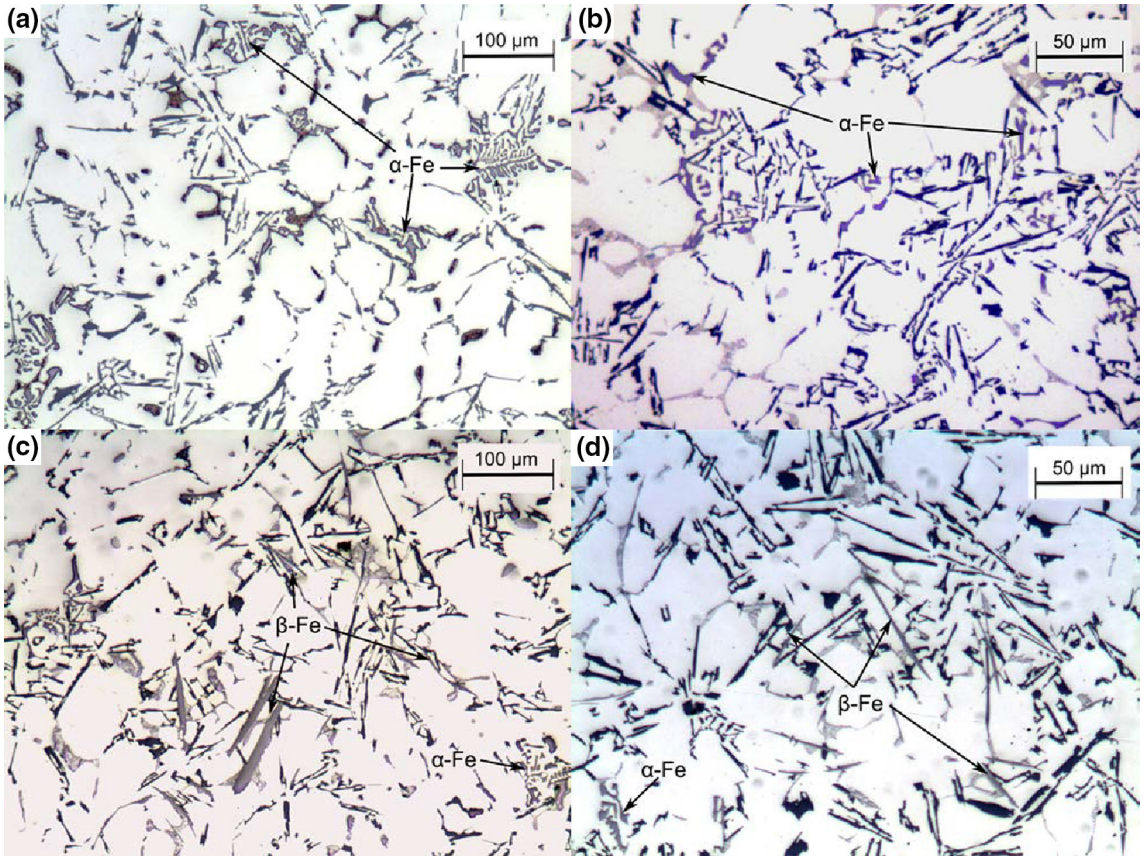

Figure 5. Optical micrographs taken from (a, c) 5-mm and (b, d) 20-mm steps of step casting. The micrographs correspond to (a, b) non-grain-refined alloy and (c, d) grain-refined alloy with AlTi5B1.

density and the size of microstructural features, such as β-Fe particles.[25,26]

Precipitation of Al_5FeSi Particles

It is known that the existence of needle-like β-Fe compounds in the microstructure can induce negative impacts on the material's mechanical properties. Adding Mn to promote the formation of α-Fe phase at the expense of β-Fe is a well-diffused practice in Al foundries, since the non-faceted α-Fe phase is thought to be less deleterious. It has been stated how Mn can completely avoid the crystallization of β-Fe when the Mn content at a sufficient level;[27] contrarily, it has been also found that adding Mn even at relatively high levels cannot result in a complete β-Fe to α-Fe transformation.[21] Thus, it can be noted that the nucleation and growth kinetics of the competing phases, such as α-Fe and β-Fe, has an essential role in selection of the phase forming during solidification of an alloy.

In the present study, the β-Fe particles, as previously mentioned, tend to precipitate only after the grain refinement of AlSi7Cu3Mg alloy with AlTi5B1. The nucleation of Fe-rich phases, particularly β-Fe phase, is generally thought to occur on some substrates such as Al_2O_3 and AlP particles,[7,28–30] requiring a certain amount of undercooling as a driving force. Although both Al_2O_3 and AlP particles tend typically to exist in molten Al alloys, their presence in the liquid bath seems not to facilitate the nucleation of β-Fe during solidification of the base material in the present investigation conditions, even though the phase diagram presented in Figure 4 suggests the precipitation of β-Fe during the later stages of solidification. This behaviour can be explained by considering the nucleation and growth kinetics of the α-Fe and β-Fe phases.

The non-faceted α-Fe grows more easily in irregular and curved crystal form conforming to the complicated shape of the interdendritic spaces during solidification.[31] In contrast, the β-Fe phase is thought to grow with the twin plane re-entrant (TPRE) mechanism in a lateral or faceted mode and contains multiple (001) growth twins parallel to the growth direction,[32,33,33] and thus, there is no need to nucleate a new plane. Recently, quite a high lateral growth rate of β-Fe phase has been observed by means of in situ microtomography using high-energy X-ray synchrotron.[9,29] The faceted phases have a growth disadvantage over non-faceted phases due to the relative difficulty in atomic attachment. In other words, with increasing solidification velocity, and hence reduced time for growth, a greater degree of undercooling is required to overcome the barrier to atomic attachment to (and hence growth of) the faceted phase than to the non-

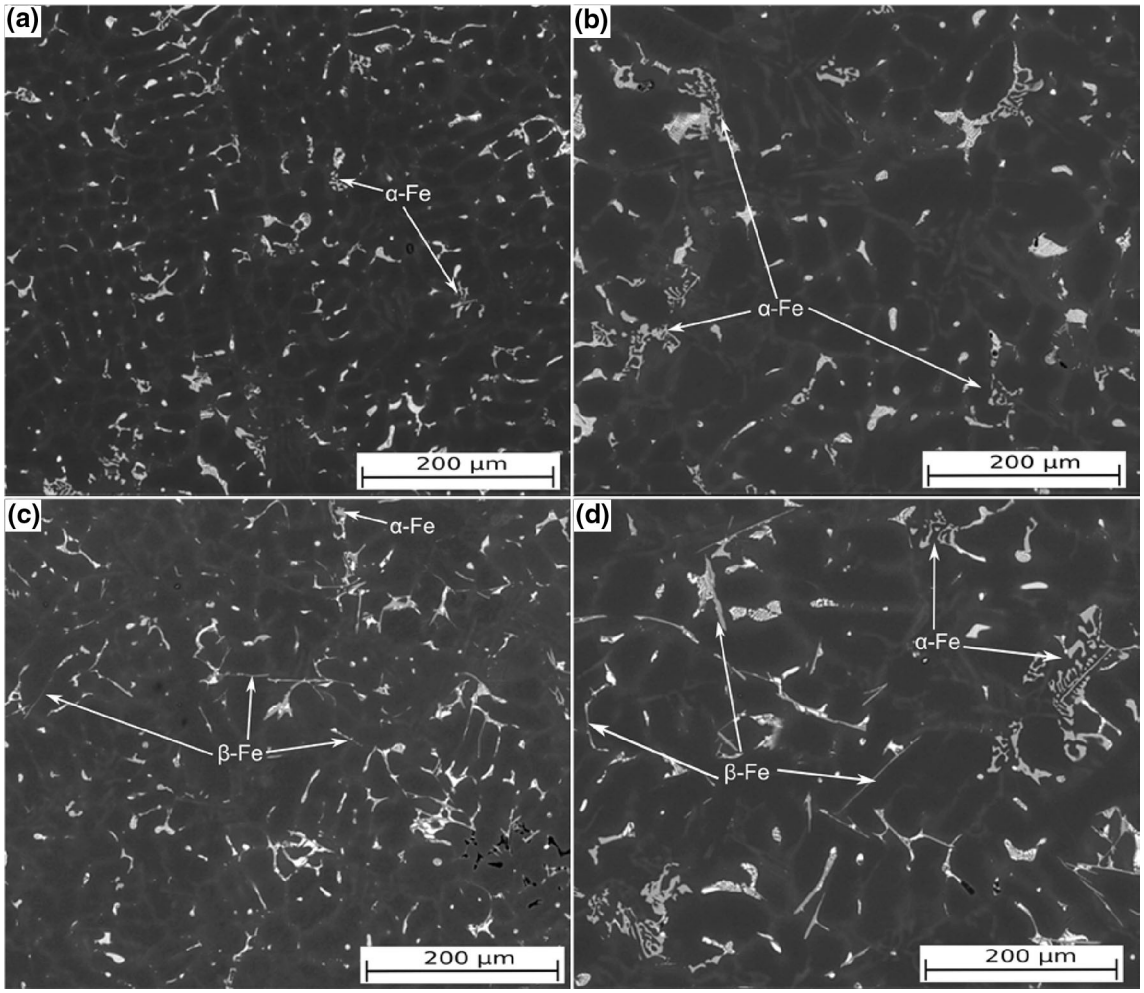

Figure 6. BSE images taken from (a, c) 5-mm and (b, d) 20-mm steps of step casting. The micrographs correspond to (a, b) non-grain-refined alloy and (c, d) grain-refined alloy with AlTi5B1.

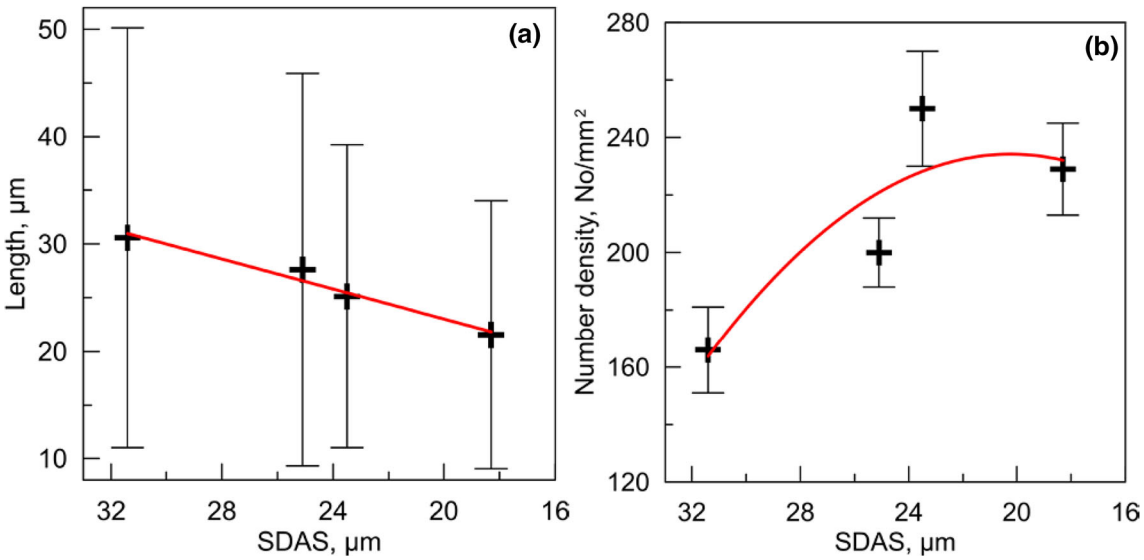

Figure 7. (a) The average length, and (b) the number density of β-Fe particles as function of SDAS evolution in grain-refined alloy with Al–Ti–B.

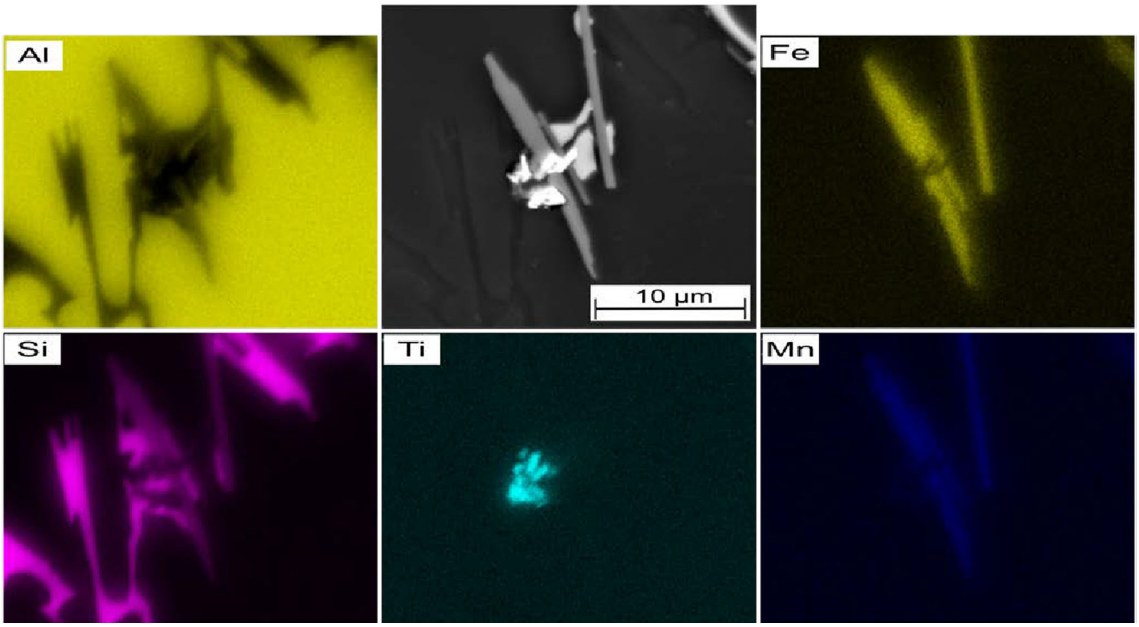

Figure 8. BSE image of Al_5FeSi particles with corresponding EDS composition maps, showing the distributions of Al, Fe, Mn, Si and Ti.

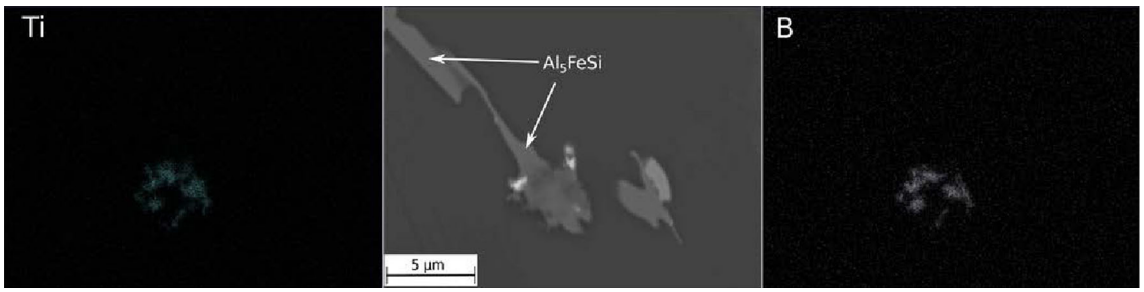

Figure 9. BSE image of Al_5FeSi particles with corresponding WDS composition maps, showing the distributions of Ti and B elements.

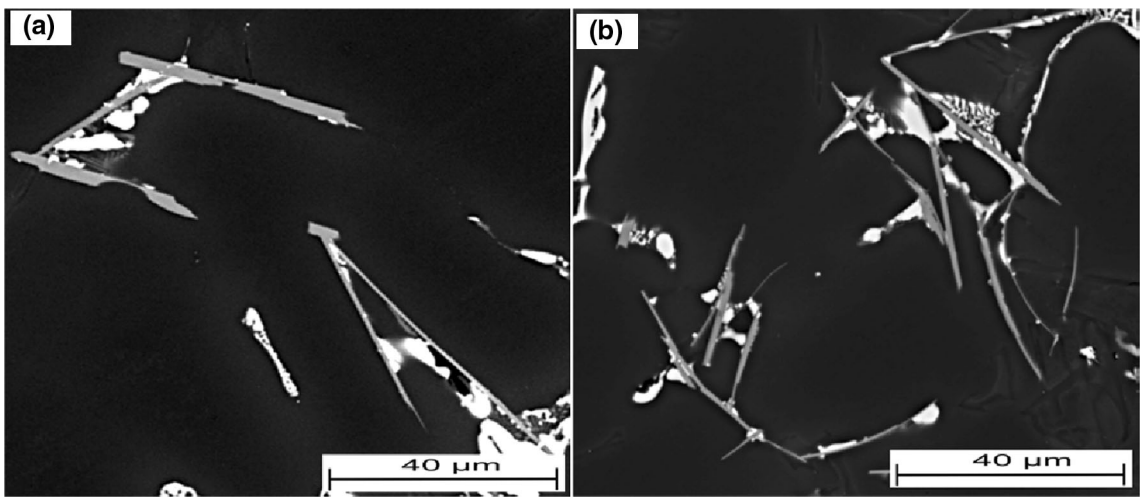

Figure 10. BSE images obtained from (a) 20- and (b) 5-mm step thicknesses of grain-refined alloy with AlTi5B1, showing branched β-Fe particles.

faceted morphology.[34] Therefore, the metastable α-Fe phase is thought to dominate at high cooling rates, if compared to the stable β-Fe particles,[31] which agrees well with Reference 34, where it has been demonstrated how the faceted Al_6Fe phase can be replaced by non-faceted Al_3Fe at higher solidification front velocities. However, this seems to be the case when competitive growth becomes more important rather than competitive nucleation theory, i.e. both the stable and metastable phases tend to nucleate easily. Considering that in the present study, the β-Fe phase dominates at high cooling rates of the grain-refined alloy, as can be observed by comparing Figure 2c with Figures 5c, d and 6c, d, it can be implied that the role of the competitive nucleation model is more relevant than the competitive growth theory in understanding non-equilibrium solidification of the alloys investigated.

The fact that the β-Fe-involving reaction remains unfavourable during solidification of a base material can be due to a greater undercooling needed for nucleation of β-Fe; however, nucleation of α-Fe seems to be more favourable on certain substrate in the undercooled melt, thus avoiding the precipitation of β-Fe in the microstructure. In other words, once the segregation line, presented in Figure 4, reaches line 2a, α-Fe starts to form. This phase continues to crystallize until the segregation line crosses the line 2b, where the precipitation of both α-Fe and β-Fe is expected to occur; however, due to the lack of a potent nucleation site for β-Fe, nucleation of a metastable α-Fe seems to occur more easily.

Understanding the mechanism by which the grain refinement of a base alloy with AlTi5B1 causes significant changes in the precipitation sequence of Fe-rich phase forming during solidification is crucial. With the introduction of AlTi5B1 master alloys into the melt, a release of TiB_2 occurs into the melt. The TiB_2 particles act as heterogeneous nucleation for α-Al.[35] However, only a certain amount of TiB_2 particles can take part in the nucleation of α-Al; therefore, the remaining TiB_2 are pushed towards interdendritic regions by growing dendrites, then being available to act as nucleation site for the occurrence of some eutectic reactions.

The EDS and WDS investigations of grain-refined alloy with AlTi5B1 revealed the presence of TiB_2 particles adjacent to β-Fe compounds (Figures 8, 9). This behaviour has been frequently observed in the present investigation. It is, therefore, proposed that the TiB_2 particles promote the crystallization of β-Fe over α-Fe by acting as an effective nucleation site, which seems to be consistent with Reference 36, where it has been demonstrated by using transmission electron microscopy (TEM) how TiB_2 can nucleate β-Fe in 6xxx series wrought Al alloys due to low lattice mismatch. Similar results have also been reported in Reference 37.

In the present study, the majority of β-Fe compounds tend to appear in eutectic colonies; thus, it can be concluded that TiB_2 particles, pushed into the remaining liquid by growing dendrites, are acting as nucleants for β-Fe. This finding could explain why the addition of Al–Ti-B grain refiner is causing a thickening of β-Fe, as reported in Reference 12, and also precipitation of β-Fe at earlier stages of solidification.[38] The TiB_2 crystals seem to promote the nucleation of β-Fe without any need for greater degree of undercooling, and as a result, thickening and branching of β-Fe occur due to the increased solidification range of β-Fe (Figure 10).

The impact of higher cooling rate on further promoting the precipitation of β-Fe phase in the microstructure of the alloy grain-refined with AlTi5B1 can be explained by that at higher cooling rates, the line 2a in Figure 4, where the α-Fe-involved reactions are expected to occur, tends to pass quickly, involving only a small amount of Fe in the crystallization of α-Fe phase. Thus, the remaining Fe is available for the formation of β-Fe, occurring through the line 2b in Figure 4. In other words, high cooling rates can provide greater undercooling, leading to the reduction in temperature below the melting point of the metastable phase, and as a consequence, the nucleation of metastable phase can be favoured if there is no need for a large undercooling for its formation. A similar observation has been reported in Reference 8, where the β-Fe is found to nucleate efficiently on TiB_2 particles in an alloy containing a higher solute concentration, in contrast to the alloys with less alloying elements, where the TiB_2 appears to be inactive for β-Fe nucleation. This behaviour shows the role of constitutional undercooling in improving the potency of the nucleation sites.

Conclusions

The influence of AlTi10 and AlTi5B1 addition on the precipitation behaviour of Fe-rich intermetallics in secondary AlSi7Cu3Mg alloys has been studied. The following conclusions can be drawn from this work.

- The presence of transition elements such as Mn, Cr and V is able to completely avoid the formation of β-Fe phase in non-grain-refined and AlTi10-grain-refined alloys.
- The AlTi5B1 grain refinement of the base alloy alters the precipitation sequence of Fe-rich phases. The β-Fe particles are the dominating Fe-rich phase in the microstructure, particularly at higher cooling rates.
- The TiB_2 particles are favourable substrates for nucleation of β-Fe crystals.
- In the considered experimental conditions, the cooling rate has no influence on the precipitation sequence of Fe-rich phases in non-grain-refined and AlTi5B1- or AlTi10-grain-refined alloys.

Acknowledgments

This work was developed within the ERASMUS MUNDUS Project (Silkroute—Strand 1/Lot L09, Project No. 545765). The author would like to acknowledge Raffineria Metalli Capra Spa (Brescia, Italy) for the experimental support to the research and Mr. G. Muneratti (Foseco) for the experimental contribution to this research. Many thanks are also due to Mr. L. Mariani (Media System Lab Srl) and Dr. F. Reinauer (AMETEK EDAX BU) for the support with WDS analysis.

REFERENCES

1. M. Javidani, D. Larouche, X.G. Chen, Assessment of post-eutectic reactions in multicomponent Al-Si foundry alloys containing Cu, Mg, and Fe. Metall. Mater. Trans. A **46A**, 2933–2946 (2015)
2. W. Khalifa, F.H. Samuel, J.E. Gruzleski, Iron intermetallic phases in the Al corner of the Al–Si–Fe system. Metall. Mater. Trans. A **34A**, 807–825 (2003)
3. S. Murali, K.S. Raman, K.S.S. Murthy, Effect of magnesium, iron (impurity) and solidification rates on the fracture-toughness of Al–7Si–0.3Mg casting alloy. Mater. Sci. Eng. A **151**, 1–10 (1992)
4. A. Pennors, A.M. Samuel, F.H. Samuel, H.W. Doty, Precipitation of beta-Al5FeSi iron intermetallic in Al–6% Si–3.5% Cu (319) type alloys: role of Sr and P. AFS Trans. **106**, 251–264 (1998)
5. X.J. Cao, J. Campbell, Morphology of beta-Al5FeSi phase in Al-Si cast alloys. Mater. Trans. **47**, 1303–1312 (2006)
6. G. Timelli, E. Fiorese, Methods to neutralize the effects of iron in Al-Si foundry alloys. Metall. Ital. **102**, 9–23 (2011)
7. L.A. Narayanan, F.H. Samuel, J.E. Gruzleski, Crystallization behavior of iron-containing intermetallic compounds in 319 aluminum-alloy. Metall. Mater. Trans. A **25**, 1761–1773 (1994)
8. W. Khalifa, F.H. Samuel, J.E. Gruzleski, H.W. Doty, S. Valtierra, Nucleation of Fe-intermetallic phases in the Al–Si–Fe alloys. Metall. Mater. Trans. A **36A**, 1017–1032 (2005)
9. C. Puncreobutr, A.B. Phillion, J.L. Fife, P. Rockett, A.P. Horsfield, P.D. Lee, In situ quantification of the nucleation and growth of Fe-rich intermetallics during Al alloy solidification. Acta Mater. **79**, 292–303 (2014)
10. G. Timelli, G. Camicia, S. Ferraro, Effect of grain refinement and cooling rate on the microstructure and mechanical properties of secondary Al–Si–Cu alloys. J. Mater. Eng. Perform. **23**, 611–621 (2014)
11. S. Haro-Rodriguez, R.E. Goytia-Reyes, D.K. Dwivedi, V.H. Baltazar-Hernandez, H. Flores-Zuniga, M.J. Perez-Lopez, On influence of Ti and Sr on microstructure, mechanical properties and quality index of cast eutectic Al–Si–Mg alloy. Mater. Des. **32**, 1865–1871 (2011)
12. A.M. Samuel, F.H. Samuel, H.W. Doty, Observations on the formation of β-Al5FeSi phase in 319 type Al–Si alloys. J. Mater. Sci. **31**, 5529–5539 (1996)
13. D. Casari, M. Merlin, G.L. Garagnani, A comparative study on the effects of three commercial Ti–B-based grain refiners on the impact properties of A356 cast aluminium alloy. J. Mater. Sci. **48**, 4365–4377 (2013)
14. M.H. Mulazimoglu, A. Zaluska, J.E. Gruzleski, F. Paray, Electron microscope study of Al-Fe-Si intermetallics in 6201 aluminum alloy. Metall. Mater. Trans. A **27**, 929–936 (1996)
15. H. Zahedi, M. Emamy, A. Razaghian, M. Mahta, J. Campbell, M. Tiryakioglu, The effect of Fe-rich intermetallics on the Weibull distribution of tensile properties in a cast Al-5 pct Si–3 pct Cu–1 pct Fe–0.3 pct Mg alloy. Metall. Mater. Trans. A **38A**, 659–670 (2007)
16. M.B. Djurdjevic, I. Vicario, G. Huber, Review of thermal analysis applications in aluminium casting plants. Rev. Metall. **50**, e004 (2014)
17. Q. Wang, Y.X. Li, X.C. Li, Grain refinement of Al–7Si alloys and the efficiency assessment by recognition of cooling curves. Metall. Mater. Trans. A **34A**, 1175–1182 (2003)
18. E. Samuel, B. Golbahar, A.M. Samuel, H.W. Doty, S. Valtierra, F.H. Samuel, Effect of grain refiner on the tensile and impact properties of Al–Si–Mg cast alloys. Mater. Des. **56**, 468–479 (2014)
19. C.M. Dinnis, J.A. Taylor, A.K. Dahle, Iron-related porosity in Al–Si–(Cu) foundry alloys. Mater. Sci. Eng. A **425**, 286–296 (2006)
20. Q.G. Wang, D. Apelian, D.A. Lados, Fatigue behavior of A356/357 aluminum cast alloys. Part II—Effect of microstructural constituents. J. Light Met. **1**, 85–97 (2001)
21. S. Seifeddine, S. Johansson, I.L. Svensson, The influence of cooling rate and manganese content on the beta-Al5FeSi phase formation and mechanical properties of Al–Si-based alloys. Mater. Sci. Eng. A **490**, 385–390 (2008)
22. Z. Ma, E. Samuel, A.M.A. Mohamed, A.M. Samuel, F.H. Samuel, H.W. Doty, Influence of aging treatments and alloying additives on the hardness of Al–11Si–2.5Cu–Mg alloys. Mater. Des. **31**, 3791–3803 (2010)
23. K. Liu, X. Cao, X.G. Chen, Effect of Mn, Si, and cooling rate on the formation of iron-rich intermetallics in 206 Al-Cu cast alloys. Metall. Mater. Trans. B **43**, 1231–1240 (2012)
24. A. Hernandez-Rodriguez, M.D.J. Castro-Roman, M. Herrera-Trejo, S. Belmares-Perales, P. Orozco-Gonzalez, Effects of the Fe/Mn weight ratio and cooling rate on the area fractions of alpha-AlFeSi and beta-AlFeSi phases in Al–7.5Si–3.75Cu–0.5Mg–0.55Fe–xMn aluminum alloy. Metalurgija **53**, 314–316 (2014)
25. P. Ashtari, H. Tezuka, T. Sato, Influence of Sr and Mn additions on intermetallic compound morphologies in

Al–Si–Cu–Fe cast alloys. Mater. Trans. **44**, 2611–2616 (2003)
26. R. Chen, Y.-F. Shi, Q.-Y. Xu, B.-C. Liu, Effect of cooling rate on solidification parameters and microstructure of Al–7Si–0.3Mg–0.15Fe alloy. Trans. Nonferr. Met. Soc. China **24**, 1645–1652 (2014)
27. J.Y. Hwang, H.W. Doty, M.J. Kaufman, The effects of Mn additions on the microstructure and mechanical properties of Al–Si–Cu casting alloys. Mater. Sci. Eng. A **488**, 496–504 (2008)
28. J.A. Taylor, G.B. Schaffer, D.H. StJohn, The role of iron in the formation of porosity in Al–Si–Cu-based casting alloys: Part III. A microstructural model. Metall. Mater. Trans. A **30**, 1657–1662 (1999)
29. S. Terzi, J.A. Taylor, Y.H. Cho, L. Salvo, M. Suery, E. Boller, A.K. Dahle, In situ study of nucleation and growth of the irregular alpha-Al/beta-Al5FeSi eutectic by 3-D synchrotron X-ray microtomography. Acta Mater. **58**, 5370–5380 (2010)
30. Y.H. Cho, H.C. Lee, K.H. Oh, A.K. Dahle, Effect of strontium and phosphorus on eutectic Al–Si nucleation and formation of β-Al5FeSi in hypoeutectic Al–Si foundry alloys. Metall. Mater. Trans. A **39**, 2435–2448 (2008)
31. L. Backerud, G. Chai, J. Tamminen, *Solidification Characteristics of Aluminum Alloys*, 9th edn. (AFS/ScanAluminium, Oslo, 1990)
32. S.K. Tang, T. Sritharan, Morphology of beta-AlFeSi intermetallic in Al-7Si alloy castings. Mater. Sci. Technol. **14**, 738–742 (1998)
33. B. Closset, F. Paray, J. Gruzleski, H. Mulazimoglu, Microstructures and properties of strontium treated aluminum electrical conductor alloys. Light Met. **1996**, 737–744 (1996)
34. C.M. Allen, K.A.Q. O'Reilly, B. Cantor, P.V. Evans, Intermetallic phase selection in 1XXX Al alloys. Prog. Mater Sci. **43**, 89–170 (1998)
35. G.K. Sigworth, T.A. Kuhn, Grain refinement of aluminum casting alloys. Int. J. Metalcast. **1**, 31–40 (2007)
36. G. Sha, K. O'Reilly, B. Cantor, R. Hamerton, J. Worth, Effect of grain refiner on intermetallic phase formation in directional solidification of 6xxx series wrought al alloys. Mater. Sci. Forum **331**, 215–222 (2000)
37. T. Smith, K. O'Reilly, S. Kumar, I. Stone, Influence of grain-refiner addition on the morphology of fe-bearing intermetallics in a semi-solid processed Al–Mg–Si alloy. Metall. Mater. Trans. A **44**, 4866–4871 (2013)
38. B. Suarez-Pena, J. Asensio-Lozano, Influence of Sr modification and Ti grain refinement on the morphology of Fe-rich precipitates in eutectic Al–Si die cast alloys. Scr. Mater. **54**, 1543–1548 (2006)

SUPPLEMENT 3

Comparison of the effects of Al-5B and Al-5Ti-1B grain refiners on the formation of Fe-rich phases in secondary Al-7Si-3Cu-0.3Mg alloys

J. Rakhmonov, G. Corradin, G. Timelli and H. Liu, Proceedings of the 6th Decennial International Conference on Solidification Processing, Old Windsor, 2017, 162-165

Comparison of the Effects of Al-5B and Al-5Ti-1B Grain Refiners on the Formation of Fe-rich Phases in Secondary Al-7Si-3Cu-0.3Mg Alloys

J. Rakhmonov[1] G. Corradin[1] G. Timelli[1] and H. Liu[2]

[1] University of Padua, Dep. of Management and Engineering, Str. San Nicola 3, I-36100 Vicenza, Italy
[2] University of Sydney, Australian centre for microscopy and microanalysis, Sydney, Australia

Abstract

Effect of adding varying levels of Al-5B (400 and 800 ppm B) and Al-5Ti-1B (40 and 80 ppm B) grain refiners on the formation of Fe-rich intermetallics in secondary Al-7Si-3Cu-0.3Mg alloy has been investigated using metallographic analysis technique. While non-refined alloy exhibits α-$Al_{15}(FeMn)_3Si_2$ as a sole Fe-bearing phase in the microstructure, both α-$Al_{15}(FeMn)_3Si_2$ and β-Al_5FeSi tend to form in an alloy refined with Al-5Ti-1B, independently of the cooling rate. Both higher cooling rate and higher Al-5Ti-1B addition levels promote β-Al_5FeSi formation over α-$Al_{15}(FeMn)_3Si_2$ in alloy refined with Al-5Ti-1B. In contrast, grain refinement with Al-5B shows no influence on the precipitation sequence of Fe-rich phases, independently of cooling rate and grain refiner addition levels. Changes occurring in the crystallization of Fe-rich phases is explained in terms of phase diagram relationship and the nucleation kinetics of Fe-rich phases (β-Al_5FeSi and α-$Al_{15}(FeMn)_3Si_2$).

Keywords: Al-Si Alloys, Fe-rich Phases, Grain Refinement

1. Introduction

Iron is generally considered the most harmful impurity in Al-Si alloys; due to its low solubility in α-Al matrix, the precipitation of Fe-rich phases, such as platelet-like β-Al_5FeSi or Chinese script-like α-$Al_{15}(Fe,Mn)_3Si_2$, form during solidification. Since β-Fe is more deleterious than α-Fe, different techniques have been developed to promote the precipitation of the latter phase; among them, Mn addition in the level of around half of Fe is the most common method [1].

Recently, it has been demonstrated by present authors how Mn can completely avoid the formation of β-Fe in non-grain-refined secondary Al-7Si-3Cu-0.3Mg alloys; however, after grain refinement treatment with Al-5Ti-1B, both α-Fe and β-Fe appear in the microstructure. This behaviour is thought to be attributable to the role of TiB_2 particles in easily nucleating β-Fe at lower undercooling [1-2]. Further investigations are necessary to determine the effect of adding lower levels of Al-5Ti-1B on the formation of Fe-rich phases and, thus, gain further understanding about the role of grain refinement in the nucleation and growth of Fe-rich compounds.

Chemical grain refinement via melt inoculation with Al-5Ti-1B master alloys is a common practice in foundries to improve the material's performance. As the grain refining performance of Al-5Ti-1B is negatively affected by higher Si concentrations in Al-Si alloys, research still continues to develop new types of grain refiners. Al-B can be a substitute for Al-Ti-B system because AlB_2 particles have been found to be highly efficient in grain refinement of Al-Si alloys with higher Si levels [3]. It can be of interest to compare the performance of two different grain refiners (Al-Ti-B and Al-B) in terms of reactions involving Fe-rich intermetallics.

This study is aimed to investigate the effects of adding different levels of Al-B and Al-Ti-B grain refiners on the formation of Fe-rich intermetallics in secondary Al-7Si-3Cu-0.3Mg alloy.

2. Experimental procedure

In this study, a secondary Al-7Si-3Cu-0.3Mg-0.44Fe-0.24Mn-0.7Zn-0.02Ti (equivalent to the US designation A320) was used as base alloy. The material also contained other elements such as Zr, V, Ca, Bi, P and Sb in amounts less than 0.01 wt.% as impurities. Al-5Ti-1B and Al-5B (in wt. %) master alloys were used to grain refine the material.

About 3 kg charge of base alloy was melted in a SiC crucible in an electric furnace at 750°C. After complete dissolution, the melt was stirred and surface skimmed, followed by a 10 min of holding. The molten metal was then cast into two different boron nitride-coated cylindrical steel moulds, one with inner diameter of 50 mm

and height of 60 mm, the other with inner diameter of 20 mm and height of 100 mm, both preheated at 550°C. The remaining liquid was grain refined by pre-calculated amount of Al-5Ti-1B master alloy to produce alloys with increased B (40 and 80 ppm) and Ti (400 and 600 ppm) levels. Similarly, a separately-melted 3 kg of base alloy was treated with pre-calculated amount of Al-5B master alloy to produce alloys with increased B levels (400 and 800 ppm). The molten metal was stirred 5 min after metal treatment and the holding time between stirring and pouring stages was 20 min. Specimens for chemical analysis were poured prior to each set of experiments and analysed by optical emission spectrometry. While the measured chemical composition in alloys refined with Al-5Ti-1B was similar to the target values, the measured B, Ti, V and Zr levels in alloys refined with Al-5B were lower than the target concentrations due to the formation and then removal of transition metal diborides (TiB_2, ZrB_2 and VB_2) settled at the bottom of the crucible. Average values of secondary dendrite arm spacing (SDAS) in the specimens poured in large- and small-diameter moulds were about 60 µm and 20 µm, respectively.

Samples were sectioned at 30 and 25 mm from the bottom surfaces of large- and small-diameter castings, respectively, mounted ground and polished using the standard procedure. Optical microscope (OM), scanning electron microscope (SEM) equipped with energy-dispersive (EDS) and wavelength-dispersive spectrometers (WDS) were used for microstructural investigations. Several optical micrographs, representing a total area of 6 mm^2, were captured from each specimen to investigate the area fraction of β-Fe particles in the microstructure.

To quantitatively calculate the grain size, the polished specimens obtained from large-diameter castings were etched in concentrated Keller's reagent (7.5 ml HNO_3, 2.5 ml HF, 5 ml HCl and 35 ml H_2O). The grain size was measured using the intercept method.

3. Results and discussion

3.1 Grain refinement with Al-5Ti-1B master alloy

Microstructural characterization confirms the refined grain structure obtained after the addition of grain refiners; greater Ti and B levels induce better grain refinement level (Table 1).

It is also well-known that the majority of TiB_2 particles added into the melt do not contribute to the nucleation of α-Al grains, and, as a result, these particles can be pushed to interdendritic regions, where they can be active to nucleate certain eutectic phases.

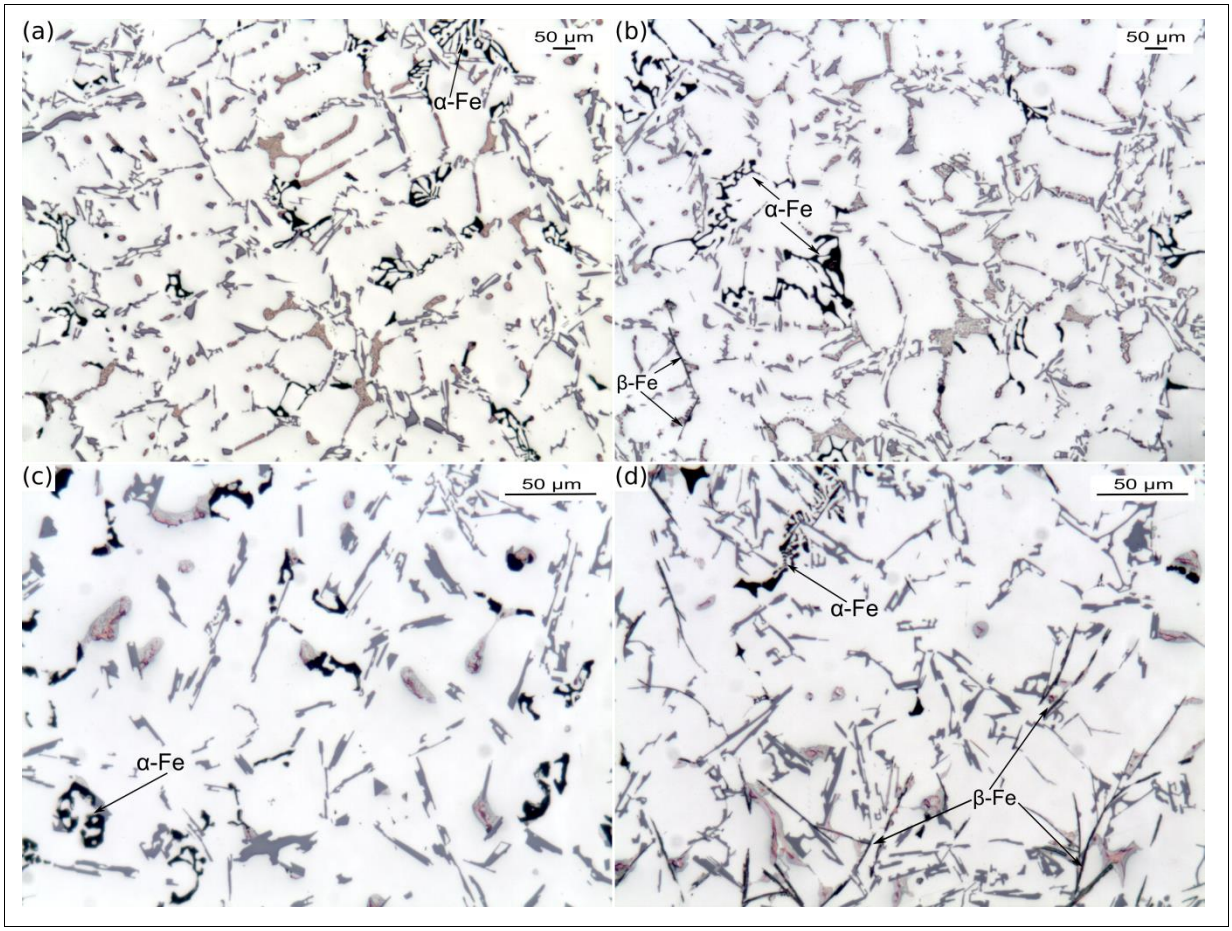

Figure 1: Typical microstructures representing (a,c) the base alloy and (b,d) the alloy refined with Al-5Ti-1B (80 ppm B). The micrographs correspond to specimens produced with (a,b) large-diameter mould (60 µm SDAS) and (c,d) small-diameter mould (20 µm SDAS). The samples were etched to highlight Fe-rich compounds.

Table 1: Average grain size and corresponding standard deviation (in mm) measured in base alloy (0 ppm B) and after metal treatment with Al-5Ti-1B (40 and 80 ppm B) and Al-5B (400 and 800 ppm).

B content (ppm)				
0	40	80	400	800
2.1 (0.8)	0.6 (0.2)	0.44 (0.1)	0.8 (0.2)	0.41 (0.1)

Table 2: Average area fraction (%) of β-Fe phase observed in the base alloy (0 ppm B) and after grain refinement with Al-5Ti-1B (40 and 80 ppm B) and Al-5B (400 and 800 ppm), cast in large-diameter (60 µm SDAS) and small-diameter (20 µm SDAS) moulds.

SDAS	B content (ppm)				
	0	40	80	400	800
60	-	0.15	0.2	-	-
20	-	0.31	0.47	-	-

- Not revealed from OM analysis

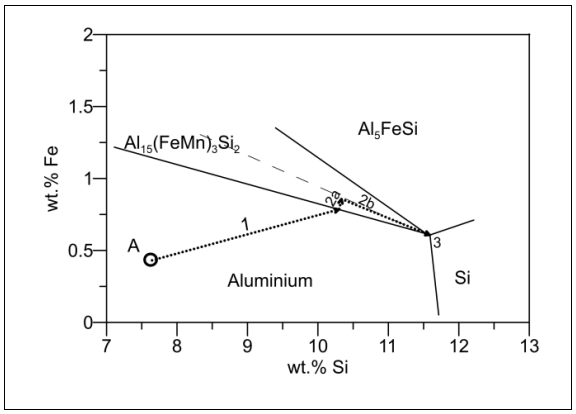

Figure 2: Simplified Al-Si-Fe-Mn phase diagram at 0.2 wt.% Mn level [4]. The composition of the base material investigated in this study is indicated by the point A.

Table 3: Average EDS results of α-Fe and β-Fe phases (at.%).

Alloy	Al	Si	Fe	Mn	Cr	Cu
α-$Al_{15}(Fe,Mn)_3Si_2$	73	11	11	2	0.14	bal.
β-Al_5FeSi	70	17	10	1	-	bal.

In a previous research [1], it has been demonstrated how the addition of Al-5Ti-1B grain refiner (170 ppm B) favours the precipitation of β-Fe compounds. The present investigations also confirm that the precipitation sequence of Fe-rich compounds varies after Al-5Ti-1B addition (Figure 1) and this occurs independently of the grain refiner levels. While α-Fe appears as a sole Fe-rich phase in the base alloy regardless of the cooling rate, both α-Fe and β-Fe tend to form in the alloy refined with Al-5Ti-1B independently of the addition levels and the cooling rate; however, both high cooling rate and Al-5Ti-1B grain refinement tend to promote β-Fe formation at the expense of α-Fe (Table 2).

The simplified Al-Si-Fe-Mn phase diagram at constant Mn level (0.2 wt.%) and the solidification path depicted on the Al-rich corner (Figure 2) show how the occurrence of both α-Fe and β-Fe reactions can be expected in the present study. The fact that the β-Fe involving reaction remains unfavourable during solidification of the base material can be due to a greater undercooling needed for the nucleation of β-Fe; however, nucleation of α-Fe seems to be more favourable on certain substrate in the undercooled melt, thus avoiding the precipitation of β-Fe in the microstructure.

In contrast, solidification of the alloy refined with Al-5Ti-1B proceeds by involving both α-Fe and β-Fe reactions. This suggests the melt contains certain particles which facilitate nucleation of β-Fe at low undercooling. The WDS investigations revealed the presence of TiB_2 particles adjacent to β-Fe compounds (Figure 3); thus, the TiB_2 particles are thought to be directly responsible for the formation of β-Fe. TiB_2 particles appear to act as an effective nucleation site for β-Fe phase [5].

Higher cooling rate tends to further promote β-Fe formation in the material refined with Al-5Ti-1B (Figure 1 and Table 1); β-Fe needles become the dominant Fe-rich phase largely replacing α-Fe in the microstructure. Greater undercooling provided by higher cooling rates causes the solidification to proceed through the line 2a quickly (see Figure 2), involving only a small amount of Fe in the crystallization of α-Fe phase. As a result, the remaining Fe is available for the formation of β-Fe, occurring through the line 2b, where the precipitation of β-Fe compounds occur more favourably due to the presence of potent substrates, TiB_2, for their nucleation.

The chemical compositions of α-Fe and β-Fe phases, analysed by EDS, are presented in Table 3; it is evident that Mn has also a strong solubility in β-Fe phase, indicating that the local chemistry is favourable for the occurrence of both α-Fe and β-Fe reactions.

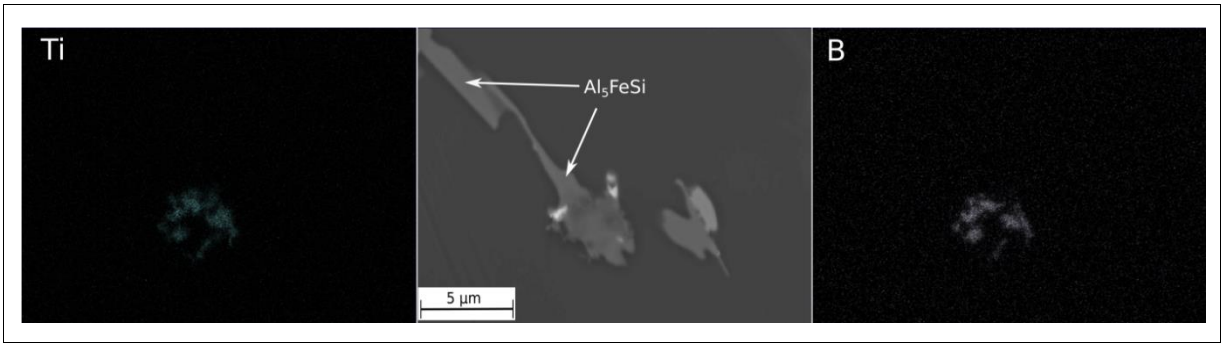

Figure 3: Backscattered electron image of β-Al_5FeSi with corresponding WDS composition maps, showing the distributions of Ti and B.

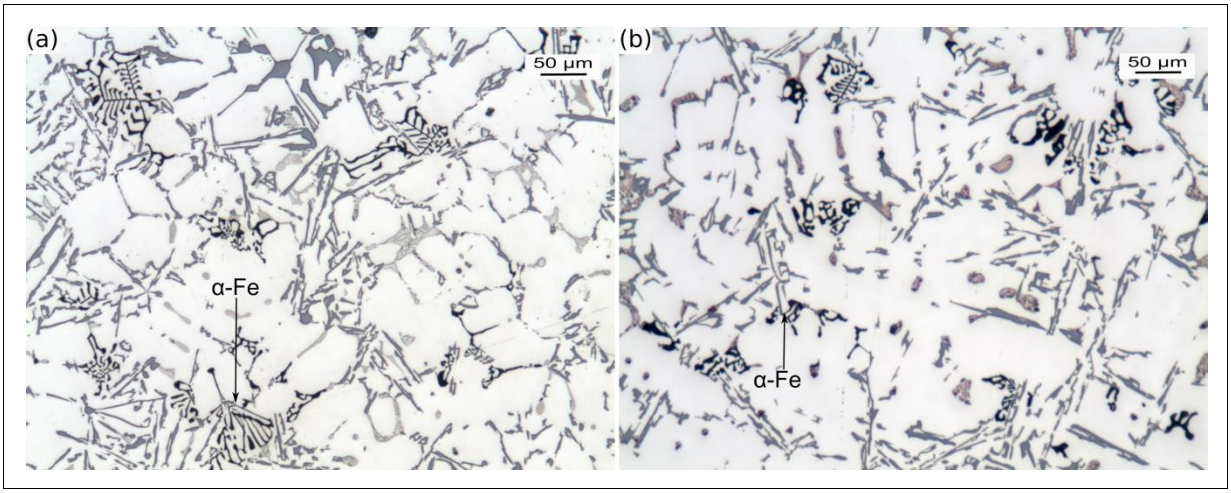

Figure 4: Typical microstructures of alloy refined with Al-5B (800 ppm B), and cast in (a) large diameter mould (60 µm SDAS) and (b) small diameter mould (20 µm SDAS). The samples were etched to highlight Fe-rich compounds.

3.2 Grain refinement with Al-5B

It is clear from Figure 4 how Al-5B grain refiner (800 ppm B) is quite efficient in refining the grain structure of base alloy and it is comparable with Al-5Ti-1B grain refiner. However, it has to be noted that part of B react with Ti, Zr and V, which are present in the base alloy as trace elements (impurities), to form transition metal diborides (TiB_2, ZrB_2 and VB_2) directly in the melt. Therefore, the required level of Al-B master alloy should be in excess of that needed for the formation of TiB_2, ZrB_2 and VB_2 in order to achieve effective grain refinement. In this study, 400 ppm of B added seems to be mainly involved in the formation of transition metal diborides and lesser amount of B remains available for the formation of AlB_2 during solidification, leading to a moderate grain refinement (see Table 1). However, the B content in the level of 800 ppm seems to exert effective refinement of the grain structure that occurs in addition to a complete removal of transition metal diborides from the melt via settlement.

Figure 4 shows typical microstructures obtained from the alloy refined with Al-5B and processed at two different cooling conditions. It is evident that α-Fe appears to be again as a sole Fe-rich phase in the microstructure regardless of the cooling rate. This implies that the AlB_2 particles appear to be inactive to nucleate β-Fe, even though AlB_2 is isomorphous with TiB_2. This can be due to either larger lattice mismatch between AlB_2 and β-Fe or the formation of an Al overlay or else on the AlB_2 compounds, thus deactivating the nucleation of β-Fe. The formation of SiB_6 [6] and Al [7] layers on AlB_2 have been reported in the literature to explain the mechanisms responsible for the grain refinement of Al-Si alloys with Al-B master alloys.

4. Conclusions

The influence of Al-5B and Al-5Ti-1B addition on the precipitation of Fe-rich intermetallics in secondary Al-7Si-3Cu-Mg alloy was investigated. The following conclusions can be drawn from this work.

1. Grain refinement with Al-5Ti-1B alters the precipitation sequence of Fe-rich phases by promoting the crystallization of β-Fe in the microstructure; both high cooling rates and great addition of grain refiner tend to increase the volume fraction of β-Fe at the expense of α-Fe. TiB_2 particles appear to be directly responsible for β-Fe formation due to their action to heterogeneously nucleate β-Fe.
2. Grain refinement with Al-5B shows no influence on the precipitation sequence of Fe-rich phases. Although AlB_2 and TiB_2 are isomorphous and possess similar lattice parameters, AlB_2 appears not to be a potent nucleation site for β-F phase, which can be due to the existence of Al-AlB_2 eutectic reaction during the early stages of solidification.

Acknowledgements

The author would like to acknowledge Mr. R. Zambelli (Raffmetal Spa, Italy) and Mr. G. Muneratti (Foseco, Italy) for the experimental support to the research.

References

1. J. Rakhmonov et al. *Int. J Metalcast.*, 2016, 1.
2. J. Rakhmonov et al., *Metall. Mater. Trans. A*, 2016, **47**: 5510.
3. Y. Birol: *Mater. Sci. Technol.*, 2012, **28**: 363.
4. L. Backerud et al., *Solidification Characteristics of Aluminum Alloys*. AFS/ScanAluminium, Oslo, 1990.
5. G. Sha et al., *Mater. Sci. Forum*, 2000, **331**: 253.
6. Z. Chen et al., *Acta Mater.*, 2016, **120**: 168.
   Y. Liu et al., *Trans. Nonfer. Met. Soc. China*, 2011, **21**: 1435

SUPPLEMENT 4

Characterization of the solidification path and microstructure of secondary Al-7Si-3Cu-0.3Mg alloy with Zr, V and Ni additions

J. Rakhmonov, G. Timelli and F. Bonollo, Materials characterization, 2017 (128), 100-108

Materials Characterization 128 (2017) 100–108

Contents lists available at ScienceDirect

Materials Characterization

journal homepage: www.elsevier.com/locate/matchar

Characterization of the solidification path and microstructure of secondary Al-7Si-3Cu-0.3Mg alloy with Zr, V and Ni additions

Jovid Rakhmonov*, Giulio Timelli, Franco Bonollo

University of Padova, Department of Management and Engineering, Stradella S. Nicola, 3 I-36100 Vicenza, Italy

ARTICLE INFO

Keywords:
Aluminium alloys
Transition metals
Microstructure
Solidification
Peritectic reactions
Thermal analysis

ABSTRACT

The effect of individual and combined Zr, V and Ni additions on solidification path and microstructural evolution of secondary Al-7Si-3Cu-0.3Mg alloy were investigated using microscopy and thermal analysis techniques. The results show how the Zr addition caused remarkable grain refinement due to the precipitation of primary pro-peritectic Al_3Zr particles that lead to a peritectic reaction to yield α-Al during solidification; however, the peritectic transformation was incomplete due to a limited solid-state diffusion. Moreover, with Zr addition, few numbers of flaky $(AlSi)_3(ZrTi)$ compounds appeared in the microstructure. Vanadium addition showed also grain refinement level similar to that of Zr-added alloy. However, the role of V cannot be explained by the precipitation of primary pro-peritectic particles that would provide potent nucleation sites; instead, vanadium addition substantially increases the degree of constitutional undercooling, thus activating certain particles to more easily nucleate α-Al. Excess vanadium were mainly bound to pro-eutectic and polyhedral-shaped $(AlSi)_2(VMnTi)$ compounds. Combined Zr and V addition exerted better grain refinement level than the individual Zr or V addition; this occurred due to both increased the population of Al_3Zr phase particles as a result of its enrichment with V, and enhanced the degree of constitutional undercooling. Nickel addition exerted no apparent influence on the formation of both α-Al and eutectic Si; however, significant changes occurred in the sequence of post-eutectic reactions: the script-like Al_6Cu_3Ni and flaky-like $Al_9(FeCu)Ni$ phases formed in addition to the Al_2Cu and $Al_5Si_6Cu_2Mg_8$ particles; this led to a substantial reduction in the alloy's freezing range. The findings of this study can benefit and contribute to developing a new Al-Si based foundry alloys intended for high-temperature applications.

1. Introduction

Aluminium-Silicon based foundry alloys are widely used in the automotive industry, particularly for pistons, cylinder blocks and -heads, due to their low thermal-expansion coefficient, high wear resistance, good corrosion resistance, and improved mechanical performance [1,2]. A remarkable improvement in the mechanical properties of Al-Si alloys can be achieved by alloying with Cu and Mg via precipitation strengthening mechanism [3]. However, these Cu- and Mg-rich precipitates can only be effective for strength and creep resistance at temperatures below 200 °C [4]. At higher temperatures, dissolution and/or coarsening of Cu- and Mg-rich strengthening particles can occur [5], hence, inducing an adverse effect on the mechanical performance. Progress in fuel efficiency and performance of internal combustion engines has led to an increase in the operating temperature and pressure of the engines, thus indicating the need for developing new creep resistant Al alloys [6]. One approach might be to enable the formation of thermally stable and coarsening resistant precipitates inside the α-Al grains. Some transition metals (TM), such as Mo, Zr, V and Sc, can yield a remarkable effect on retaining the strength of Al alloys at higher operating temperatures due to their slow diffusivity in α-Al, low solid solubility into the α-Al matrix with the possibility to form trialuminide phases; these compounds possess low interfacial free energy with α-Al [7,8].

The strengthening effect of TM in Al-Si alloys is, however, limited primarily due to their quite low solid solubility in α-Al, which leads to a low fraction of TM-rich precipitates after heat treatment. Furthermore, TM-rich particles, such as Al_3Zr, tend to mainly concentrate at the centre of α-Al grains, i.e. the TM-rich precipitates tend to distribute unevenly throughout the microstructure formed during non-equilibrium solidification because, k_0, which is the equilibrium partitioning coefficient for solidification, is greater than unity for some binary Al-TM systems, such as Al-Zr. Alloying the binary precipitates (typically trialuminides) with appropriate elements to yield ternary or quaternary compounds can result in larger volume fraction and smaller average diameter of the TM-rich precipitates, as well as the formation of TM-

* Corresponding author.
E-mail address: rakhmonov@gest.unipd.it (J. Rakhmonov).

http://dx.doi.org/10.1016/j.matchar.2017.03.039
Received 24 October 2016; Received in revised form 7 December 2016; Accepted 21 March 2017
Available online 24 March 2017

rich compounds with more desirable morphology [7,9,10].

Moreover, the level of TM in Al-Si alloys should be strictly controlled, since their excess amount causes the precipitation of primary TM-rich compounds during solidification. Although these primary intermetallics appearing at the grain boundaries can be beneficial to high-temperature mechanical performance [5,11], their increased fraction can be also deleterious due to their undesired morphology [12,13], and their action in depleting TM that would be expected to remain inside the α-Al matrix [8,14]. Further, a greater content of peritectic-forming elements can cause difficulties during casting process, as the alloys then require higher melting temperature [7].

The addition of appropriated levels of TM in Al-based alloys is also necessary to contribute to the grain refinement of the alloy, which is normally carried out by adding AlTiB-based grain refiners. However, the combined presence of peritectic-forming elements (Zr and V) and boron-containing inoculants can result in their mutual interactions; as a consequence, neither effective grain refinement nor the formation of favourable Zr- and V-rich particles can occur [15]. Although peritectic-forming elements can induce grain refinement of the alloy [16], further investigations in this regard can contribute on maximizing their efficiency.

In this study, an attempt is made to investigate the effect of Ni, V and Zr additions on the solidification path and microstructural evolution of secondary Al-7Si-3Cu-0.3Mg alloy, one of most used alloys in the automotive industry for the engine production [17]. The aim of this work is to compare the effect of combined and individual Ni, V and Zr additions on macro- and microstructural features, such as the grain refinement level and the characteristics (size, morphology, chemical composition and crystal structure) of phases forming during solidification. The findings of this study can allow gaining further understanding of the role of TM-involved systems in the possibility of developing a new generation of heat-resistant Al-Si based foundry alloys.

2. Experimental Details

2.1. Materials

Secondary Al-7Si-3Cu-0.3Mg alloy (equivalent to the US designation A320) was supplied by Raffineria Metalli Capra and used as the baseline material. The chemical composition of the alloy was measured by optical emission spectrometry on separately poured samples and presented in Table 1. Other elements, such as Bi, Sb, P, Ca, B and Sn, are present in amounts less than 0.01 wt% and these elements are not included in Table 1. The base material was then alloyed with Al-10V, Al-5Zr and Al-25Ni (in wt%) waffle-shaped master alloys, when necessary, and the concentration of Ni, V and Zr, shown in Table 2 were obtained. Chemical composition analyses were performed with optical emission spectrometry.

A SiC crucible was used to melt about 3 kg material inside a resistance-heated furnace at 760 °C. After homogenization at 760 °C for at least 30 min, the melt was then stirred and the surface skimmed to remove the dross. The molten metal was poured into a boron nitride-coated cylindrical steel cup (outer diameter 45 mm, height 60 mm, and a uniform wall thickness of 3 mm), preheated at 700 °C.

2.2. Thermal Analysis

The two-thermocouples method and differential scanning calorimetry (DSC) were used for thermal analysis experiments.

For the two-thermocouples method, K-type thermocouples (ø1 mm), fixed at the lid of the cup and covered with tightly fitting steel tubes, were inserted into the melt, one in the centre and one adjacent to the wall, 30 mm below the surface of the specimen. The temperature and time were collected by means of a data acquisition system with a sampling rate of $0.25\ s^{-1}$, analog-to-digital converter accuracy of 0.1 °C, and connected to a personal computer. The system was allowed to cool in air and gave a cooling rate of 0.17 ± 0.1 °C/s in the solidification interval. A minimum of two thermal analysis runs was made for each experimental alloy. The thermocouples were calibrated against the melting point of pure aluminium, assuming a melting point of 933 K (660.0 °C). For each set of temperature/time relations in the centre of the sample, the cooling curves and the corresponding derivative curves were plotted to determine the characteristic temperatures related to the formation of phases based on the first derivative cooling curve approach [18]. The definition method and the description of thermal analysis parameters used in the present study can be found elsewhere [15].

For DSC analyses, cylindrical-shaped discs weighing about 35 mg were drawn from the specimens used for chemical composition analysis. The DSC analysis was carried out at a scan rate of 5 °C/min for both heating and cooling conditions. A detailed explanation of DSC operation can be found in Reference [19].

2.3. Metallographic Characterization

Samples for macro- and microstructural investigations were sectioned transversely, near the tip of the thermocouple in centre region. The samples then were mounted, ground and polished using the standard procedure. Optical microscope (OM), scanning electron microscope (SEM) coupled with energy-dispersive spectrometer (EDS) and electron backscattered diffraction (EBSD) unit were used to characterize the type and morphology of the phases. In order to reveal grain boundaries, polished specimens were etched in concentrated Keller's reagent (7.5 ml HNO_3, 2.5 ml HF, 5 ml HCl and 35 ml H_2O).

3. Results

3.1. Thermal Analysis

The cooling curves and the corresponding first derivatives obtained from thermal analysis of Al-7Si-3Cu-0.3Mg and Al-7Si-3Cu-0.3Mg + Ni,V,Zr are shown as examples in Fig. 1a. The crystallisation region of the main phases, such as α-Al, Al-Si eutectic and Cu-rich compounds, can be easily observed [20]. The distinctive features between the cooling curves are the formation temperatures of the α-Al phase and the Cu-rich compounds. The lack of peaks related to the formation of other phases, such as Ni-, V- and Zr-bearing particles can be explained by a limited fraction of these phases precipitated in the specimen. Table 3 presents a summary of the characteristic temperatures that were determined by analyzing the cooling curves.

In addition to traditional thermal analysis, DSC of all experimental alloys was carried out and the cooling and heating curves of two different alloys are presented as examples in Fig. 1b. The cooling and heating DSC curves of the base material (Fig. 1b) exhibit the same phase reactions detected by means of thermal analysis, whereas the DSC investigations of the Ni, V and Zr-containing alloy (Fig. 1b) reveals an additional peak evolving due to post-eutectic reaction, and hence, this

Table 1
The chemical composition of as-received Al-7Si-3Cu-0.3 Mg alloy (wt%).

Alloy	Si	Fe	Cu	Mn	Mg	Zn	Cr	Ni	Ti	Pb	Sr	V	Zr	Al
Al-7Si-3Cu-0.3Mg	7.68	0.44	3.02	0.23	0.31	0.78	0.04	0.02	0.01	0.03	0.0001	0.01	0.01	Bal.

Table 2
The achieved Ni, V and Zr contents in the alloys prepared for this study (wt%).

Elem.	Experimental alloys							
	A (Al-7Si-3Cu-0.3Mg)	A + V	A + Ni,V	A + Zr	A + Zr,V	A + Ni	A + Ni,Zr	A + Ni,V,Zr
Ni			0.25			0.25	0.25	0.25
V		0.25	0.25		0.25			0.25
Zr				0.12	0.12		0.12	0.12

peak is identified to be Ni-rich intermetallics [21]. This behaviour was observed in all Ni-containing alloys.

Fig. 2 compares the cooling curves obtained from different experimental alloys in the region of the α-Al formation. The Ni addition to the base alloy has no apparent influence on the formation temperature of α-Al; contrary, individual Zr or V addition tends to move the α-Al formation towards higher temperatures, with even stronger influence arising after combined Zr and V addition.

Nickel seems to largely affect the sequence of post-eutectic reactions. The Ni-rich intermetallics precipitating prior to Cu-rich phases can be responsible for the increase in the nucleation temperature of Cu-bearing compounds, as well as the solidus temperature, which also indicates the end of the growth of Cu-rich phases (Table 3). In the case of the alloys containing only Zr and/or V, the reaction which is really affected by the compositional variation is the nucleation of Cu-rich phases, whereas the solidus temperature remains largely unaffected (Table 3). This can be due to V- and/or Zr-rich particles affecting the nucleation kinetics of the Cu-rich phases; however, a limited number of Zr- and V-rich particles could be insufficient to nucleate all Cu-rich particles.

Varying the alloying additions exerted no demonstrable influence on the formation temperature of the Al-Si eutectic, as revealed by both thermal analysis techniques. This finding implies that the nuclei population remained unchanged regardless of the precipitation of Zr- and V-rich phases prior to Si nucleation, i.e. there are no competition between Zr- or V-rich particles and eutectic Si for a common nucleation agent. This result indicates also how the presence of constitutionally undercooled zone ahead of the eutectic interface after the Ni addition produces no evident changes in the formation temperature of Al-Si eutectic. This seems to be consistent with Reference [22], where it has been reported how the addition of Cu, Ni and Mg has no apparent influence on the nucleation frequency of unmodified Al-Si eutectic.

3.2. General Macrostructure

The grain structure of four different alloys prepared for this study are shown in Fig. 3, where it can be seen how the size of α-Al grains appears to be significantly influenced by the compositional variations. The equiaxed growth mode of α-Al grains seems to be achievable in all cases. Nickel exerts no apparent influence on the size and morphology of α-Al grains, whereas the addition of both V and Zr tends to further decrease the grain structure. The mutual V and Zr additions appear to be more effective in the grain refinement if compared to the impact of individual V or Zr additions.

3.3. Microstructure and Phase Identification

3.3.1. General Microstructure

The typical microstructures of Al-7Si-3Cu-0.3Mg and Al-7Si-3Cu-0.3Mg + Zr,V,Ni alloys are displayed in Fig. 4. The microstructure of the base alloy exhibits α-Al matrix, Al-Si eutectic, Al_2Cu, $Al_5Si_6Cu_2Mg_8$, $Al_{15}(FeMn)_3Si_2$ phases (Fig. 4a); in addition, small and rare $Al_8Mg_3FeSi_6$ and Ca-, Bi-, Pb-rich particles are observed in the microstructure at higher magnifications. The introduction of V, Zr and Ni to Al-7Si-3Cu-0.3Mg alloy resulted in the formation of respective V-, Zr- and Ni-rich intermetallics in addition to the phases observed in the base material (Fig. 4b). The effects of V, Ni and Zr additions on the microstructural evolution of Al-7Si-3Cu-0.3Mg alloy are elaborated in detail in the next sections.

The secondary dendrite arm spacing (SDAS) ranged around 60 μm, remaining almost unaffected by the compositional variations; it is well-known how the evolution of SDAS is highly dependent on the cooling rate, rather than the small variations in solute amount.

3.3.2. Zirconium Addition

Zirconium, added to the base material, interacts with Si, Ti and Al at an earlier stage of solidification, causing the precipitation of plate-like or flaky AlSiZrTi compounds (Fig. 5), which are referred as (Al-

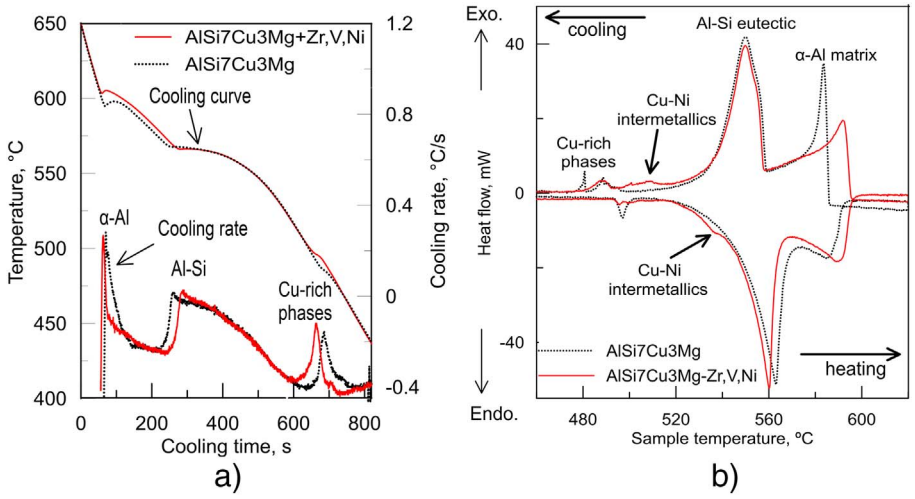

Fig. 1. (a) Cooling curves and corresponding first derivatives obtained from the thermal analysis of Al-7Si-3Cu-0.3Mg alloy before and after 0.25% Ni, 0.25% V and 0.12% Zr additions; (b) heating and cooling DSC curves obtained from the same alloys.

Table 3
Characteristic temperatures from traditional thermal analysis of experimental alloys in (°C).

Alloys	$T_{nuc,\ Al}$	$T_{min,\ Al}$	$T_{rec,\ Al}$	$T_{nuc,\ Si}$	$T_{min,\ Si}$	$T_{growth,\ Si}$	$T_{nuc,\ Al\text{-}Cu}$	$T_{solidus}$
A (Al-7Si-3Cu-0.3 Mg)	600.12	595	2.9	573.12	567.61	567.67	497.2	459.26
A + Ni	601.35	594.42	3.08	572	566.35	566.32	504.5	473.5
A + V	606.3	599	2.2	573.4	566.45	566.65	499.5	455
A + Ni, V	606.6	599.13	2.07	573.77	566	566.3	507.41	476.12
A + Zr	605.04	598.45	1.95	573.34	567.06	567	498.7	459
A + Zr, Ni	606.3	599.4	1.9	572.9	566.7	566.63	503.54	472.64
A + V, Zr	609.2	603.12	1.78	573.1	566.28	566.31	500	457.13
A + Ni, Zr, V	609.6	603.4	1.74	572.12	566.1	566.23	505	474.52

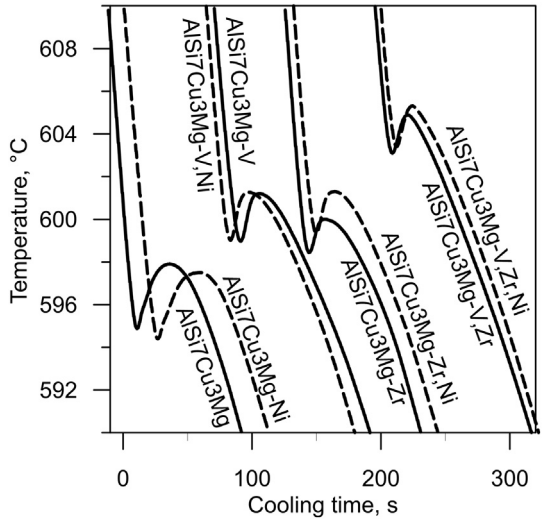

Fig. 2. Comparison of the cooling curves in the formation region of α-Al phase from all the experimental alloys. Time-scale in the horizontal axis is adjusted for easy observation.

$Si)_3$(TiVZr) phase in the literature [23]; however, the solid solubility of V in AlSiZrTi particles appears to be limited in the present investigations, reaching up to 0.5 at.% in the Al-7Si-3Cu-0.3Mg + Zr,V or Al-7Si-3Cu-0.3Mg + Zr,V,Ni alloys.

It has to be noted how the $(AlSi)_3$(TiVZr) particles rarely appeared in the microstructure and they were in a size range of 15–70 μm. In addition, these particles tended to act as heterogeneous nucleation sites for the precipitation of Cu- and Fe-rich phases (Fig. 6), shifting the nucleation temperature of Cu-rich particles towards higher temperatures by ~3 °C (see Alloys A (Al-7Si-3Cu-0.3Mg) and A + Zr in Table 3).

3.3.3. Vanadium Addition

The V addition to Al-7Si-3Cu-0.3Mg alloy favoured the crystallisation of polyhedral-shaped V-rich phase, $(AlSi)_2$(VTiMn), in the microstructure, with a size of ~15 μm. The phase was indexed well with hexagonal $CrSi_2$ (Fig. 7), which is structurally isomorphous with the Si_2V phase [24]. Therefore, it is proposed that the formation of $(AlSi)_2$(VTiMn) occurs on the basis of Si_2V phase. The presence of Al in this phase can be due to the similarity in the atomic radius of Si and Al, which can substitute each other [25]. Similar behaviour can be related to Cr, Mn and Fe elements, all of which are more likely accumulating into Si_2V by substituting V. Zirconium shows no solubility in this phase, while it is evident from Fig. 8 how some part of V can be bound to $Al_{15}(FeMn)_3Si_2$ phase [26,27].

As stated earlier, the nucleation temperature of Al_2Cu increases after V addition (see Alloys Al-7Si-3Cu-0.3Mg and Al-7Si-3Cu-0.3Mg + V in Table 3); however, this seems not to be the result of $(AlSi)_2$(VTiMn) phase, since these particles are few in number and no physical interaction between $(AlSi)_2$(VTiMn) and Al_2Cu particles was observed. Conversely, this can be due to the accumulation of some V into $Al_{15}(FeMn)_3Si_2$ crystals affecting the precipitation sequence of $Al_{15}(FeMn)_3Si_2$ phase, and thus, the nucleation of Cu-rich compounds.

3.3.4. Nickel Addition

As mentioned earlier, two different Ni-rich phases appear in the microstructure of the Ni-containing alloys, regardless of Zr and V levels. These are Al_9(FeCu)Ni and Al_6Cu_3Ni phases, as confirmed by the analysis of chemical composition and crystallographic structure (Figs. 9 and 10). Due to low solid solubility of Ni in α-Al matrix, almost all Ni tend to segregate into the interdendritic regions during solidification, resulting in the formation of Ni-bearing intermetallics. The monoclinic Al_9(FeCu)Ni appears with the undesired morphology, whereas the cubic Al_6Cu_3Ni compounds exhibit bone-like morphology.

4. Discussion

4.1. Zirconium and Vanadium Additions

The primary role of both Zr and V appears in refining the grain structure of the alloys prepared for this study. With individual V or Zr addition, α-Al grains tend to become finer, ~700 μm, if compared to the base material, ~1200 μm. The combined V and Zr addition seems to exert further refinement of α-Al grains, ~500 μm. The presence of 0.1 wt% Ti and 10 ppm B seems to be enough to induce a partial grain refinement of the base material.

With the addition of Zr, the precipitation of primary pro-peritectic particles can take place, nucleating the α-Al dendrites. Fig. 11 shows a

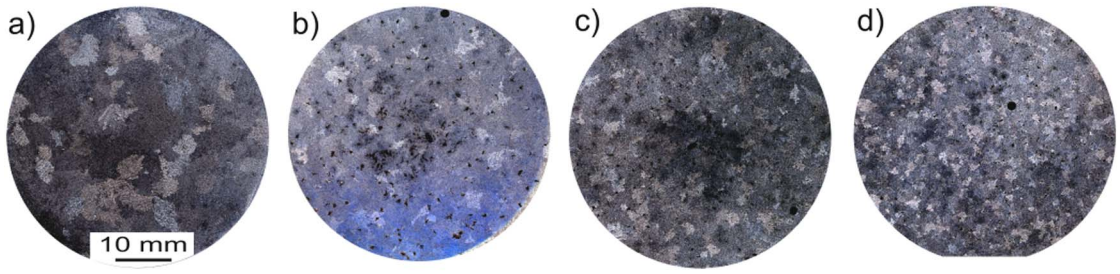

Fig. 3. Grain structures of Al-7Si-3Cu-0.3Mg alloy from thermal analysis test sections; the macrographs refer to (a) the base alloy and after (b) 0.12% Zr, (c) 0.25% V, and (d) 0.12% Zr and 0.25% V additions.

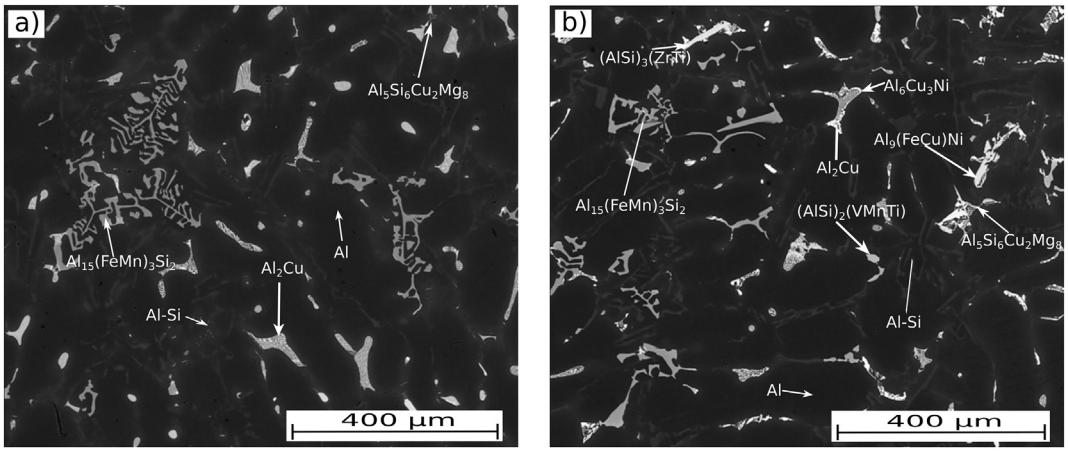

Fig. 4. SEM micrographs obtained from (a) Al-7Si-3Cu-0.3Mg, and (b) Al-7Si-3Cu-0.3Mg + Ni,Zr,V alloys. The different phases are indicated by arrows throughout.

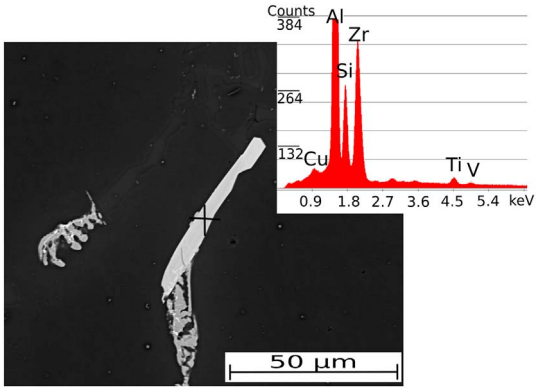

Fig. 5. SEM micrograph showing an AlSiZrTi particle with the corresponding EDS spectra in the Zr-containing alloy (Alloy A + Zr).

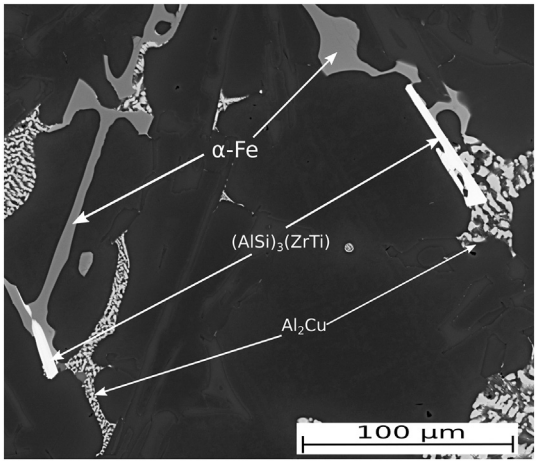

Fig. 6. SEM micrograph showing the nucleation of Cu- and Fe-rich phases on AlSiZrTi particles.

Zr-rich particle lying within the α-Al matrix. The EDS line-scan analysis confirms that the particle remains unaffected by Si, V and Ti that are present in the base material (see Fig. 11).

Therefore, considering the EDS results and the equilibrium Al-Zr system, it is confirmed that the particles observed at, or near, the grain centre are Al_3Zr particles, which is a potent nucleation site for the α-Al phase [14,28,29]. This also implies that the peritectic reaction was incomplete during solidification due to higher cooling rate than needed for solid-state diffusion to occur. The mechanism of grain refinement by Zr addition in Al alloys is well discussed in Reference [28]. The fact that some Al_3Zr particles tend not to interact with other elements can be explained by considering their formation temperature. It is therefore assumed that the particles forming in very early stages of solidification tend to enrich Ti and Si due to the availability of time for this process to occur, leading to the formation of coarse $(AlSi)_3(ZrTi)$ compounds; whereas the Al_3Zr particles mainly appearing inside α-Al matrix, probably form slightly prior to the formation of α-Al matrix, and as a result, there is no time available for the enrichment of other elements, such as Ti and Si, to occur.

Although it is confirmed how adding V induces grain refinement (see Fig. 3), no any V-rich particles that would be responsible for the grain refinement were revealed in the present investigation. According to the binary Al-V phase diagram, several V-rich pro-peritectic precipitates, such as $Al_{21}V_2$ and Al_3V can form [30], all of which have low interfacial energy with α-Al [8]. It seems that the formation of V-rich pro-peritectic particles appears not to occur in the secondary Al-7Si-3Cu-0.3Mg alloy, and instead, the formation of $(AlSi)_2(VTiMn)$ particles is more favourable. Further, a certain amount of V can accumulate into α-$Al_{15}(FeMn)_3Si_2$ phase (see Fig. 8). Therefore, it is proposed that the role of V is more apparent in increasing the growth restriction factor (Q), which is a parameter used to measure the effect of solute on grain refinement [31]

$$Q = mc_0(k - 1) \tag{1}$$

where m is the gradient of the liquidus, c_0 is the alloy composition, k is the partitioning coefficient. For multicomponent alloys, the Eq. (1) is extended to include the contribution of each alloying element [32]. Although the concentration of V is quite low, 0.25 wt%, the $m(k-1)$ factor is quite high in comparison to the other elements such as Si, Mg, Cu, etc. Consequently, 0.25 wt% V can exert substantial impact in the Al-Si alloys on undercooling the liquid lo a greater level in the solidifying front, leading to the activation of heterogeneous nuclei present in the liquid.

The role of V addition in refining the α-Al grains of Al-Si alloys is disputed in the literature. A moderate grain refinement with the addition of V has been observed [26,33]. Conversely, the V addition has shown no apparent influence in other works [27,34]. It has been also stated how V has no grain refining effect due to the poisoning effect of Si [27]. Based on the findings of present study, it can be argued that the role of V is significant in restricting the growth of α-Al crystals and activating certain solid particles to nucleate α-Al phase.

The greater efficiency of combined Zr and V additions than the individual ones on grain refinement can be associated with the increased number density of heterogeneous nucleants, as well as further enhanced growth restriction of α-Al grains. Fig. 12 shows how some vanadium atoms are accumulated into Zr-rich particles, thus increasing number density of potent nucleation particles.

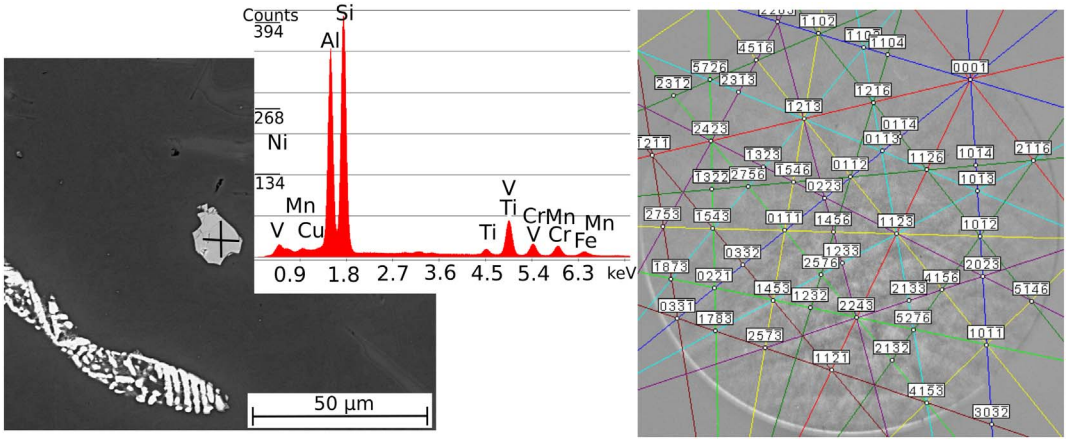

Fig. 7. SEM micrograph showing hexagonal $(AlSi)_2(VTiMn)$ particle in V-containing Al-7Si-3Cu-0.3Mg alloy, with corresponding EDS spectra and indexed EBSD pattern.

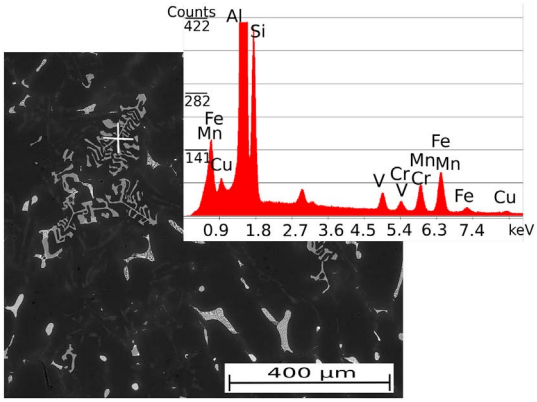

Fig. 8. SEM micrograph showing the presence of V in $Al_{15}(FeMn)_3Si_2$ particle in Al-7Si-3Cu-0.3Mg + V alloy.

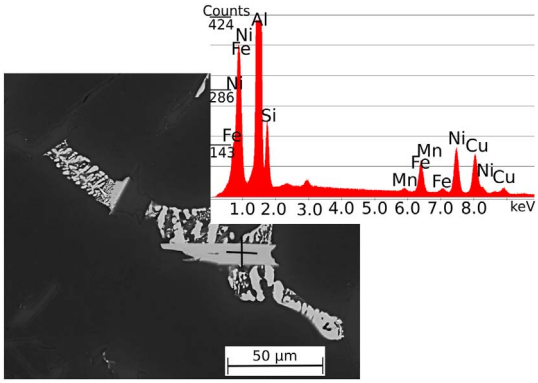

Fig. 9. SEM micrographs showing $Al_9(CuFe)Ni$ phase, with corresponding EDS spectra.

It is known how minor Zr and/or V additions to Al-Si alloys can result in the formation of secondary Zr- and V-rich dispersoids throughout the microstructure upon heat treatment, leading to the improvements of material's high-temperature mechanical properties [12,13,35,36]. The precipitation strengthening effect of transition metals in Al-Si alloys is significantly limited mainly due to their quite low solid solubility in the α-Al phase; thus, the transition metals, added into the melt, cause the formation of a limited number of TM-rich precipitates in the microstructure. Further, TM-rich precipitates concentrate mainly in the central regions of α-Al grains.

Fig. 13 shows the distribution of Zr, V, Ti and Mn elements inside an α-Al cell in Al-7Si-3Cu-0.3Mg + Zr,V. The centre of the cell is more enriched with V and Ti. Although similar distribution is expected for Zr, this appears uniformly distributed across the α-Al cell (see Fig. 13). This behaviour can be associated with the crystallisation of primary Zr-rich particles, causing the remaining liquid to become less-enriched with Zr.

Both non-homogeneous distribution of TM throughout the microstructure and the precipitation of primary TM-bearing particles are undesirable for further heat treatments because the homogenization of TM cannot be attained with the traditional heat treatments due to the limited diffusivity of TM at conventional temperatures. Therefore, in order for the precipitation strengthening with TM to be effective, the solidification conditions and the content of TM in Al-Si alloys need to be properly controlled. It is known how certain heat treatment's conditions can lead to the precipitation of a high fraction of metastable coherent trialuminides with cubic structure within α-Al matrix [37,38]. This behaviour is highly desirable for the homogeneous distribution of strengthening precipitates throughout the microstructure. Therefore, further investigations concerning the precipitation of TM-containing secondary precipitates upon subsequent heat treatment needs to be carried out in order to gain further understanding of the role of Al-Zr-V-Ti-Mn system in precipitation behaviour of TM-containing secondary particles.

Manganese appears to be evenly distributed across α-Al (Fig. 13) due to its partitioning coefficient, which is almost equal to unity. In the present study, it has been observed how a certain amount of Mn can be bound to TM-containing particles (Fig. 7).

4.2. Nickel Addition

The microstructural investigations revealed how Ni is almost completely bound to Cu-rich phases, resulting in the formation of Al_6Cu_3Ni and $Al_9(FeCu)Ni$ intermetallic compounds (Fig. 14). Precipitation of both Al_6Cu_3Ni and $Al_9(FeCu)Ni$ particles can impart high-temperature strength [21,39,40]. It has been stated how thermally stable Ni-rich intermetallics tend to maintain better interconnectivity of the eutectic network, that is contiguity [41]. The $Al_9(FeCu)Ni$ phase exhibits plate-like or blocky morphology, which is undesirable due to sharp edges of the particles that can act as crack initiation points. In contrast, the Al_6Cu_3Ni phase has a script-like morphology, as well as a cubic structure, which makes the phase as more preferred one. The similarity in crystallographic structure of the adjacent phases is thought to maintain their coherency at elevated temperature expositions, contributing to higher creep resistance of material.

However, since a certain amount of Cu is bound to Al_6Cu_3Ni and $Al_9(FeCu)Ni$ compounds, which remain almost undissolved during solution heat treatment, lower amount of Cu is available for the precipitation of secondary Cu-rich phases during aging treatment. Accordingly, the strengthening contribution of Cu decreases.

In the present study, it was clearly evident that the precipitation of Al_6Cu_3Ni and $Al_9(FeCu)Ni$ throughout the microstructure was pro-

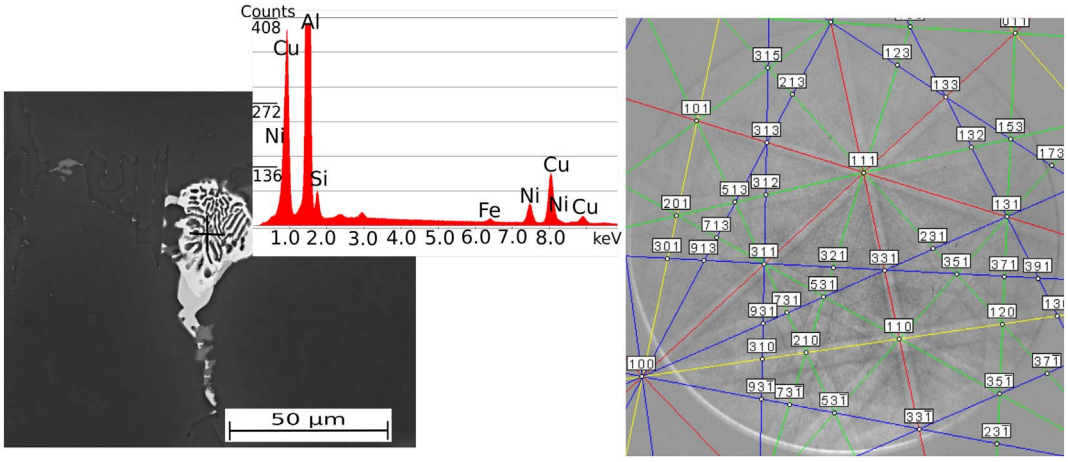

Fig. 10. SEM micrographs showing cubic Al_6Cu_3Ni, as revealed by EDS spectra and indexed EBSD patterns.

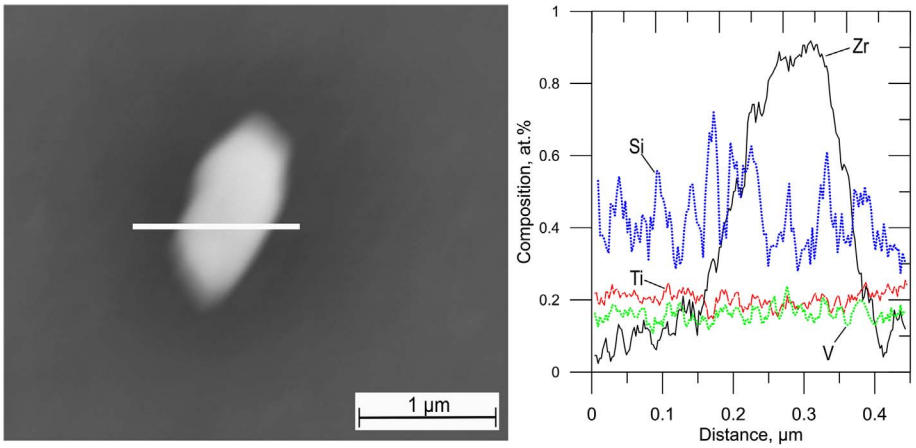

Fig. 11. SEM image of Zr-rich phase in Al-7Si-3Cu-0.3Mg + Zr alloy with corresponding EDS line-scan, showing the distributions of Ti, Si, V and Zr elements.

moted with the addition of Ni (0.25 wt%), although the Al_2Cu particles remain as predominant Cu-rich compounds in the microstructure. Due to the greater concentration of Cu (about 3 wt%) with respect to that analyzed in References [13,41], it is believed that a sufficient amount of both Al_2Cu secondary precipitates and Cu-Ni intermetallics can be obtained by applying an appropriate heat treatment processing route.

5. Conclusions

The effects of individual and combined Ni, V and Zr additions on the solidification parameters and the microstructural evolution of secondary Al-7Si-3Cu-0.3Mg alloy were investigated. The following conclusions can be drawn from this study.

- With the addition of 0.12 wt% Zr, precipitation of primary properitectic Al_3Zr particles occurs, leading to a considerable refinement of α-Al matrix. The Al_3Zr particles lying within α-Al matrix appear without any enrichment by Si and Ti. However, few numbers of Al_3Zr particles precipitating in very early stages of solidification were found to interact with Si and Ti, loosening their potency to

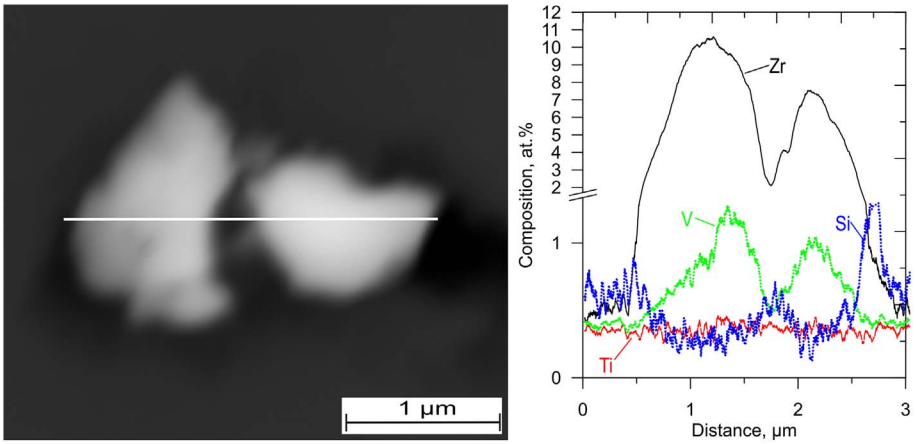

Fig. 12. SEM image of Zr-rich phase in alloy Al-7Si-3Cu-0.3Mg + Zr,V with corresponding EDS line-scan, showing the distributions of Ti, Si, V and Zr elements.

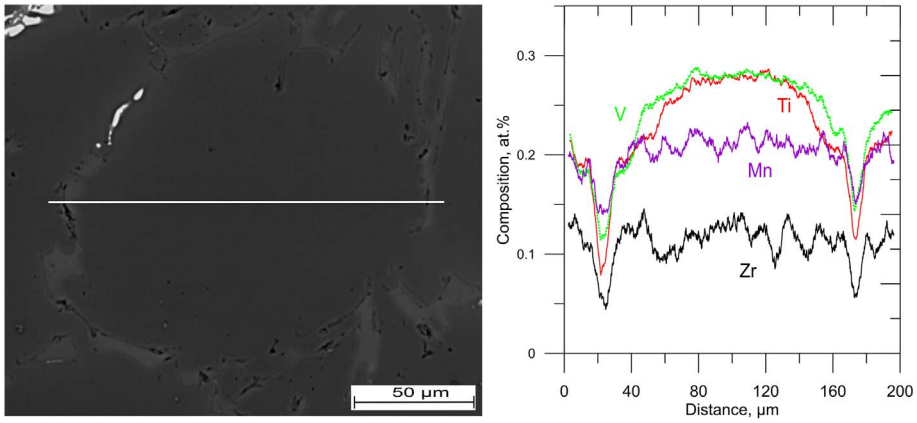

Fig. 13. SEM image of α-Al grain in Al-7Si-3Cu-0.3Mg + Zr,V alloy with corresponding EDS line-scan, showing the distributions of Zr, V, Ti and Mn elements.

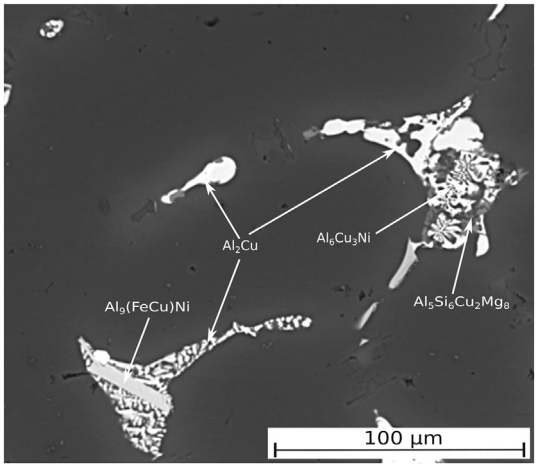

Fig. 14. SEM micrograph showing post-eutectic Cu- and Ni-bearing phases formed in Ni-containing Al-7Si-3Cu-0.3Mg alloy.

nucleate α-Al matrix. Furthermore, the formation of primary Zr-rich particles causes α-Al matrix to be less-enriched with Zr, reducing its ability to improve the mechanical properties. Thus, zirconium level needs to be properly established by considering the alloy composition and solidification conditions to avoid the formation of primary and undesired $(AlSi)_3(ZrTi)$ platelets.

- With the addition of 0.25 wt% V, similar grain refining efficiency to that of Zr addition was observed. However, the role of V appears to be significant in increasing the growth restriction factor, thus providing greater level of constitutional undercooling, causing some particles to become active for nucleation of α-Al. Vanadium appears to be also bound to primary polyhedral-shaped $(AlSi)_2(VMnTi)$ and α-Fe phase, thereby, avoiding the formation of pro-peritectic V-rich particles.
- Combined V and Zr addition yielded a greater level of grain refinement if compared to the individual Zr and V additions. This is mainly attributable to the fact that some V accumulated into Al_3Zr particles, increasing the number density of Zr-rich trialuminides, and also to the role of V in increasing the level of constitutional undercooling.
- Nickel addition tends to introduce changes in post-eutectic reactions through the precipitation of Al_6Cu_3Ni and $Al_9(CuFe)Ni$ phases, in addition to Al_2Cu and $Al_5Si_6Cu_2Mg_8$ intermetallics. Initially-precipitated Ni-rich intermetallics, in turn, consume some amount of Cu and act as nucleation sites for Al_2Cu and $Al_5Si_6Cu_2Mg_8$ phases to form, thus, decreasing the freezing range of the alloy. Cubic Al_6Cu_3Ni phase appears in Chinese-script morphology, thus can be a preferable Ni-rich phase, if compared to the other Ni-rich compounds, such as platelet-like $Al_9(FeCu)Ni$ phase.

Acknowledgements

This work was developed within the ERASMUS MUNDUS Project (Silkroute - Strand 1/Lot L09, project n. 545765). The author would like to acknowledge Raffineria Metalli Capra Spa (Brescia, Italy) for the experimental support to the research.

References

[1] I. Aguilera-Luna, M.J. Castro-Román, J.C. Escobedo-Bocardo, F.A. García-Pastor, M. Herrera-Trejo, Effect of cooling rate and Mg content on the Al–Si eutectic for Al–Si–Cu–Mg alloys, Mater. Charact. 95 (2014) 211–218.
[2] W. Zhang, Y. Liu, J. Yang, J. Dang, H. Xu, Z. Du, Effects of Sc content on the microstructure of As-Cast Al-7 wt.% Si alloys, Mater. Charact. 66 (2012) 104–110.
[3] K. Du, Q. Zhu, D. Li, F. Zhang, Study of formation mechanism of incipient melting in thixo-cast Al–Si–Cu–Mg alloys, Mater. Charact. 106 (2015) 134–140.
[4] M. Javidani, D. Larouche, Application of cast Al-Si alloys in internal combustion engine components, Int. Mater. Rev. 59 (2014) 132–158.
[5] S.K. Shaha, F. Czerwinski, W. Kasprzak, J. Friedman, D.L. Chen, Improving high-temperature tensile and low-cycle fatigue behavior of Al-Si-Cu-Mg alloys through micro-additions of Ti, V, and Zr, Metall. Mater. Trans. A 46 (2015) 3063–3078.
[6] A.R. Farkoosh, X.G. Chen, M. Pekguleryuz, Dispersoid strengthening of a high temperature Al-Si-Cu-Mg alloy via Mo addition, Mater. Sci. Eng. A 620 (2014) 181–189.
[7] J. Rakhmonov, G. Timelli, F. Bonollo, The effect of transition elements on high-temperature mechanical properties of al-Si foundry alloys - a review, Adv. Eng. Mater. 18 (2016) 1096–1105.
[8] K.E. Knipling, D.C. Dunand, D.N. Seidman, Criteria for developing castable, creep-resistant aluminum-based alloys - a review, Int. J. Mater. Res. 97 (2006) 246–265.
[9] A.R. Farkoosh, X. Grant Chen, M. Pekguleryuz, Interaction between molybdenum and manganese to form effective dispersoids in an Al-Si-Cu-Mg alloy and their influence on creep resistance, Mater. Sci. Eng. A 627 (2015) 127–138.
[10] A.K. Lohar, B. Mondal, D. Rafaja, V. Klemm, S.C. Panigrahi, Microstructural investigations on as-cast and annealed Al–Sc and Al–Sc–Zr alloys, Mater. Charact. 60 (2009) 1387–1394.
[11] S.K. Shaha, F. Czerwinski, W. Kasprzak, D.L. Chen, Tensile and compressive deformation behavior of the Al-Si-Cu-Mg cast alloy with additions of Zr, V and Ti, Mater. Des. 59 (2014) 352–358.
[12] T. Gao, D. Li, Z. Wei, X. Liu, Evolution, microhardness of ZrAlSi intermetallic and its impact on the elevated-temperature properties in Al-Si alloys, Mater. Sci. Eng. A 552 (2012) 523–529.
[13] J. Hernandez-Sandoval, G.H. Garza-Elizondo, A.M. Samuel, S. Valtiierra, F.H. Samuel, The ambient and high temperature deformation behavior of Al-Si-Cu-Mg alloy with minor Ti, Zr, Ni additions, Mater. Des. 58 (2014) 89–101.
[14] K.E. Knipling, D.C. Dunand, D.N. Seidman, Precipitation evolution in Al-Zr and Al-Zr-Ti alloys during isothermal aging at 375–425 degrees C, Acta Mater. 56 (2008) 114–127.
[15] J. Rakhmonov, G. Timelli, F. Bonollo, Influence of melt superheat, Sr modifier, and Al-5Ti-1B grain refiner on microstructural evolution of secondary Al-Si-Cu alloys, Metall. Mater. Trans. A 47 (2016) 5510–5521.
[16] F. Wang, Z.L. Liu, D. Qiu, J.A. Taylor, M.A. Easton, M.X. Zhang, Revisiting the role of peritectics in grain refinement of Al alloys, Acta Mater. 61 (2013) 360–370.
[17] G. Timelli, G. Camicia, S. Ferraro, R. Molina, Effects of grain refinement on the microstructure, mechanical properties and reliability of AlSi7Cu3Mg gravity die cast cylinder heads, Met. Mater. Int. 20 (2014) 677–686.
[18] M.B. Djurdjevic, I. Vicario, G. Huber, Review of thermal analysis applications in aluminium casting plants, Rev. Metal. 50 (2014).
[19] G. Timelli, S. Capuzzi, A. Fabrizi, Precipitation of primary Fe-rich compounds in

secondary AlSi9Cu3(Fe) alloys, J. Therm. Anal. Calorim. 123 (2016) 249–262.
[20] L. Backerud, G. Chai, J. Tamminen, Solidification Characteristics of Aluminum Alloys, 2 Foundry Alloys, Des Plaines, IL, USA, 1990.
[21] A.R. Farkoosh, M. Javidani, M. Hoseini, D. Larouche, M. Pekguleryuz, Phase formation in as-solidified and heat-treated Al-Si-Cu-Mg-Ni alloys: thermodynamic assessment and experimental investigation for alloy design, J. Alloys Compd. 551 (2013) 596–606.
[22] A. Darlapudi, S.D. McDonald, D.H. StJohn, The Influence of Cu, Mg and Ni on the Solidification and Microstructure of Al-Si alloys, 4th International Conference on Advances in Solidification Processes, ICASP 2014, July 8, 2014–July 11, 2014, Institute of Physics Publishing, Windsor, United kingdom, 2016.
[23] S.K. Shaha, F. Czerwinski, W. Kasprzak, J. Friedman, D.L. Chen, Thermal stability of (AlSi)(x)(ZrVTi) intermetallic phases in the Al-Si-Cu-Mg cast alloy with additions of Ti, V, and Zr, Thermochim. Acta 595 (2014) 11–16.
[24] W.B. Pearson, Chapter VI - Crystallographic data on “structurbericht” types, A Handbook of Lattice Spacings and Structures of Metals and Alloys, 1958, pp. 79–121. Pergamon.
[25] B. Huber, H.S. Effenberger, K.W. Richter, Phase equilibria in the Al-Si-V system, Intermetallics 18 (2010) 606–615.
[26] A.K.P. Rao, Influence of vanadium on the microstructure of A319 alloy, T. Indian I. Metals 64 (2011) 447–451.
[27] T.H. Ludwig, P.L. Schaffer, L. Arnberg, Influence of Vanadium on the Microstructure of A356 Foundry Alloy, Light Metals 2012–TMS 2013 Annual Meeting and Exhibition, March 3, 2013–March 7, 2013, Minerals, Metals and Materials Society, San Antonio, TX, United states, 2013, pp. 1023–1028.
[28] F. Wang, D. Qiu, Z.L. Liu, J.A. Taylor, M.A. Easton, M.X. Zhang, The grain refinement mechanism of cast aluminium by zirconium, Acta Mater. 61 (2013) 5636–5645.
[29] F. Wang, D. Qiu, Z.L. Liu, J. Taylor, M. Easton, M.X. Zhang, Crystallographic study of Al3Zr and Al3Nb as grain refiners for Al alloys, Trans. Nonferrous Metals Soc. China 24 (2014) 2034–2040.
[30] B. Huber, K.W. Richter, Observation of the new binary low temperatures compound AlV, J. Alloys Compd. 493 (2010) L33–L35.
[31] M. Easton, D. StJohn, An analysis of the relationship between grain size, solute content, and the potency and number density of nucleant particles, Metall. Mater. Trans. A 36A (2005) 1911–1920.
[32] D.H. StJohn, A. Prasad, M.A. Easton, M. Qian, The contribution of constitutional Supercooling to nucleation and grain formation, Metall. Mater. Trans. A 46A (2015) 4868–4885.
[33] W.M. Edwards, R.C. Thomson, S.J. Barnes, S.I. Barnes, Development of near-eutectic Al-Si casting alloys for piston applications, Mater. Sci. Forum 396-4 (2002) 625–630.
[34] R. Cook, M.A. Kearns, P.S. Cooper, Effects of residual transition metal impurities of electrical conductivity and grain refinement of EC grade aluminum, Light Met. 1997 (1997) 809–814.
[35] M. Garat, G. Laslaz, Improved aluminium alloys for common rail diesel cylinder heads, AFS Transactions 07-002 (2007) 1–8.
[36] G. Tong, L. Dakui, W. Zuoshan, L. Xiangfa, Evolution, Microhardness of ZrAlSi Intermetallic and Its Impact on the Elevated-temperature Properties in Al-Si Alloys, Elsevier, Kidlington, Royaume-Uni, 2012.
[37] W. Kasprzak, B.S. Amirkhiz, M. Niewczas, Structure and properties of cast Al-Si based alloy with Zr-V-Ti additions and its evaluation of high temperature performance, J. Alloys Compd. 595 (2014) 67–79.
[38] T. Gao, A. Ceguerra, A. Breen, X.F. Liu, Y.Y. Wu, S. Ringer, Precipitation behaviors of cubic and tetragonal Zr-rich phase in Al-(Si-)Zr alloys, J. Alloys Compd. 674 (2016) 125–130.
[39] X.G. Dong, J. Zhou, Y.J. Jia, B. Liu, Effect of alloying on high temperature fatigue performance of ZL114A (Al-7Si) alloy, Trans. Nonferrous Metals Soc. China (Engl. Ed.) 22 (2012) s661–s667.
[40] R. Molina, P. Amalberto, M. Rosso, Mechanical characterization of aluminium alloys for high temperature applications Part1: Al-Si-Cu alloys, Metall. Sci. Technol. 29 (2011) 5–15.
[41] F. Stadler, H. Antrekowitsch, W. Fragner, H. Kaufmann, P.J. Uggowitzer, Effect of main alloying elements on strength of Al-Si foundry alloys at elevated temperatures, Int. J. Cast Met. Res. 25 (2012) 215–224.

SUPPLEMENT 5

Effect of V and Zr microalloying and heat treatment on microstructure and mechanical properties of secondary Al-7Si-3Cu-0.3Mg alloy

J. Rakhmonov, G. Timelli, A. Fabrizi and F. Bonollo, submitted for publication in Metallurgical and materials transactions A, 2017

Effect of V and Zr Microalloying, and Heat Treatment on Microstructure and Mechanical Properties of Secondary Al-7Si-3Cu-0.3Mg Alloy

Jovid Rakhmonov*, Giulio Timelli, Alberto Fabrizi, Franco Bonollo

University of Padova, Department of Management and Engineering, Stradella S. Nicola, 3 I-36100 Vicenza, Italy. (Jovid Rakhmonov: rakhmonov@gest.unipd.it, Giulio Timelli: timelli@gest.unipd.it, Alberto Fabrizi: fabrizi@gest.unipd.it, Franco Bonollo: bonollo@gest.unipd.it)

(*Corresponding author. Tel.: 00 39 0444 998769; fax. 00 39 0444 998889. E-mail address: rakhmonov@gest.unipd.it (J. Rakhmonov)).

Abstract
The Al-Si-Cu alloys, which are widely used in automotive powertrain exhibit limited high-temperature strength properties; the high diffusivity of the main strengthening elements Cu and Mg in α-Al at temperatures between 473 (200) and 573 K (300 ºC) is a dominating factor in alloy softening. In this study, effects of slow-diffusing elements (Zr and V) and heat treatment on microstructure and mechanical properties of secondary Al-7Si-3Cu-0.3Mg alloy were investigated. Majority of both Zr and V were retained inside α-Al matrix during solidification. T6 heat treatment induced the solid-state precipitation of multiple, nano-sized particles in α-Al grains interior. Unlike Cu/Mg-rich strengthening precipitates that form during aging, the Zr/V-rich precipitates formed during solution heat treatment, which indicates high potential for high-temperature strengthening in Al-Si alloys via transition metals addition. Other transition metals, such as Mn, Fe, Cr and Ti, which were present as impurities in the base alloy significantly promoted the formation of nano-sized Zr/V-rich precipitates inside α-Al grains. These thermally more stable precipitates were credited for the enhanced high-temperature strength properties of Al-7Si-3Cu-0.3Mg alloy by ~ 20 %.

Keywords
Al-Si alloys; Microstructure; Mechanical properties; High-temperature strength; Transition elements;

1. Introduction

Light-weighting in the automotive industry for fuel efficiency has led to a large-scale application of aluminum alloys. Some engine components, such as cylinder-head and -block, have been increasingly fabricated using Al-Si-Mg or Al-Si-Cu-Mg alloys as these alloys offer a combination of excellent casting characteristics and relatively high mechanical properties [1, 2]. The presence of Cu and/or Mg in the alloy provides significant strengthening by precipitation hardening mechanism [3]. However, the Cu/Mg-rich precipitates can only be effective for the strength at temperatures below 473 K (200 ºC) [4]. At higher temperatures, solute diffusion of Cu and Mg tends to be increasingly effective in promoting the precipitate coarsening, also called Ostwald ripening, within the matrix, thus contributing to the alloy softening [5]. The operating temperature in engine combustion chamber can often exceed 473 K (200 ºC) during service [6, 7]. Moreover, a further increase in operating temperature is anticipated due to the expected enhancement in engine power in near future, which indicates the necessity for the development of a new creep-resistant Al alloys [8]. A new alloy must resist degradation of mechanical properties at high temperatures [473 - 573 K (200 - 300 ºC)]. Addition of some transition metals, such as Sc, Zr, V, Mo, Ni and etc. are thought to give this characteristic as these elements have low diffusivity in α-Al at higher temperatures and

can form coherent or semi-coherent precipitates in stable and/or meta-stable states [9]. Owing to low solid solubility in α-Al matrix, these transition elements, if added individually, make less contribution to the strengthening of the material due to the limited volume fraction of precipitates forming during heat treatment. Combined addition of appropriate types of transition metals, in contrast, can yield higher volume fraction of precipitates, thus positively influencing the thermal stability of the alloy [9, 10]. Adding transition metals in an effort to improve the high-temperature mechanical properties of Al-Si based alloys has been a research topic of several studies [8, 11-18]. Kasprzak et al. [19] reported how minor Ti, Zr and V additions can yield the formation of nano-sized $(AlSi)_3(ZrVTi)$ precipitates in grain interiors, however, their effect on high-temperature tensile properties has been found to be negligible, which can be due to the limited volume fraction of thermally stable precipitates. Shaha et al. [8] stated how the addition of 0.56 % Zr, 0.3 % V and 0.3 % Ti can improve the low-cycle fatigue properties of Al-Si-Cu-Mg based alloy due to the formation of both interdendritic and intradendritic Zr/V-rich precipitates. However, the addition levels of peritectic-forming elements need optimization as too high levels also lead to the premature nucleation and growth of phases with undesired morphology, thus exhibiting deleterious impact on alloy performance, as observed in References [13, 16]. Farkoosh et al. [20] found how the interaction between the eutectic-forming Mn and peritectic-forming Mo leads to the formation of a substantial volume fraction of Al(MoMnFe)Si precipitates inside α-Al matrix, with a significant contribution to the high-temperature strengthening of Al-Si-Cu-Mg alloy. Shaha et al. [21] reported that the formation of both micro- and nano-sized Mo/Mn-rich dispersoids formed in inter- and intradendritic regions respectively enhanced high-temperature tensile properties of Al-Si-Cu-Mg alloys. Nevertheless, too high level of Mn also tended to increase the volume fraction of interdendritic compounds, thus deteriorating the alloy mechanical properties [20]. Hence, we can infer that the introduction of appropriate types of transition metals and strict control of the addition levels is a critical step in generating a microstructure more favorable for high-temperature applications.

Moreover, there is no research in the literature with regard to the effects of adding Zr and V on high-temperature mechanical properties of secondary (recycled) Al-Si-Cu-Mg based alloys, one of the most used alloys for the engine production, particularly for cylinder head castings [22]. The presence of trace (impurity) elements, such as Ti, Mn, Fe, Cr and Ni in minor levels in these alloys may induce changes in the solid-state precipitation sequence due to their possible interactions with deliberately-added transition metals, such as Zr and V, thus yielding the formation of various types of precipitates inside α-Al grains at higher volume fractions.

This study thus attempts to investigate the effect of adding Zr and V and age-hardening heat treatment on microstructural evolution and tensile properties of the secondary Al-7Si-3Cu-0.3Mg alloy, with the aim of forming a new type of thermally stable, intradendritic precipitates having potential in high-temperature strengthening of Al-Si based alloys.

2. Experimental procedure

A secondary Al-7Si-3Cu-0.3Mg alloy (EN AB-46300, equivalent to the US designation A320), supplied by Raffineria Metalli Capra as commercial ingots was used as a baseline material. The Al-10Zr and Al-10V (in wt-%) waffle-shaped master alloys were used to add to the base alloy melt and prepare a new alloy. Hereafter, the new alloy prepared for this study is referred to as a (Zr/V-) modified alloy. The melting of ingots was conducted in an electrical-resistance furnace at 1033 K (760 ºC). To produce Zr/V-modified alloy, the pre-calculated amounts of Al-10Zr and Al-10V master alloys were added to the melt to achieve desired levels of Zr and V in the alloy. The H_2 gas level and the melt temperature were continuously monitored using Alspek-H hydrogen gas analyzer machine and the melt was stirred and surface skimmed 15 min prior to pour. The chemical

composition was analyzed using optical spectroscopy on the specimens separately poured at the beginning and the end of every casting conditions; the averaged compositions of the base and Zr/V-modified alloys are listed in Table 1.

A steel mold was used to produce castings. The casting design can be seen in Ref. [23]. The boron nitride was used to coat the mold inner surfaces. At a time of pouring, the temperature of the die was increased to 523 K (250 ºC). The temperature was monitored by means of thermocouples embedded in the die to ensure a good reproducibility of the tests. The average secondary dendritic arm spacing (SDAS) of the produced castings was ~15 μm in both the base and Zr/V-modified alloys.

The cylindrical tensile bars were sectioned from castings, and then, analyzed using Bosello SRE 80 industrial machine equipped with a macro-focus X-ray source to assure the soundness of the specimens.

The age-hardening heat treatment (T6 state) of some selected specimens were then performed in an air-circulating furnace; the solution heat treatment was performed at 758 K (485 ºC) for 24 h and then quenched in water at room temperature, followed by aging at 453 K (180 ºC) for 8 hours. The temperature for solution heat treatment was selected on the basis of the results from differential scanning calorimetry (DSC) analyses performed in our previous research [24]. Longer solutionizing time was applied to enable the precipitation reactions involving transition metals, such as Zr and V, inside α-Al grains [25].

Several tensile specimens representing the base and Zr/V-modified alloys both in the as-cast and heat-treated states were chosen for microstructural analyses and sectioned from the cross-section of the gauge length. The specimens obtained were then mounted, grinded and polished following the standard techniques. Optical microscope (OM), scanning electron microscope (SEM) equipped with energy-dispersive spectroscopy (EDS) and transmission electron microscopy (TEM) equipped with EDS were used to investigate the microstructure. Some microstructural features, such as the roundness of Si particles, and the fraction of Fe-rich compounds, were quantitatively analyzed using an image analyzer. Several optical micrographs, representing a total area of 5 mm^2, were captured from each specimen to obtain a statistical average of the analyzed parameters.

All the as-cast and heat-treated tensile bars were then machined to produce specimens with total length of 175 mm, a gauge length of 65 mm, and a diameter of 10 mm. The tensile tests were conducted at MTS 810 tensile testing machine at a strain rate of 10^{-3} s^{-1}. The strain was measured using a 25-mm extensometer. The as-cast specimens were only tested at room temperature [293 K (20 ºC)], whereas the heat-treated specimens were tested at both room [293 K (20 ºC)] and high temperatures [473 and 573 K (200 and 300 ºC)]. For the cases of high-temperature tests, the tensile specimens were held at testing temperature for 30 min before starting the test. At least four tensile tests were conducted for each condition. Experimental data were collected and processed to provide yield strength (YS), ultimate tensile strength (UTS) and elongation to fracture (% El).

Table 1. The chemical composition of the base and Zr/V-modified alloys (wt-%).

Alloy type	Si	Fe	Cu	Mn	Mg	Zn	Cr	Ni	Ti	Pb	V	Zr	Al
Base	7.8	0.46	3.1	0.23	0.32	0.78	0.040	0.02	0.1	0.03	0.01	0.01	bal.
Modified	7.5	0.45	3.0	0.22	0.30	0.76	0.037	0.02	0.1	0.03	0.30	0.15	bal.

3. Results

3.1 Microstructural evolution

Fig. 1 shows typical as-cast microstructures observed in the base and Zr/V-modified alloys. The microstructure of the base alloy exhibits α-Al matrix, eutectic Si, $Al_{15}(FeMn)_3Si_2$ and Cu-rich phases (see Fig. 1a); in addition, small and rare $Al_8Mg_3FeSi_6$ and Ca-, Bi-, Pb-rich particles are observed in the microstructure, as discussed in detail in our previous study [26, 27]. Microstructural

characterization of the Zr/V-modified alloy (see Fig. 1b) revealed the presence of Zr-rich compounds in addition to the phases observed in the base alloy; these Zr-rich intermetallic compounds are identified as $(AlSi)_3(ZrTi)$ phase [24]. The $(AlSi)_3(ZrTi)$ compounds reside in the interdendritic regions in a size range of 10 µm (Fig. 1). The excess solute of V rejected into the interdendritic liquid during alloy solidification was found to be solely bound to pro-eutectic α-$Al_{15}(FeMn)_3Si_2$ compounds (see Fig. 2), thus slightly increasing the fraction of Fe-rich phases from 0.4 % in the base alloy to 0.5 % in the Zr/V-modified alloy. In our previous study [24], a few amount of pro-eutectic $(AlSi)_2(VTiMn)$ compounds were detected in the microstructure generated at a lower cooling rate corresponding to the SDAS value of ~65 µm. In the present study, however, higher cooling rate corresponding to the SDAS of ~15 µm seems to retain more V in the α-Al solid solution, thus avoiding the precipitation of pro-eutectic $(AlSi)_2(VMn)$ phase.

As shown in Fig. 3, both V and Zr added into the alloy tended to mainly concentrate in the α-Al grain interiors. The Fig. 3 also shows how the peritectic-forming Zr and Ti tended to segregate towards the core/centre of α-Al grains due to their partitioning coefficient, which is larger than the unity, while Mn showed more homogeneous distribution over the cross section of α-Al matrix as its partitioning coefficient is equal to unity. In other words, non-equilibrium solidification can result in the inhomogeneous distribution of Zr and V inside the α-Al grains, i.e. positive and negative segregation of these elements in dendrite cores and edges, respectively, due to a limited solid-state diffusion (see Fig. 3).

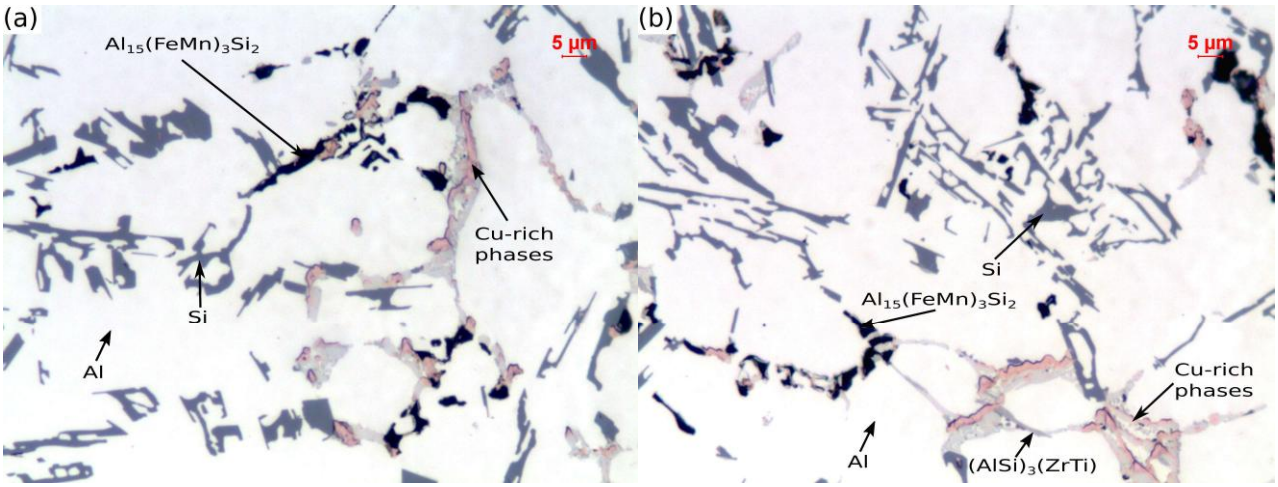

Fig. 1. Typical microstructures of the (a) base and (b) Zr/V-modified alloys in as-cast states. The samples were etched in a mixture of H_2O and H_2SO_4, preheated to 70 ºC to highlight Fe-rich compounds.

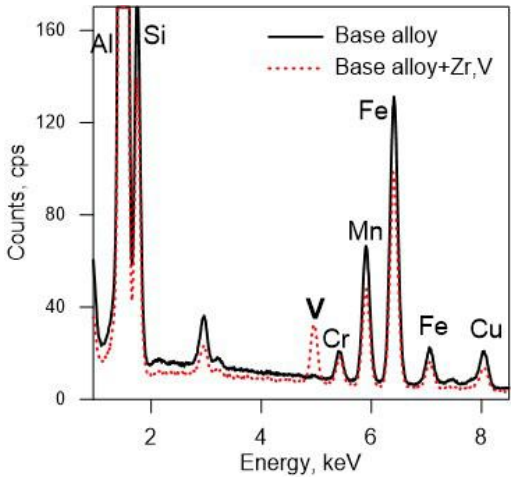

Fig. 2. Typical EDS spectra of α-$Al_{15}(FeMn)_3Si_2$ phase observed in the (a) base and (b) Zr/V-modified alloys in as-cast states.

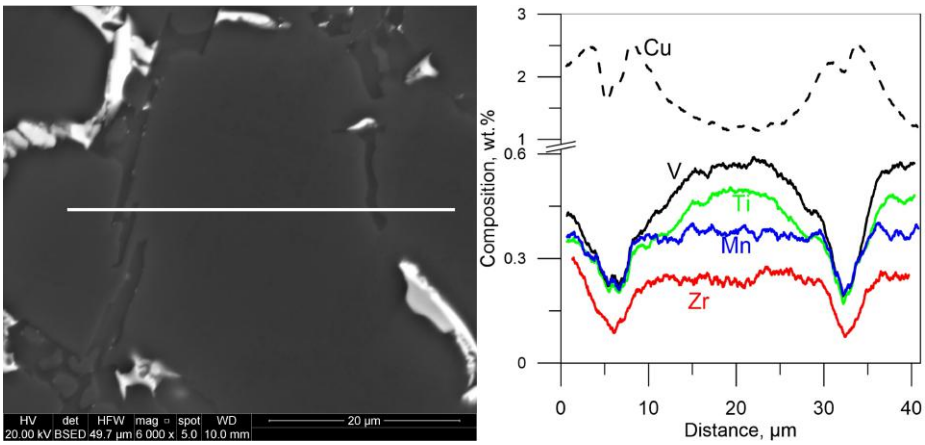

Fig. 3. SEM image of α-Al grain in Zr/V-modified alloy with corresponding EDS line-scan, showing the distributions of Zr, V, Ti, Mn and Cu elements.

Fig. 4 shows the typical microstructures representing the base and Zr/V-modified alloys after T6 heat treatment. Qualitative comparison of as-cast and T6 heat-treated microstructures indicates how applying heat treatment changed the size and morphology of eutectic Si particles and led to the dissolution of Cu/Mg-rich interdendritic particles into the α-Al matrix. It is known that eutectic Si particles tend to undergo fragmentation and spheroidization during solution heat treatment [28]. Quantitative analysis of eutectic Si particles in the base and Zr/V-modified alloys revealed that the roundness value changes from ~5 in the as-cast state to ~ 2 in the heat-treated state, respectively. A few amounts of Cu-rich compounds still exist in interdendritic regions (see Fig. 4) indicating their incomplete dissolution into the α-Al matrix, whereas the α-$Al_{15}(FeMn)_3Si_2$ and $(AlSi)_3(ZrTi)$ phases showed no tendency to dissolve into the α-Al matrix and remained stable in grain boundaries and interdendritic regions (Fig. 4 and Fig. 5).

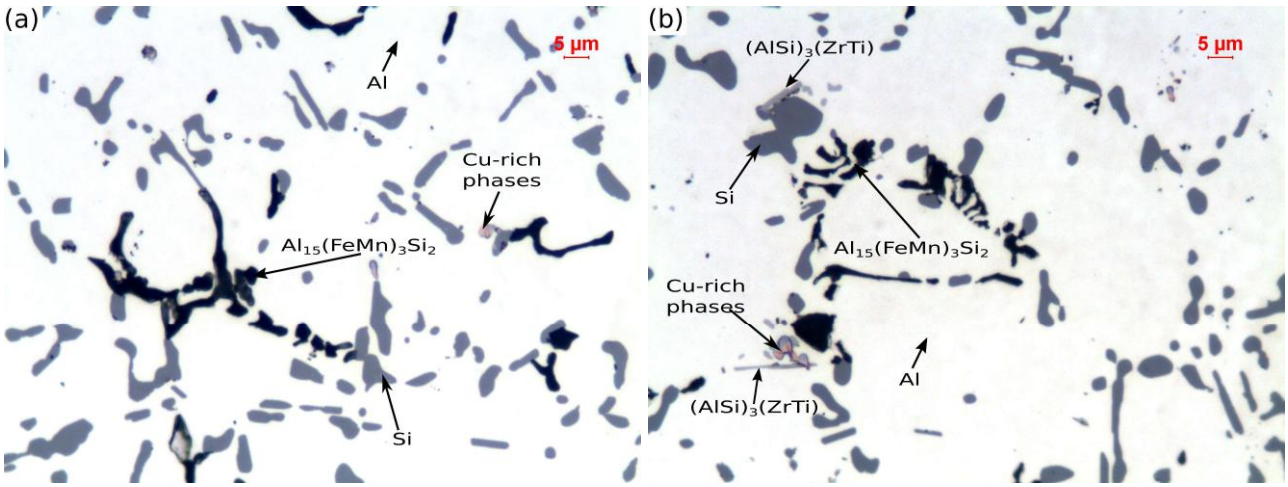

Fig. 4. Typical microstructures of the (a) base, and (b) Zr/V-modified alloys in the heat-treated states. The samples were etched in a mixture of H_2O and H_2SO_4, preheated to 70 °C to highlight Fe-rich compounds.

X-ray mapping analyses (Fig. 5 and Fig. 6) suggest that the undissolved Cu-rich particles are mainly $Al_5Si_6Cu_2Mg_8$ and some blocky Al_2Cu compounds; this indicates the necessity for higher solutionizing temperature. Moreover, the trace amounts of Ni (~250 ppm) appears to be sufficient to form some thermally more stable Al-Ni-Cu interdendritic intermetallics, which remained undissolved into the α-Al matrix during the solutionizing stage (Fig. 6).

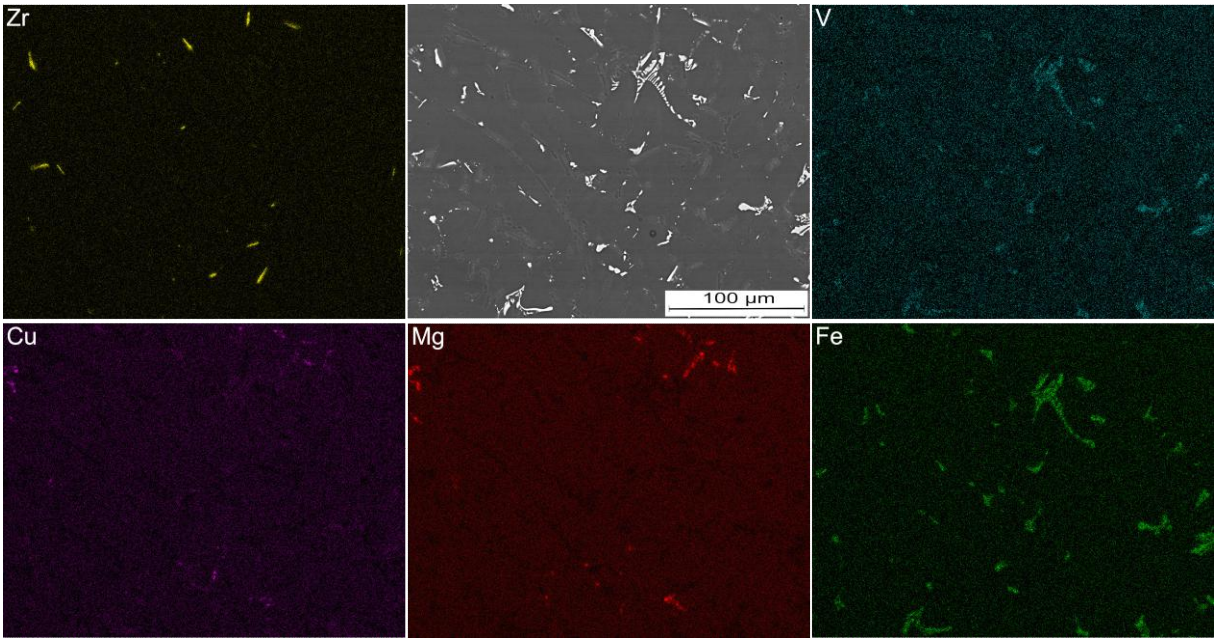

Fig. 5. Backscattered electron image of a typical microstructure of Zr/V-modified alloy after T6 heat treatment with corresponding EDS composition maps, showing the distributions of Zr, V, Cu, Mg and Fe elements.

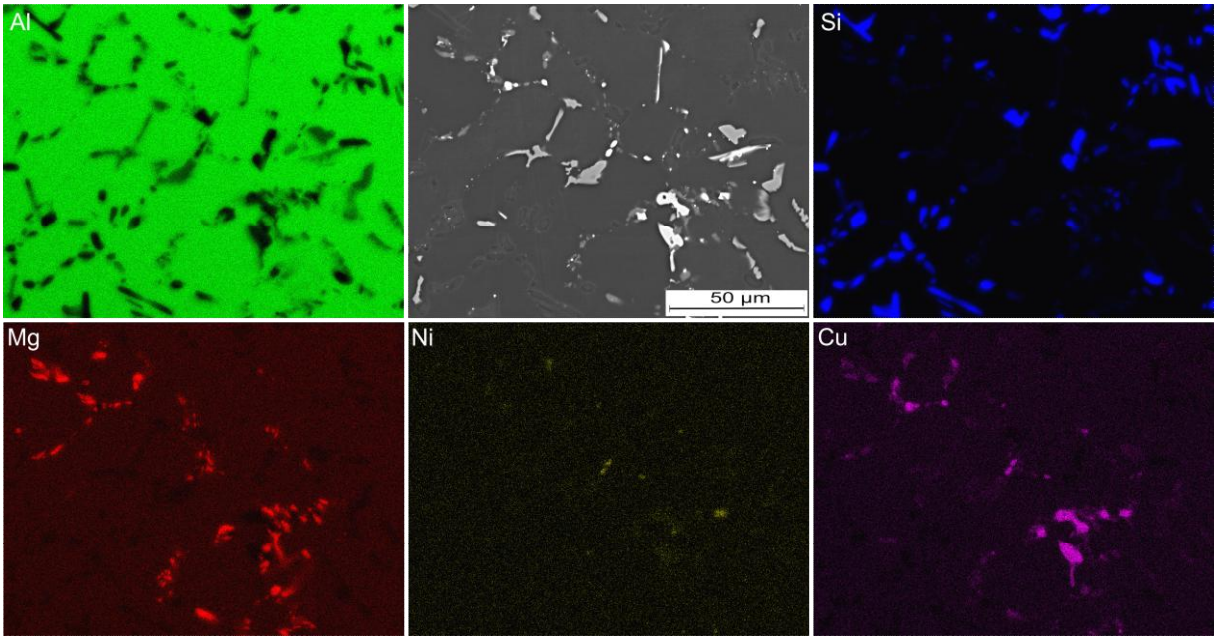

Fig. 6. Backscattered electron image of a typical microstructure of Zr/V-modified alloy after T6 heat treatment with corresponding EDS composition maps, showing the distributions of Al, Si, Mg, Ni and Cu elements.

It is known that the mechanical properties of Al-Si alloys containing Cu and Mg can be significantly improved by applying the age-hardening heat treatment. The bright field (BF) TEM micrographs in Fig. 7 show the precipitation occurred upon T6 heat treatment in the intradendritic regions (α-Al grain interiors). The needle-like precipitates, which are believed to be θ′ phase [29], are dominant throughout the microstructure (Fig. 7). Detailed characterization of the solid-state precipitation reactions involving Cu and Mg in Al-Si-Cu-Mg alloys can be found elsewhere [29-31]. Comparison of the microstructures of the base and Zr/V-modified alloys revealed the presence of Zr/V-rich precipitates inside α-Al matrix of Zr/V-modified alloy. Due to limited diffusivity of Zr and V in α-Al matrix, the solid-state precipitation reactions involving these elements require higher temperatures than that applied during aging stage. Microstructural investigations of the alloys after

solution heat treatment and quenching stages confirmed the occurrence of solid-state precipitation reactions involving Zr and V during solution heat treatment, as shown in Fig. 8. It is evident that the density of precipitates in the Zr/V-modified alloy is substantially higher than that of the base alloy.

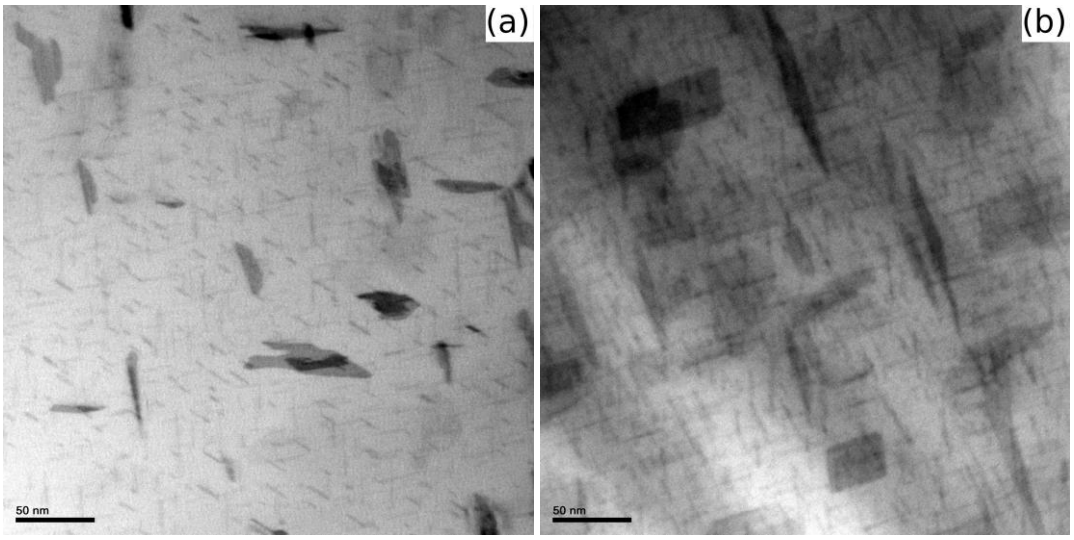

Fig. 7. BF TEM micrographs showing the precipitation observed after T6 heat treatment in the (a) base and (b) Zr/V-modified alloys.

The EDS analysis of the base alloy (Fig. 9) suggests that a few precipitates observed in the α-Al grain interiors are of α-Al(MnFe)Si type [32, 33]. The EDS investigation of the precipitates formed in the Zr/V-modified alloy suggests the presence of three different types of Zr- and V-rich phases (Fig. 10). The precipitate numbered 1 in Fig. 10a is believed to be the α-Al(MnVFe)Si phase, which is also observed in the grain interiors of the base alloy in the form of α-Al(MnFe)Si [33-35]. The α-Al(MnVFe)Si particles appear in plate-like morphology with the average size of 100 nm and account for a major part of the precipitates formed during solution heat treatment of the Zr/V-modified alloy. The role of V appears to be significant in promoting the precipitation of α-Al(MnFe)Si by substituting Mn in this phase. The flaky-like Zr-rich precipitates numbered 2 in Fig. 10a and identified as $(AlSi)_3(ZrTi)$ in Ref. [19] are rarely observable in the α-Al grain interiors, which can be due to the low solubility of both Zr and Ti in α-Al. The irregular-shaped V-rich precipitate numbered 3 in Fig. 10a is believed to be an $(AlSi)_2(VCr)$ phase according to its composition; however, further TEM investigations seem necessary to conduct the crystallographic studies of this phase. This precipitate is also hardly apparent in the microstructure (grain interiors), which can be explained by more preferential involvement of V in the precipitation of α-Al(MnVFe)Si phase.

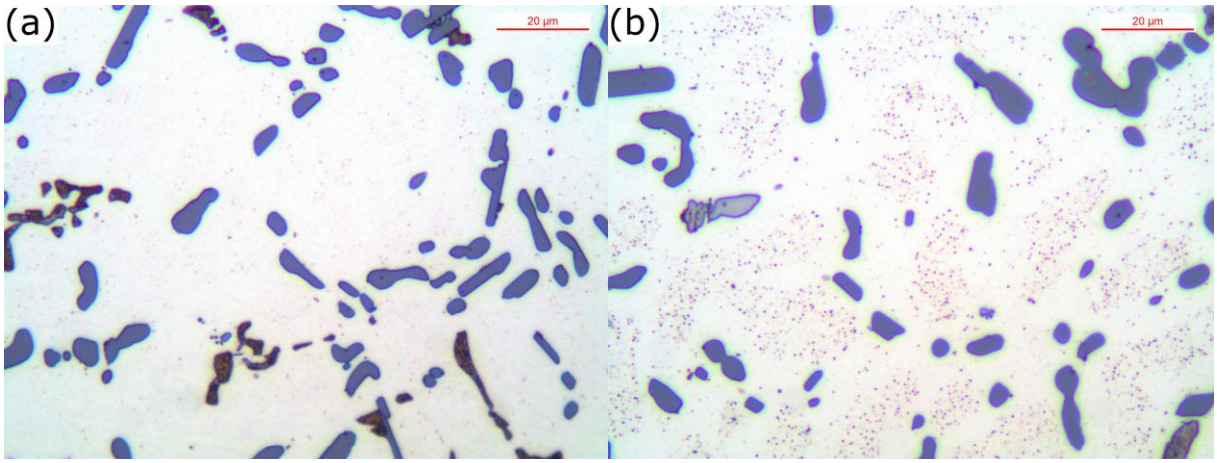

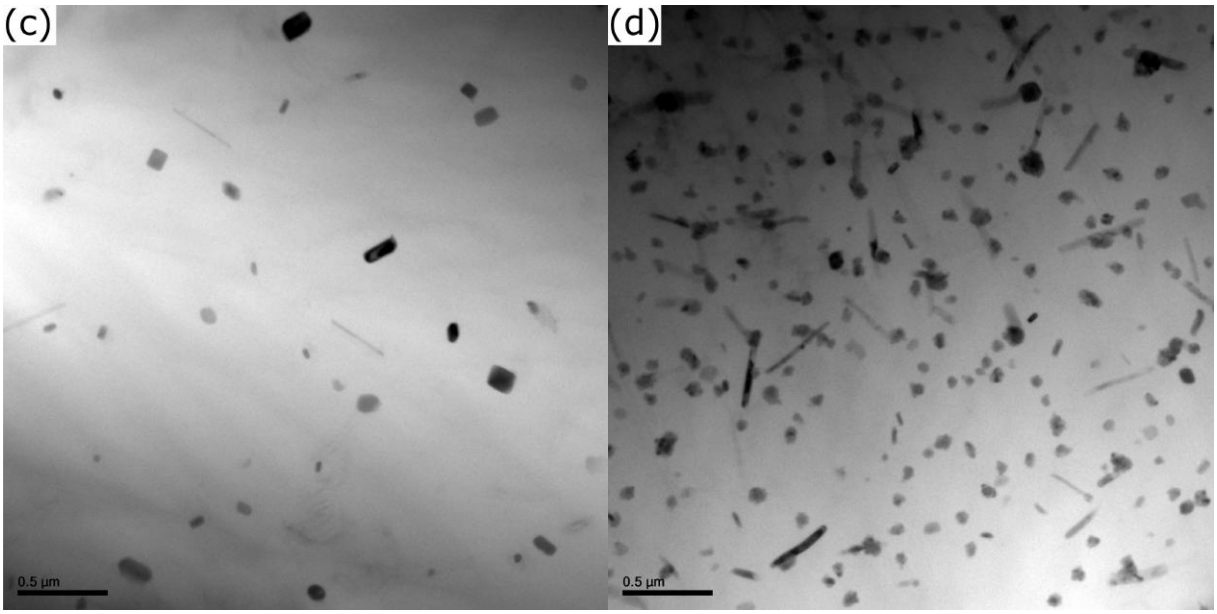

Fig. 8. (a,b) Optical micrographs and (c,d) BF TEM micrographs showing the precipitates formed during solution heat treatment of the (a,c) base and (b,d) Zr/V-modified alloys. Optical micrographs were obtained from the samples etched in 1% HF for 30 s to reveal secondary precipitates.

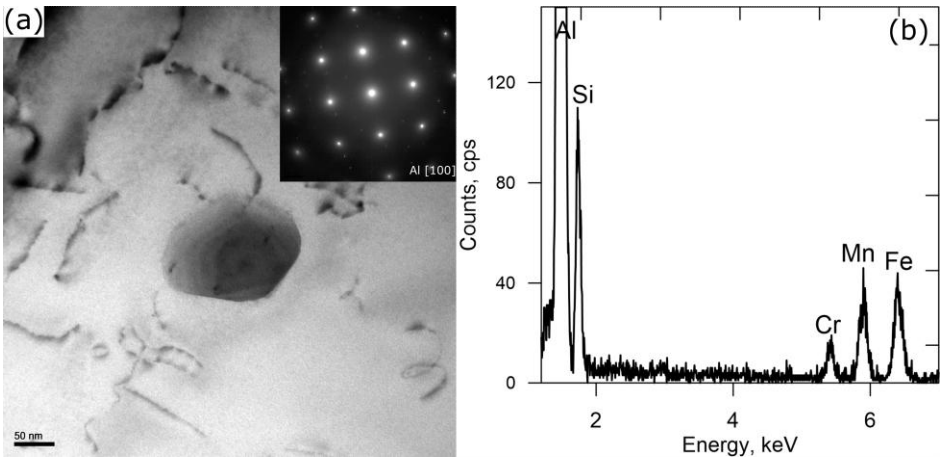

Fig. 9. (a) BF TEM micrograph showing the α-Al(MnFe)Si precipitate formed in α-Al grain interior during solution heat treatment of the base alloy, and (b) EDS spectrum of α-Al(MnFe)Si precipitate shown in Fig. 9a.

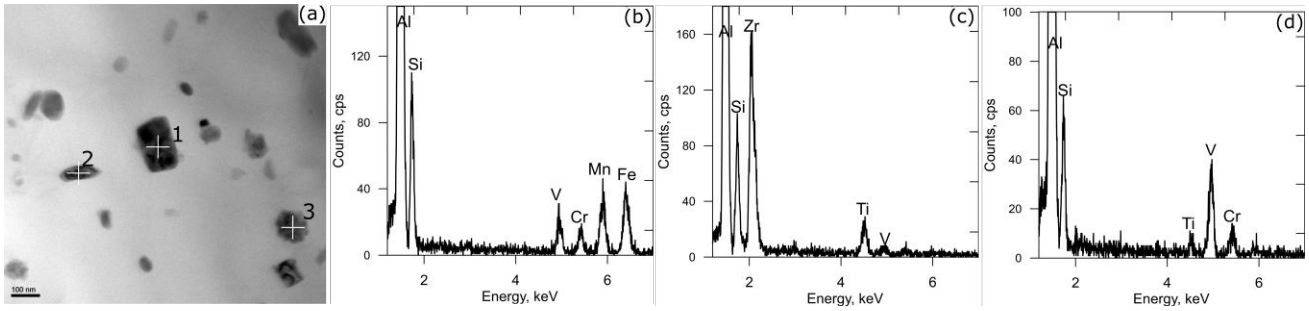

Fig. 10. (a) BF TEM micrograph showing the precipitates formed in α-Al grain interiors during solution heat treatment of Zr/V-modified alloy; (b) EDS spectrum of Al(MnVFe)Si precipitate numbered 1 in Fig. 10a; (c) EDS spectrum of $(AlSi)_3(ZrTi)$ precipitate numbered 2 in Fig. 10a; (d) EDS spectrum of $(AlSi)_2(VCr)$ precipitate numbered 3 in Fig. 10a.

3.2 Tensile properties

Table 2 presents the room-temperature tensile properties in the as-cast and heat-treated states of both the base and Zr/V-modified alloys. The response of both the base and Zr/V-modified alloys to heat treatment seems to be similar. While the yield strength (YS) and ultimate tensile strength

(UTS) of the base alloy increased from 155 and 248 MPa in the as-cast state to 364 and 415 MPa in T6 heat treated states, respectively, the elongation to failure (% El) remained almost constant in the range of ~ 2 % in both the as-cast and heat-treated states. The Zr/V-modified alloy exhibits slightly better YS in both the as-cast and heat-treated states (see Table 2).

Table 2. Tensile properties with corresponding standard deviation (in parentheses) of the base and Zr/V-modified alloys before and after T6 heat treatment at room temperature.

Alloy type	As-cast			T6 treatment		
	YS	UTS	% El	YS	UTS	% El
base	155 (5.2)	248.2 (2.8)	1.95 (0.20)	364.4 (2.8)	415.17 (4.6)	1.98 (0.26)
modified	158.6 (0.3)	248.8 (1.5)	1.77 (0.12)	368.8 (2.1)	414.8 (3.5)	1.7 (0.30)

Fig. 11 shows the tensile properties of the base and Zr/V-modified alloys after T6 heat treatment as function of testing temperature. It is evident that tensile properties tend to decrease as the testing temperature increases [36]; the YS and UTS of the base alloy decreased from approximately 364 and 415 MPa at room temperature to about 262 and 271 MPa at 473 K (200 ºC), followed by a further decrease to 83 and 86 MPa at 573 K (300 ºC) testing temperatures respectively, whereas the % El increased from ~2% at 293 K (20 ºC) to approximately 2.5% at 473 K (200 ºC), and 8% at 573 K (300 ºC). Adding Zr and V showed no significant improvement on room-temperature tensile properties of the alloy, however, With increasing the testing temperature, the positive effects of Zr and V became more evident (Fig. 11a,c). The UTS and YS of Zr/V-modified alloys at 573 K (300 ºC) testing temperature are higher by around 20 % compared to the base alloy. The achieved improvement, however, was also followed by a slight decrease in % El (Fig. 11c).

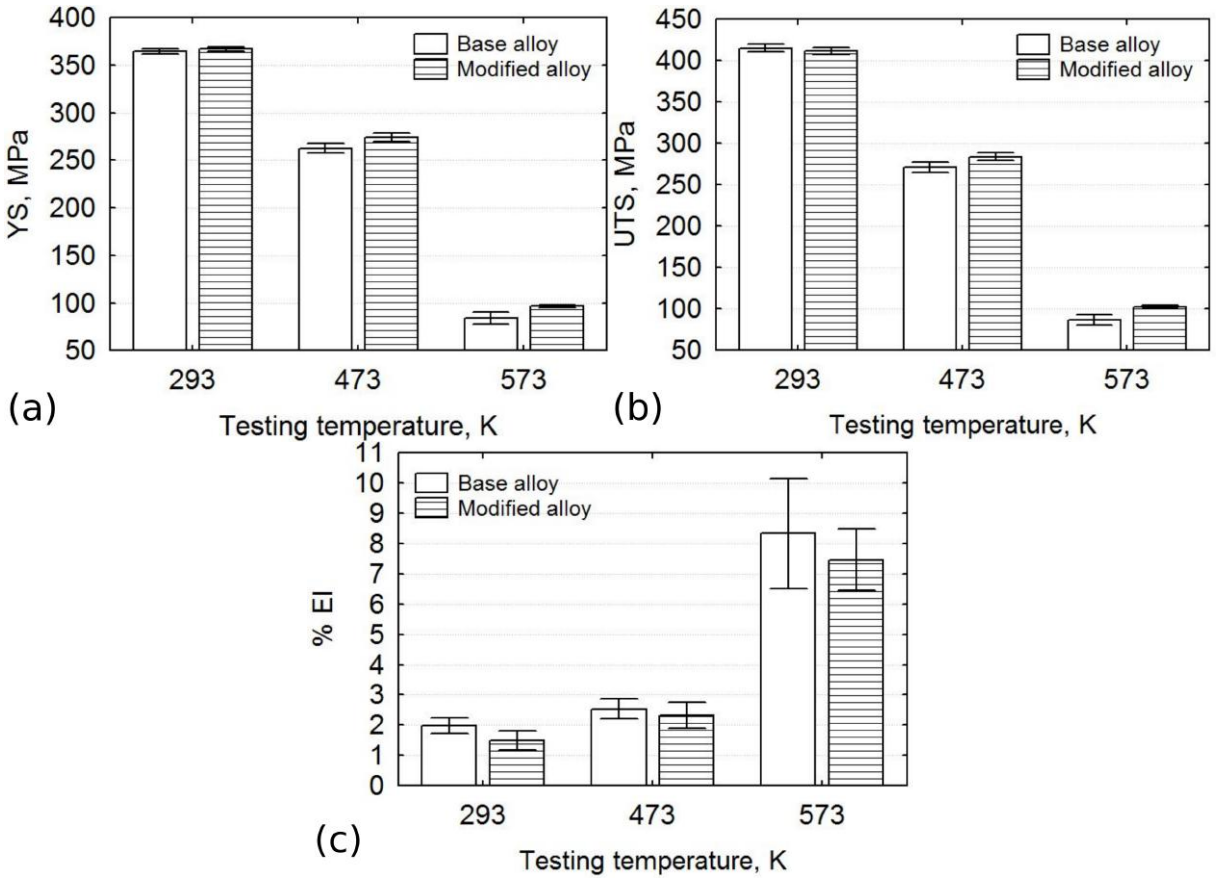

Fig. 11. A comparison of the tensile properties of the base and Zr/V-modified alloys after T6 heat treatment, obtained at different testing temperatures: (a) yield strength, (b) ultimate tensile strength and (c) elongation to failure.

3.3 *Fractographic observations*

The typical examples of SEM fractographs observed on the fractured surfaces of the studied alloys tested at 293 (20) and 593 K (300 ºC) temperatures are shown in Fig. 12. The presence of casting defects, such as oxide inclusions and shrinkage, appear to govern the fracture of the tensile-tested specimens; these casting defects can act as preferable sites for crack initiation [37]. Once the damage is initiated by the casting defects, the propagation occurs through the cracking of interdendritic brittle phases, such as eutectic Si and Fe/Cu-rich intermetallic particles, (see Fig. 13 and Fig. 14) due to the development of internal stresses in the particles by plastic deformation. Microcracks originated in those interdendritic, brittle intermetallics propagate through the a-Al matrix and subsequently connect to each other to produce the main crack.

As can be seen in Fig. 13, the main fracture profile line of the base and Zr/V-modified alloys in as-cast state reflects the shape of dendritic structure. The cleavage fracture of eutectic Si and Cu/Fe-rich intermetallics are evident. The plastically deformed microregions (micronecks) of the a-Al dendrites are also noticed in both the base and Zr/V-modified alloys, which suggests that a mixed interdendritic-transdendritic fracture mode was operative in the as-cast state of the studied alloys, with the intergranular brittle fracture mode being the dominant one. The SEM fractograph representing Zr/V-modified alloy in as-cast state also shows the tear ridges and fractured brittle phases, such as Si and Cu/Fe-rich intermetallics (Fig. 15a). Since the α-Al matrix is relatively soft and ductile, the stress incompatibilities evolved at the particle/matrix interfaces favour cracking of brittle, interdendritic phases, which dominates the fracture mode [38].

Applying T6 heat treatment showed no significant influence on the fracture profile of the alloys tested at room temperature (see Fig. 14a,d and Fig. 15b). Although solutionizing stage caused spheroidization of eutectic Si particles, some Si particles still remained elongated and coarser and these particles crack more easily as they possess lower fracture stress [39-41]. Although more spheroidized Si particles in heat-treated alloys would contribute to higher elongation to failure, the hardening of α-Al matrix induced by T6 heat treatment restrains the plastic deformation of α-Al matrix. These microstructural changes can be responsible for having nearly the same elongation to failure observed in both the as-cast and heat-treated states of the studied alloys.

When the testing temperature is increased to 473 K (200 ºC), the fracture profile of the studied alloys remains almost unchanged compared to the alloys tested at room temperature, even though some dimples can be seen at fracture surfaces; a slight increase in the elongation to failure of the alloys tested at 473 K (200 ºC) temperature compared to the alloys tested at room temperature also confirms the occurrence of slight plastic deformation. The absence of significant amount of dimples on the fracture surfaces of the alloys tested at 293 (20) and 473 K (200 ºC) temperatures (Fig. 15a,b,c) is an indication of the brittle fracture mode that was operative in these investigation conditions.

Further increase of the testing temperature to 573 K (300 ºC) resulted in brittle-to-ductile transition of fracture mode in both alloys. Although interdendritic particles cracking and micronecks can be also seen on the fractured surfaces (see Fig. 14c,f), the fracture path mainly follows the sheared α-Al matrix (see Fig. 12). Fracture of the alloys tested at 300 ºC was dominated by ductile dimple fracture with the cavities containing multiple fragmented intermetallic phases (Fig. 15d) [38, 42]. Note that at low temperatures, a single dominant cleavage crack of brittle, interdendritic phases was observable on the fracture surfaces (Fig. 15a,b,c). When the testing temperature is raised to 573 K (300 ºC), the α-Al matrix becomes much softer than at room temperature, thus increasing the plasticity of the alloys.

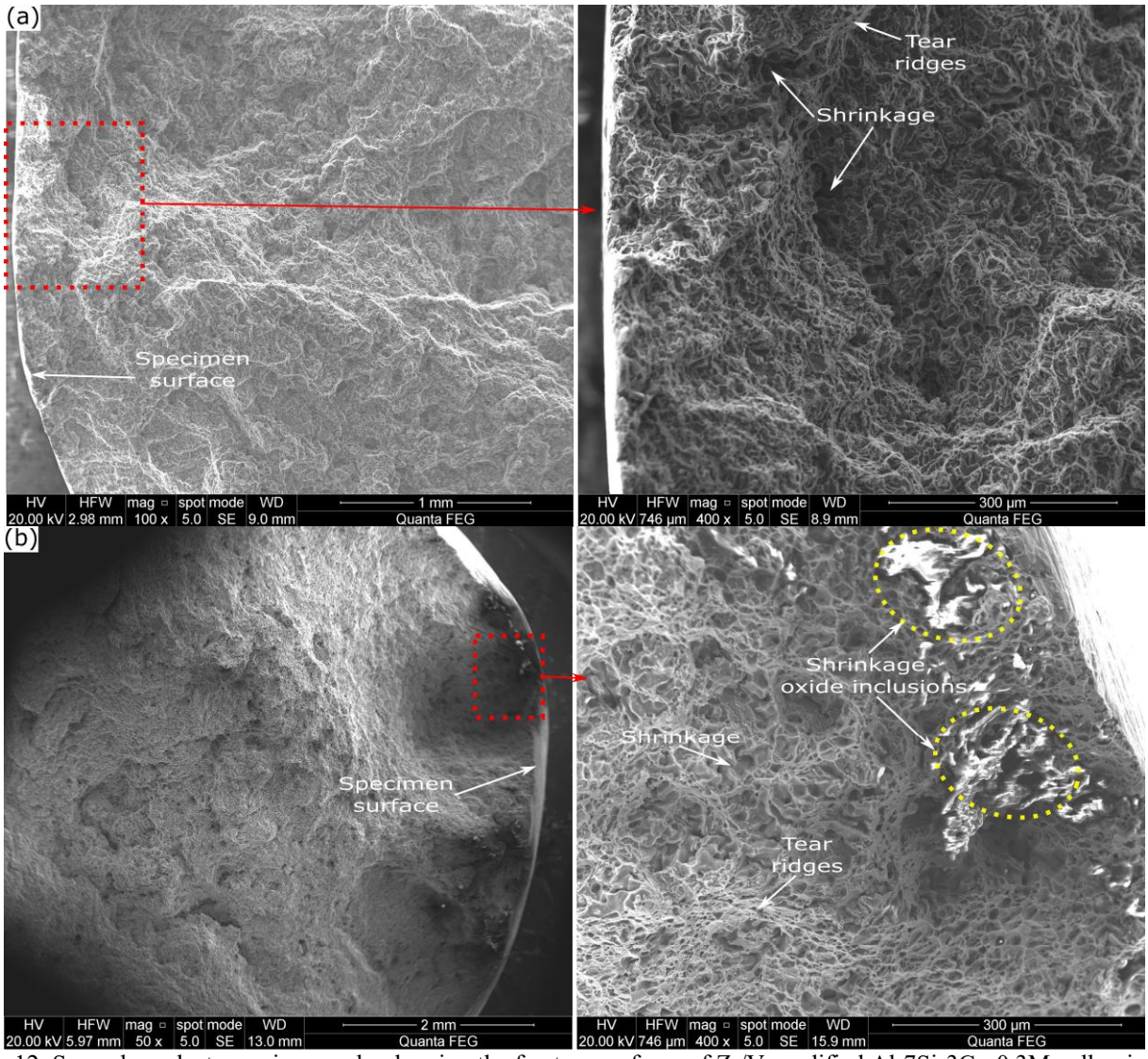

Fig. 12. Secondary electron micrographs showing the fracture surfaces of Zr/V-modified Al-7Si-3Cu-0.3Mg alloy in T6 heat-treated state and tested at (a) 293 (20) and (b) 573 K (300 °C) temperatures. The location of crack initiation, and the casting defects, such as shrinkage and oxide inclusions, that initiated the crack can be seen.

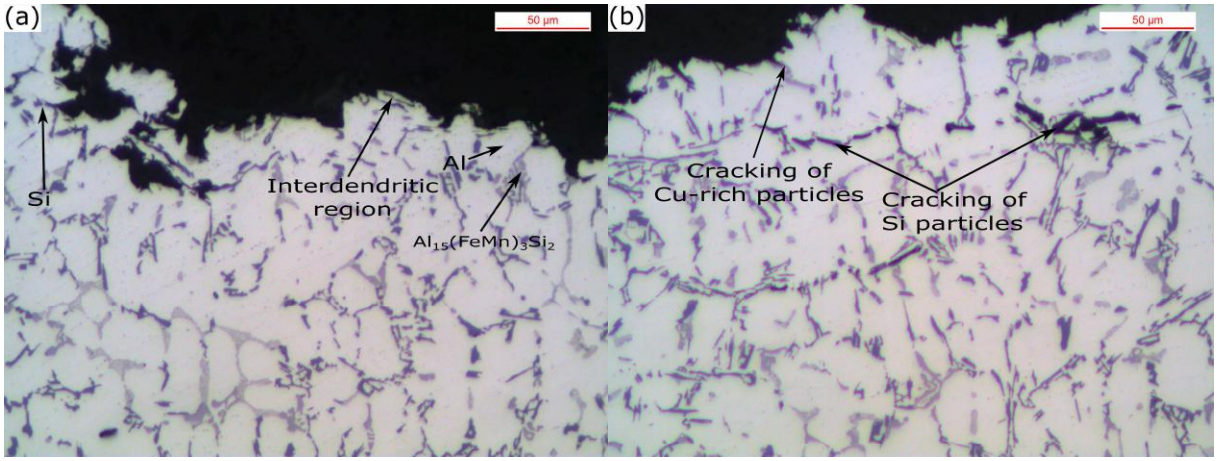

Fig. 13. Optical micrographs of fracture profiles, showing a mixed transdendritic-interdendritic fracture on (a) the base and (b) Zr/V-modified alloys.

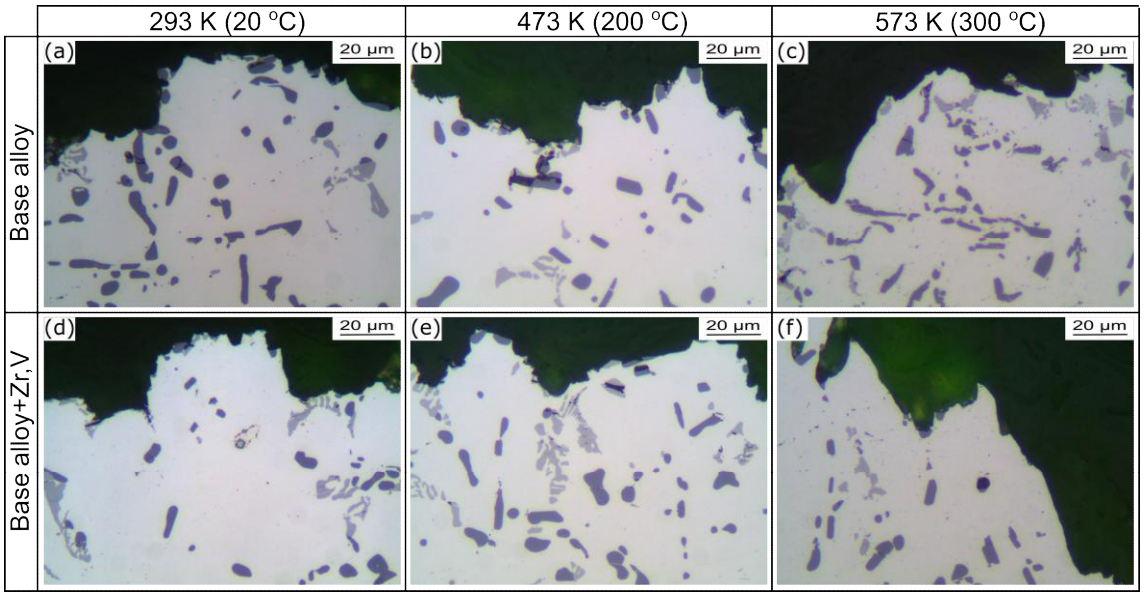

Fig. 14. Optical micrographs of the tensile fracture profile of the (a,b,c) base and (d,e,f) Zr/V-modified alloys tested at (a,d) 293 (20), (b,e) 473 (200) and (c,f) 573 K (300 °C) temperatures.

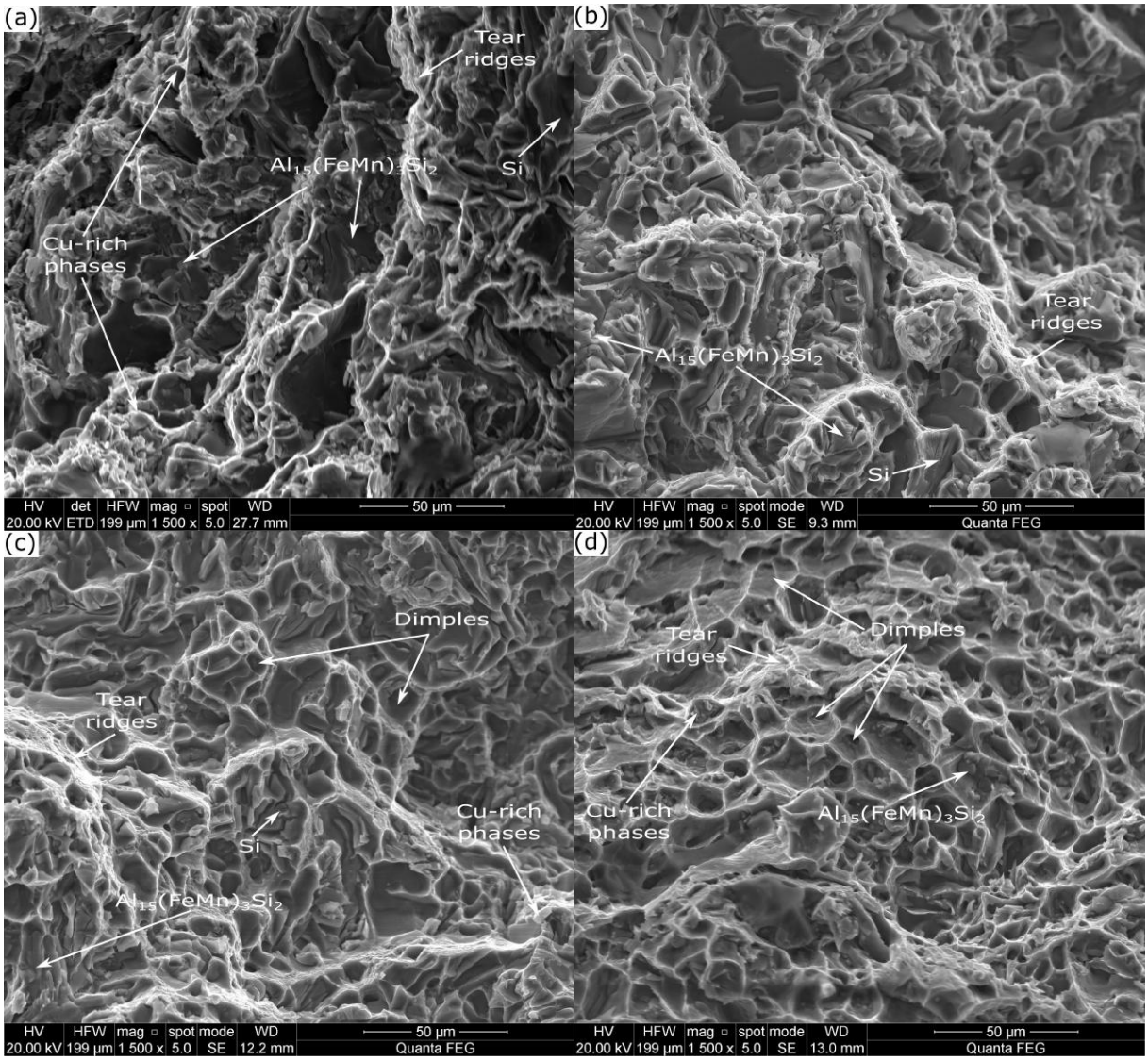

Fig. 15. Secondary electron micrographs of fractured surfaces of Zr/V-added Al-7Si-3Cu-0.3Mg alloy in (a) as-cast and (b,c,d) T6 heat-treated states and tested at (a,b) 293 (20), (c) 473 (200) and (d) 573 K (300 °C) temperatures.

4. Discussion

4.1 Microstructural evolution and phase transformations

Although the added level of Zr in this study is quite low (0.15 %), a limited amount of primary $(AlSi)_3(ZrTi)$ compounds with flaky morphology can be seen throughout the microstructure (Fig. 1b and Fig. 5). The majority of Zr and V added to the alloy tends to reside inside α-Al matrix (Fig. 3) and contribute to the refinement of the α-Al grains [24]. The amount of V rejected to interdendritic regions were solely bound to pro-eutectic α-$Al_{15}(MnFe)_3Si_2$ phase (Fig. 1 and Fig. 5), which caused a slight increase of the fraction of interdendritic α-$Al_{15}(MnFe)_3Si_2$ in the microstructure. The previous investigation [24] revealed the presence of interdendritic $(AlSi)_2(VMn)$ phase in the slowly-solidified microstructure. On the contrary, in the present study, the higher cooling rate appears to facilitate the α-Al solid solution to retain more V during solidification and, as a result, lower amount of V can segregate to interdendritic regions, thus suppressing the formation of $(AlSi)_2(VMn)$ phase. Worthy to note that the selected addition levels of V (0.3 wt. %) and Zr (0.15 wt. %) in the present study, showed no significant influence on the fraction of insoluble intermetallics.

Solution treatment, which is the first stage of T6 heat treatment, is normally applied to dissolve interdendritic Cu- and Mg-rich particles into the α-Al matrix, and also spheroidize the eutectic silicon particles [3, 28, 43]; however, this study also revealed that the solutionizing stage can also promote the precipitation of a large volume fraction of Zr/V-rich precipitates inside α-Al matrix (see Fig. 8b,d). Considering that the peritectic-forming Zr and V elements tend to partition towards the α-Al grain cores during solidification and remain in α-Al solid solution (Fig. 3) and their excess amounts tended to form the insoluble, interdendritic intermetallics (see Fig. 5), it can be thus inferred that the supersaturated Zr and V amounts in solid solution of α-Al matrix obtained during non-equilibrium solidification can be only involved in the solid-state precipitation occurring inside α-Al matrix.

As mentioned earlier, a very limited amount of α-Al(MnFe)Si precipitates formed in α-Al grain interiors of the base alloy at solution heat treatment stage (see Fig. 8a,c). Since Mn is normally added to promote the formation of α-$Al_{15}(MnFe)_3Si_2$ over β-Al_5FeSi during solidification [27], some amount of Mn can also accumulate into primary α-Al matrix during solidification. Non-equilibrium solidification, in turn, can also result in the supersaturated Mn, Cr and Fe in α-Al solid solution; hence, the solid-state precipitation reaction involving Mn occurred during solution heat treatment.

As stated earlier (Section 3.1), the presence of V in the Zr/V-modified alloy significantly increased the density of α-Al(MnFe)Si intradendritic precipitates. This behavior can be explained by the peritectic nature of V and its ability to substitute Mn in α-Al(MnFe)Si phase. The combined involvement of V and Mn to form precipitates in the α-Al grain interiors is highly beneficial; the partitioning behavior of V during solidification is opposite to that of Mn and this behavior can lead to a more uniform distribution of the precipitates. Moreover, both Mn and V are the slow diffusers, with relatively high solid solubility in α-Al; hence, the solid-state precipitation of α-Al(MnVFe)Si phase occurs in relatively high-volume fractions. It can be also noted that the size of precipitates is in the order of 100 nm (see Fig. 9 and Fig. 10), which is significantly larger than the Cu-rich precipitates formed at ageing heat treatment stage (see Fig. 7). Muggerud et al. [32] investigated the solid-state precipitation behavior of α-Al(MnFe)Si in direct-chill cast 3xxx alloy annealed at 648 K (375 ^{o}C) for a various time duration, and it has been found that too long annealing time considerably decreases the volume fraction of precipitates due to their coarsening behavior. Optimization of solution heat treatment parameters of secondary Al-7Si-3Cu-0.3Mg alloy with Zr and V additions may result in the precipitation of α-Al(MnVFe)Si in smaller sizes and higher number density, thus contributing much better to the high-temperature strengthening of Al-Si alloys. Majority of α-Al(MnVFe)Si precipitates possess nearly a cubic shape and seem to have the

same orientation to the α-Al matrix. The α-Al(MnFe)Si dispersoids have been recently shown to be partly coherent with the Al matrix [37].
The solutionizing stage also caused the α-Al solid solution supersaturated with Zr to decompose and precipitate inside the α-Al matrix in the form of $(AlSi)_3(ZrTi)$ phase in a very limited amounts and average length of around 100 nm. Gao et al. [21] have reported how Ti and V can accumulate into Al_3Zr phase [44]; however, in the present study, only Ti, which is present in the alloy as a trace element, tended to substitute Zr, whereas V showed no tendency to contribute to the formation of $(AlSi)_3(ZrTi)$ phase. This can be due to a more favorable involvement of V in the formation of α-Al(MnVFe)Si phase. Sepehrband et al. [25] revealed that solution heat treatment of A319 alloy containing Zr, at 778 K (505 ºC) for 24 h caused the precipitation of Al_3Zr particles with the length of around 210-250 nm in grain interiors. The smaller size of these rod-like precipitates observed in the present study can be due to lower solutionizing temperature [758 K (485 ºC)] applied. In a recent study, the $(AlSi)_3(ZrTi)$ precipitates have been shown to be partly coherent with the Al matrix [19].
A few amounts of V appear to be also bound to irregular-shaped V-rich precipitate, which is believed to be $(AlSi)_2(VCr)$ phase, in the α-Al grain interiors, however, further crystallographic investigations of this precipitate are necessary.
It is worthy to note that the presence of several types of transition metals, such as trace (impure) Mn, Fe, Ti and Cr, and deliberately-added Zr and V, in the Zr/V-modified alloy yielded the formation of substantial volume fraction of Zr/V-rich precipitates during solution heat treatment stage (see Fig. 8).

4.2 Microstructure-property relationship

The addition of Zr and V showed a slight influence on the tensile properties of Zr/V-modified alloy in the as-cast state; the YS increased slightly by ~5 MPa, which can be associated with the contribution of alloying additions to solid solution strengthening [45].
The role of T6 heat treatment in the strengthening of Al-Si-Cu-Mg based alloys is well-known [28]. The solid-state precipitation reactions involving Cu and Mg can provide significant strengthening by precipitation hardening mechanism [28]; comparison of the tensile properties of the base and Zr/V-modified alloys reveals slightly higher YS by ~4 MPa in Zr/V-modified alloy. This indicates that the enhanced properties of both alloys upon T6 heat treatment is primarily the consequence of intradendritic Cu/Mg-rich precipitates while the influence of intradendritic Zr/V-rich particles on alloy strength at room temperature appears to be negligible.
Increasing the testing temperature decreased the tensile properties (UTS and YS) of both alloys (Fig. 11a,b). It is also noticed (Fig. 11a,b) that UTS parameter is more sensitive to temperature compared to YS of the alloys [47]. With increasing the temperature, the cross slips are thermally activated by climbing of dislocations resulting in the reduction of material strength [13, 21, 36, 48]. In addition, the solute diffusion of Cu and Mg becomes increasingly effective in promoting precipitate coarsening within the matrix, hence further contributing to the alloy softening [5, 36]. Comparison of the tensile properties of the alloys as function of testing temperature (Fig. 11a,b) indicates that the effect of Zr and V additions seems to be more evident at high temperatures; both the YS and UTS parameters of the Zr/V-modified alloy are higher by ~ 20 % with respect to the base alloy. This improvement is attributed to the formation of intradendritic V/Zr-rich precipitates, which are much more thermally stable in comparison with the Cu/Mg-rich precipitates.
The effect of adding Zr and V on elongation to failure remains almost negligible (see Fig. 11c), which can be explained by the fact that both Zr and V tended to concentrate mainly in grain interiors during solidification, and showed less impact on the evolution of insoluble, interdendritic intermetallics.

Conclusions

The effects of combined V and Zr additions, and heat treatment on microstructure and mechanical properties of the secondary Al-7Si-3Cu-0.3Mg alloy were investigated. The following conclusions can be drawn from this study.

Majority of Zr and V added to the alloy were retarded inside α-Al matrix during solidification. The excess Zr amount that was rejected to interdendritic regions during alloy solidification was involved in the formation of flaky-like, interdendritic $(AlSi)_3(ZrTi)$ compounds, whereas excess V was bound to script-like $Al_{15}(MnFe)_3Si_2$ phase. A slight increase in yield strength of Zr/V-modified alloy in the as-cast state can be attributed to the solid solution hardening effects of V and Zr.

Upon heat treatment, the interdendritic intermetallics containing Zr and V, such as $(AlSi)_3(ZrTi)$ and $Al_{15}(FeMnV)_3Si_2$ compounds, remained undissolved into the α-Al matrix. The supersaturated solid solution of Zr and V in α-Al matrix, obtained during solidification, tended to decompose and precipitate inside α-Al grains during solution heat treatment stage. The interaction between the deliberately-added Zr and V, and impure (trace) Mn, Fe, Ti and Cr elements promoted the formation of a substantial volume fraction of multiple intradendritic, nano-sized precipitates: the blocky-like α-Al(MnVFe)Si, the flaky-like $(AlSi)_3(ZrTi)$ and the irregular-shaped $(AlSi)_2(VCr)$ phases. The α-Al(MnVFe)Si accounted for the major part of the thermally stable phases formed during solutionizing stage; the interaction between peritectic-forming V and eutectic-forming Mn to form the α-Al(MnVFe)Si precipitate is believed to be highly beneficial due to their opposite partitioning behavior, as well as their higher solubility and lower diffusivity in α-Al matrix. An increase of the UTS and YS of Zr/V-modified alloy with respect to the base alloy at elevated temperatures by ~ 20% are believed to be the consequence of the thermally stable precipitates formed during solution heat treatment.

Acknowledgements

This work was developed within the ERASMUS MUNDUS Project (Silkroute - Strand 1/ Lot L09, project n. 545765). The author would like to acknowledge Raffineria Metalli Capra Spa (Brescia, Italy) for the experimental support to the research.

References

[1] Y. Birol, Mater. Sci. Technol., 28 (2012) 363-367.
[2] N.A. Belov, A.N. Alabin, I.A. Matveeva, D.G. Eskin, Trans. Nonferrous Met. Soc. China, 25 (2015) 2817-2826.
[3] M.M. Makhlouf, H.V. Guthy, Journal of Light Metals, 1 (2001) 199-218.
[4] M. Javidani, D. Larouche, Int. Mater. Rev., 59 (2014) 132-158.
[5] S.W. Choi, Y.M. Kim, K.M. Lee, H.S. Cho, S.K. Hong, Y.C. Kim, C.S. Kang, S. Kumai, J. Alloys Compd., 617 (2014) 654-659.
[6] M.T. Di Giovanni, E. Cerri, D. Casari, M.A.T.T.I.A. Merlin, L.A.R.S. Arnberg, G.L. Garagnani, Metall. Mater. Trans. A, 47 (2016) 2049-2057.
[7] A.R. Farkoosh, X. Grant Chen, M. Pekguleryuz, Mater. Sci. Eng., A, 620 (2014) 181-189.
[8] S.K. Shaha, F. Czerwinski, W. Kasprzak, J. Friedman, D.L. Chen, Metall. Mater. Trans. A, 46 (2015) 3063-3078.
[9] K.E. Knipling, D.C. Dunand, D.N. Seidman, International Journal of Materials Research, 97 (2006) 246-265.
[10] J. Rakhmonov, G. Timelli, F. Bonollo, Adv. Eng. Mater., 18 (2016) 1096-1105.
[11] S.K. Shaha, F. Czerwinski, W. Kasprzak, J. Friedman, D.L. Chen, Thermochim. Acta, 595 (2014) 11-16.
[12] S.K. Shaha, F. Czerwinski, W. Kasprzak, D.L. Chen, Mater. Des., 59 (2014) 352-358.
[13] J. Hernandez-Sandoval, G.H. Garza-Elizondo, A.M. Samuel, S. Valtiierra, F.H. Samuel, Mater. Des., 58 (2014) 89-101.
[14] D. Stefanescu, Casting, ASM International, 1988.
[15] M. Tupaj, A.W. Orlowicz, M. Mroz, A. Trytek, O. Markowska, Arch Foundry Eng, 16 (2016) 125-128.
[16] T. Gao, D. Li, Z. Wei, X. Liu, Mater. Sci. Eng., A, 552 (2012) 523-529.

[17] H.A. Elhadari, H.A. Patel, D.L. Chen, W. Kasprzak, Mater. Sci. Eng., A, 528 (2011) 8128-8138.
[18] U.M.J. Boin, M. Bertram, JOM, 57 (2005) 26-33.
[19] W. Kasprzak, B.S. Amirkhiz, M. Niewczas, J. Alloys Compd., 595 (2014) 67-79.
[20] A.R. Farkoosh, X. Grant Chen, M. Pekguleryuz, Mater. Sci. Eng., A, 627 (2015) 127-138.
[21] J.G. Kaufman, E.L. Rooy, Aluminum Alloy Castings: Properties, Processes, and Applications, ASM International, Materials Park, 2004.
[22] G. Timelli, G. Camicia, S. Ferraro, R. Molina, Met. Mater. Int., 20 (2014) 677-686.
[23] D. Casari, M. Merlin, G.L. Garagnani, J. Mater. Sci., 48 (2013) 4365-4377.
[24] J. Rakhmonov, G. Timelli, F. Bonollo, Mater. Charact., 128 (2017) 100-108.
[25] P. Sepehrband, R. Mahmudi, F. Khomamizadeh, Scripta Mater., 52 (2005) 253-257.
[26] J. Rakhmonov, G. Timelli, F. Bonollo, Metall. Mater. Trans. A, 47 (2016) 5510-5521.
[27] J. Rakhmonov, G. Timelli, F. Bonollo, L. Arnberg, Int J Metalcast, (2016) 1-11.
[28] E. Sjolander, S. Seifeddine, J. Mater. Process. Technol., 210 (2010) 1249-1259.
[29] J. Barrirero, J.H. Li, M. Engstler, N. Ghafoor, P. Schumacher, M. Oden, F. Mucklich, Scripta Mater., 117 (2016) 16-19.
[30] H.M. Medrano-Prieto, C.G. Garay-Reyes, C.D. Gómez-Esparza, I. Estrada-Guel, J. Aguilar-Santillan, M.C. Maldonado-Orozco, R. Martínez-Sánchez, Mater. Charact., 120 (2016) 168-174.
[31] S. Capuzzi, G. Timelli, A. Fabrizi, F. Bonollo, in: 7th International Light Metals Technology Conference, LMT 2015, July 27, 2015 - July 29, 2015, Trans Tech Publications Ltd, Port Elizabeth, South africa, 2015, pp. 212-218.
[32] S. Shankar, Y.W. Riddle, M.M. Makhlouf, Metall. Mater. Trans. A, 35A (2004) 3038-3043.
[33] Y.J. Li, A.M.F. Muggerud, A. Olsen, T. Furu, Acta Mater., 60 (2012) 1004-1014.
[34] M. Tocci, R. Donnini, G. Angella, A. Pola, Mater. Charact., 123 (2017) 75-82.
[35] H.-W. Huang, B.-L. Ou, Mater Design, 30 (2009) 2685-2692.
[36] A.M.A. Mohamed, F.H. Samuel, S. Al Kahtani, Mater. Sci. Eng., A, 577 (2013) 64-72.
[37] A.M.A. Mohamed, F.H. Samuel, A Review on the Heat Treatment of Al-Si-Cu/Mg Casting Alloys, Heat Treatment, in: F. Czerwinski (Ed.) Heat Treatment - Conventional and Novel Applications, InTech, 2012.
[38] E. Rincon, H.F. Lopez, M.M. Cisneros, H. Mancha, Mater. Sci. Eng., A, 519 (2009) 128-140.
[39] Q.G. Wang, C.H. Caceres, J.R. Griffiths, Metall and Mat Trans A, 34 (2003) 2901-2912.
[40] W.H. Hunt, J.R. Brockenbrough, P.E. Magnusen, Scripta Metallurgica et Materialia, 25 (1991) 15-20.
[41] M. Zamani, S. Seifeddine, A.E.W. Jarfors, Materials & Design, 86 (2015) 361-370.
[42] G. Rajaram, S. Kumaran, T.S. Rao, Materials Science and Engineering: A, 528 (2010) 247-253.
[43] S.Z. Lu, A. Hellawell, Metall Trans A, 18 (1987) 1721-1733.
[44] T. Gao, X. Liu, Journal of Materials Science & Technology, 29 (2013) 291-296.
[45] D. Casari, T.H. Ludwig, M. Merlin, L. Arnberg, G.L. Garagnani, Mater. Sci. Eng., A, 610 (2014) 414-426.
[46] S. Saleem, H. Fredriksson, Mater. Sci. Forum, 765 (2013) 135-139.
[47] Y. Sun, S.P. Pang, X.R. Liu, Z.R. Yang, G.X. Sun, Trans. Nonferrous Met. Soc. China, 21 (2011) 2186-2191.
[48] A.K. Dahle, K. Nogita, S.D. McDonald, C. Dinnis, L. Lu, Mater. Sci. Eng., A, 413 (2005) 243-248.